

Stellingen
behorende bij het proefschrift

**Development of dustproof, low pressure drop reactors
with structured catalyst packings**

—
**the Bead String Reactor and
the Zeolite-covered Screen Reactor**

door H.P.A. Calis

1. Een greep uit de stellingen bij proefschriften doet vermoeden dat de stellingen vooral ten doel hebben, de spitsvondigheid van de promovendus te etaleren.
2. Het feit dat docenten aan een universiteit nog steeds les mogen geven zonder ook maar één cursus didactiek of leerplanontwikkeling te hebben gevolgd, relativeert de grootse plannen voor verbetering van het universitaire onderwijs.
3. Technologen moeten hun best blijven doen om onderzoekers uit de 'fundamentele hoek' ervan te overtuigen, dat ook technologie tot de wetenschap behoort.
4. Het leggen van een relatie tussen katalysatoractiviteit en 'space velocity' duidt op een gebrekkige kennis van de reactorkunde.
S. Sato, Y. Yu-u, H. Yahiro, N. Mizuno en M. Iwamoto, Appl. Catal. 70 (1991) L1-L5.
5. 'Meten is weten' geldt helaas alleen voor degenen die geoefend zijn in de statistiek.
6. Protocollen zijn bijzonder nuttig voor computers, en tevens voor mensen die twijfelen aan hun eigen improvisatievermogen of dat van anderen.

Development of dustproof, low pressure drop reactors
with structured catalyst packings

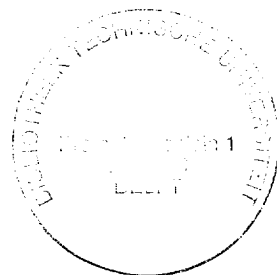
—
the Bead String Reactor and
the Zeolite-covered Screen Reactor

PROEFSCHRIFT

ter verkrijging van de graad van doctor
aan de Technische Universiteit Delft,
op gezag van de Rector Magnificus Prof.ir. K.F. Wakker,
in het openbaar te verdedigen ten overstaan van een commissie,
door het College van Dekanen aangewezen,
op maandag 29 mei 1995 te 16.00 uur
door

Hans Peter Alexander CALIS

scheikundig ingenieur,
geboren te Woudenberg



Dit proefschrift is goedgekeurd door de promotor:
Prof.ir. C.M. van den Bleek

Toegevoegd promotor: Dr.ir. A.W. Gerritsen

Samenstelling promotiecommissie:

Rector Magnificus, voorzitter
Prof.ir. C.M. van den Bleek, Technische Universiteit Delft, promotor
Dr.ir. A.W. Gerritsen, Technische Universiteit Delft, toegevoegd promotor
Prof.dr.ir. H. van Bekkum, Technische Universiteit Delft
Prof.dr. R. Krishna, Universiteit van Amsterdam
Prof. B. Scarlett M.Sc., Technische Universiteit Delft
Prof.dr.ir. S.T. Sie, Technische Universiteit Delft
Dr.ir. H. Hölscher, Shell Research B.V.



Het grootste deel van dit werk is financieel ondersteund door de Nederlandse organisatie voor Wetenschappelijk Onderzoek (NWO) en Shell Research B.V.

CIP-GEGEVENS KONINKLIJKE BIBLIOTHEEK, DEN HAAG

Calis, Hans Peter Alexander

Development of dustproof, low pressure drop reactors with
structured catalyst packings : the bead string reactor and
the zeolite-covered screen reactor / Hans Peter Alexander
Calis. — Delft : Eburon P&L
Proefschrift Technische Universiteit Delft. — Met
samenvatting in het Nederlands.
ISBN 90-5651-005-3
NUGI 812/813
Trefw.: reactoren

Distributie:
EburonP&L, Postbus 2867, 2601 CW Delft

Drukwerk:
Ponsen & Looijen BV, Wageningen

Copyright © 1995 by H.P.A. Calis
All rights reserved

Abstract

Many concepts for low pressure drop reactors with more or less structured catalyst packings have been marketed; commercially successful ones are the monolithic reactor, radial flow reactor, lateral flow reactor and parallel passage reactor. In addition to and as an alternative for these existing concepts of low pressure drop reactors with structured catalyst packings, two new concepts are proposed in this thesis: the Bead String Reactor (BSR) and the Zeolite-covered Screen Reactor (ZSR). The BSR is characterized by the fact that the catalyst material is fixed (by virtue of its shape) on strings that are arranged, parallel to each other, in the reactor, parallel (or cross) to the flow. Many possible attractive features of this reactor come to mind when thinking about the concept: a low pressure drop; the design freedom to choose the voidage between 100% and as low as 10%; the possibility to have lateral transport of heat and reactants across the complete diameter of the reactor; effective mass and heat transfer between fluid and catalyst phase; the possibility to fill the reactor with (*i.e.* make strings of) standard ring-shaped or hollow catalyst particles; the possibility of virtually dustproof operation; the elimination of maldistribution of gas or liquid in three-phase processes; the possibility to operate three-phase processes not only in cocurrent but also in countercurrent mode at high gas and liquid flow rates; the possibility to supply heat directly to the catalyst by using the strings onto which the catalyst material is fixed as electrical heating elements.

As a first step in the assessment of the feasibility of the BSR concept for gas/solid systems, three reactor engineering aspects of the BSR have been investigated theoretically and experimentally:

- (i) momentum transport (*i.e.* pressure drop and flow distribution);
- (ii) mass transfer (between fluid and catalyst);
- (iii) susceptibility to fouling with dust.

Ad (i) In the study of momentum transport phenomena in a BSR, a cold flow test section was used with lab-scale BSR modules filled with regular square arrays of smooth rods, strings of ceramic beads and strings of extruded catalyst particles. In this test section the pressure drop across a representative part of the reactor was measured as a function of the rod or particle diameter, the relative pitch, the roughness of the rods or strings, and the gas velocity. Using the theory and experimental data presented in this thesis, the pressure drop across a typical BSR can be predicted with an inaccuracy ranging from a few percents (for laminar flow or a small relative roughness) to *ca.* 50% (for the transition regime or for fully rough turbulent flow).

Ad (ii) Theoretical relations were derived to describe the mass transfer rate in laminar flow, as a function of the reactor voidage and the ratio of the time constants for reaction and mass transfer. For turbulent flow, mass transfer coefficients were determined experimentally by measuring the mass decrease of sublimating beads of naphthalene inserted in the bead strings. In the experiments the influence was tested of the axial and lateral position of the naphthalene beads, the diameter of the beads, the pitch of the strings and the gas velocity. The most important result of the experimental study is that based on simple pressure drop measurements, the mass transfer coefficient in a typical BSR can be predicted with an inaccuracy of *ca.* 30%, using the Chilton-Colburn analogy between momentum and mass transfer.

Ad (iii) The fouling of the BSR with dust was studied in a cold flow test section, using industrial fly ash. As a comparison also the fouling characteristics of the Parallel Passage Reactor (PPR) were studied. Under the tested conditions, the accumulation of dust in either reactor has no significant effect on the pressure drop. It is expected that the added mass transfer resistance due to accumulated dust is negligible in a BSR; in a PPR, however, the accumulation of dust may result in a decimation of the apparent catalyst activity.

To predict the performance of a BSR, several mathematical models were developed. These models were validated experimentally, using the selective catalytic reduction (SCR) of nitric oxide (NO) with excess ammonia, oxygen and water as the test reaction. The NO conversion in lab-scale BSR modules could be adequately predicted (with an average relative error of 5%) with a simple model containing only one ordinary differential equation, using generalized algebraic equations to estimate the catalyst particle effectiveness factor. The other models systematically under- or overpredicted the conversion, which could be explained from the model assumptions; these models showed average relative errors of *ca.* 10%. The accuracy of the mathematical models is satisfying, considering the fact that they contained no parameters to be fitted from the validation experiments: all parameters in the models were estimated from theoretical relations or from independent experiments on pressure drop, mass transfer, reaction kinetics and catalyst pore diffusion. The latter two were studied separately in an internal recycle reactor of the Berty type.

Based on this study of the BSR, the claimed attractive features cannot be rejected. Whether the BSR concept is economically feasible, however, fully depends on the price tags of pressure drop, mass transfer rate, reactor voidage, *etc.*, and on the cost of manufacturing modules containing strings of catalyst particles. The cost of mechanically stringing catalyst particles is expected to be several dollars per kilogram, which seems not to be prohibitive for 'specialty' catalysts. This allows the tentative conclusion that a gas/solid BSR will become economically attractive for processes where pressure drop is expensive (*i.e.* where flowrates are high and the pressure is low), where reactor space is expensive (because of high pressure or limited space), and where intensive or rapid heating of the catalyst material is important. The

feasibility of the BSR and related reactors for gas/liquid/solid systems (trickle flow), will be investigated in a subsequent PhD project.

The second novel reactor presented in this thesis, the Zeolite-covered Screen Reactor (ZSR), is characterized by catalyst packings prepared through *in situ* crystallization of zeolite crystals on structured supports. The support may consist, for example, of metal wire gauze or thin metal sheets, of which flat or corrugated plates are stacked or rolled-up to create the packing. The ZSR concept opens the way to low pressure drop reactors with zeolitic catalysts that are optimally accessible for the reactants. It shares the advantages of the washcoated monolithic reactor with a metal or ceramic support, and is therefore especially attractive when very fast reactions are involved. Possible applications are catalytic flue gas treatment and hydrocarbon conversions, such as selective partial oxidation of small hydrocarbons. Especially in the latter application the advantage of the high accessibility is important, because the short contact time promotes a high selectivity.

To demonstrate the feasibility of the ZSR concept, a packing was prepared consisting of ZSM-5 crystals *in situ* grown on metal wire gauze. After incorporating copper ions in the zeolites (through ion exchange), the packing was tested on its activity for SCR of nitric oxide with ammonia at 350°C. Both the activity and selectivity of the catalyst packing proved to be superior to conventional vanadia/titania catalysts. This demonstrates the feasibility of the ZSR concept, and therefore the further development of this reactor will be the subject of a separate PhD project.

Contents

Abstract	3
Chapter 1. Introduction	9
Chapter 2. Momentum Transport in a Bead String Reactor	25
Chapter 3. Mass Transfer in a Bead String Reactor	63
Chapter 4. Kinetic study of the test reaction—SCR of NO with excess NH ₃ .	99
Chapter 5. Modeling of the Bead String Reactor and experimental validation of the models	143
Chapter 6. Mass transfer in a Parallel Passage Reactor	175
Chapter 7. Fouling of Bead String Reactors and Parallel Passage Reactors with dust	197
Chapter 8. Demonstration of the Zeolite-covered Screen Reactor concept . .	231
Samenvatting	255
Dankwoord	261
Curriculum Vitae	265

**Full tables of contents of the chapters are listed
on the reverse sides of the chapter title pages**



Chapter 1

Introduction

partly based on:

H.P. Calis, A.W. Gerritsen and C.M. van den Bleek, 1994, Gestructureerde katalysatorpakkingen bieden specifieke voordelen—de 'bead string' reactor en de 'zeolite-covered screen' reactor. *NPT Procestechologie*, March 1994, 33-39.

Contents

1	The why and how of reactors with structured catalyst packings	11
1.1	The incorporated monolithic reactor	13
1.2	The washcoated monolithic reactor	14
1.3	The glued-catalyst reactor	15
1.4	The parallel passage reactor and lateral flow reactor	15
2	New concepts	17
2.1	The bead string reactor	17
2.2	The zeolite-covered screen reactor	21
3	Goal of the thesis work and structure of the thesis	22
	References	24

1 The why and how of reactors with structured catalyst packings

For many reactor systems in which gaseous reactants react over solid catalysts (gas/solid reactors), pressure drop is a major factor in the overall costs of the process. A striking example are reactors for catalytic flue gas treatment, such as selective catalytic reduction (SCR) of NO_x with ammonia. In this process, a pressure drop higher than 10 to 20 mbar is intolerable from an economic point of view. The reason is that a higher pressure drop has to be compensated for by a ventilator to force the flue gas through the stack, combined with the fact that flue gas flows are usually very large — an average electric power plant easily produces 500 m³ of flue gas per second. A simple calculation shows that at this flow rate, a pressure drop of 20 mbar corresponds to a dissipated power of 1 MW, or an annual energy bill of approximately \$ 500,000.

Another example of the importance of pressure drop is the catalytic dehydrogenation of hydrocarbons, *e.g.* paraffins. In this process the pressure plays an important role, because the conversion of the reactants in the reactor is limited by the thermodynamic equilibrium, which depends on the hydrogen pressure. A high pressure drop across the reactor corresponds to a necessarily high pressure at the reactor inlet, which has a negative influence on the dehydrogenation rate.

In such situations it may be advantageous to geometrically divide the reactor into parts occupied by catalyst and empty parts through which the fluid flows. Such a division may be obtained by structuring the catalyst packing rather than randomly packing the reactor with catalyst particles. By creating such a structure that the fluid follows a path as little tortuous as possible, the friction between the fluid and the catalyst is minimized, resulting in a minimum pressure drop. This consideration has led to the development of various ingenious concepts for low pressure drop reactors with structured catalyst packings, the most successful of which are discussed in the following section. In this thesis two new concepts will be proposed and compared with existing members of the same family.

Though a low pressure drop is one of the most important incentives for the development of structured catalyst packings, it is not the only one. An obvious incentive is the dustproof operation that can be obtained by creating more or less straight flow paths for the gas flow. Indeed, decreasing the contact between the two phases leads to a decrease of the collision frequency of dust particles with the catalyst, resulting in a slower accumulation of dust on the catalyst. This aspect is important in (a.o.) the catalytic removal of NO_x from flue gas of coal-fired furnaces and power

plants, since these flue gases contain dust concentrations up to 20 g/m^3 . Although it is technically possible to arrange the deNO_x reactor downstream of an electrostatic precipitator or another type of dust-removal unit, it is usually preferred to arrange the deNO_x unit upstream of the dust-removal unit. Dustproof operation of the deNO_x catalyst packing then is a prerequisite.

Application of structured catalyst packings is not limited to gas/solid reactors: also gas/liquid/solid reactors may benefit from the geometrical division of the phases. Like distillation, absorption and stripping towers with structured packings, a reactor with a well thought-out catalyst packing enables countercurrent operation at high gas and liquid flows, that in randomly packed reactors would result in maldistribution and flooding.

The various types of reactors with structured catalyst packings that have been described in the literature over the years, can be subdivided into three groups:

- Reactors in which one or more very large catalyst 'particles' are stacked, and where the reactor derives its characteristics from the structure of the catalyst 'particles'. An example of this type of reactor is the monolithic reactor. The word 'monolith' is reserved—in this thesis—for extruded ceramic bodies containing many parallel channels, where the catalytically active material is distributed more or less homogeneously over the ceramic material of the body. This type of monolithic reactor is sometimes called 'incorporated monolith', to distinguish it from the 'washcoated monolith' described below. A review of monolithic reactor technology was recently given by Cybulski and Moulijn (1994).
- Reactors filled with a structured packing to which the catalyst material is attached. An example of such a packing is a honeycomb shaped ceramic or metal body, on the surface of which a thin coating is deposited of a high surface area material—the so-called 'washcoat'. On the external surface of the coating, the catalytically active material is deposited. This type of reactor is sometimes called 'washcoated monolith'.

Other examples of this type of packing are structures of wires, wire gauze or thin plates onto which small catalyst particles are glued.

- Reactors that are partially filled with 'cages' or 'envelopes' containing randomly packed beds of catalyst particles. In these reactors the fluid flows along or laterally through the beds. Examples of this type of reactor are the parallel passage reactor (PPR; *cf.* Calis *et al.*, 1994) and the lateral flow reactor (LFR; *cf.* Woldhuis, 1992), see Figures 1-1 and 1-2.

Apart from the advantage that these reactor concepts have in common, *i.e.*, a low pressure drop compared to traditional, randomly packed reactors, they all have more or less specific advantages and disadvantages, that make them suitable or not for a specific application.

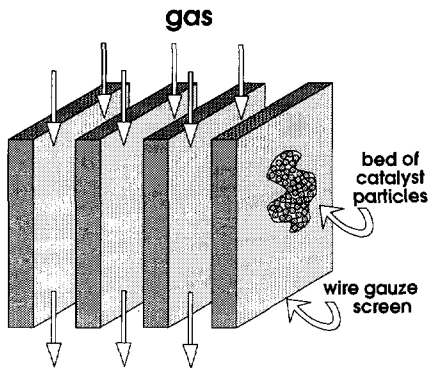


Figure 1-1 Concept of the parallel passage reactor.

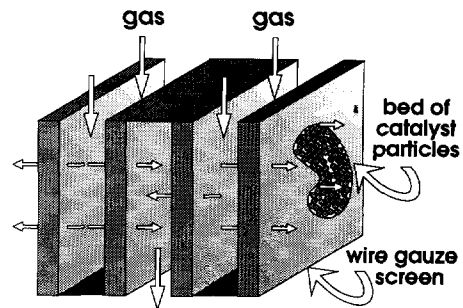


Figure 1-2 Concept of the lateral flow reactor.

In the remainder of this chapter the pros and cons of these reactor concepts will be briefly discussed, and two new concepts will be introduced. Furthermore the goal of this thesis work will be stated, and the structure of the thesis will be explained.

1.1 The incorporated monolithic reactor

The most important attractive features of the incorporated monolithic reactor, besides the low pressure drop, are the relatively high stability with respect to dust and the fact that the monolithic reactor is considered 'proven technology'. Stability toward dust implies two features: slow accumulation of dust in the channels and the durability of the monolith structure with respect to the abrasive force of dust. Although it is true that dust only slowly accumulates in monolithic reactors, the process of dust trapping is self-accelerating and can only be reversed using soot blowers. Once dust accumulates on the walls of a specific channel, the gas velocity through these channels decreases, and so does the drag force acting on the accumulated dust. As a result more dust will settle on the walls of this channel. Once a channel has been blocked completely, it can only be re-opened by forcing the plug of dust through the channel. The danger of channel plugging sets a lower limit on the channel diameter in applications with dust-containing gases.

In the durability of the incorporated monolithic reactor with respect to the abrasive force of dust, it distinguishes itself from the washcoated monolithic reactor, in which abrasion of the relatively soft washcoat can result in fast deactivation. For this reason the incorporated monolithic reactor is widely used, in contrast to the washcoated monolithic reactor, for catalytic deNO_xing of dust-containing flue gas from installations fired with coal or heavy oil.

An attractive feature of the incorporated monolithic reactor for special applications is the possibility of leading reactants separately through adjacent channels, the reaction taking place in the porous wall separating the channels.

Against these attractive features, there are various drawbacks that make the incorporated monolithic reactor unattractive for many applications. One of the most important disadvantages follows from the fact that the ceramic body has a double function. On one hand it serves as the skeleton of the packing, requiring a high mechanical stability, on the other hand it serves as the carrier for the catalytically active material, requiring a high internal surface area. As a result of the necessary compromise, incorporated monolithic reactors often have a low specific internal surface area, and a correspondingly low catalytic activity per unit mass of catalyst packing. Other important drawbacks of the monolithic reactor are the fact that lateral or radial transport of the reactants is limited to the diameter of the channels, and the poor radial and axial transport of heat. The last drawback that will be mentioned here is the fact that due to the extrusion process, the monolith units are longitudinally isomorphic. Consequently the channels are smooth in the direction of flow, which, in combination with the relatively small diameter of the channels, results in laminar flow under typical conditions. Obviously this feature favors a low pressure drop, but it also results in ineffective heat and mass transfer.

1.2 The washcoated monolithic reactor

The washcoated monolithic reactor resembles the incorporated monolithic reactor in many respects, and consequently shares its attractive features concerning pressure drop and accumulation of dust. Furthermore also the washcoated monolithic reactor is 'proven technology'. An important advantage compared to the incorporated monolithic reactor is the fact that the function of skeleton and catalyst carrier are separated: the skeleton can be optimized with respect to pressure drop and mechanical stability, whereas the washcoat can be optimized with respect to catalyst activity. This allows the use of strong ceramic materials, of which honeycomb structures with thin walls (< 1 mm) can be manufactured. In combination with thin washcoats, this yields reactors that are especially suited for very fast reactions with low pressure drops. The application of the washcoated monolithic reactor for automotive exhaust gas cleaning is thus explained.

Manufacture of a washcoated monolithic reactor using thin sheets of metal for the support of the washcoat, offers two interesting possibilities. In the first place it is possible to use the metal structure as an electric heating element. This enables very fast warming-up (*i.e.*, starting-up) of the reactor, which might be useful in the application for automotive exhaust gas cleaning (*cf.* Bell *et al.*, 1995). Furthermore it enables very effective heat supply to the catalyst in strongly endothermic reactions. In the second place units can be manufactured that are not longitudinally isomorphic. The sheets of metal can be shaped in such a way that upon stacking or rolling-up of the sheets, channels are created that have, *e.g.*, a slight zigzag shape. This results in more effective heat and mass transfer to the channel walls. Another advantage of the metal structure is the better radial transport of heat.

Disadvantages of the washcoated monolithic reactor compared to the incorporated monolithic reactor are the considerably smaller stability with respect to attrition by dust (as discussed) and the limited thickness of the washcoat (*ca.* 100 μm). The latter point renders the washcoat reactor unattractive for intrinsically slow reactions. A drawback shared with the incorporated monolithic reactor is the absence of radial mass transfer between the channels. However, when a metal body is used, this drawback can be partially overcome by creating holes in the channel walls or by creating more complicated structures such as those known from static mixers like Sulzer packings.

1.3 The glued-catalyst reactor

The small reputation of catalyst packings consisting of wire, wire gauze or sheet structures onto which catalyst particles have been glued, suggests that the advantages of this concept are normally outweighed by the disadvantages. Nevertheless this type of catalyst packing has been (re-)invented and patented time and again over the last 25 years. Often claimed advantages are the low pressure drop (compared to randomly packed reactors) and the freedom to use commercially available, standard catalyst particles. The latter feature saves the trouble of re-optimizing an existing catalyst formula, which is necessary for application of a catalyst in monolithic reactors. When a metal structure is used, there is again the possibility to supply electric heat to the catalyst. However, the heat transfer rate is limited by the layer of glue between the catalyst particle and the support.

A limitation of this concept is that only a monolayer of catalyst particles can be glued to the structure, and that only small particles ($< 1\text{ mm}$) can be attached with sufficient mechanical stability. This limits the fraction of reactor volume that is occupied by catalyst material to about that of a monolithic reactor. However, because catalyst particles with a high specific internal surface area and an optimum pore structure can be used, the activity per unit reactor volume may be higher than that of a monolithic reactor.

An inherent drawback of gluing catalyst particles, is that the particles either are partially submerged in the glue, or have only a small contact area with the support, making the packing mechanically unstable. Finally, the sensitivity for dust of these packings is expected to be higher than that of the monolithic reactors, due to the rough surface of the channels which lends itself for settling of dust.

1.4 The parallel passage reactor and lateral flow reactor

Like the glued-catalyst reactor, the concept of reactors partially filled with randomly packed shallow beds of catalyst particles springs from the wish to use standard catalyst particles in a low pressure drop reactor. In a parallel passage reactor (PPR, see

Figure 1-1) the fluid flows along the 'envelopes', and the reactants have to be transported to the catalyst particles in the beds by dispersion and diffusion. The pressure drop across a PPR is comparable to that across a monolithic reactor. Due to the roughness of the wire gauze that constitutes the wall of the channels through which the fluid flows, both pressure drop and heat and mass transfer rates are higher in a PPR than in a monolithic reactor.

The application of the PPR concept is limited by the slow rate of mass transfer in the catalyst beds. Since the fluid *in* the beds is virtually stagnant (except near the gauze walls of the beds), the mass transfer rate is limited to the effective diffusivity in packed beds. For this reason the thickness of the beds should not be more than *circa* 5 catalyst particle diameters. In thicker beds the overall rate is stronger limited by interparticle mass transfer in the beds than by intraparticle pore diffusion. Another important fact is that for beds thinner than *circa* 0.5 cm, the costs of the wire gauze construction become prohibitively high. Together this sets a lower limit of *circa* 1 mm to the size of the catalyst particles. Consequently, the PPR concept is less attractive for processes with a high reaction rate. A typical borderline case is a first-order reaction rate constant of 15 s^{-1} (reaction rate expressed per unit catalyst volume).

The accumulation of dust in a PPR is more severe than in monolithic reactors. Since the gas in the beds is virtually stagnant, the chances of a dust particle having entered a bed (due to turbulent movement in the gas channel) to be re-entrained, are slim. Consequently, the beds will slowly fill with dust. Furthermore the mazes of the wire gauze walls of the beds are prone to plugging with dust, which slows down the mass transfer rate. A preliminary study of dust trapping in parallel passage reactors, fixed bed reactors and bead string reactors is reported in Chapter 7.

The mass transfer problem of the PPR can be overcome by inducing convective transport of reactants within or through the catalyst beds. The most effective way to accomplish this, is by in turn blocking the inlet or outlet of the gas channels between the beds, thereby forcing the fluid to flow laterally through the beds. This is the concept of the lateral flow reactor (LFR, see Figure 1-2) and the radial flow reactor (RFR). Even though the fluid flows *through* the catalyst beds in an LFR/RFR, it is a true low pressure drop reactor. The catalyst particle size, the bed thickness and the fluid velocity through the beds can be designed in such a way that the pressure drop across an LFR/RFR is comparable to that across the earlier mentioned reactor types. Depending on the size of the catalyst particles and the type of dust in the gas, the problem of dust trapping in an LFR/RFR may be either less or more important than in a PPR. Dust with favorable flowing properties may simply flow through beds of large catalyst particles in an LFR/RFR, whereas dust with unfavorable properties may eventually completely block the beds. This was demonstrated experimentally for shallow fixed bed reactors, which could serve as a model system for one bed of an LFR/RFR; see Chapter 7

A point of concern in the design of an LFR/RFR is the even distribution of the flow over the various catalyst beds. Since the bed thickness is small (compared to normal

fixed bed reactors), small variations in bed thickness may result in maldistribution of the flow.

2 New concepts

In addition to and as an alternative for these existing concepts of low pressure drop reactors with structured catalyst packings, two new concepts are proposed in this thesis, both of which are being developed at Delft University of Technology. The bead string reactor (BSR) was invented in the section Chemical Reactor Engineering as an alternative for a PPR with extremely thin catalyst beds, viz. beds of only one catalyst particle diameter wide. The zeolite-covered screen reactor (ZSR) was invented on the interface between the Chemical Reactor Engineering section and the Laboratory of Organic Chemistry and Catalysis (Prof. Van Bekkum and dr. Jansen), from the wish to apply zeolites in reactors with structured catalyst packings. For both reactor concepts patent applications have been filed (Jansen *et al.*, 1992, and Gerritsen, 1989).

2.1 The bead string reactor

The BSR is characterized by the fact that the catalyst material is fixed on parallel strings that are arranged in the reactor, parallel (or cross) to the flow; see Figure 1-3. Important in the definition of this concept is that the catalyst material is fixed to the strings due to its shape, without being glued. The catalyst material may consist of commercially available hollow extrudates or ring shaped pellets that are mechanically stringed on wires or stacked on rods. It is also possible to extrude silica or alumina *around* a carrier fiber (like the insulation material of electric cords).

It cannot be doubted that with such techniques structured catalyst packings can be manufactured. Valid questions are, however, how the manufacturing costs of a BSR compare to those of other reactors with structured catalyst packings, and which reactor engineering advantages the BSR concept offers in specific applications. Although the development of mechanical processes to manufacture bead strings or catalyst rods is beyond the calling of a chemical reactor engineer, it was deemed appropriate to briefly investigate which techniques could be suitable and to obtain a 'guestimate' of the manufacturing costs. It was found that mechanical stringing or

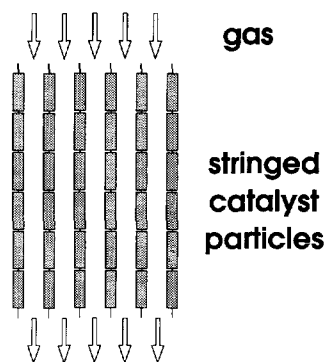


Figure 1-3 Concept of the bead string reactor.

stacking of catalyst particles is fairly simple, provided that the particles have constant, well-defined dimensions. The manufacturing costs are not prohibitive (several dollars per kg for particles 5 mm in diameter), though they increase rapidly with decreasing particle size. The expected feasible lower limit is 2 mm.

Extrusion of catalyst precursor paste around wires is also very well possible, although concessions may have to be made with respect to the formulation of the paste, to adapt its rheological behaviour. Even though the manufacturing costs are less dependent on the catalyst 'rod' diameter, the estimated feasible lower limit is 2 mm. This lower limit implies that the BSR concept is less suitable for processes with very high reaction rates. A typical borderline case is a first-order reaction rate constant of 15 s^{-1} (reaction rate expressed per unit catalyst volume), at which cylindrical particles or rods with a diameter of 2 mm have an efficiency factor of 75 to 85%. However, the upper limit on the rate constant may be increased by using catalyst particles with a non-uniform distribution of the active material ('egg-shell catalysts').

Below several claimed attractive features of the BSR concept are listed and ways are indicated in which these features can be exploited.

- **Low pressure drop.**

Because of the shape of the void space through which the fluid flows, *i.e.* non-circular channels that are straight in the direction of the flow, the pressure drop across a BSR is comparable to that of a monolithic reactor. This feature is most profitable in processes operating at low pressure and high space velocities, such as catalytic removal of NO_x , SO_x or volatile organic compounds (VOC's) from flue gases; see Figure 1-4. It is interesting to notice that the pressure drop can be manipulated by means of the voidage (see next item).

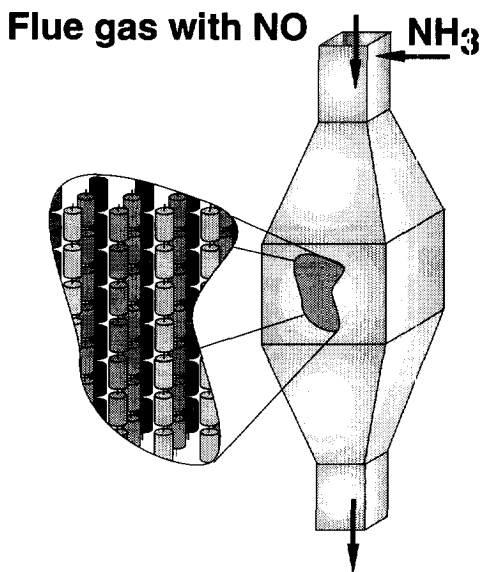


Figure 1-4 Artist's impression of a BSR for catalytic removal of NO_x from flue gas.

- **Voidage can be varied between 100% and as low as 10%.**

By choosing the pitch of the strings in a BSR, the voidage can be optimized with respect to pressure drop on one hand and reactor size on the other hand. The lower voidage limit of 10% is obtained by arranging the strings in a regular triangular array, at such a pitch that the strings (almost) touch each other. Note that in a traditional, randomly packed catalyst bed the voidage is typically *ca.* 45%. In Lateral Flow Reactors, Parallel Passage Reactors and incorporated monolithic reactors it is often higher than 70%. In washcoated monolithic reactors the fraction of the reactor volume that is occupied by the active catalyst material (*i.e.*, the washcoat) is even less than suggested by the voidage, because the inactive ceramic body usually occupies even more space than the washcoat. The attainable low voidage of a BSR allows the design of very compact reactors with a still relatively low pressure drop.

- **Lateral transport of heat and reactants across the diameter of the reactor.**

This feature is important when the reaction has a high heat effect or when insufficient mixing of the reactants would have a strong adverse effect on the performance. One example is formed by selective oxidation processes (highly exothermic), where lateral or radial temperature gradients would decrease the selectivity of the conversion. Another example is the Selective Catalytic Reduction process of nitric oxide with ammonia, where mixing of ammonia with the flue gas is often a point of great concern. Because the void space in a BSR is not only continuous in the axial direction but also in the lateral direction, lateral dispersion of heat and reactants is much better than in a monolithic reactor. An interesting observation was reported by Rehme (1992), who found that lateral transport in longitudinal flow through rod bundles (as in a nuclear reactor) is significantly enhanced by spontaneous pulsating flows in the lateral plane, at highly turbulent flows.

- **Effective mass and heat transfer between gas and catalyst phase.**

Because the BSR geometry induces transition to turbulent flow at relatively low Reynolds numbers (as low as 500), mass and heat transfer between gas and catalyst phase is faster than in monolithic reactors. This is due to the fact that the flow in a monolithic reactor is usually laminar. The advantage of the BSR can be exploited in processes with a large heat effect, where heat transfer through the film layer is generally more important than intraparticle heat and mass transfer.

- **Possibility to use 'standard' catalyst particles.**

When hollow extrudates or ring-shaped pellets are used as the catalyst material for the BSR, the catalyst can be manufactured according to standard procedures. Consequently, no additional catalyst development is necessary to apply an existing catalyst in a BSR. This is an advantage over the monolithic reactors, because with those reactors one has to deal with the peculiarities of the washcoat or the ceramic carrier body serving as the support of the active sites.

- **Virtually dustproof operation.**

This feature results from the continuous channel structure of the BSR: small 'piles' of dust collected between strings can collapse in several directions and be entrained by gas flowing along it. This effect can be increased by a gentle swinging movement of the strings, induced by the gas flow, when the strings are only connected at the top end and not at the bottom end of the reactor. In combination with a suitable choice of the voidage or pitch of the strings, this feature enables treatment of flue gases with a high dust content that would cause rapid fouling in other reactor types.

- **No maldistribution of gas or liquid in three-phase processes.**

Regarding application of the BSR concept to gas/liquid/solid processes, an important advantage of the BSR is the fact that adjacent strings do not (have to) touch. Because of the liquid surface tension, liquid will not spill over from one BSR string to another. Consequently, the initial liquid distribution is maintained throughout the BSR module. This feature is especially advantageous when incomplete catalyst wetting (which results from liquid maldistribution in traditional, randomly packed trickle flow reactors) would lead to hot spots and decreased selectivity.

- **Possibility to operate three-phase processes not only in cocurrent but also in countercurrent mode at high gas and liquid flow rates.**

Because the liquid flow is 'guided' by the BSR strings, flooding in countercurrent operation is prevented up to high loads, unlike in traditional trickle flow reactors. The possibility to operate in countercurrent operation can be exploited especially in three-phase processes in which reaction products inhibit the reaction. An example is deep hydrodesulfurization of gas oil. An additional advantage of the small gas phase pressure drop across the reactor is the comparatively high partial pressure of gas phase reactants (*e.g.* hydrogen) at the reactor outlet, from which the reaction rate may benefit.

- **Possibility to supply heat directly to the catalyst by using the strings onto which the catalyst material is fixed as electrical heating elements.**

Clearly this feature can be exploited for quick start-up of reactors and for highly endothermic reactions, as was mentioned in the discussion of metal washcoated monolithic reactors. An additional advantage of the BSR compared to that reactor is the possibility to use larger catalyst pellets. This enables, for example, the steam reforming of methane in a BSR. Steam reforming is nowadays carried out in large numbers (often more than a thousand) of parallel tubular reactors placed in large furnaces. The high number of tubes is necessary because of limited diameter (*circa* 10 cm) of the tubes, set by the high heat requirement of the reaction. Using the BSR concept, all catalyst could be contained in one reactor, the heat being supplied from within the catalyst. Because of the low pressure drop, much smaller catalyst particles could be used (the standard reforming catalyst has an efficiency factor of a few percent). The size of a reformer, as well as gas compression costs, could thus be decreased by at least a factor hundred. These cost savings may

weigh up to the extra costs of electrical heating and the more complicated construction of a BSR.

2.2 The zeolite-covered screen reactor

The zeolite-covered screen reactor (ZSR) is characterized through catalyst packings prepared by *in situ* crystallization of zeolite crystals on a structured support. The support may consist, for example, of metal wire gauze or thin metal sheets, of which flat or corrugated plates are stacked or rolled-up to create the packing.

In situ growth of zeolite crystals on a support is realized by submerging the bare support in the liquid mixture that contains the nutrients for zeolite synthesis. When the right procedure is followed, zeolites will preferentially grow on the surface of the support. A SEM picture of MFI zeolite that has been grown on metal wire gauze, is shown in Figure 1-5.

This technique yields crystals that are chemically (*ergo*: rigidly) bonded to the support. Consequently the catalyst packing is very stable with respect to mechanical and thermal shocks. The optimum contact between the zeolite crystals results in a rapid levelling out of temperature gradients and enables effective supply of electric heat to the catalyst.

The orientation of the crystals with respect to the support surface can be manipulated through the synthesis conditions. Packings can be obtained in which all crystals are oriented perpendicular to the surface (like skyscrapers), or along the surface, or in a random way; see Figure 1-6. Both 'monolayer' and 'multilayer' covering of the surface are possible. For application as a catalyst, multilayer covering in a random way seems to be most advantageous, considering the accessibility of the zeolite pores.

The ZSR concept opens the way to low pressure drop reactors with zeolitic catalysts that are optimally accessible for the reactants. This offers an advantage when very fast reactions are involved. Indeed, the alternative for *in situ* growth on a support is extrusion, pelletization or granulation of the zeolite crystals with a binder. With these techniques monolith structures can be obtained, or particles with a size of several millimeters that can be used in a PPR or LFR/RFR. Particles of this size have a low efficiency factor for very fast reactions.



Figure 1-5 MFI crystals, *in situ* grown on metal wire gauze with a wire diameter of 35 μm and a mesh size of 40 μm .

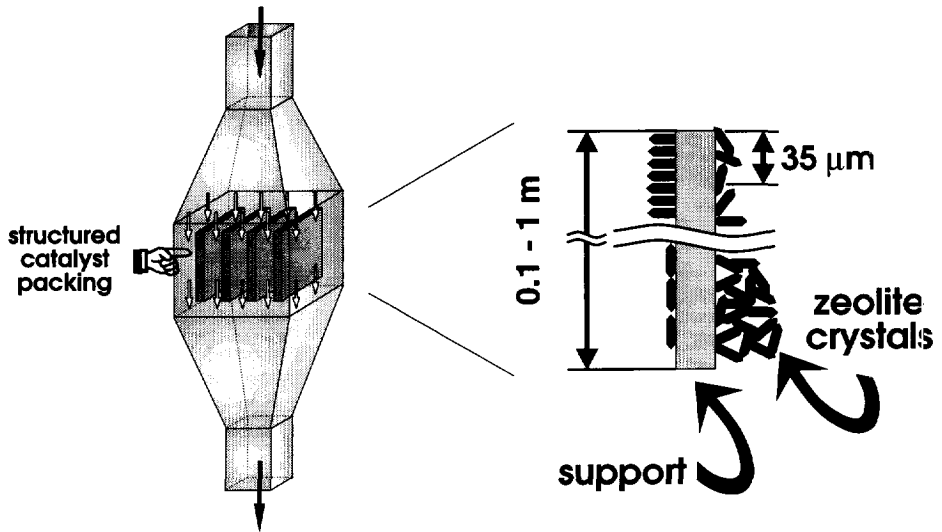


Figure 1-6 Concept of the zeolite-covered screen reactor.

The ZSR shares the advantages of the washcoated monolithic reactor with a metal support. Possible applications are catalytic flue gas treatment and hydrocarbon conversions, such as selective partial oxidation of small hydrocarbons. Especially in the latter application the advantage of the high accessibility is important, because the short contact time promotes a high selectivity.

3 Goal of the thesis work and structure of the thesis

Originally the goal of the PhD project was phrased as 'the development of an experimentally verified engineering model for a gas/solid BSR with longitudinal flow.' The model should predict pressure drop and chemical conversion as a function of all design parameters and the reaction kinetics, taking into account the effects of limited film layer and intraparticle mass and heat transfer. Furthermore an idea should be obtained of the susceptibility of a BSR to fouling by dust, and the effect of accumulated dust on the pressure drop across the reactor. Finally, based on the gathered knowledge of the BSR, this reactor concept should be compared qualitatively to that of the most important players in the field (*i.e.*, the monolithic reactors, PPR and LFR/RFR).

To this end a research program was set up consisting of five parts:

- (1) A study of momentum transport phenomena in a BSR, using a cold flow test section and lab-scale BSR modules filled with smooth rods, strings of ceramic beads and strings of extruded catalyst particles. In this test section the pressure drop across a part of the reactor was measured as a function of the rod or particle diameter, the relative pitch, the roughness of the rods or strings, and the gas velocity. Using the experimental data, literature relations pertaining to heat exchangers and nuclear reactors were verified.
- (2) A study of mass transport phenomena in a BSR, using a resembling test section. The mass transfer coefficient was determined experimentally by measuring the mass decrease of sublimating beads of naphthalene inserted in the bead strings. In the experiments the influence was tested of the axial and lateral position of the naphthalene beads, the diameter of the beads, the pitch of the strings and the gas velocity. The results were used to verify predictions based on numerical solutions of the balance equations (for laminar flow) and the Chilton-Colburn analogy between momentum and mass transfer. Because of the analogy between heat and mass transfer, no separate study was done of heat transfer phenomena.
- (3) A study of the kinetics of a test reaction, to be used in the validation of the reactor model. Considering the possible applications of the BSR, the selective catalytic reduction of NO with NH₃ was chosen to serve as the test reaction. To render the kinetics of this reaction as simple as possible, the reaction was carried out at low temperatures, with excess ammonia, oxygen and water. The reaction kinetics were studied in an internal recycle reactor of the Berty type.
- (4) Development of a mathematical model integrating the results of the three parts mentioned above, and validation of this model using a hot BSR test section in which the test reaction was carried out. Reactor modules were used that were filled with strings of deNO_x catalyst in the form of cylindrical extrudates.
- (5) An experimental study of dust trapping in a BSR, PPR and fixed bed reactor, using two types of dust with completely different flow characteristics: ceramic powder and fly-ash. This study was considered to be preliminary only, since the complexity of the subject would require much more time and energy than could be spent in the framework of this project. Consequently the experiments were performed under cold and dry conditions.

These parts of the project are reported in Chapters 2 (momentum transport), 3 (mass transfer), 4 (reaction kinetics), 5 (modelling and validation), and 7 (dust trapping). Two more studies are reported in this thesis. Chapter 6 deals with a study of transport phenomena and reactor modelling of the PPR. Since hardly any literature on the modeling of the PPR was available from the literature, the model derived in this chapter was essential in the comparison of the PPR with the BSR. Chapter 8 deals with the development and testing of the ZSR. The concept of the ZSR was born as an off-spin of the work on the BSR: one of the investigated techniques to manufacture catalyst packings for BSR-like reactors was to grow catalyst material

on wires or wire structures. The expertise on growing zeolites on supports was supplied by the group of Prof. Van Bekkum and dr. Jansen of the Laboratory of Organic Chemistry and Catalysis. Considering the interesting results obtained with the first ZSR structures, it was deemed appropriate to include this work in the present thesis.

References

- Bell, A.T., L.E. Manzer, N.Y. Chen, V.W. Weekman, L.L. Hegedus and C.J. Pereira, 1995, Protecting the Environment Through Catalysis. *Chem. Engng Prog.* February 1995, 26-34.
- Calis, H.P., T.S. Everwijn, A.W. Gerritsen, C.M. van den Bleek, F.G. van Dongen and F. Goudriaan, 1994, Mass Transfer Characteristics of Parallel Passage Reactors. *Chem. Engng Sci.* **49**, 4289-4297.
- Cybulski, A., and J.A. Moulijn, 1994, Monoliths in Heterogeneous Catalysis, *Catal. Rev.—Sci. Eng.* **36**(2), 179-270.
- Gerritsen, A.W., 1989, Dutch Patent Application Nr. 9000454, *Kralenreactor*, February 26.
- Jansen, J.C., C.H. Legein, H.P.A. Calis, H. van Bekkum, A.W. Gerritsen and C.M. van den Bleek, 1992, "Catalyst System of the Structured Type". International Application published under the Patent Cooperation Treaty (PCT), no. PCT/NL93/00234; extension of Dutch Patent Appl. no. 9201940, priority date 5 November 1992.
- Rehme, K., 1992, The Structure of Turbulence in Rod Bundles and the Implications on Natural Mixing between the Subchannels, *Int. J. Heat Mass Transfer* **35**(2), 567-581.
- Woldhuis, A.F., 1992, Shell Denox Systeem: NO_x-verwijdering bij lage temperatuur. *Procestehnologie* September 1992, 16-19.

Chapter 2

Momentum Transport in a Bead String Reactor

Contents

Summary	27
1 Introduction	28
2 Relations for laminar flow	30
2.1 Governing equation and domains	30
2.2 Solutions for the central subchannels	32
2.3 Solutions for the wall and corner subchannels	34
2.4 Laminar geometry parameters for finite bundles — wall effects	36
2.5 Hydrodynamic entrance length	38
3 Relations for turbulent flow	40
3.1 Critical Reynolds numbers for onset and completion of turbulence	40
3.2 Semi-empirical relations for smooth rod bundles	42
3.3 Influence of surface roughness	43
3.4 CFD techniques for flow in rod bundles	45
4 Experimental work	46
4.1 Test section and experimental procedure	46
4.2 Experiments conducted	48
4.3 Results and discussion	50
4.3.1 Hydrodynamic inlet effects	51
4.3.2 Comparison of experimental friction factors with theory for smooth rod bundles	54
4.3.3 Comparison of experimental friction factors with models for rough rod bundles	57
5 Conclusions and recommendations	58
Acknowledgements	59
Notation	60
References	61

Summary

Momentum transport in longitudinal flow across bundles of smooth cylinders ('rods') has been extensively studied since 1960, due to the importance of nuclear reactors and heat exchangers. Suitable engineering relations, due to Rehme¹, are available to predict the friction factor and the distribution of the flow over the reactor, as a function of the reactor geometry and the flow conditions, both for laminar and turbulent flow. Momentum transport in bundles of rods with the type of artificial roughness encountered in a BSR, has received little attention in the literature.

Pressure drop measurements have been done with lab-scale reactors containing bundles of smooth rods, smooth rods with wire wraps, strings of ceramic beads and strings of extruded catalyst particles. Under typical conditions the hydrodynamic entrance length is shorter than predicted by the theory, and hydrodynamic inlet effects can be neglected. The flow regime changes from laminar to turbulent much more gradually than with flow through circular channels. The transition starts at Reynolds numbers (based on the hydraulic diameter of the reactor with strings) between *ca.* 400 and 3000, the lower value pertaining to low voidages (*ca.* 35%), the higher number to high voidages (80% or higher). Fully turbulent flow is reached at Reynolds numbers between $3 \cdot 10^3$ and 10^4 .

The experimental friction factors for smooth rods are well-described by correlations available from the literature, both in the laminar and the turbulent flow regime. In the tested range of Reynolds numbers (300-5000) the tested strings of ceramic beads and extruded catalyst particles can be described as hydraulically smooth when the relative roughness is smaller than 0.04; when it is higher than 0.04, a roughness function has to be introduced to correlate the results. The results found with the bead strings can be rationalized with the common boundary layer theory for turbulent flow.

Using the theory and experimental data presented in this chapter, the pressure drop across a typical BSR can be predicted with an inaccuracy ranging from a few percents (laminar flow or small relative roughness) to *ca.* 50% (transition regime or fully rough turbulent flow).

¹ Rehme, K., Convective Heat Transfer over Rod Bundles, in *Handbook of Single-Phase Convective Heat Transfer*, S. Kakaç, R.K. Shah and W. Aung (Eds.), John Wiley & Sons, New York, 1987.

1 Introduction

In traditional fixed bed reactors with unstructured catalyst packings, the optimum size of the catalyst particles strongly depends on the trade-off between pressure drop and catalyst efficiency. Upon decreasing the particle size, not only the catalyst efficiency increases, but also the pressure drop. In a BSR there is an extra degree of freedom that can be used to manipulate the pressure drop without affecting the catalyst efficiency: the pitch of the strings. The optimum pitch depends on another trade-off, pressure drop costs versus manufacturing costs and plant space costs. An upper limit on the pitch might be set by mass or heat transfer requirements.

Momentum and heat transport phenomena of longitudinal flow through regular assemblies of cylindrical rods (commonly called 'rod bundles') have been studied quite extensively: it is estimated that over 500 articles have appeared on this subject since 1959. The main incentive for that work has been the growing importance of compact heat exchangers and nuclear reactors several decades ago. Important literature reviews in this field are those by Kakaç and Spalding (1979), Johannsen (1983) and Rehme (1987).

An engineering equation that is often used to calculate pressure drop across straight conduits or channels with a constant cross-section, as in a BSR, is:

$$(-\nabla p) = 4f \frac{1}{2} \rho \langle u \rangle^2 \frac{1}{d_h} \quad (2-1)$$

This relation follows directly from the force balance across the channel and the definition of the friction factor:

$$\frac{4f}{4} \equiv f \equiv \frac{\tau_{f,w}}{\frac{1}{2} \rho \langle u \rangle^2} \quad (2-2)$$

Consequently, the problem of predicting the pressure drop across a BSR can be rephrased as the problem of predicting $4f$.

The purpose of this chapter is to present experimentally verified relations predicting $4f$ as a function of the BSR geometry, *i.e.*, pitch, particle size and reactor size (wall effect), and as a function of the Reynolds number and the roughness of the strings. Although various types of string arrays are possible (*e.g.*, square, triangular, or circular), only one type, the regular square array, will be discussed. The analysis of the other types of array is analogous to that of the square array.

Only steady state flow is considered, because the time scale on which the flow reaches a steady state is very small compared to the time scale of process changes. Furthermore it is assumed that there is only convective flow in the longitudinal direction,

parallel to the strings. Although it has been shown (*e.g.*, Rehme, 1992) that lateral secondary flows and flow pulsations occur in longitudinal flow through rod bundles, the effect of these lateral flows on the axial pressure gradient is negligible.

Three flow regimes are distinguished, based on the prevailing transport mechanism. In the *laminar flow regime*, there is only molecular transport of momentum, mass and heat. In the *turbulent flow regime* the molecular transport is only dominant in the laminar sub-layer, whereas convective or dispersive transport by eddies is dominant in the bulk flow. The ill-defined region between the laminar and turbulent flow regime, where both mechanisms are important, is the *transition flow regime*.

An important question is in which flow regime(s) a BSR is expected to be operated. Consider the case that: catalyst particles of 3 to 17 mm are used; the catalyst efficiency factor is 0.75; the pitch is such that the reactor voidage is 40%; the space velocity is such that the reactant conversion is 0.9; the reactor length over diameter is 1 to 5; and the reactor diameter is 1 to 3 m. When these specifications are met, the Reynolds numbers will be below 2000. The Reynolds number is based on the average linear gas velocity and the hydraulic diameter of the channels 'between' the strings. Although for circular tubes this would imply laminar flow only, it will be shown in this chapter that in a BSR turbulent flow may occur at Reynolds numbers as low as 500. Consequently, in this chapter both laminar and turbulent flow will be discussed.

Another important question is whether hydrodynamic inlet effects have to be taken into account under typical conditions. In the hydrodynamic inlet zone the friction factor is considerable higher than for fully developed flow. It will be shown that for both laminar and turbulent flow, under the conditions mentioned in the previous paragraph, the hydrodynamic entrance length predicted from the theory may be up to 0.5 m. Since this number corresponds to the expected length of the modules in a real BSR application, as well as to the length of the experimental modules, inlet effects would be expected to be significant.

In Sections 2 and 3 relations for laminar and turbulent momentum transport in BSR-like structures are discussed, based on literature and own work. No extensive literature review will be given, since this has already been done fairly recently by Rehme (1987). Many references to this review will be given in this chapter, because Rehme presents many graphs and correlations that combine all available literature data. Furthermore, a considerable part of the literature quoted by Rehme consists of internal reports and conference proceedings that are difficult to obtain. In Sections 2 and 3 considerable attention will be given to the effect of the reactor wall on the flow distribution and the pressure drop. This is necessary because in the lab-scale BSR modules used in the present study, the wall effect is considerable, as will be shown. Note, however, that for all larger-scale applications the wall effect will be negligible. In Section 4 experimental work is discussed, covering pressure drop experiments with arrays of smooth rods, strings of ceramic beads, strings with a very high roughness

and strings of real catalyst particles. In Section 5 a recipe will be given for estimation of the pressure drop and flow distribution in a BSR.

2 Relations for laminar flow

2.1 Governing equation and domains

The momentum balance over a small element of fluid, for incompressible, steady state, fully developed flow in the z -direction, results in the following partial differential equation (PDE):

$$\nabla \cdot (\mu \nabla u_z) = \frac{dp}{dz} \quad (2-3)$$

Note that the Nabla operator (∇) is in fact two-dimensional in this equation, because u_z is constant in the z -direction (in fully developed flow). The pressure gradient dp/dz is a constant, *i.e.* place independent.

In laminar flow μ is the molecular diffusivity constant; in that case Eq. (2-3) is a second order, linear, two-dimensional PDE of the Poisson type. In turbulent flow μ also depends on the velocity gradients (hence on the lateral position), and Eq. (2-3) then is quasilinear or non-linear.

The procedure to find analytical or numerical relations for $4f$ is quite straightforward: (1) solve the momentum balance over a unit cell of the channel for a given pressure gradient, either analytically or numerically, to find the velocity distribution; (2) integrate the velocity profile over the cross-sectional area of the channel, to obtain the average velocity; (3) combine the obtained average velocity and the given pressure gradient with Eq. (2-1), to obtain $4f$.

For the simplest geometry of all, the circular channel, this procedure yields:

$$4f = \frac{64}{\text{Re}} \quad \text{or} \quad 4f\text{Re} = 64 \quad (2-4)$$

The product of $4f$ and Re is usually called the *laminar geometry parameter*, as for laminar flow its value only depends on the geometry of the channel and not on Re . To see in which domains Eq. (2-3) should be solved for a BSR, first some geometric definitions have to be made. In Fig. 2-1 two basic types of array are shown, the regular square array and the regular triangular array (cross-sections perpendicular to

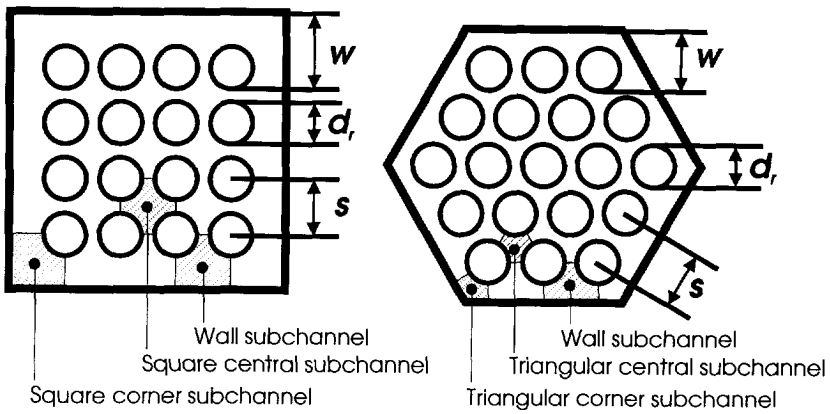


Figure 2-1 Geometrical definitions for a BSR or a rod bundle. s is the pitch, w the wall distance, s/d , the relative pitch and w/d , the relative wall distance. N is the number of strings or rods per row, in this case 4 for the square array and 2 (!) for the triangular array. n is the total number of strings or rods.

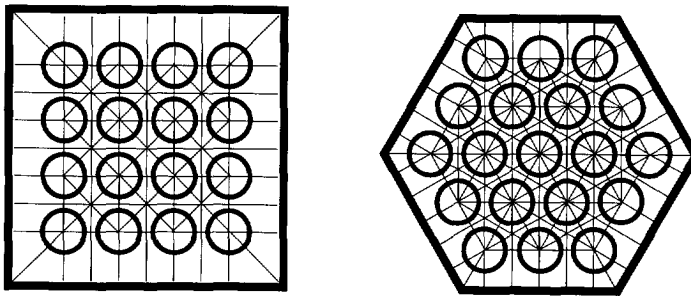


Figure 2-2 Symmetry lines in rod bundles. On the symmetry lines, $\partial u / \partial \underline{n} = 0$, where \underline{n} is the normal vector of the symmetry line.

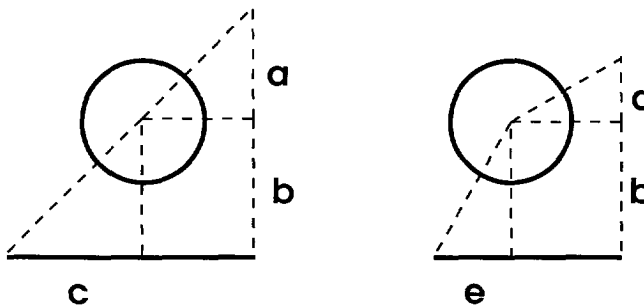


Figure 2-3 The unit cells that make up the subchannels in rod bundles. a and d: central subchannels; b: wall subchannel; c and e: corner subchannels. The dashed boundaries of the unit cells indicate symmetry.

the direction of flow). Both are characterized by three subchannels each: a central, wall and corner subchannel. Note that the wall channel of the square array is identical to that of the triangular array.

Under the important assumption (to be discussed in Section 2.3) that the flow through central channels is negligibly influenced by the walls, and that the flow through wall channels is only influenced by the nearest wall, there is a high degree of symmetry within the channels. In Fig. 2-2 all symmetry lines are shown for both arrays. A symmetry line is defined here as a line connecting points at which the derivative of the longitudinal velocity, with respect to the normal vector of the line, is zero.

From Fig. 2-2 it is seen that there are only three unit cells in each of these arrays, which are shown in Fig. 2-3; one subchannel contains 2 to 8 unit cells. The unit cells are the domains for which Eq. (2-3) should be solved to obtain the flow profile in these arrays.

The boundary conditions are that (1) at the surface of the cylinder and the reactor wall, the fluid velocity equals zero, and (2) on the symmetry lines the derivative of u with respect to the normal vector of the symmetry lines equals zero.

2.2 Solutions for the central subchannels

In one of the first articles on this subject, Sparrow and Loeffler Jr. (1959) derived the general analytical solution of Eq. (2-3). This general solution is easy to find, but it contains infinite series and (integration) constants that depend on the boundary conditions. Sparrow and Loeffler determined those for the central cells of square and triangular arrays, using the boundary collocation method. More recent publications on this subject are mostly based on complete numerical solution using a finite element method.

Since, for a given type of array, the geometry of a rod bundle is characterized by the relative pitch (or the voidage), $4fRe$ is a function of the relative pitch. Ohnemus, as reported by Rehme (1987), correlated literature data on the laminar central cell geometry parameter for the range of relative pitches that is of greatest practical interest. For regular square arrays the following correlation is accurate within 2%:

$$4fRe = 162.8 \left(\frac{s}{d_r} - 1 \right) = 162.8 \left(\sqrt{\frac{\pi}{4(1-\varepsilon)}} - 1 \right) \quad (2-5)$$

for $1.05 \leq s/d_r \leq 2.0$, or $0.29 \leq \varepsilon \leq 0.80$.

When the spacing of the rods is increased, the flow along a rod is less influenced by the surrounding rods. As a result the flow will become more axially symmetric. At high relative pitches the central subchannels in Fig. 2-1 can be approximated by the inner ringzone of an annulus, for which $\partial u/\partial r = 0$ at a certain radius r^* ; see Fig. 2-4. The radius r^* is chosen such that the flow area of the ringzone equals that of the actual subchannel. The solution of Eq. (2-3) for this so-called *equivalent annular ringzone* approximation is easily obtained, and the resulting geometry parameter can be most conveniently expressed as a function of the voidage:

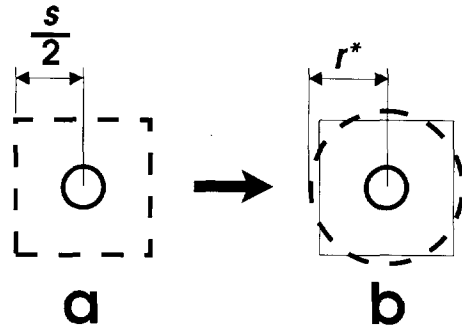


Figure 2-4 Approximation of a subchannel in a square array (a) by the inner ringzone of an annulus (b).

The resulting geometry parameter can be most conveniently expressed as a function of the voidage:

$$4fRe = \frac{64 \epsilon^3}{(\epsilon - 1)(\epsilon^2 + 2\ln(1 - \epsilon) + 2\epsilon)} \quad (2-6)$$

This relation is accurate within 1.5% for relative pitches higher than 2.8 ($\epsilon > 0.90$) in a square array, or higher than 2.1 ($\epsilon > 0.80$) in a triangular array (Rehme, 1987).

In Fig. 2-5 the central subchannel laminar geometry parameter for a square array, calculated with Eqs. (2-5) and (2-6), is compared with the value obtained by numerical solution of Eq. (2-3), as a function of the relative pitch and the voidage. The numerical solution of Eq. (2-3) was obtained with SPDE, a commercial PC software package for solving elliptic partial differential equations using a finite element method (Oudshoorn, 1993). From Fig. 2-5 it is seen that the numerical results are in good agreement with Eqs. (2-5) and (2-6).

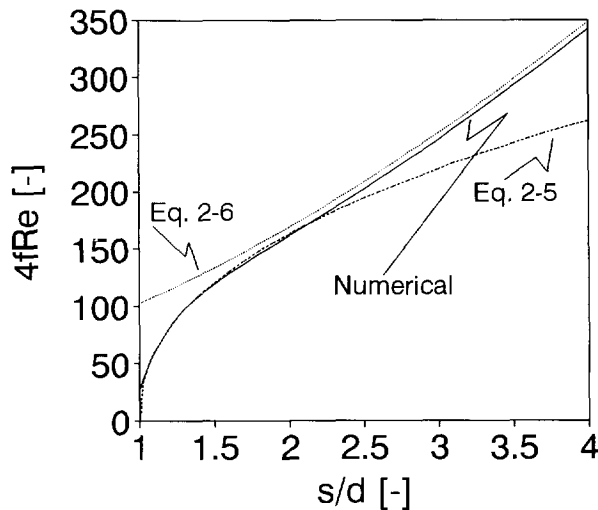


Figure 2-5 Comparison of laminar geometry parameter values of the central subchannel of a regular square array, obtained from correlations and from numerical solution with SPDE.

2.3 Solutions for the wall and corner subchannels

Schmid (1966) showed that an accurate estimation of the flowrate through wall and corner subchannels is obtained when symmetry on the boundary with the neighbouring central subchannel is assumed. This is the justification for the symmetry lines drawn in Fig. 2-2. Schmid semi-analytically solved Eq. (2-3) for the system indicated in Fig. 2-6, as a function of J , relative pitch and relative wall distance. Note that the wall and central subchannels defined in Fig. 2-6 are not fundamentally different from the ones defined in Fig. 2-1. The boundary conditions were: zero velocity at the surface of the wall and the cylinders (indicated by solid lines), and symmetry at the top, bottom and right hand boundaries (indicated by dashed lines).

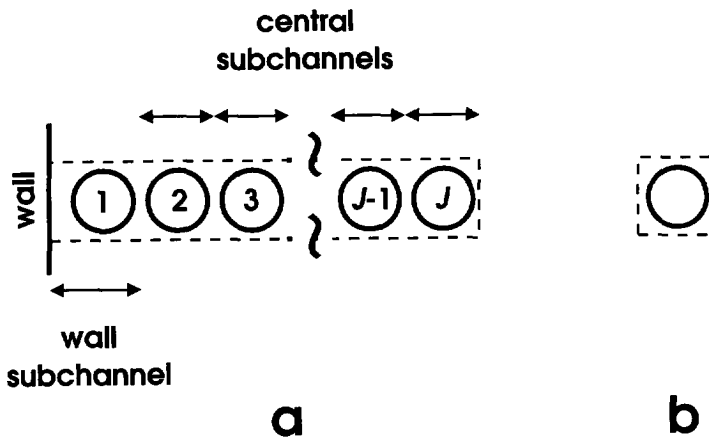


Figure 2-6 a: Definition of Schmid's system.
b: Central subchannel of an infinite regular square array.

It was shown that the flowrates through the wall subchannel and the neighbouring central subchannel were virtually independent of J for $J > 4$. Comparing the flowrates through the wall subchannel for $J = 1$ and $J > 4$, Schmid showed that the difference between the two is less than 1% for relative pitches smaller than 2.5 and relative wall distances between 0.6 and 1.3.

In the same way Schmid compared the flowrates through the central subchannel neighbouring the wall subchannel in Fig. 2-6, for $J > 4$, and a central subchannel of an infinite array. It was shown that the difference between the two is less than 1% for relative pitches smaller than 2.5 and relative wall distances between 0.6 and 1.3. These results show that the pressure drop characteristics of all subchannels that make up a finite rod bundle, are closely approximated by those of the cells indicated in Fig. 2-3.

In Fig. 2-7, that is based on calculations with SPDE, it is shown that the assumption of symmetry at the boundary between the wall subchannel and the neighbouring central subchannel leads not only to an accurate approximation of the flowrate through the wall subchannel (an average over the wall subchannel), but also to an accurate flow profile. Fig. 2-7 shows the longitudinal velocity profile at the lower boundary indicated in Fig. 2-6, calculated for $J = 1$ and $J = 3$. It was checked that the velocity profile didn't change for $J > 3$. The profiles for $J = 1$ and $J = 3$ coincide almost perfectly.

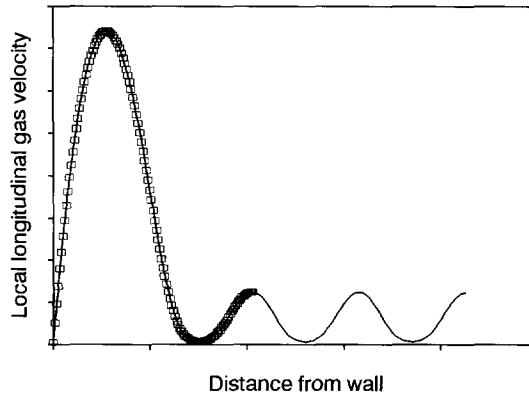


Figure 2-7 Velocity profiles at the lower boundary of Schmid's system, obtained with SPDE for $J = 1$ (\square) and $J = 3$ (solid line). Relative pitch 1.1, relative wall distance 2.0.

Based on numerical solution of Eq. (2-3) for the wall subchannel indicated in Fig. 2-3, Rehme (1971) presented a nomogram that gives the laminar geometry parameter for wall subchannels, as a function of the relative pitch and the relative wall distance. This nomogram is valid for both the square and the triangular array, since the wall channels of these arrays have the same geometry. Unfortunately no numerical correlation of this nomogram is available.

Rehme (1987) also presented a graphical relation between the laminar geometry parameter for corner subchannels in square and triangular arrays, and the relative wall distance.

2.4 Laminar geometry parameters for finite bundles — wall effects

Under the plausible assumption of (1) an equal pressure drop across all individual subchannels of a finite rod bundle and (2) a total flow rate through the bundle equal to the sum of the flow rates through the subchannels, the geometry parameter of a finite bundle follows from:

$$\frac{1}{(4fRe)_b} = \sum_{i=1}^n \frac{1}{(4fRe)_i} \left(\frac{P_{w,b}}{P_{w,i}} \right)^2 \left(\frac{A_i}{A_b} \right)^3 \quad (2-7)$$

The subscript i indicates the corresponding value of the i -th subchannel, b that of the total rod bundle. Note that the wetted perimeter of wall and corner subchannels, as well as that of the total rod bundle, includes the reactor wall. The definition of the geometry parameter of a finite rod bundle follows from Eq. (2-1), when the velocity is averaged over the total flow area and the hydraulic diameter equals $4A_b/P_{w,b}$.

According to Rehme (1987) the subchannel analysis, *i.e.* the combination of Eq. (2-7) with the relations discussed in Sections 2.2 and 2.3, yields predictions that deviate less than 5% from experimental results and numerical solutions for finite rod bundles. This has been proven for relative pitches ranging from 1.1 to 2.3, relative wall distances ranging from 1.04 to 2.5 and bundles of up to 37 rods.

Using the subchannel analysis, Johannsen (1983) showed that there is a significant effect of the reactor wall on the geometry parameter of the reactor. Johannsen presented graphs of the laminar bundle geometry parameter relative to the laminar geometry parameter of the central subchannel, as a function of the number of rods, the relative pitch and the relative wall distance, for a regular triangular array.

Because in the current study mostly regular square arrays were used, an analogous graph was made for this array, using the subchannel analysis; see Fig. 2-8. It is seen that when the wall effect is neglected, and the bundle geometry parameter is assumed to equal the central subchannel geometry parameter (as if the bundle were infinite), the pressure drop across the reactor may be overestimated by 20% even when the number of rods per row (N) is 100, corresponding to a total number of 10,000 rods (for a relative pitch of 1.2 and a relative wall distance of 2).

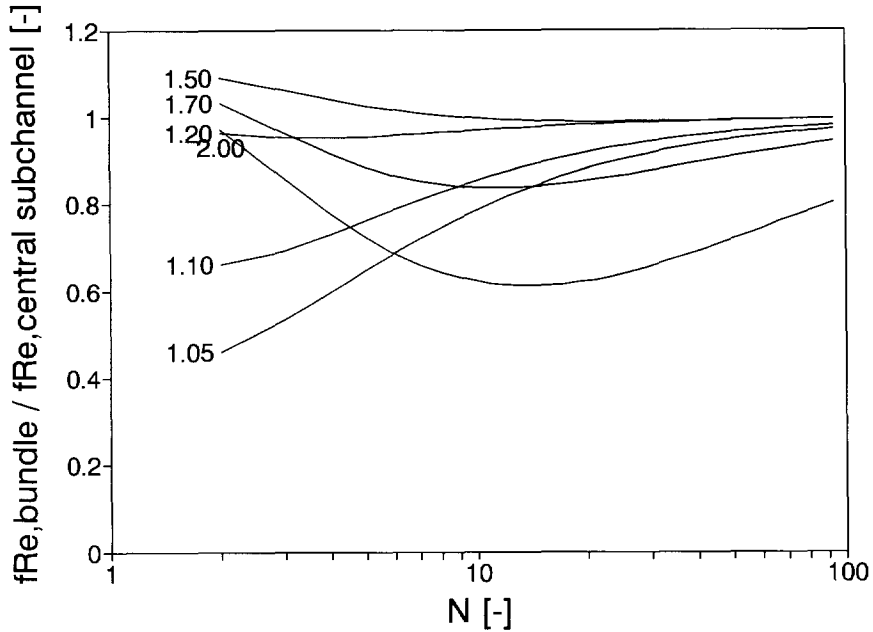


Figure 2-8 Wall effect on the laminar geometry parameter of a finite rod bundle (square array), with a relative pitch 1.2. The lines represent different relative wall distances.

Quite logically, the wall effect is most significant when the relative wall distance is large in comparison with the relative pitch. The combination in that case of a high average velocity through the wall and corner channels compared to the central channels, with the relatively high flow area of the wall and corner channels, results in a significant 'by-pass' of the fluid. In the example mentioned in the previous paragraph ($N = 100$, $s/d_r = 1.2$, $w/d_r = 2.0$) only 68% of the fluid flows through the central channels, whereas in flow area they represent 92% and in number they represent 96% of the total. The average fluid velocity in the wall channels is 5.4 times higher than in the central channels, in the corner channels it is even 6.3 times higher. Although the given example might sound alarming, it should be noted that using the relations presented in this chapter, it is perfectly well possible to choose combinations of relative pitch and wall distance such that the average fluid velocity or the flowrate through the wall channels equals that through the central channels.

2.5 Hydrodynamic entrance length

Because the flow in a rod bundle is bounded by the surface of the rods and the reactor wall on all sides in a lateral plane, a fully developed flow profile will be arise within a finite length (the hydrodynamic entrance length) from the inlet. The fully developed profile is reached when all boundary layers that develop along all walls in the bundle, touch the boundary layer developing at the opposite wall. This is illustrated in Fig. 2-9. From that point onward, the flow profile doesn't change any more.

Since in the hydrodynamic inlet region the boundary layer is not as thick as in case of fully developed flow, the transport of momentum from the fluid to the wall is more effective. As a result, the local friction factor for developing flow is higher than for developed flow. When the length of the reactor is much longer than the hydrodynamic entrance length, the entrance effect on the pressure drop across the total reactor is small. However, when the reactor length is small, the pressure drop across the reactor may be several times as high as would be predicted for fully developed flow. Therefore it is necessary to estimate the entrance length.

A simple expression for the entrance length in a rod bundle can be derived from the theory on developing boundary layers (e.g., Coulson and Richardson, 1979, Ch. 9), which shows that the thickness of the hydrodynamic boundary layer on a flat surface is given by:

$$\delta_h = 4.64 \sqrt{\frac{v x}{u_s}} \quad (2-8)$$

where u_s is the 'undisturbed' velocity; in channels this would be the velocity in the middle of the channel. For a circular channel, the boundary layers touch when δ_h

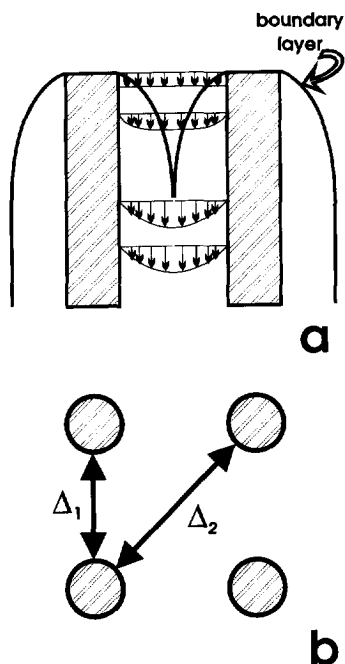


Figure 2-9

- a: Development of laminar flow in a rod bundle (side view).
 b: Definition of wall-to-wall distances in a rod bundle (top view).

equals $d_h/2$. From this it is expected that the hydrodynamic entrance length, ℓ_h , for a circular channel is given by:

$$\frac{\ell_h}{d_h Re} = \frac{u_s / \langle u \rangle}{9.28^2} = 0.023 \quad (2-9)$$

Experimentally it has been found that for a circular channel $\ell_h/(d_h Re)$ equals 0.04 to 0.05; consequently, the right hand side of Eq. (2-9) should be multiplied by a correction factor of 2. The deviation of Eq. (2-9) from the experimental value is not surprising, since in its derivation the curvature of the channel has been neglected, as well as the acceleration of the flow at the center of the channel.

In a rod bundle, the flow is fully developed when δ_h equals $1/2 \Delta_2$ (see Fig. 2-9). Using the same correction factor of 2 as for the circular channel, it is easily derived that the hydrodynamic entrance length ℓ_h can be estimated with:

$$\frac{\ell_h}{d_h Re} = 2 \frac{u_s / \langle u \rangle}{9.28^2} \left[\frac{\frac{s}{d_r} \sqrt{2} - 1}{\frac{4}{\pi} \left(\frac{s}{d_r} \right)^2 - 1} \right]^2 \quad (2-10)$$

Calculations with SPDE showed that the ratio $u_s / \langle u \rangle$ is *ca.* 2 in the central sub-channel of a rod bundle. The (dimensionless) entrance length is plotted as a function of the relative pitch in Fig. 2-10.

Rehme (1987) presented a graph of the local geometry parameter $f_x Re$ for developing flow through a central subchannel in a regular square array, as a function of the dimensionless axial coordinate $x^+ \equiv x/(d_h Re)$. This graph is based on solution of the momentum balance for developing flow. The hydrodynamic entrance length that follows from this graph, is obtained from the value of x^+ where $f_x Re$ has approximated the value for fully developed flow to within 5%. Eq. (2-10) appears to agree quite well with Rehme's graph.

For the case mentioned at the end of Section 1, entrance lengths ranging from 4 to 66 cm are calculated. From the fact that the boundary layer theory predicts that the local friction factor is proportional to $x^{-1/2}$, it follows that the average friction factor over a length L equals twice the local friction factor at L . Consequently, when the length of the reactor exactly equals the entrance length, the pressure drop across the reactor will

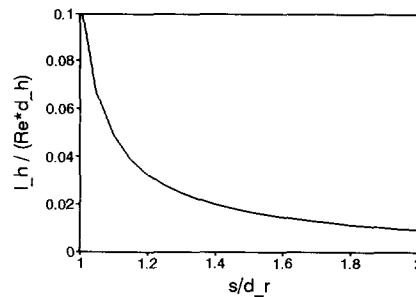


Figure 2-10 Predicted hydrodynamic entrance length for laminar flow in a rod bundle, as a function of the relative pitch.

be twice as high as would be expected for fully developed flow. When the reactor is shorter than the entrance length, the deviation will be even bigger.

3 Relations for turbulent flow

3.1 Critical Reynolds numbers for onset and completion of turbulence

Whereas a circular channel has only one characteristic size (its diameter), a rod bundle has two: Δ_1 and Δ_2 , defined in Fig. 2-9. When the pressure gradient across a rod bundle is increased, the flow in the narrow part of a subchannel (at Δ_1) will remain laminar longer than in the wide part (at Δ_2). This explains the observation often reported in the literature that in a rod bundle the transition from laminar to turbulent flow takes place over a much wider Reynolds range than in circular channels.

The onset of turbulence is defined as the Reynolds number at which $4fRe$ starts to deviate from the laminar geometry parameter. The completion of turbulence is defined as the Reynolds number at which the friction factor has become proportional to $Re^{-0.25}$ ¹⁰⁰. The order (or power) of the turbulent friction in Re depends on the roughness of the rods: for smooth rods the order will be approximately -0.25, for very rough rods 0.

The dependence of the friction factor on the surface roughness can be explained from models for turbulent flow. For an introduction to this subject, see (e.g.) Coulson and Richardson (1979), Ch. 9. According to these models, the turbulent flow profile in a tube can be described by three relations that together constitute the so-called *law of the wall* or *universal flow profile*. The first relation pertains to the laminar sub-layer at the wall, the third one to the turbulent core; the second one pertains to the so-called *buffer layer* that connects the laminar sub-layer with the turbulent core.

The thickness of the laminar sub-layer and the buffer layer is expressed in the dimensionless distance from the wall (y^+) and the so-called friction velocity (u^*):

$$y^+ \equiv \frac{\rho u^* y}{\mu} \quad \text{with:} \quad u^* \equiv \sqrt{\frac{\tau_{f,w}}{\rho}} = \langle u \rangle \sqrt{\frac{f}{2}} \quad (2-11)$$

The laminar sub-layer extends from the wall to $y^+ \approx 5$ and the buffer layer extends to $y^+ \approx 30$.

The (average) height of the wall roughness, h , is usually expressed in a dimensionless form:

$$h^+ \equiv \frac{\rho u^* h}{\mu} \quad (2-12)$$

When the wall roughness height is smaller than the laminar sub-layer thickness ($h^+ < 5$), the wall roughness does not result in extra friction. In this case the friction factor is a function of Re only, and relations for smooth channels can be used. This is the *hydraulically smooth regime*.

When the wall roughness protrudes into the buffer layer ($5 < h^+ < 30$ or 70 , according to some authors), it results in extra friction; consequently, the friction factor is a function of both Re and roughness height. This is the *transition regime*.

When the roughness height is bigger than the total thickness of the laminar sub-layer and the buffer layer ($h^+ > 30$ to 70), there is no longer a real laminar sub-layer. As a result the friction factor no longer depends on Re. This is the *fully rough regime*.

It is important to realize that these numbers on the sub-layer thickness were determined experimentally for flat surfaces, *i.e.*, flow along flat plates or through channels with a small curvature compared to the sub-layer thickness. For projected applications of a BSR, the thickness of the sub-layers may be of the same order of magnitude as the radius of the strings. In that case the true sub-layer thickness is expected to be smaller or more easily disturbed than for a flat surface at the same Reynolds number, because there is less surface to stabilize the sub-layer.

Rehme (1987) presents a graph containing all experimental results on the onset and completion of turbulence in smooth rod bundles. There appears to be a wide spread in the experimental data, attributed to differences between the test sections with which the data were obtained, notably differences in relative wall distance and number of rods. There is no clear correlation between the onset and completion Reynolds numbers and the relative pitch, despite the curves that Rehme suggests. For regular triangular arrays the onset Reynolds numbers range from 300 to 2000, for regular square arrays the values are even lower (down to $Re = 200!$). The completion of turbulence takes place between $Re = 3000$ and $Re = 10^4$.

An important point is that these results have been obtained with bundles of smooth rods, as used in heat exchangers and nuclear reactors. In circular tubes, especially the completion Reynolds number depends strongly on the relative wall roughness. From this it can be expected that for a BSR containing strings of catalyst particles, at least the completion Reynolds numbers and probably also the onset Reynolds numbers are lower than mentioned above.

3.2 Semi-empirical relations for smooth rod bundles

In Section 2.2 the equivalent annular ringzone approximation was discussed, which gives an accurate prediction of the laminar geometry parameter of central subchannels for relative pitches larger than 2.8 (square array) or 2.1 (triangular array). For turbulent flow the velocity profile in a channel is less pronounced than for laminar flow, ergo, the influence of the wall on the flow profile fades away at a shorter distance from the wall. From this it might be expected that the annular ringzone approximation for turbulent flow might be accurate at even lower relative pitches.

Maubach (1970) derived the solution of the turbulent annular ringzone problem, using the universal velocity profile for turbulent flow in circular tubes to describe the flow profile. Relating the friction factor of central subchannels to $4f_c$, the friction factor of hydraulically smooth circular channels, the ringzone predicts values of $4f/4f_c$ increasing linearly with the relative pitch, from 1.04 at a relative pitch of 1.0, to 1.09 at a relative pitch of 2. These values pertain to a Reynolds number of 10^5 , but the solution depends only weakly on Re.

Experimental results of friction factors for fully developed transition and turbulent flow in regular arrays of smooth rods were presented graphically, as a function of the relative pitch, by Rehme (1987). The graphs for $Re = 10^4$ and $Re = 10^5$ again show a wide scattering of the experimental data. The equivalent ringzone approximation adequately describes the data down to relative pitches of 1.4. At lower relative pitches it overestimates the average experimental friction factor by 10% on the average.

Rehme (1973) related the friction factor for turbulent flow in channels with circular or non-circular cross-sections, to the geometry parameter for laminar flow. The laminar geometry parameter determines the values of the parameters A and G^* in the following expression for the turbulent friction factor:

$$\sqrt{\frac{2}{f}} = A \left[2.5 \ln Re \sqrt{\frac{f}{2}} + 5.5 \right] - G^* \quad (2-13)$$

Eq. (2-13) is based on the universal flow profile for turbulent flow. Values of A and G^* were obtained from the theoretical analysis of the laminar and turbulent pressure drop characteristics of assemblies of circular channels with different diameters. These values proved to give accurate friction factor predictions also for non-circular channels, such as symmetric and asymmetric annuli and rod bundles.

Correlations of A and G^* with the laminar geometry parameter are given by Rehme (1987). These relations predict Rehme's own experimental data within 6%. Furthermore the line of $4f/4f_c$ versus relative pitch, predicted by this method, crosses the cloud of points of the other experimental data, albeit on the higher side.

Based on the observation that the friction factors for turbulent flow in rod bundles differ only little from those of circular tubes, Kirillov (quoted by Pustyl'nik *et al.*, 1990) proposed a very simple empirical correlation:

$$4f = \left(0.57 + 0.18 \left(\frac{s}{d_r} - 1 \right) + 0.53 [1 - e^{-a}] \right) 4f_t \quad (2-14)$$

where $a = 0.58 + 9.2 (s/d_r - 1)$. The friction factor for turbulent flow in hydraulically smooth circular channels may be calculated with the widely used Prandtl/Karman/Nikuradse relation.

For relative pitches between 1.08 and 2.7, the friction factors predicted by the methods of Rehme (1973) and Kirillov (Pustyl'nik *et al.*, 1990) deviate less than 10%, the latter always giving the highest prediction.

3.3 Influence of surface roughness

A simple calculation shows that in a BSR with stringed catalyst particles, the roughness of the strings is expected to influence the turbulent friction factor, unless large catalyst particles and/or a large relative pitch are used. In Fig. 2-11 theoretical friction factors, calculated from the relations for smooth rod bundles discussed in the previous two sections, are plotted as a function of Re , for different reactor voidages. As a typical example, consider a voidage of 50%, a string diameter of 5 mm, and a Re of 2000. The average gas velocity then is 6 m/s, and $4f$ is *ca.* 0.053. From Eq. (2-11) a laminar boundary layer thickness of 0.15 mm is estimated and a total thickness of laminar and buffer layer of 0.9 to 2.1 mm. Although the intrinsic surface roughness of the catalyst material is estimated to be less than 0.1 mm, the unevenness of the string, at the transition from one particle to the next one, will be much bigger. Two types of unevenness will exist, as indicated in Fig. 2-12: 'bumps' or 'positive roughness', where particles are not perfectly aligned, and 'chinks' or 'negative roughness', where particles don't touch completely. Roughness heights of 0.15 mm or higher are realistic. Consequently, under the conditions in this example it can be expected that

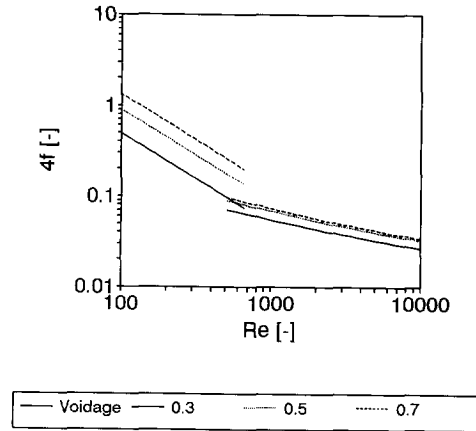


Figure 2-11 Predicted friction factors of hydraulically smooth rod bundles, vs Re , for various reactor voidages.

the friction factor depends on both the unevenness of the strings and the Reynolds number.

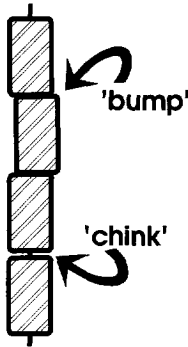


Figure 2-12 Two types of artificial roughness in a BSR.

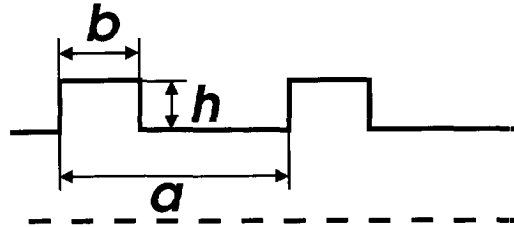


Figure 2-13 Definition of the dimensions of artificial roughness, according to Maubach (1970).

The distinction between the intrinsic roughness of the channel material and the roughness induced by more or less artificial bumps, is also made in the literature. The first type of roughness is generally called *sand-roughness*, as the surface resembles sandpaper: it is covered with evenly distributed protrusions, that have a certain size distribution. The second type of roughness, the unevenness, is referred to as *artificial roughness*; in most cases described in the literature, the surface is then covered with ribs of constant dimensions.

Maubach (1970) studied pressure drop characteristics of flow through annuli, circular channels and parallel plates, with artificially rough surfaces containing rectangular ribs. The definition of the rib dimensions is indicated in Fig. 2-13. Based on the universal velocity profile for hydraulically fully rough turbulent flow in sand-rough pipes, Maubach derived the following implicit expression for the turbulent friction factor:

$$\sqrt{\frac{4f}{8}} = 2.5 \ln \frac{d_h}{h} + R_M(h^+) - G \quad (2-15)$$

where $R_M(h^+)$ is the so-called roughness function. For sand-roughness, the (empirical) roughness function is 8.5 in the fully rough regime, independent of the dimensionless roughness height. For artificial roughness consisting of rectangular ribs, Maubach correlated literature data to a graph that gives $R_M(h^+)$ as a function of h/b and a/h . Unfortunately the experiments reported in the literature always pertain to situations where h/b (the relative depth of the chink) is at least 0.5. This is because artificial roughness is usually studied because of its enhancement of heat transfer, which is best accomplished with relatively thin and high ribs (or even fins). Since in a BSR the relative depth of the chinks cannot be bigger than the particle radius over its length,

which will normally be smaller than 0.5, Maubach's model can only be used after extrapolation of the graphical correlation.

A model to account for roughness in a BSR in the regime between hydraulically smooth (Eq. (2-13)) and fully rough (Eq. (2-15)), may be derived from Eq. (2-13). The part of Eq. (2-13) within brackets, represents the universal velocity profile for turbulent flow along hydraulically smooth surfaces. For sand-rough surfaces, the same expression for the velocity profile has been proved experimentally to be adequate, but then the second constant is smaller than 5.5; the first constant, 2.5, appears not to depend on the surface roughness. From this it can be made plausible that the roughness in rod bundles could be described with a roughness function, $R(h^+)$, implemented in Eq. (2-13):

$$\sqrt{\frac{2}{f}} = A \left[2.5 \ln \text{Re} \sqrt{\frac{f}{2}} + 5.5 + R(h^+) \right] - G^* \quad (2-16)$$

Note that $R(h^+)$ defined in Eq. (2-16) is different from $R_M(h^+)$ defined in Eq. (2-15). By analogy with sand-rough surfaces, $R(h^+)$ would be expected to be between -5.5 and 0.

Another model to account for roughness in a BSR in the transition regime between hydraulically smooth and fully rough flow, may be based on Kirillov's method (Eq. (2-14)). The friction factor for turbulent flow in a circular channel, serving as input for Kirillov's equation, should then be calculated with the Colebrook-White correlation, that is widely used for this transition regime. The Colebrook-White correlation contains the parameter h/d_h to account for sand-roughness; this parameter should be replaced by a roughness function, to be fitted to experimental data for artificial roughness.

3.4 CFD techniques for flow in rod bundles

Using the methods discussed in Section 3, it is possible to predict friction factors and distribution of the flow over the subchannels in a BSR, for hydraulically smooth turbulent flow. For a more detailed analysis, *e.g.* investigation of secondary flows in the lateral plane within subchannels, or the lateral mixing between subchannels, Computational Fluid Dynamics (CFD) techniques are necessary. An introduction to the application of CFD techniques for flow in rod bundles is given by Spalding (1979). Unfortunately the standard versions of commercial CFD programs like FLUENT and PHOENIX are not suited for rod bundles, because of the combination of cartesian and cylindrical domains. Consequently, one would have to purchase special software packages, or obtain access to the software used by research institutes in the field of nuclear reactors or heat exchangers.

However, it was considered beyond the scope of the current project to do so, taking into account the considerable effort that is involved in using CFD techniques. Nevertheless, CFD techniques would be very helpful in the development of correlations to describe the influence of the artificial roughness in a BSR. Of course this would have to be combined with experiments to check the CFD predictions, as the modelling of turbulence is not developed far enough at the moment to allow *a priori* predictions.

4 Experimental work

4.1 Test section and experimental procedure

The pressure drop experiments were performed in the same test section as the experiments for validation of the BSR model, discussed in Chapter 5. Pressurized air at ambient temperature was used, the flow being controlled by an electronic mass flow controller with a capacity of 1000 ℓ_n/min . Diffusors with a top angle of 8° were used to connect the reactor module with the supply and exhaust pipes, to prevent swirls in the first and last part of the reactor. In the diffusor at the inlet, a honeycomb element was placed to dampen out any big swirls in the gas supply.

Rectangular reactor modules of 500 mm long were used, with an inner diameter of 35 or 70 mm. Most of the reactors were made of perspex, allowing visual observation of possible movements of the rods or strings in the reactor, caused by the gas flow. Metal or glass rods, or strings of particles were attached to wire gauze grids at the top and bottom end of the modules, at the top end through hooks and at the bottom end through springs; see Fig. 2-14.

The reactors had pressure taps at spacings of 50 mm along the length of the reactor, allowing measurement of pressure drop across various longitudinal sections of the reactor. The first pressure connection was at 2.5 cm from the beginning of the reactor module, at approximately the same axial position as the upper particles on the strings. Two differential pressure transducers were used (Validyne HVAC DP 850), one ranging to 63.5 Pa (0.25" H_2O), the other one to 635 Pa. Both transducers had an accuracy of 0.5% FS. The measurements with these pressure transducers were regularly checked using inclined manometers filled with oil.

Process control and data acquisition was done by a personal computer, using the software package 'The FIX' (Intellution Inc.) and the hardware system 'Transport System' (Transport Technology Inc.). For each reactor configuration a programmed series of flow set points was run. Set points, in random order, ranged from 50 to 1000

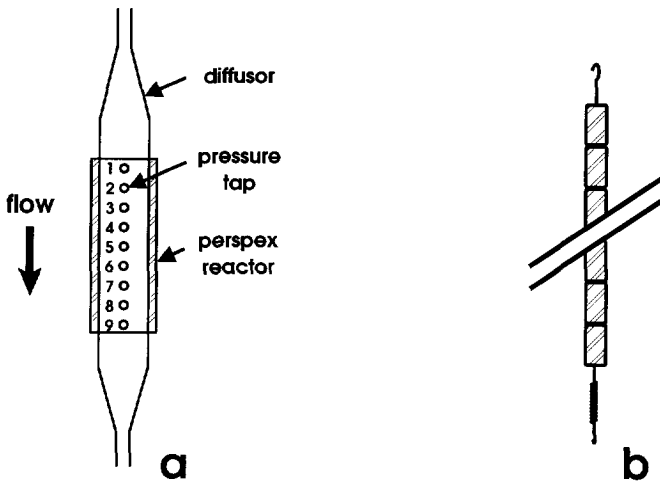


Figure 2-14 a: Reactor module used for pressure drop measurements.
b: Construction of the bead strings.

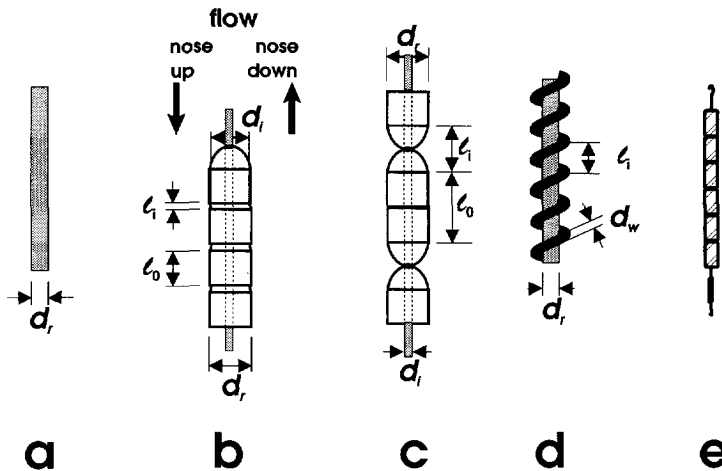


Figure 2-15 The rods and strings used for pressure drop measurements:
a: Smooth rods of brass (\varnothing 2 mm) or glass (\varnothing 8 or 10 mm).
b: Strings of steatite beads (\varnothing 4.6, 6.5, 8 or 10 mm), 'nose up' and 'nose down'.
c: Strings of steatite beads (\varnothing 10 mm), in turn oriented 'nose up' and 'nose down'.
d: Smooth rods of brass (\varnothing 2 mm), with wire wraps.
e: Strings of extruded cylindrical catalyst particles (\varnothing 1.6 or 3.2 mm).

ℓ_n /min, with intervals of 50 ℓ_n /min. Each set point was maintained for ten minutes, during which flow rate, absolute pressure, pressure drop and gas temperature were registered every minute. The series of flow set points was repeated for 24 hours or more, implying that each set point was run at least seven times during one experiment. For each instance of a flow set point, the median value from the ten minutes was taken; for each set point, the seven or more median values were averaged, and this average was used as the pressure drop corresponding to that flow. Standard statistical procedures were used to check for outliers and to estimate the reproducibility of the measurements.

4.2 Experiments conducted

Experiments were performed with 5 types of rods or strings, illustrated in Fig. 2-15:

- (1) Smooth rods of brass (\varnothing 2 mm) or glass (\varnothing 8 or 10 mm), with an estimated surface roughness of 1.5 μm . These experiments served as a reference, to allow comparison of the experiments with theories on flow in smooth rod bundles;
- (2) Strings of 'fish bone' beads made of steatite *i.e.* soapstone (\varnothing 4.6 to 10 mm). These strings served as a model system for strings of real cylindrical catalyst beads. The steatite beads were used because (a) they were available in more sizes than real catalyst beads, (b) they were easier to string, and (c) the strings of steatite beads were better defined and more uniform than strings of catalyst particles. As can be seen from Fig. 2-15, a string of steatite beads has chinks between catalyst beads, resembling those in a string of catalyst beads.
The strings of steatite beads were tested in two orientations, indicated in Fig. 2-15, designated as 'nose up' and 'nose down'. This was done to test the influence of the shape of the chink, that was not symmetric in the lateral plane.
- (3) Strings with steatite beads in turn oriented 'nose up' and 'nose down'. The roughness of these strings is extreme, compared to strings of real catalyst particles. The purpose of this experiment was to check whether the hydraulically fully rough regime could be reached.
- (4) Brass rods (\varnothing 2 mm) with helically wrapped wires (stretched springs with a wire thickness of 0.25 mm). In these experiments the predicted thickness of the laminar sub-layer was comparable to the radius of the rods. It allowed verification of the hypothesis stated in Section 3.1 that in this situation the laminar sub-layer is thinner than predicted by Eq. (2-11), or at least easier to disturb than when the curvature of the surface is negligible. Furthermore, comparison of the results obtained from the wire wrapped rods (that have a 'positive roughness', *i.e.*, bumps), with results from strings of cylindrical extrudates (mainly 'negative roughness', *i.e.*, chinks), would give an indication of the different effects of positive and negative roughness.
- (5) Strings of real catalyst particles, *viz.* cylindrical extrudates of 1.6 or 3.2 mm in diameter and *ca.* 6 mm in length, with an axial hole of 0.4 mm in diameter.

Table 2-1 Overview of the pressure drop experiments.

Run #	Reactor diameter [mm]	d_r [mm]	s/d_r [-]	w/d_r [-]	n [-]	d_h [mm]	ϵ [$\frac{\text{m}^3_{\text{void}}}{\text{m}^3_{\text{reactor}}}$]	$d_i / w_i / w_o$ [mm]	material	$\langle u \rangle_{\text{max}}$ [m/s]	Re_{max} [-]	δ (Re) [mm]
1	70	1.6	3.13	3.63	169	16.2	0.93	-	extrudates	3.7	4500	0.24 (4500)
2	70	1.6	2.25	2.71	342	8.43	0.86	-	extrudates	4.0	2500	0.19 (2500)
3	35	3.2	1.38	1.16	64	3.63	0.58	-	extrudates	14.0	4000	
4	35	3.2	1.00	1.00	100	0.78	0.22	-	extrudates	20.5	1200	
5	70	2.0	2.70	1.80	169	13.0	0.89	-	brass	3.8	3500	0.24 (3500)
6	70	10.0	1.50	1.00	25	11.0	0.60	-	glass	5.7	4500	0.19 (4500)
7	70	8.0	1.09	1.05	64	3.56	0.34	-	glass	10.0	2500	0.10 (2500)
8	70	10.0	1.50	1.00	25	11.0	0.60	9 / 2 / 6	steatite nose up	5.7	4500	0.19 (4500)
9	70	8.0	1.09	1.05	64	3.56	0.34	7 / 1 / 5	steatite nose up	10.0	2500	0.10 (2500)
10	70	10.0	1.50	1.00	25	11.0	0.60	9 / 2 / 6	steatite nose down	5.7	4500	0.19 (4500)
11	70	2.0	2.70	1.80	169	13.0	0.89	$d_w = 0.2$	brass wire wrap	3.8	3500	0.39 (2000)
12	70	10.0	1.50	1.00	25	11.0	0.60	5 / 9 / 12	steatite in turn	5.7	4500	0.27 (3000)
13	70	6.5	1.38	1.74	49	10.2	0.67		steatite nose up	7.3	6300	0.28 (2500)
14	70	6.5	1.11	1.45	81	4.58	0.45		steatite nose up	11.3	4100	0.14 (4100)
15	35	4.6	1.38	1.54	25	6.46	0.66		steatite nose up	29.8	15000	M3

To study the hydrodynamic inlet effects discussed in Section 2.5, the pressure drop across various longitudinal sections of the reactor was measured for the configuration for which the largest entrance length is predicted, based on Eq. (2-10). The pressure gradient (as a function of Re) across pressure connections 1 and 8 was compared with that across connections 2 and 7, and across connections 4 and 8. Based on the results of these experiments, it was decided to use connections 2 and 7 for all other experiments.

An overview of all conducted pressure drop experiments is given in Table 2-1.

4.3 Results and discussion

Whereas in case of bundles of smooth rods the calculation of the voidage, average velocity, hydraulic diameter and Reynolds number is unambiguous, it is not for bundles of rods with artificial roughness. For example, for strings of steatite beads with an outer diameter of 10.0 mm, the average perimeter of a string is less than 10 mm, due to the chinks. Furthermore the voidage of a bundle of these strings is higher than that of a bundle of glass rods of the same diameter. Consequently, the average velocity in the bundle of strings is lower than in the bundle of glass rods. The opposite holds for wire wrapped rods compared to smooth rods.

It was decided not to take into account the increase or decrease of wetted wall and voidage due to the artificial roughness. The decision was based on the fact that (1) for sand-rough pipes the increase of wetted wall surface due to the roughness is not taken into account either, even though the microscopic perimeter of the pipe can be several times higher than πd ; (2) it is doubtful whether there actually is a net axial gas flow through the chinks; the chinks could be occupied by vortices, in which case they do not result in extra flow area and a lower average gas velocity; (3) in practice it would be difficult to estimate the increase or decrease of the wetted wall surface or voidage for bundles of strings of catalyst particles.

The reproducibility of the pressure drop measurements was very high: the standard deviation was usually not higher than one percent. Nevertheless, it should be noted that at the lowest Reynolds numbers (especially for large hydraulic diameters), the measured pressure drops are extremely low (typically 1 Pa). At such low pressure drops the systematic error due to the limited accuracy of the differential pressure transducer is about 30% of the measured value. As a result the accuracy of those data points is considerably lower than that of the points at high Reynolds numbers and small hydraulic diameters.

4.3.1 Hydrodynamic inlet effects

In Fig. 2-16 the experimental friction factors of runs **1a**, **1b** and **1c** are plotted versus Re . The difference between the runs is the section of the reactor across which the pressure drop was measured: in run **1a** across connections 1/8, in **1b** across 2/7 and in **1c** across 4/8.

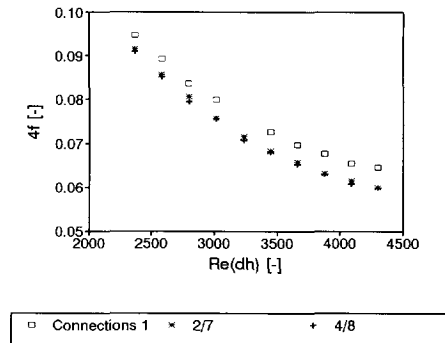
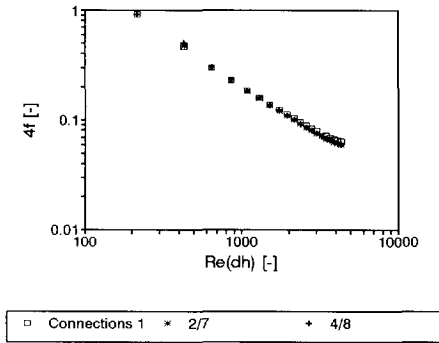


Figure 2-16 Dependence of $4f$ on the reactor section.

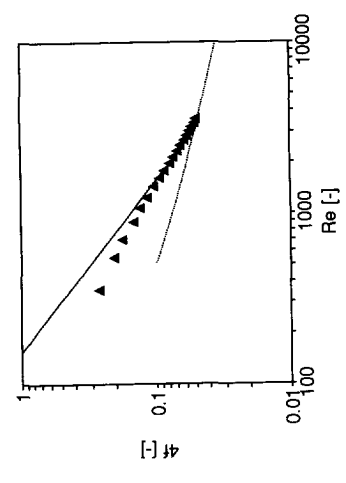
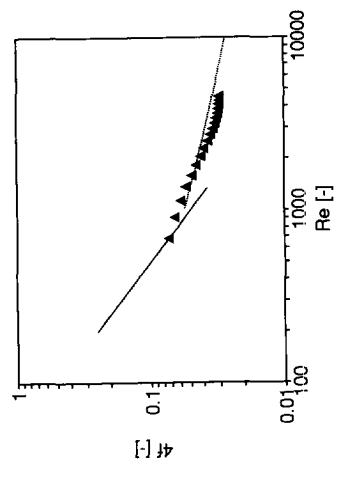
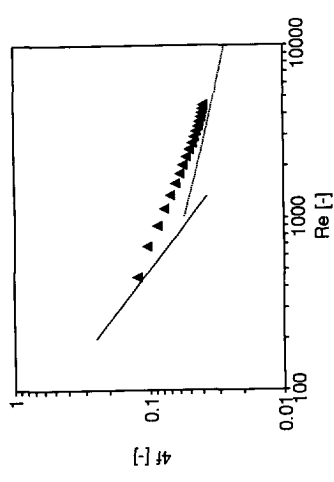
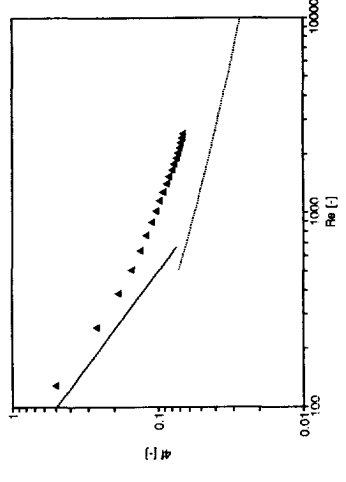
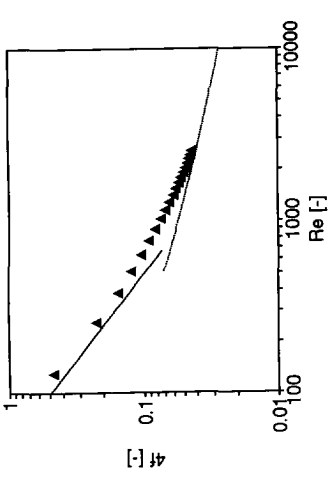
Figure 2-17 Detail of Figure 2-16. NB: linear scale.

The straight line with slope -1 that could be drawn through the data points, indicates that the flow remains laminar up to $Re \approx 2500$. For this Re , a hydrodynamic inlet length of *circa* 0.17 m is expected from Eq. (2-10). Based on this it would be expected that at this Reynolds number, the average friction factor of the section between connections 1/8 is 43% higher than of the section between connections 4/8. From Fig. 2-17, a detail of Fig. 2-16 (on a linear scale instead of double logarithmic), it is seen that the difference is much smaller. This indicates that the experimental hydrodynamic inlet length is smaller than the theoretical value. Further support for this conclusion is lent by the fact that the average friction factors of the section between connections 2/7 practically coincide with those of the section between connections 4/8, indicating that at connection 2 (*i.e.*, 0.05 m from the first particles on the strings) the flow has practically fully developed.

It is not clear why the hydrodynamic inlet effect is smaller than was expected, or why the inlet length is shorter. Possible causes for the discrepancy are the wire gauze grid at the inlet of the reactor, to which the strings or rods are attached, and the blunt top side of the strings. These may enhance the disturbance of the flat velocity profile that, according to the hydrodynamic model from which Eq. (2-10) was derived, enters the reactor.

For all other experiments, the hydrodynamic inlet length predicted by Eq. (2-10) is smaller than for the experiment discussed in the previous paragraph. Consequently it was concluded that laminar flow hydrodynamic inlet effects for all experiments would be insignificant if the pressure drop was measured across connections 2 and 7.

For turbulent flow, hydrodynamic entrance lengths are usually expressed relative to the hydraulic diameter of the channel. Presser, as quoted by Rehme (1987), found that



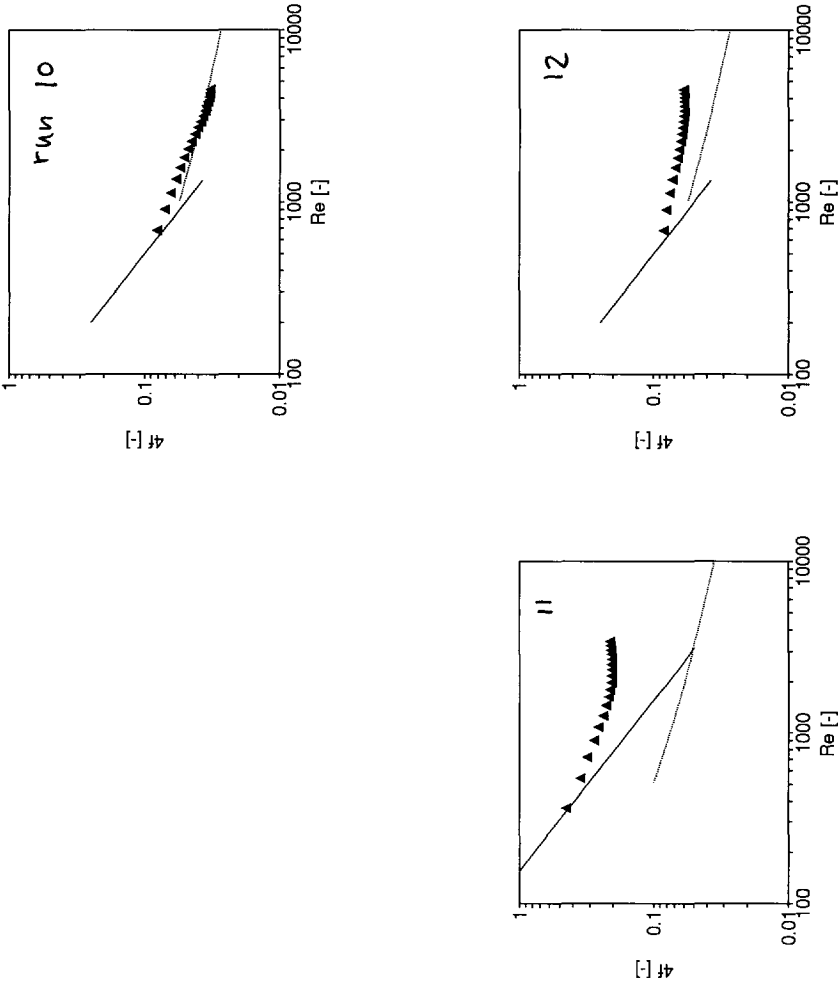


Figure 2-18 Experimental friction factors obtained with strings of steatite beads. See Table 2-1.

the turbulent flow hydraulic entrance length in rod bundles depends on the average distribution of the flow among the subchannels. For a uniform distribution $\ell_h/d_h \approx 20$, whereas for very non-uniform distributions ℓ_h/d_h may be up to 40. In our experiments the flow distribution, as estimated with Eq. (2-13), was often quite non-uniform: estimated ratios of the gas velocity in the central subchannels to that in the wall subchannels ranged from 2 to 4. Using $\ell_h/d_h = 40$, inlet lengths up to the reactor length are predicted.

In Fig. 2-18, graphs 5 and 6, the experimental friction factors of bundles of smooth glass rods are plotted versus the Reynolds number. The dotted lines represent the friction factors predicted by Eq. (2-13). Although for these two runs turbulent flow entrance lengths of 0.44 m and 0.14 m are predicted, the data points seem to closely approximate the theoretical friction factors. From this it was concluded that in all experiments turbulent flow hydrodynamic inlet effects were insignificant.

4.3.2 Comparison of experimental friction factors with theory for smooth rod bundles

The experimental friction factors of runs 5 to 12 are plotted as a function of Re in Fig. 2-18. In these graphs the solid and dotted lines represent the friction factors predicted by the theory; at low Reynolds numbers by the subchannel analysis (Eq. (2-7)), at high Reynolds numbers by Rehme's AG* method (Eq. (2-13)). The smaller accuracy of the points at the lowest Reynolds numbers is the most probable explanation for the apparent deviation at low Re of the slope of the imaginary line through the data points, from the theoretical value of -1.

The graphs in Fig. 2-18 are arranged in such a way that from left to right the relative pitch decreases (at constant absolute wall roughness), and from top to bottom the wall roughness increases (at constant relative pitch). From Table 2-1 it can be seen that runs 5 to 7 would be predicted to remain in the hydraulically smooth regime, even at the highest Reynolds numbers. For runs 8 to 10 the depth of the chinks is bigger than the thickness of the laminar sub-layer; however, the disturbance of the boundary layer caused by a chink of a certain size will be less pronounced than that caused by a bump of the same size. Therefore it cannot be predicted whether runs 8 to 10 will be in the hydraulically smooth or in the transition regime at the highest Reynolds numbers. For run 11 the predicted laminar sub-layer thickness at the highest flow is about the same as the thickness of the wires wrapped around the rods. Therefore the flow would be expected to remain in the hydraulically smooth regime at the tested Reynolds numbers, unless the relatively high curvature of the rod surface leads to a less stable sub-layer. Finally, run 12 is expected to be in the hydraulically fully rough regime at the highest flow.

Comparing these predictions with the observations, the following comments can be made:

- (a) For hydraulically smooth rods, the theory gives a good prediction of $4f$. This is best seen from graph 7, which is most accurate. It nicely illustrates the very

gradual transition from laminar flow (up to $Re \approx 400$) to fully turbulent flow (which seems to be reached at $Re \approx 2500$).

- (b) The observations on the onset and completion of turbulence in the smooth rod bundles agree fairly well with the numbers mentioned in Section 3.1. Turbulence may start at Reynolds number well below 1000 (graph 6), but the laminar flow regime can extend to Reynolds numbers as high as 3000 (graph 5). Completion of turbulence seems to be reached at Reynolds numbers between 3000 and 10^4 .

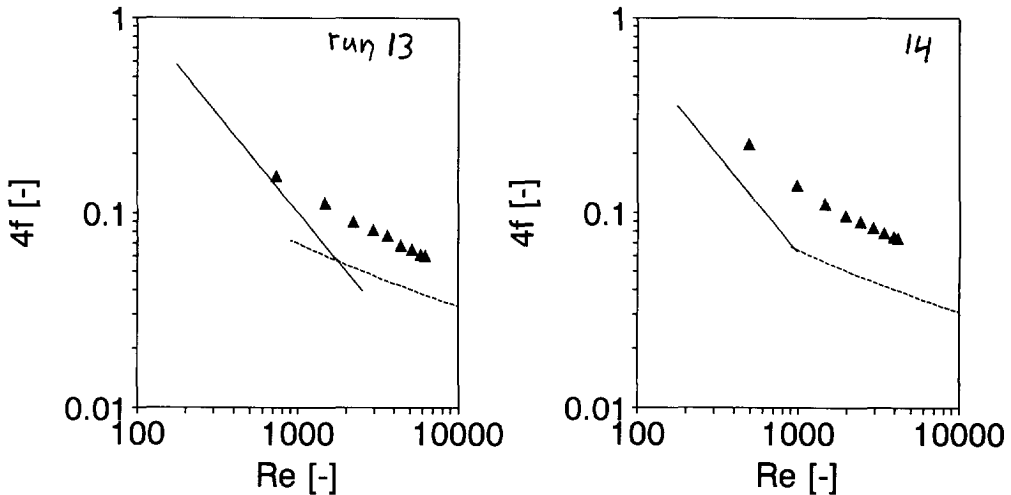


Figure 2-19 Additional experimental friction factors obtained with strings of steatite beads.

- (c) For rod bundles with artificial roughness, the effect of roughness increases with decreasing hydraulic diameter of the subchannels or, equivalently, with increasing relative roughness. This follows from comparison of graphs 8 and 10 with 9 and Fig. 2-19. For runs 8 and 10 the predicted thickness of the laminar sub-layer is 0.19 mm at the highest flow. Since the data points for these runs practically coincide with the predicted friction factors for hydraulically smooth bundles, the laminar sub-layer is apparently not disturbed by the chinks between the particles, which are 0.5 mm deep. However, in run 9 and also in runs 13 and 14, there is an obvious effect of the roughness, even though the laminar sub-layer thickness in those runs is approximately the same as in runs 8 and 10. A possible explanation is the considerable difference in relative roughness between the experiments. In runs 8 and 10 the relative roughness of the central subchannels is 0.027, whereas in runs 9, 13 and 14 it is 0.14, 0.054 and 0.14, respectively. When the relative roughness is high, the disturbance of the laminar sub-layer will extend relatively deep into the channel, leading to a relatively strong effect on the pressure drop.

- (d) Based on runs **8** and **10**, no conclusion can be made as to the influence of the shape of a chink on the pressure drop. Since both runs stayed in the hydraulically smooth regime, the chinks had no influence whatsoever.
- (e) In contrast to the expectation, run **11** appears to reach the fully rough regime at $Re \approx 2000$, where the predicted laminar sub-layer thickness is 0.39 mm, which is much thicker than the thickness of the wires wrapped around the rods. This supports the hypothesis that the laminar sub-layer is thinner or less stable for a highly convex surface than for a flat surface.
- (f) For strings of steatite beads in turn oriented 'nose up' and 'nose down' (run **12**), the fully rough regime is reached at $Re \approx 3000$. At that point the predicted total thickness of the laminar sub-layer and the buffer layer is 1.6 to 3.8 mm, whereas the depth of the chinks is 2.5 mm. Consequently, the observation agrees with the theory.

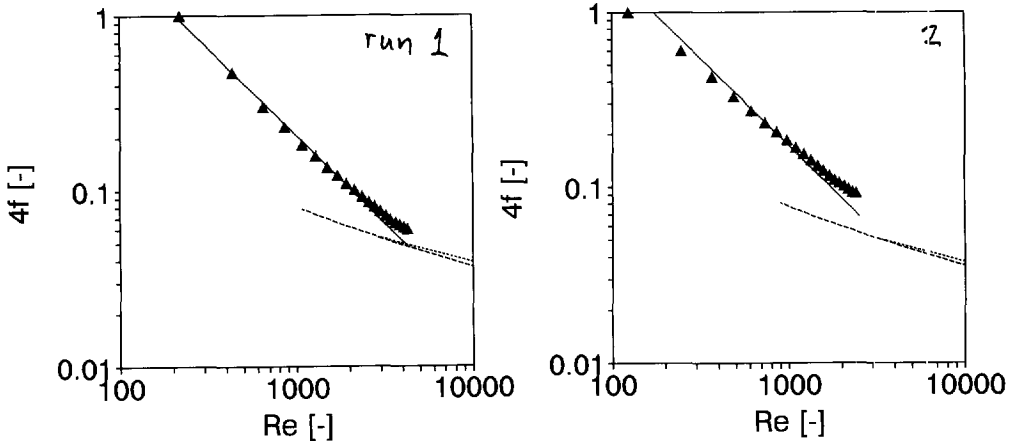


Figure 2-20 Experimental friction factors obtained with strings of extruded catalyst particles.

The results of the pressure drop experiments with the strings of extruded catalyst particles are presented in Fig. 2-20. Comparison of graphs 1 and 2 with graph 11 of Fig. 2-18 shows that there is indeed an important difference between positive and negative roughness, or bumps and chinks. Even though the size of the chinks in the bead strings is *circa* 0.8 mm (*i.e.*, the radius of the particles), the effect on the friction factor is negligible; in contrast, the wrapped wires with a thickness of 0.25 mm result in hydraulically fully rough flow.

Comparison of graphs 1 and 2 of Fig. 2-20, in combination with comparison of graphs 5 and 6 of Fig. 2-18, indicates that at a higher relative pitch, the laminar flow regime extends to a higher Reynolds number.

4.3.3 Comparison of experimental friction factors with models for rough rod bundles

As discussed in Section 3.3, Rehme's AG^+ method (Eq. (2-13) for turbulent flow in hydraulically smooth rod bundles can be extended to rough bundles, using Eq. (2-16). Values of the roughness function $R(h^+)$ were fitted for runs **9**, **13** and **14**; see Fig. 2-21. Values of -3.5 and -4.0 appear to give a satisfactory description of the experimental data over the upper Re range. Although these values could be used in the design of a BSR with a high *relative* roughness, more experiments would be needed to find a relation between $R(h^+)$ and (1) the size, shape and surface density of the roughness, and (2) the pitch and rod diameter of the bundle.

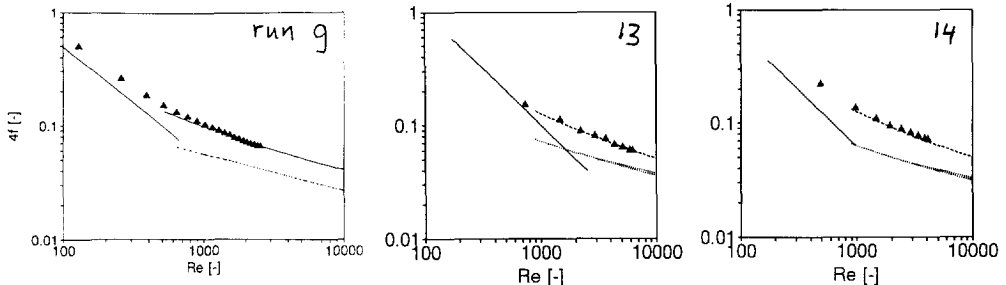


Figure 2-21 Fit of the roughness function to the experimental friction factors for strings of steatite beads. Solid lines: theoretical, smooth rods; dashed lines: fit for turbulent flow with fitted roughness function; symbols: experimental.

Another model for the prediction of the turbulent friction factor in rough rod bundles, suggested in Section 3.3, was based on Kirillov's correlation (Eq. (2-14)). For runs **9**, **13** and **14** the friction factors for turbulent flow in rough pipes were calculated with the Colebrook-White correlation for sand-rough circular channels. Using these values in combination with Kirillov's correlation for rod bundles, however, yielded predicted friction factors that were much less dependent on Re than the experimental friction factors. Probably better results could be obtained when the turbulent friction factor in pipes would be predicted from a correlation for pipes with artificial roughness instead of sand roughness.

It was attempted to describe the friction factors for flow in the hydraulically fully rough regime, runs **11** and **12** by Eq. (2-15) due to Maubach (1970). It must be noted that the graphical correlation presented by Maubach was developed for a dimensionless roughness h^+ (see Eq. (2-12)) higher than 50, whereas in run **11** it was only *circa* 6 and in run **12** only *circa* 34.

For run **11**, $R_M(h^+)$ as predicted by Maubach's correlation is 4.0; this compares well to the value of 3.15 that was fitted from the experimental data. For run **12** the dimensions of the roughness are out of the range of Maubach's correlation; an experimental value for $R_M(h^+)$ of 15.1 was fitted, which is indeed out of the range of values predicted by Maubach's correlation.

5 Conclusions and recommendations

Under the conditions tested in this study, which are expected to be typical for an industrial BSR, the hydrodynamic entrance length is shorter than predicted by the theory, and hydrodynamic inlet effects can be neglected. The shorter entrance length may result from the wire gauze grid at the reactor inlet and/or the blunt top side of the rods or bead strings.

The flow regime starts to change from laminar to turbulent at Reynolds numbers between *ca.* 400 and 3000. The lower value pertains to low voidages (*ca.* 30%), the higher number to high voidages (80% or higher). The transition from laminar to turbulent flow in rod bundles takes place much more gradually than in circular channels. Fully turbulent flow is reached at Reynolds numbers between $3 \cdot 10^3$ and 10^4 . The experimental friction factors for smooth rods are well-described by correlations available from the literature, both in the laminar and the turbulent flow regime. For the purpose of the development of the BSR, no more experiments with smooth rods are necessary.

In the tested range of Reynolds numbers (300-5000), the tested strings of ceramic beads and extruded catalyst particles can be described as hydraulically smooth when the relative roughness is smaller than 0.04, even when the depth of the chinks between the beads is larger than the laminar sub-layer thickness. When the relative roughness is higher than 0.04, a roughness function has to be introduced to correlate the results. The fitted values of the roughness function are not in contradiction with values that are expected from the universal velocity profile for turbulent flow.

Momentum transport in bundles depends strongly on the type of roughness: ribs on the surface of rods have a much stronger effect on the flow characteristics than chinks in the surface (as in bead strings). Since little literature is available on momentum transport in rod bundles with chinks, a study using CFD techniques is recommended, in combination with experimental validation.

Based on the theory and experimental data presented in this chapter, a recipe is given to predict friction factors for a BSR:

1. Calculate the geometry parameter for laminar flow, using the subchannel analysis (Eq. (2-7)) in combination with laminar geometry parameters for the subchannels, obtained from numerical solution of the Poisson equation or from correlations given by Rehme (1987). If a BSR is being designed, this is the right stage to find (by trial-and-error) the relative wall distance that leads to the preferred flow distribution over the subchannels. Note that for turbulent flow, the distribution will even out.

The laminar geometry parameter is valid for Reynolds numbers below 400 (low relative pitch, voidage $\approx 35\%$) to 3000 (high relative pitch, voidage $> 80\%$).

2. For non-laminar flow, calculate the bundle friction factor, as a function of Re , for hydraulically smooth turbulent flow, using the laminar geometry parameter for the bundle, in combination with Rehme's AG^* method (Eq. (2-13)). From this also the distribution of the turbulent flow over the subchannels can be estimated.
3. Using the turbulent friction factor for smooth bundles, calculate the dimensionless roughness height, h^+ , from Eq. (2-12). How to estimate the absolute roughness height, h , depends on the type of beads. The upper limit is the bead radius or the spacing between two beads on a string, whichever is smaller.
4. If $h^+ \ll 5$, the relations for smooth bundles are valid.
If $h^+ \approx 5$, the relations for smooth bundles are most suitable if the relative roughness, h/d_h , is smaller than 0.04. If $h/d_h > 0.04$, Eq. (2-16) is most suitable. For a typical BSR, a value of -3.5 to -4.0 for the roughness function seems to be appropriate.
If $h^+ > 50$, Eq. (2-15) should be used; the value of the roughness function should be estimated from Maubach's graphical correlation. For a typical BSR it will probably be necessary to extrapolate from this correlation.

Using this recipe, the pressure drop across a typical BSR can be predicted with an inaccuracy ranging from a few percents (laminar flow or small relative roughness) to ca. 50% (transition regime or fully rough turbulent flow).

Acknowledgements

Jos van Reisen, Freddy Koetse, Christien Groenendaal and Otto Oudshoorn are gratefully acknowledged for their substantial contribution to the work reported in this chapter.

Notation

A	flow area of a subchannel or a rod bundle	[m ²]
A	dimensionless parameter in Rehme's $A-G^*$ method	[-]
d_h	hydraulic channel diameter	[m]
d_r	rod or string diameter	[m]
f	(Fanning) friction factor ($\equiv 4f/4$)	[-]
f_t	friction factor of a circular tube	[-]
f_x	local friction factor	[-]
$4f$	(Darcy-Weisbach) friction factor	[-]
$4fRe$	laminar geometry parameter	[-]
G	dimensionless parameter in Maubach's method	[-]
G^*	dimensionless parameter in Rehme's $A-G^*$ method	[-]
h	(average) height of surface roughness	[m]
h^+	dimensionless (average) height of surface roughness	[-]
l_h	hydrodynamic entrance length	[m]
L	length over which a variable is averaged	[-]
n	total number of subchannels in a bundle	[-]
N	number of rods per row in a bundle	[-]
P_w	wetted perimeter of a subchannel or a rod bundle	[m]
$R(h^+)$	roughness function	[-]
$R_M(h^+)$	roughness function	[-]
s	pitch of rod or strings in a bundle	[m]
$\langle u \rangle$	average fluid velocity in a channel	[m/s]
u_s	'undisturbed' fluid velocity in developing flow	[m/s]
u^*	friction velocity	[m/s]
u_z	axial fluid velocity	[m/s]
w	wall distance	[m]
x	longitudinal distance from the reactor inlet	[m]
x^+	dimensionless longitudinal distance from the reactor inlet	[-]
y	lateral distance from a surface	[m]
y^+	dimensionless lateral distance from a surface	[-]

Greek letters

δ_h	hydrodynamic boundary layer thickness	[m]
Δ_1, Δ_2	shortest and longest surface-to-surface distance in a BSR	[m]
ε	voidage of a bundle of rods or strings	$[\text{m}^3_{\text{void}}/\text{m}^3_{\text{reactor}}]$
μ	dynamic fluid viscosity, molecular or turbulent	[Pa·s]
ν	kinematic fluid viscosity	$[\text{m}^2/\text{s}]$
ρ	fluid density	$[\text{kg}_{\text{fluid}}/\text{m}^3_{\text{fluid}}]$
$\tau_{f,w}$	friction stress exerted by the fluid on the wall	$[\text{N}/\text{m}^2]$
∇p	pressure gradient across a channel	[Pa/m]

References

- Coulson, J.M. and Richardson, J.F., 1979, *Chemical Engineering* 3rd Ed., vol. 1. Pergamon Press, Oxford.
- Johannsen, K., 1983, Longitudinal Flow over Tube Bundles, in *Low Reynolds Number Flow Heat Exchangers* (Edited by S. Kakaç, R.K. Shah and A.E. Bergles), pp. 229-273. Hemisphere Publishing Corporation, Washington.
- Kakaç, S. and Spalding, D.B. (eds.), 1979, *Turbulent Forced Convection in Channels and Bundles* vol. 1. Hemisphere Publishing Corporation, Washington.
- Maubach, K., 1970, Reibungsgesetze turbulenter Strömungen. *Chemie-Ing.-Techn.* **42**(15), 995-1004.
- Oudshoorn, O.L., 1993, Pressure Drop across the Bead String Reactor. *M.Sc. Thesis*. Delft University of Technology, Delft, The Netherlands.
- Pustyl'nik, P.N., Balunov, B.F. and Blagoveshchenskii, A.Y., 1990, Heat Transfer with Forced Longitudinal Flow of Air through a Bundle of Tubes with Boundary Condition $T_w = \text{const}$. *Thermal Engineering* **37**, 135-138.
- Rehme, K., 1971, Laminarströmung in Stabbündeln. *Chemie-Ing.-Techn.* **43**(17), 962-966.
- Rehme, K., 1973, Simple Method of Predicting Friction Factors of Turbulent Flow in Non-Circular Channels. *Int. J. Heat Mass Transfer* **16**, 933-950.
- Rehme, K., 1987, Convective Heat Transfer over Rod Bundles, in *Handbook of Single-Phase Convective Heat Transfer* (Edited by S. Kakaç, R.K. Shah and W. Aung), pp. 7.1-7.62. John Wiley & Sons, New York.
- Rehme, K., 1992, The Structure of Turbulence in Rod Bundles and the Implications on Natural Mixing between the Subchannels. *Int. J. Heat Mass Transfer* **35**(2), 567-581.

- Schmid, J., 1966, Longitudinal Laminar Flow in an Array of Circular Cylinders. *Int. J. Heat Mass Transfer* **9**, 925-937.
- Spalding, D.B., 1979, Theoretical Prediction of Single-Phase Turbulent Flow and Heat Transfer in Ducts and Rod Bundles, in *Turbulent Forced Convection in Channels and Bundles* (Edited by S. Kakaç and D.B. Spalding), vol. 1, pp. 115-152. Hemisphere Publishing Corporation, Washington.
- Sparrow, E.M. and Loeffler Jr., A.L., 1959, Longitudinal Laminar Flow Between Cylinders Arranged in Regular Array. *AIChE J.* **5**(3), 325-330.

Chapter 3

Mass Transfer in a Bead String Reactor

Contents

Summary	65
1 Introduction	66
2 Theoretical and empirical heat and mass transfer relations	67
2.1 Introduction	67
2.2 Governing equations and boundary conditions	68
2.3 Theoretical relations for laminar flow	72
2.3.1 Angular dependence of Sh	72
2.3.2 Influence of relative pitch on Sh	73
2.3.3 Influence of Da_{II} on Sh	74
2.3.4 Change of Sh in a developing concentration boundary layer	74
2.4 Relations for turbulent flow	76
2.4.1 Empirical relations	76
2.4.2 Chilton-Colburn analogy	77
2.4.3 Change of Sh in a developing concentration boundary layer	78
3 Experimental mass transfer study	79
3.1 Introduction	79
3.2 Experimental set-up and procedures	79
3.3 Experiments conducted	81
4 Results and discussion	84
4.1 Introduction	84
4.2 Pressure drop experiments	85
4.3 Effect of the 'chink' between particles on the local mass transfer coefficient	86
4.4 Dependence of Sh on the axial position in the reactor	87
4.5 Development of the mass transfer boundary layer	88
4.6 Dependence of Sh on the lateral position	89
4.7 Dependence of Sh on Re	92
5 Conclusions	95
Acknowledgement	96
Notation	96
References	98

Summary

In a properly designed BSR, the reactor performance should not be limited by the rate of mass transfer from the bulk flow to the catalyst surface. It is therefore important to have relations that adequately predict the Sherwood number (Sh) as a function of the reactor geometry and the process conditions, the more so because the low pressure drop that is aimed for with a BSR, is generally associated with proportionally low mass transfer rates.

A large amount of literature is available in which all aspects of heat transfer in so-called 'rod bundles' of compact heat exchangers and nuclear reactors are described and modeled; for example, correlations are available that give the Nusselt number (Nu) as a function of the relative pitch and (for turbulent flow) the Reynolds number. These correlations allow a reasonably accurate prediction of the mass transfer characteristics of a BSR, using the analogy between heat and mass transfer. Deviations from predictions based on literature correlations may occur because of two facts:

1. The boundary condition of the governing partial differential equation that describes mass transfer in a reactor with catalytic walls, differs from the standard boundary conditions assumed in most texts on heat transfer in rod bundles, namely CONSTANT SURFACE TEMPERATURE (or concentration) and CONSTANT WALL HEAT FLUX (or mass flux). It can be shown, however, that the Sherwood number of a reactor with catalytic walls will lie between the values obtained for these two standard boundary conditions.
2. The literature usually deals with hydraulically smooth rod bundles; the type of artificial roughness of the BSR strings seems to be unique.

For the laminar flow regime, the balance equations that describe mass transfer in a BSR can be solved semi-analytically or numerically, and for this flow regime it can be shown that the effect of the boundary condition is relatively unimportant, except for relative pitches smaller than 1.1. In the latter case the Sh and Nu values obtained for the two limiting boundary conditions may deviate more than 30%, up to a factor 2 at a relative pitch of 1.0 (for regular square arrays). It can also be shown that for relative pitches smaller than 1.1, the so-called 'mass transfer entrance length' (*i.e.* the length needed for the concentration profile to fully develop), becomes of the same order of magnitude as the length of a typical BSR module. The Sherwood number averaged over the length of the reactor may then be more than 25% higher than the Sherwood number for a fully developed concentration profile. However, the effect of the enhanced mass transfer in the mass transfer entrance zone will usually only have a small effect on the overall reactor performance, except in the unlikely situation that the reactor performance is limited by the mass transfer rate.

The influence of the roughness of the BSR strings on the mass transfer characteristics in turbulent flow was studied experimentally, using the well-known technique of naphthalene sublimation. The experimental Sherwood numbers were related to the friction factors, using the Chilton-Colburn analogy. As can be expected, for any Reynolds number in the turbulent flow regime the experimental Sherwood number falls between the two values predicted from (A) the experimentally determined friction factor for the tested reactor, and (B) the theoretical friction factor for a smooth rod bundle with the same relative pitch. Using these two predictions as the limiting values, the experimental Sherwood numbers could be predicted with an accuracy of *ca.* 30%, which is usually acceptable.

In the experimental study it was further found that for all practical situations, the dependence of the Sherwood number on the axial or lateral position in the reactor may be neglected in case of turbulent flow.

1 Introduction

As was mentioned in Chapter 2, heat transport phenomena of longitudinal flow through rod bundles have been studied quite extensively in the past and is still receiving constant attention, due to the importance of compact heat exchangers and nuclear reactors. This has led to many theoretical and empirical relations to predict Nusselt numbers as a function of the relative pitch and (for non-laminar flow) the Reynolds number; a relatively recent review of those relations, that pertain to smooth rod bundles, is from Rehme (1987).

Knowing this, one might expect that a study of the existing literature would be sufficient to allow modeling of mass transfer in a Bead String Reactor, because usually heat transfer relations can be directly translated into mass transfer relations, as the governing differential equations are identical. Unfortunately this is not completely true, because of two reasons.

The first reason is that in the translation of heat transfer relations, special attention has to be given to the boundary conditions. Most texts on heat transfer only deal with the standard boundary conditions of constant wall temperature or constant heat flux, whereas in a chemical reactor only in special cases constant surface concentration or constant mass flux can be assumed.

The second reason is that no relations have been found that predict heat (or mass) transfer in rod bundles with the unusual type of roughness that is encountered in the BSR. The known relations on smooth rods will obviously underestimate the heat (or mass) transfer rate in a BSR in turbulent flow.

Consequently, the goal of this chapter is to:

- give a brief overview of the most convenient heat transfer relations that are proposed in the literature; no extensive literature review will be given, since this has already been done fairly recently by Rehme (1987).
- discuss the consequences of the non-standard boundary conditions arising in the description of mass transfer in a plug flow reactor with catalytically active walls;
- present experimental data on mass transfer for turbulent flow in a BSR with hydrodynamically rough strings of beads.

Like in the discussion of momentum transfer in a BSR, only the regular square array of strings will be discussed. The analysis of the other types of array (*e.g.* triangular or circular) is analogous to that of the square array.

Only steady state flow is considered, because the time scale on which the mass transfer reaches a steady state is very small compared to the time scale of process changes. Furthermore it is again assumed that there is only convective flow in the longitudinal direction, parallel to the strings.

The structure of this chapter is as follows. In Section 2 theoretical and empirical heat and mass transfer relations are discussed. The theoretical relations pertain to laminar flow, because for that flow regime the governing equations can be relatively easily solved numerically. The empirical relations pertain to turbulent flow in smooth rod assemblies. In this section also the implications of the non-standard boundary conditions in a BSR are discussed.

In Section 3 the experimental study of turbulent flow mass transfer in a BSR with hydrodynamically rough strings of beads is described. In Section 4 the results of the experiments are presented, and related to theoretical relations and empirical relations from the literature.

2 Theoretical and empirical heat and mass transfer relations

2.1 Introduction

In this section heat and mass transfer relations for rod bundles with a regular square array are discussed. Like in the discussion of momentum transfer (Chapter 2), a distinction should be made between central, wall and corner subchannels. For momentum transfer it was shown that the gas velocity through wall and corner

subchannels can strongly deviate from the velocity through the central subchannels, whereas the difference between two central subchannels is usually negligible. To calculate the total flow rate through a rod bundle for a given axial pressure gradient, it was shown to be important—at least for lab-scale BSR modules—to take the flow through the wall and corner subchannels into account. This is because in case of large wall distances (*i.e.*, a relatively large gap between the reactor wall and the first string), a considerable part of the flow goes through the wall channels.

Such a flow distribution would be expected to result in different Sherwood numbers for central, wall and corner subchannels. However, the effect of these variations on the performance of a BSR in practice (*i.e.* in larger scale modules) can be expected to be small, because (1) the fraction of the total external catalyst surface facing a wall or corner subchannel is quite small, and (2) in a properly designed BSR, film layer mass transfer should never be the only rate limiting step.

Therefore only relations for mass transfer in central subchannels are discussed in this section. In the discussion of the experimental study (Sections 3 and 4), the dependence of the Sherwood number on the lateral position in the reactor will be discussed.

Because in the BSR the pressure drop is supposed to be small compared to the total pressure, incompressible flow may be assumed. Furthermore, as it was shown in Chapter 2 that the hydrodynamic entrance length is negligibly short under the conditions of the present study, only relations for fully developed flow will be discussed. Please note that a (hydrodynamically) fully developed flow does not imply a fully developed thermal or concentration boundary layer.

2.2 Governing equations and boundary conditions

The discussion of mass and heat transfer in rod bundles pertains to the same geometrical and mathematical domains as the discussion of momentum transfer; a unit or elementary cell of a central subchannel is shown in Fig. 3-1.

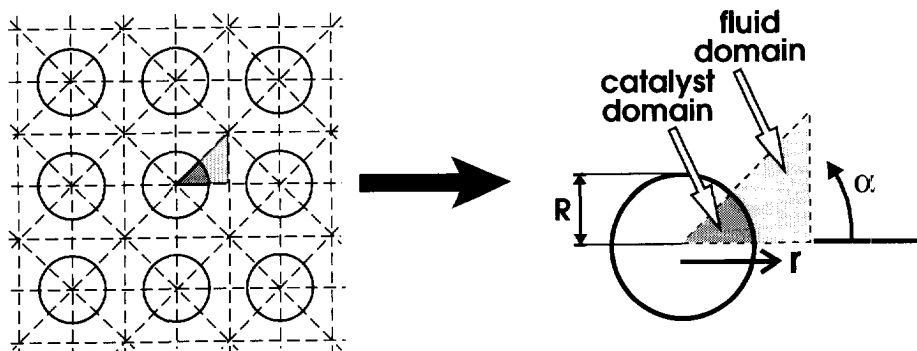


Figure 3-1 Unit cell of a central subchannel of a regular square array.

The aim of this discussion is to obtain relations to predict the value of the mass transfer coefficient k_g , that is defined by:

$$\Phi_{mol,A}'' \equiv k_g (c_{A,b} - c_{A,s}) \quad (3-1)$$

In this equation the bulk concentration $c_{A,b}$ is defined as the cup mixing average of the concentration in the fluid domain; the surface concentration $c_{A,s}$ is defined as $c_A|_{r=R}$. According to Fick's law, the flux to the catalyst surface is given by:

$$\Phi_{mol,A}'' = -D_{free} \left. \frac{\partial c_A}{\partial r} \right|_{r=R, \text{fluid domain}} \quad (3-2)$$

Combining Eqs. (3-1) and (3-2), it is seen that k_g can be obtained from:

$$k_g = \frac{-D_{free} \left. \frac{\partial c_A}{\partial r} \right|_{r=R, \text{fluid domain}}}{c_{A,b} - c_{A,s}} \quad (3-3)$$

The procedure that leads to relations for k_g as a function of the reactor geometry and process conditions, is to obtain values for the right hand side of Eq. (3-3) by analytically or numerically solving the partial differential equations (PDE's) that govern mass transfer in this system, for various reactor geometries and process conditions. This will be shown below.

First, however, a complication of the situation should be discussed. In circular ducts (*i.e.* normal pipes) there is axial symmetry, which implies that $(\partial c_A / \partial r)|_{r=R}$ and $c_{A,s}$ in Eq. (3-3) are constant along the perimeter of the wall, *i.e.* circumferentially. In a rod bundle, however, symmetry with respect to the axis of each rod is only approximated at high relative pitches (> 2.8 for a regular square array); *cf.* the discussion of the annular ringzone approximation in Chapter 2, Section 2.2. At lower relative pitches, $(\partial c_A / \partial r)|_{r=R}$ and/or $c_{A,s}$ will vary circumferentially. Consequently, k_g and Sh ($\equiv k_g d_h / D_{free}$) will then be local variables that depend on the angular coordinate α :

$$k_{g,\alpha} \equiv \frac{-D_{free} \left. \frac{\partial c_A}{\partial r} \right|_{r=R, \alpha=\alpha, \text{fluid domain}}}{c_{A,b} - c_{A,s}|_{\alpha=\alpha}} \quad (3-4)$$

In the case of circumferential variations of k_g , a suitable mass transfer coefficient that is of engineering use is the circumferential average (indicated by the prefix $^\circ$) of $k_{g,\alpha}$:

$$^\circ k_g \equiv \frac{-D_{free} \left(\frac{\partial c_A}{\partial r} \right)_{r=R, \text{fluid domain}}}{c_{A,b} - ^\circ c_{A,s}} \quad (3-5)$$

The importance of the circumferential variations in case of laminar flow will be discussed in Section 2.3.1.

The governing equation for mass transfer that should be solved to find values of k_g , follows from the component balance over a small element of the fluid domain. For steady state, fully developed, incompressible flow in the z -direction, the component balance results in:

$$\nabla \cdot (D \nabla c_A) = u_z \frac{\partial c_A}{\partial z} \quad (3-6)$$

For turbulent flow the diffusivity D is a function of the velocity gradients, hence of the lateral position; for laminar flow it is the constant free molecular diffusivity D_{free} . The axial gas velocity u_z follows from the momentum balance over a small element of the fluid domain, as discussed in Chapter 2, Section 2.1.

At the symmetry lines that bound the fluid domain (see Fig. 3-1), the boundary conditions of Eq. (3-6) are simple: the derivative of c_A with respect to the normal vector should equal zero. The boundary condition at the external catalyst surface is the relation that couples the fluid domain with the catalyst domain:

$$D_e \frac{\partial c_A}{\partial r} \Big|_{r=R, \text{catalyst domain}} = D_{free} \frac{\partial c_A}{\partial r} \Big|_{r=R, \text{fluid domain}} \quad (3-7)$$

Consequently, also an equation describing the concentration in the catalyst domain is needed. This equation follows from a component balance over a small element of the catalyst domain; for steady state it yields:

$$\nabla^2 c_A = \frac{1}{D_e} \mathfrak{R}_A \quad (3-8)$$

The boundary condition of Eq. (3-8) at the external catalyst surface is given by Eq. (3-7); the boundary condition at the symmetry lines is that the derivative of c_A with respect to the normal vector should equal zero. Note that for the sake of simplicity, the wire on which the beads are strung in a BSR, has been neglected. Unfortunately the boundary condition that couples the fluid domain with the catalyst domain (Eq. (3-7)) differs from the standard boundary conditions assumed in most heat transfer literature (including the literature on heat transfer in rod bundles). In

standard heat transfer problems the boundary condition at the solid wall is usually idealized to one of the following conditions:

- <T> constant axial and circumferential wall temperature; this is the boundary condition of the classical Graetz-Nusselt problem (Bird *et al.*, 1960, p. 361);
- <H1> constant axial wall heat flux with constant circumferential wall temperature;
- <H2> constant axial wall heat flux with constant circumferential heat flux.

Because of the difference in boundary conditions, the applicability of the solutions (*i.e.* Nusselt relations) for the standard heat transfer problems to the BSR, remains to be investigated. In certain cases, the boundary condition of a system with a catalytic wall (like the BSR) approximates one of the standard heat transfer boundary conditions. This was shown by Tronconi and Forzatti (1992) for monolithic reactors, and before them by Brauer and Schlüter (1965) and Bräuer and Fetting (1966) for tubular catalytic wall reactors.

The first case is when the reaction rate is very fast compared to the mass transfer rate in the fluid domain. Then the surface concentration will be practically zero everywhere, which results in the boundary condition of constant axial and circumferential surface concentration. This is analogous to the <T> boundary condition, and therefore the Sherwood number for laminar flow in a monolithic reactor with circular channels then equals the solution of the classical Graetz-Nusselt <T> problem, $Nu = 3.66$.

The second case is when the reaction rate is very slow; it was shown by Bräuer and Fetting (1966) that this results in a situation with constant axial and circumferential flux (boundary condition <H2>). Consequently, the Sherwood number for laminar flow in a monolithic reactor then equals the Nusselt number of the <H2> problem (4.36 for circular channels).

In properly designed reactors with structured catalyst packings, however, the reaction rate is often limited by both the reaction rate and the film layer mass transfer. A helpful dimensionless number to analyze that situation is the second Damköhler number, which arises when the catalyst domain is lumped and described with a reaction rate at surface conditions and an effectiveness factor. A mole balance over an axial slice of the reactor then shows that for a (pseudo) first order reaction, the boundary condition of the fluid domain (Eq. (3-7)) can be rewritten as:

$$\left(\frac{\partial c_A}{\partial r} \right)_{r=R, \text{ fluid domain}} = \frac{k_r V \eta_p R}{2D_{free}} (c_{A,s}) \quad (3-9)$$

When this equation is made dimensionless, defining $c_A^+ \equiv c_A/c_{A,in}$ and $r^+ \equiv r/d_h$, it is seen that the boundary condition is a function of a dimensionless group that will be called the second Damköhler number:

$$\left(\frac{\partial c_A^+}{\partial r^+} \right)_{r=R, \text{ fluid domain}} = \frac{(k_r, v \eta_p \frac{R}{2}) d_h}{D_{free}} (c_{A,s}^+) \equiv Da_{II} (c_{A,s}^+) \quad (3-10)$$

From this analysis it is expected that in systems with catalytic walls the Sherwood number changes from $Nu(\langle H \rangle)$ to $Nu(\langle T \rangle)$ when the reaction rate changes from relatively slow to relatively fast, *i.e.* when Da_{II} changes from 0 to infinity. Values for Sh as a function of Da_{II} for laminar flow in monolithic reactors with circular, square and triangular channels were calculated by Tronconi and Forzatti (1992). For the present study the same was done for laminar flow in a BSR with a regular square array (Takács, 1994). The results will be presented in Section 2.3.

2.3 Theoretical relations for laminar flow

2.3.1 Angular dependence of Sh

Because in a rod bundle axial symmetry with respect to each rod is only approximated at high relative pitches, circumferential variations of the concentration and/or mass flux can arise along the perimeter of the rods, because of the non-symmetrical velocity field around the rod. The momentum transfer equivalent of this phenomenon was already discussed by Sparrow and Loeffler (1959); in momentum transfer, the obvious boundary condition of the governing PDE is constant axial and circumferential velocity (namely 0 everywhere!). They showed that in a regular square array, the wall shear stress has its minimum at an angle α (see Fig. 3-1) of 0, and its maximum at an angle of 45° , as is easy to understand. The circumferential variations increase with a decreasing relative pitch: for a relative pitch of 1.1 the local wall shear stress at $\alpha = 0$ is *ca.* 58% lower than the circumferential average, whereas at a relative pitch of 1.5 the value at $\alpha = 0$ is only *ca.* 12% lower than the circumferential average.

Whereas the circumferential variations of the local wall shear stress (*i.e.* the momentum flux) in itself are not of interest in the study of the BSR, the analogous variations in mass flux or surface concentration are indeed. Kim (1979) presented a graph of the local heat flux relative to the circumferential average, for the $\langle \Gamma \rangle$ boundary condition, as a function of α and s/d_p . These data are based on a semi-analytical solution of the governing PDE, following the procedure described by Sparrow and Loeffler (1959) (see Chapter 2, Section 2.2). At a relative pitch of 1.2 the local flux at $\alpha = 0$ is *ca.* 64% lower than the circumferential average; at a relative pitch of 1.5 the flux at $\alpha = 0$ is still *ca.* 20% lower than the circumferential average.

Note that in case of a constant surface temperature, the local heat fluxes are directly proportional to the local Nusselt (or Sherwood) numbers.

For the boundary condition of constant mass flux, Takács (1994) showed that significant circumferential variations in the local surface concentration will arise at low relative pitches. As expected, the surface concentration at $\alpha = 0$ then is lower than the circumferential average.

For a BSR built up of cylindrical catalyst rods (*i.e.* 'infinitely' long catalyst cylinders), the boundary condition of Eq. (3-7) will result in circumferential variation of both the mass flux and the surface concentration. Because of the varying surface concentration, the concentration profile in the rod will not be axisymmetric, which will influence the effectiveness factor of the rod. Fortunately the influence can be expected to be limited. This is because the strongest (relative to the flux) circumferential variations of the surface concentration are obtained for the boundary condition of constant flux ($\langle H_2 \rangle$ condition), but this boundary condition corresponds to a low second Damköhler number (see Section 2.2); in turn, a low second Damköhler number corresponds to a slow reaction relative to the diffusion outside the particle, which will usually correspond to small intraparticle concentration gradients.

2.3.2 Influence of relative pitch on Sh

Following the procedure described in Section 2.2, circumferentially averaged Sherwood numbers were calculated for a regular square array, as a function of the relative pitch, for both the $\langle T \rangle$ and $\langle H_2 \rangle$ boundary condition (Takács, 1994). The results are displayed in Fig. 3-2. It is seen that for relative pitches larger than 1.1 (corresponding to a reactor voidage of 0.35 or higher), the effect of the boundary condition on the calculated Sherwood number is smaller than 30%.

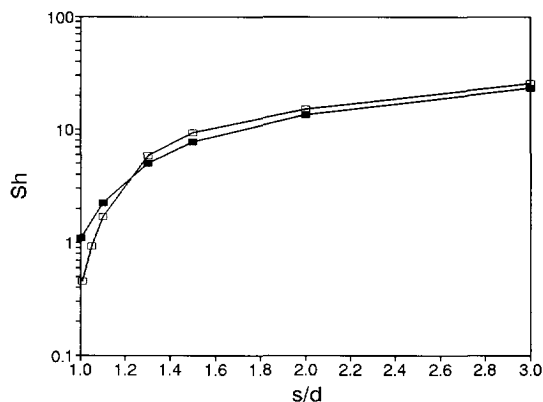


Figure 3-2 ■ $Sh(\langle T \rangle)$ and □ $Sh(\langle H_2 \rangle)$ as a function of the relative pitch.

Because the values of Sh calculated for those two boundary conditions form the limiting values for a BSR, the maximum error in Sh is limited to 30% (for $s/d_p > 1.1$) when either $Sh(\langle T \rangle)$ or $Sh(\langle H_2 \rangle)$ is used for the prediction of the mass transfer rate. In predicting the performance of a BSR, the Sherwood number is only of interest when the reaction rate is relatively fast, *i.e.* when Da_{II} is large. Since in that situation the boundary condition resembles the $\langle T \rangle$ condition, it is recommended

to use $Sh(\langle T \rangle)$ for simple engineering calculations. For very precise predictions of the mass transfer rate, however, or when the relative pitch is chosen smaller than 1.1, it will be necessary to find Sh by solving the governing equations discussed in Section 2.2.

2.3.3 Influence of Da_{II} on Sh

In Fig. 3-2 the line for $Sh(\langle H2 \rangle)$ corresponds to $Da_{II} = 0$, whereas the line for $Sh(\langle T \rangle)$ corresponds to $Da_{II} = \infty$. A plot of Sh (circumferentially averaged) as a function of Da_{II} , for a specified relative pitch, can therefore be seen as the 'connection' between the two curves of Fig. 3-2. Such a plot is given in Fig. 3-3 (Takács, 1994), for a relative pitch of 2.0. In this figure also the corresponding values of the Sherwood numbers for monolithic channels are plotted; those values were taken from Tronconi and Forzatti (1992).

From these plots it is seen that the second Damköhler number indeed is a useful number to assess which of the boundary conditions is approximated. For all four channel geometries referred to in Fig. 3-3, Sh approximates $Sh(\langle H2 \rangle)$ for $Da_{II} \leq 0.1$, and $Sh(\langle T \rangle)$ for $Da_{II} \geq 10$.

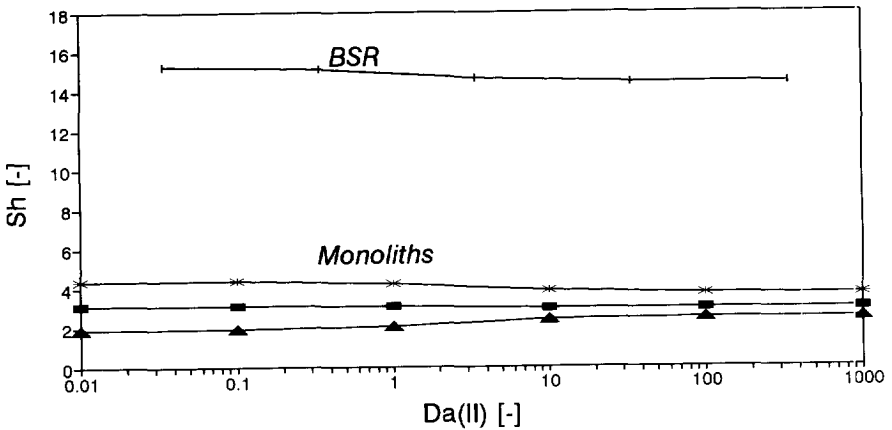


Figure 3-3 Sh as a function of the second Damköhler number. Symbols pertaining to the monolith channels: * = circular cross-section; ■ = square cross-section; ▲ = triangular cross-section.

2.3.4 Change of Sh in a developing concentration boundary layer

Because the Sherwood number is considerably higher when the concentration profile in a channel is still developing than when it has fully developed, it might be important to estimate the length of the mass transfer entrance zone, indicated as ℓ_c . ℓ_c is often defined as the distance from the point where the mass transfer started (e.g. the reactor

entrance), to the point where the local Sherwood number deviates less than 5% from Sh_∞ , *i.e.* the Sherwood number for a fully developed concentration profile.

The change of Sh in a mass transfer entrance zone depends on the flow profile: for a hydrodynamically developing flow the situation is different from that for a hydrodynamically fully developed flow.

At the entrance of a BSR, both the velocity profile and the concentration profile start to develop. The ratio of the hydrodynamic boundary layer thickness to the concentration boundary layer thickness approximately equals $Sc^{1/3}$ (for $Sc \geq 1$). As the Schmidt number of small molecules in gases is typically in the order of magnitude of 1, the two boundary layers have approximately the same thickness, which implies that they develop simultaneously.

Rehme (1987, p. 7-12) presents a graph showing the dependence of the local Nusselt number on the distance from the reactor entrance, for simultaneous development of flow and heat transfer in central subchannels of a regular square array. Setting Sh equal to Nu , $\ell_c/(d_r Re Sc)$ appears to increase with a decreasing relative pitch, from *ca.* 0.01 at $s/d = 2.0$, to *ca.* 0.2 at $s/d = 1.1$. For a Reynolds number of 500, a Schmidt number of 1 and a rod diameter of 5 mm, this implies that ℓ_c increases from *ca.* 10 cm at $s/d = 2.0$, to *ca.* 27 cm at $s/d = 1.1$. Comparing these lengths to a typical length of a BSR module (*ca.* 50 cm), it is seen that a significant part of the BSR lies in the mass transfer entrance zone (in case of laminar flow).

The effect of the developing boundary layer on the performance of a BSR can be assessed by comparing the length averaged Sherwood number in the reactor with the value of Sh_∞ . From the data presented by Rehme, the length averaged Sherwood number in the mass transfer entrance zone is easily calculated by graphical integration. For a relative pitch of 1.1, it is *ca.* 50% higher than Sh_∞ . On a reactor length of 50 cm, the entrance effect is thus seen to result in an average Sherwood number that is *ca.* 25% higher than Sh_∞ . For smaller relative pitches the influence of the entrance effect is even stronger. From this it can be concluded that for laminar flow in a BSR with a small relative pitch, in a case where the reactor performance strongly depends on the mass transfer rate, it is necessary to take the effect of enhanced mass transfer into account. However, the relative pitch in a BSR will typically be higher than 1.1, and the performance will typically not be dominated by mass transfer from the bulk flow to the catalyst particles. Therefore usually only small errors will be introduced in the prediction of the BSR performance if it is assumed that Sh equals Sh_∞ .

2.4 Relations for turbulent flow

2.4.1 Empirical relations

Unfortunately no empirical mass or heat transfer relations were found that consider the type of artificial surface roughness that is encountered in a BSR. The relations that are discussed in this section pertain to hydraulically smooth surfaces, and are therefore expected to predict the lower limit of Sherwood numbers in a BSR.

Because of the relatively flat velocity profile in turbulent flow, the channel geometry has only a small influence on the friction factor (as discussed in the previous chapter) and the Sherwood and Nusselt numbers. The turbulent Sherwood and Nusselt numbers of rod bundles can therefore be related to those of circular tubes. The few experimental data, as compiled by Rehme (1987), suggest that for relative pitches between 1.1 and 2.0 (which is expected to be the interesting range for the BSR), the deviation of the rod bundle Nusselt number from the circular tube Nusselt number is less than 20%. Often this accuracy will be sufficient. In compiling the experimental data, Rehme (1987) used the following correlation for the circular tube Nusselt number:

$$Nu_t = 0.02087 Re^{0.7878} \quad \text{for } Pr = 0.7 \quad (3-11)$$

For other Prandtl numbers Nu_t can be calculated from (3-11) using the theoretical proportionality of Nu with $Pr^{1/3}$.

A more accurate approximation is obtained by using a correlation obtained from the equivalent ringzone theory. As discussed in Chapter 2, axial symmetry is approximated for each rod in a bundle when the relative pitch becomes 'large'. Then the angular coordinate drops out of the governing equations, and they can be relatively easily solved. The equivalent ringzone solution derived by Petukhov and Roizen (1974), as compiled by Rehme (1987), predicts Nu/Nu_t ratios increasing from 1.03 for a relative pitch of 1.0, to 1.26 for a relative pitch of 2.0. The values just mentioned pertain to a Pr value of 0.7, but the influence of Pr is very weak. A fitted correlation of Petukhov and Roizen's equivalent ringzone solution ($Pr = 0.7$) was presented by Rehme (1987):

$$\frac{Nu}{Nu_t} = 0.855 \left(\sqrt{\frac{4}{\pi}} \frac{s}{d} \right)^{0.1688} \left(\sqrt{\frac{4}{\pi}} \frac{s}{d} + 1 \right)^{0.2122} \quad (3-12)$$

Although the assumption of axial symmetry is obviously wrong for relative pitches close to 1.0, the equivalent ringzone solution crosses the thin cloud of experimental data in the middle, even at the lowest relative pitches. Combination of Eqs. (3-11) and (3-12) therefore seems sufficiently accurate for engineering purposes.

An interesting point is the dependence of the turbulent Nu numbers on the boundary condition. For laminar flow it was shown that the dependence of Nu on the boundary condition rapidly fades away when the relative pitch is increased: the difference in Nu between the $\langle T \rangle$ and the $\langle H_2 \rangle$ boundary conditions is less than 30% for relative pitches larger than 1.1. Because of the flatter velocity profile in turbulent flow, it is expected that the dependence on the boundary conditions is quite small in turbulent flow, except for very small relative pitches. It is expected that an estimate of the maximum influence of the boundary condition on the turbulent Nu number can be obtained from the respective values for laminar flow.

2.4.2 Chilton-Colburn analogy

Because pressure drop measurements are much faster and cheaper than mass or heat transfer measurements, it is tempting to try to relate the Sherwood and Nusselt numbers to the friction factor. A relation that has proved successful for smooth circular tubes, is obtained from a plausible assumption, that is known as the film layer model. The assumption is that for turbulent flow the lateral velocity, temperature and concentration gradients can be assumed to be located in thin films at the wall of the channel; the thickness of those films are indicated with δ_h , δ_T and δ_c , respectively. According to the film model, the lateral velocity gradient at the channel surface equals $\langle u \rangle / \delta_h$, the lateral temperature gradient equals $(T_b - T_s) / \delta_T$ and the lateral concentration gradient equals $(c_{A,b} - c_{A,s}) / \delta_c$. From these assumptions, and the theoretical knowledge that $\delta_h / \delta_T \approx Pr^{1/3}$ and $\delta_h / \delta_c \approx Sc^{1/3}$ (for Pr and $Sc \geq 1$), the following relation is easily derived:

$$Nu \approx \frac{f}{2} Re Pr^{1/3} ; \quad Sh \approx \frac{f}{2} Re Sc^{1/3} \quad (3-13)$$

This relation is usually called after Chilton and Colburn. For smooth circular channels, the Nusselt numbers predicted with Eq. (3-13) agree with experimental data within 25% for $Re > 5 \cdot 10^3$, which supports the film layer model assumptions. Unfortunately Eq. (3-13) overestimates Nu and Sh for channels that are not hydraulically smooth; the error increases rapidly with increasing roughness. This can be attributed to the fact that the hydrodynamic boundary layer thickness is stronger affected by wall roughness than the thermal or concentration boundary layer thickness (cf. Bird *et al.*, 1960, p. 401 and p. 647).

From this the following procedure arises to predict the limits of Sherwood and Nusselt numbers in the BSR from simple pressure drop measurements:

1. Measure the pressure drop characteristics, and compare the experimentally determined friction factors with the predictions for smooth bundles, according to the relations discussed in Chapter 2. This gives an impression of the roughness of the strings.
2. For the Reynolds number of interest, calculate Sh or Nu with Eq. (3-13), using (A) the experimentally determined friction factor and (B) the predicted friction factor for smooth bundles. The true value of Sh or Nu is then expected to lie between the

predicted (A) and (B) values; the higher the roughness is (*i.e.* the deviation between the experimentally determined friction factor and the predicted friction factor for smooth rods), the closer (relatively) to (B) the true value of Sh and Nu is expected to be.

The usefulness of this procedure will be tested in Section 4.

2.4.3 Change of Sh in a developing concentration boundary layer

In the axial region of a channel where the thermal or concentration boundary layer has not yet fully developed, the thickness of those boundary layers is smaller than of the fully developed boundary layers downstream. Consequently, in the heat or mass transfer entrance regions the local Nusselt and Sherwood numbers are higher than in the regions downstream.

For turbulent flow the length of the thermal or concentration entrance region, (ℓ_T or ℓ_c), is usually found to be *ca.* 10 times the hydraulic diameter of the channel (*e.g.* Presser, 1971)). In a typical BSR this comes down to an entrance length of a few centimeters, which is short enough to neglect.

However, to allow interpretation of the experimental data presented in the next section, a description is needed of the local or average value of Nu or Sh in the entrance zone. The average value of Nu over a distance L from the point where the heat transfer surface begins, is indicated as $\langle Nu \rangle_L$. Various relations have been proposed that link $\langle Nu \rangle_L$ to Nu_∞ . For circular tubes Perry and Green (1985) recommend:

$$\frac{\langle Nu \rangle_L}{Nu_\infty} = 1 + 1.4 \left(\frac{d_h}{L} \right) \quad \text{for } 10 < \frac{L}{d_h} < 400 \quad (3-14)$$

Smith *et al.* (1984) mention:

$$\frac{\langle Nu \rangle_L}{Nu_\infty} = 1 + \left(\frac{d_h}{L} \right)^{0.7} \quad (3-15)$$

From mass transfer experiments with a smooth rod bundle, Presser (1971) found that for $Re > 10^5$ the local Sherwood number Sh_x in the entrance zone is adequately described with:

$$\frac{Sh_x}{Sh_\infty} = 1 + \frac{0.7}{x/d_h} \quad (3-16)$$

For smaller Reynolds numbers the ratio was found to be bigger.

3 Experimental mass transfer study

3.1 Introduction

As was discussed in Section 2, the relations for heat transfer in rod bundles that are proposed in the literature cannot account for the special type of artificial wall roughness that is encountered in the BSR (see Fig. 2-12). Obviously the relations for smooth rods will underestimate the heat and mass transfer rates in a BSR in case of turbulent flow. To assess the extent of this underestimation, and to check the applicability of the Chilton-Colburn analogy to take the roughness into account, an experimental study was conducted, which will be described in this section.

Two experimental mass transfer measurement techniques were tried in this study. The first method is based on continuous evaporation of liquid from a wetted particle (first described by Thoenes, 1957). Unfortunately this very elegant technique proved to be very cumbersome when applied to catalyst particles of a few millimeters. Though after much practicing, experimental Sherwood numbers for single spherical particles were obtained that were in agreement with the theoretical Sherwood numbers, this technique was deemed too complicated for the present study.

The second method is the well-known sublimation method, in which particles made of or impregnated with *e.g.* naphthalene, are weighed and subjected to a gas flow, after which they are weighed again. Although it is a discontinuous technique, this drawback is more than compensated for by the fact that it is very simple. The experiments described in this section were done with this technique. The accuracy that could be achieved was checked by finding the Sherwood number of single spheres suspended in an air flow. The experimentally determined Sherwood numbers deviated an average 2.3% from the theoretical values; this deviation was considered sufficiently small.

3.2 Experimental set-up and procedures

The experimental set-up that was used for this study was very similar to the one described in the previous chapter. A perspex or steel reactor shell was used, with a square cross-section of 70 or 35 mm and a height of 500 mm. Diffusors with a top angle of 8° were used to connect the reactor module with the supply and exhaust pipes, to prevent swirls in the first and last part of the reactor; see Fig. 2-15. The gas flow (compressed air) was controlled by electronic mass flow controllers, with a total

capacity of $1700 \ell_n/\text{min}$. The temperature of the reactor and the gas flow was kept constant at 30°C during each run.

In the reactor, strings of so-called 'steatite' beads were arranged in a regular square array. Steatite beads, also called 'fish bone beads' (see Fig. 3-4), are made of soapstone. A string of steatite beads has a type of artificial roughness that seems quite well comparable to that of strings of catalyst beads. As was already mentioned in Chapter 2, steatite beads were used instead of real catalyst

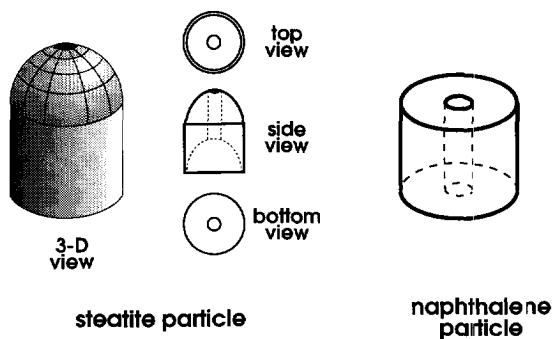


Figure 3-4 Steatite beads and naphthalene particles used in this study.

particles because they are cheaper, more uniform, available in more sizes, and much easier to string than the available catalyst extrudates.

The steatite beads were arranged 'nose up' on rigid rods (see Fig. 2-15). For each run, in several strings in the reactor one or more steatite beads was substituted by ring-shaped particles of the same size, made of naphthalene; see Fig. 3-5. Strings containing one or more naphthalene particles will be called 'active strings', strings containing only steatite beads will be called 'inert strings'.

Because steatite beads have a convex nose and a convex bottom, whereas the naphthalene particles had flat tops and bottoms, the nose was removed of each steatite bead supporting a naphthalene particle. Consequently, the top and bottom sides of the naphthalene particles were not exposed to the gas flow.

One run consisted of seven steps:

1. measuring the length, diameter and mass of each naphthalene particle;
2. stringing several naphthalene particles on several rods, yielding 'active strings';
3. arranging the active strings in the reactor, that already contained most inert strings;
4. mounting the reactor in the test section;
5. letting the gas flow for a specified time Δt ;
6. disassembling the reactor and removing the naphthalene particles from the active strings;
7. measuring the mass, length and diameter of each naphthalene particle.

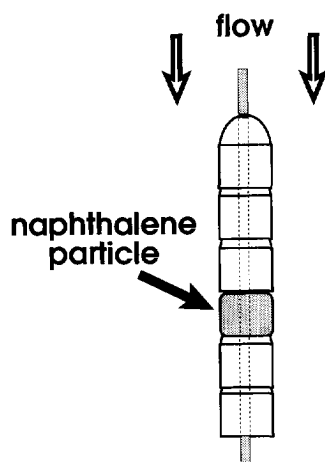


Figure 3-5 String of steatite beads containing one naphthalene particle.

From calculations and a few simple experiments it was concluded that the amount of naphthalene sublimating during steps 1-4 and 5-7 was less than 0.1% of the amount sublimating during step 5.

The average mass transfer coefficient measured for a particle was calculated with:

$$k_g = \phi_{mol,N} \frac{1}{A_p} \frac{1}{(c_{N,s} - c_{N,b})} = \frac{(\Delta m)/(\Delta t)}{M_{w,N}} \frac{1}{\pi \langle d_p \rangle \langle L_p \rangle} \left(\frac{R_g T_b}{P_N^{sat}} \right) \quad (3-17)$$

The average symbols ($\langle \dots \rangle$) indicate that the average value during the run was used ($\equiv \frac{1}{2}$ value before run + $\frac{1}{2}$ value after run). This was necessary because during a run the diameter of the naphthalene particles decreased typically by *ca.* 10% and the length by *ca.* 2%.

From Eq. (3-17) it is seen that only the area of the cylindrical surface of the naphthalene particle is counted in the calculation of k_g , and not the top and bottom surface area. However, although the top and bottom surface of each naphthalene particle were shielded from the gas flow by the steatite beads on top and under it, it must be concluded from the length decrease that they do contribute to the overall mass decrease of the particle during a run. Because the subject of interest in this study was the mass transfer at the cylindrical surface of the particles, the mass decrease due to transfer at the top and bottom surface was estimated from the length decrease, and was subtracted from the total mass decrease of the particle.

Finally it must be noted that in Eq. (3-17) it is assumed that the bulk concentration of naphthalene is zero and that the sublimation is practically isothermal. It can be easily shown that under the conditions of this study, these assumptions are justified.

3.3 Experiments conducted

Experiments were done with two particle diameters (4.6 mm and 6.5 mm) and three relative pitches (1.1, 1.4 and 1.8, corresponding to infinite bundle voidages of 35%, 60% and 76%, respectively). Five types of experiments were done:

(1) *Pressure drop experiments.*

For each reactor configuration, the pressure drop was measured as a function of the gas flow. As discussed in the previous chapter, the dependence of the friction factor on the Reynolds number gives an indication of the flow regime. The experimental friction factors were also used to predict the Sherwood numbers, using the Chilton-Colburn analogy.

(2) *Experiments with naphthalene particles positioned at varying axial positions.*

By comparing the experimental Sherwood numbers of particles on different axial positions, it can be checked whether the flow is still hydrodynamically developing between those positions. This is important to know, because the theory predicts higher Sherwood numbers for hydrodynamically developing flow than for developed flow. Although it was already concluded, based on the

study of momentum transfer (see Chapter 2), that under the conditions of the present study the hydrodynamic inlet effects are negligible, mass transfer experiments are a good means to check this conclusion.

Obviously the most accurate assessment of the effect of the axial position is obtained when the particles that are compared, are fixed on the same string. Therefore six active strings were used in this experiment, each active string containing one naphthalene particle at one-third of the reactor length and another particle at two-thirds.

Because the hydrodynamic entrance length is proportional to the hydraulic diameter of the reactor packing (see Chapter 2), the effect of the axial position is expected to be maximal at the highest particle diameter and relative pitch. Therefore this experiment was done with particles of 6.5 mm and a relative pitch of 1.8.

(3) *Experiments with several naphthalene particles in a row.*

A very important aspect of the mass transfer experiments is the fact that in experiments with only one naphthalene particle per active string, the mass transfer boundary layer only starts to develop over the length of that particle. From the relations presented in Section 2 it can be estimated that for smooth rods, in the range of conditions used in this study, the mass transfer entrance length ℓ_c is between 40 and 200 mm. Obviously the naphthalene particles, which have a length of *ca.* 4.2 or *ca.* 6.2 mm, will then lie completely within the mass transfer entrance length. Consequently the experimentally determined Sherwood numbers are expected to be not only considerably higher than the corresponding Sh_∞ , but to be also dependent on the length of the particle.

This problem can be approached in two ways. The first way is to make sure that the mass transfer boundary layer completely develops upstream of the naphthalene particle that is studied. To obtain such a situation, so-called 'leading' naphthalene particles should be positioned upstream of the studied particle, over a length that is at least as long as the mass transfer entrance length. Such an approach was followed by Presser (1971) for mass transfer from smooth rods. Drawbacks of this approach are that (1) relatively long reactors are needed, (2) one has to take into account that due to the sublimation upstream of the studied particle, the naphthalene concentration in the bulk gas passing that particle can usually no longer be assumed to be zero (note that the estimation of the bulk concentration depends heavily on the assumptions regarding radial mixing) and (3) in case of strings of particles, it implies much extra work.

The second approach, which was followed in the present study, is to do the measurements on purpose within the mass transfer entrance zone, with one naphthalene particle per active string, and to estimate Sh_∞ from the experimentally determined Sherwood number, using relations such as presented in Section 2.4.3. To verify those relations, however, it is necessary to do some experiments with several particles in a row (*i.e.*, one directly on top the other),

and study the decrease of the Sherwood numbers of the subsequent particles, going downstream. In these experiments the naphthalene particles were separated by small rings (height 0.30 mm, diameter 5.1 mm), to create a roughness comparable to that of the string of steatite particles or a string of catalyst particles.

- (4) *Experiments with naphthalene particles positioned at varying lateral positions.* In Chapter 2 it was discussed that in a rod bundle like the BSR, the gas velocity through wall and corner subchannels can strongly deviate from the velocity through the central subchannels, whereas the difference between two central subchannels is usually negligible. This leads to the expectation that the Sherwood numbers of strings directly facing the reactor wall, may deviate significantly from the Sherwood numbers of all inner strings. To verify this, in all runs discussed in the next paragraph, active strings were arranged at five to ten 'unique' positions (see Fig. 3-6), all naphthalene particles inserted at the same axial position (approximately halfway of the reactor length).

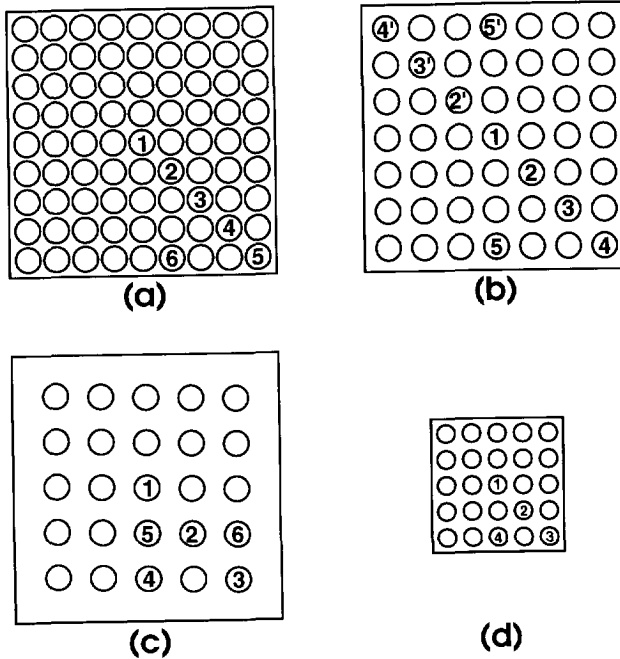


Figure 3-6 Mapping of the various lateral positions in a finite rod bundle. (a) to (c) reactor diameter 70 mm; (d) reactor diameter 35 mm. (a) $s/d = 1.1$, $d = 6.5$ mm; (b) $s/d = 1.4$, $d = 6.5$ mm; (c) $s/d = 1.8$, $d = 6.5$ mm; (d) $s/d = 1.4$, $d = 4.6$ mm.

(5) *Experiments at varying Reynolds numbers.*

According to the relations presented in Sections 2.3 and 2.4, the power of the Sherwood number in Re is expected to increase from zero for laminar flow to a constant of *ca.* 0.8 for turbulent flow, at least for smooth rods; in the fully rough regime, the power is expected to be 1.0. The dependence of Sh on Re thus is an indication of the flow regime. An interesting question is whether the power of Sh in Re can be related to the power of the friction factor in Re ; this relation is the basis of the Chilton-Colburn analogy, and if it is valid for the BSR, Sherwood numbers could be predicted from simple pressure drop experiments.

4 Results and discussion

4.1 Introduction

In this section the results of the experimental study on mass transfer for turbulent flow in hydraulically rough rod bundles are presented and compared with theoretical and empirical relations. In presenting the experimental Sherwood numbers, various definitions of Sh are possible, depending on the choice of the characteristic size. One might argue, for example, that for a particle enclosed by four central subchannels, the Sherwood number should be based on the hydraulic diameter of the central subchannel. However, this is not very practical for particles in strings that face the reactor shell: for example, a particle inserted in a string in the corner of the reactor is for one quarter in a corner subchannel, for twice one quarter in two wall subchannels, and for the remaining quarter in a central subchannel.

Therefore the Sherwood numbers reported in this section are based on one common characteristic size, namely the hydraulic diameter of the complete rod bundle (*i.e.* including the perimeter of the reactor shell). Besides simplicity this definition has the advantage that the experimental Sherwood numbers can then be easily compared with the predictions based on the theoretical and experimental friction factors, which are (almost by definition) based on the hydraulic diameter of the complete rod bundle (including the perimeter of the reactor shell). Furthermore an advantage of the same characteristic length in the definition of Sh for all subchannels is that it allows direct comparison of the mass transfer coefficients in the various subchannels, by simply comparing the Sherwood numbers, rather than having to consider the ratio of the hydraulic diameters of the subchannels.

Obviously the choice of the characteristic size in the definition of Sh influences the numeric values of the calculated Sherwood numbers. To enable conversion of the Sherwood numbers reported in this section into Sherwood numbers based on another definition of the characteristic size, the hydraulic diameters are given of all subchannels in the reactor configurations used in the mass transfer study; see Table 3-1. The final remark of this introduction is that the Sherwood numbers presented in this section correspond to the boundary condition of constant surface concentration (or temperature, in terms of heat transfer). This is obvious from the nature of the experimental technique. Because of this boundary condition, comparison with pressure drop data is allowed; indeed, momentum transfer also has a constant value boundary condition, since at the wall the velocity is axially and circumferentially constant (0).

Table 3-1 Hydraulic diameters of the subchannels

d_p [mm]	s/d [-]	d_h [mm]			
		bundle	central subchannel	wall subchannel	corner subchannel
6.5	1.1	4.6	3.7	6.4	6.8
6.5	1.4	10.2	9.3	11.6	10.7
6.5	1.8	20.6	20.3	21.8	17.8
4.6	1.4	6.5	6.6	6.5	5.7

4.2 Pressure drop experiments

The experimental friction factors of two reactor configurations are plotted in Figs. 3-7a and b. In these graphs also the theoretical relations for laminar and turbulent flow in smooth rod bundles are plotted, as well as the relation for turbulent flow with a fitted value of the roughness function; see Chapter 2. It is seen that in these configurations the flow is fully turbulent at Reynolds numbers higher than 1000, and that the roughness of the strings has a significant influence on the momentum transfer. From this it can be concluded that the laminar sub-layer is disturbed by the roughness, which is expected to result in enhanced mass transfer compared to smooth rods.

Unfortunately no reliable pressure drop data were at hand for the other two reactor configurations with which mass transfer experiments had been done.

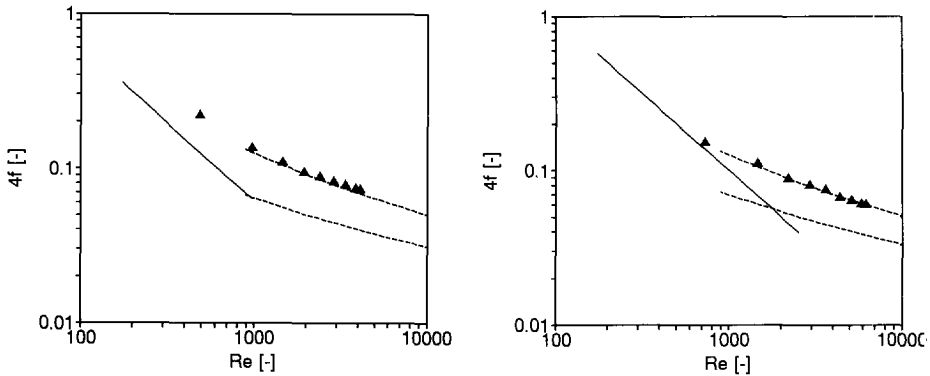


Figure 3-7 Experimental friction factors as a function Re . (a) $s/d = 1.1$; (b) $s/d = 1.4$. In both cases d equals 6.5 mm.
 ▲ = experimental data; solid line = prediction for laminar flow; lower dashed line = prediction for turbulent flow in smooth rod bundle (Eq. 2.13); upper dashed line = 'prediction' for turbulent flow with fitted roughness parameter (Eq. 2.16).

4.3 Effect of the 'chink' between particles on the local mass transfer coefficient

It was noticed that upon prolonged exposure to the gas flow, the top edge of the naphthalene particles inserted in a string changed from sharp to rounded; see Fig. 3-8. This indicates a significantly higher mass transfer coefficient at the leading edge of the particles. A likely explanation for this phenomenon is development of the mass transfer boundary layer, as a result of which the mass transfer coefficient decreases in the direction of flow.

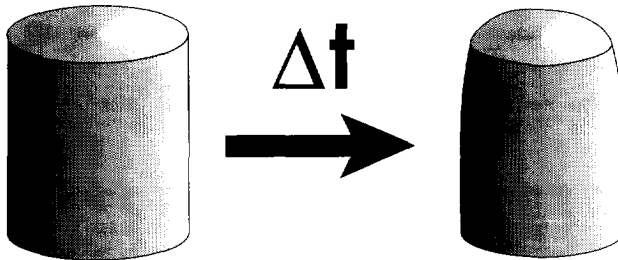


Figure 3-8 Change of shape of the naphthalene particles during long run times.

This explanation is supported by the change of shape of the first naphthalene particle when several naphthalene particles were arranged in a row; see Fig. 3-9. The naphthalene particles following the first one showed a similar change of shape, but it was much less pronounced—in fact it was almost insignificant. The fact that there is a change of shape of the following naphthalene particles, corresponds with the conclusion of the previous section, that the surface roughness created by the 'gaps' or 'chinks' between the particles (see Fig. 2-12) may result in a (limited) disturbance of the boundary layer going from one particle to the next. The fact that the change of shape of the following naphthalene particles is much smaller than of the first particle, indicates that the concentration boundary layer is not fully destroyed by the chinks; this will be confirmed in Section 4.5.

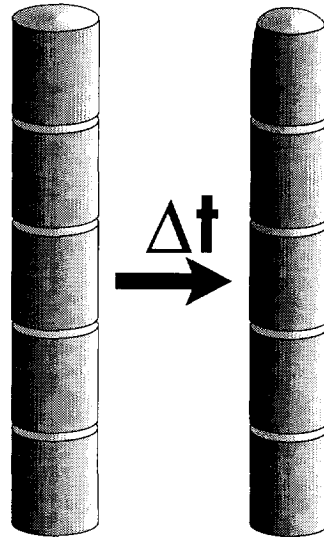


Figure 3-9 Row of naphthalene particles after long run times.

4.4 Dependence of Sh on the axial position in the reactor

No significant difference was observed between the Sherwood numbers of particles at one third of the reactor length and particles at two thirds. The difference between the two particles on each string was always less than 3%. The averages of the Sherwood numbers at one third of the reactor length differed less than 1% from the average at two thirds. This confirms the conclusion drawn in Chapter 2, based on pressure drop measurements, that under the studied conditions the flow in the BSR develops hydrodynamically within the first few centimeters of the reactor. Since in all other mass transfer experiments discussed in this chapter the naphthalene particles were inserted in the middle of the strings, the flow along the particles can be considered hydrodynamically fully developed.

4.5 Development of the mass transfer boundary layer

In Fig. 3-10 the Sherwood numbers of subsequent particles in a row on one string are plotted as a function of the axial position. Particle #1, the leading particle, was located approximately halfway of the reactor length (*i.e.* at *ca.* 25 cm from the entrance of the reactor). This experiment was done with particles of 6.5 mm \varnothing and 6.5 mm length, at a relative pitch of 1.4 and a Reynolds number of *ca.* 2000.

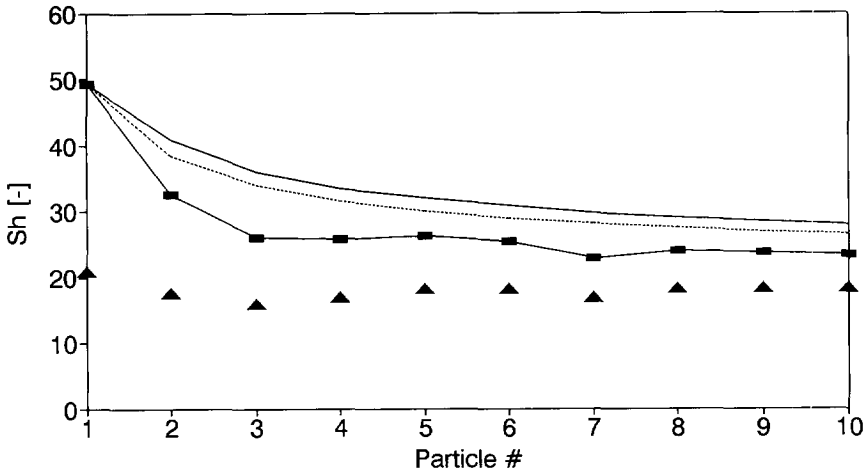


Figure 3-10 Sherwood numbers for ten particles in a row. ■ = experimental data; solid line = $\langle Sh \rangle_{L,i}$; ▲ = Sh_{∞} predicted from $\langle Sh \rangle_{L,i}$ (Eq. (3-15)); dashed line = $\langle Sh \rangle_{L,i}$ predicted from $Sh_{\infty} = 19$ (Eq. (3-15)).

It is seen that the Sherwood number decreases in the direction of flow, showing that a mass transfer boundary layer develops along the length of the string of naphthalene particles. Even at the tenth particle, the local Sherwood number seems to have not yet reached a constant value.

Also plotted is a line that shows for each particle #*i* the value of $\langle Sh \rangle_{L,i}$, *i.e.* the length averaged Sherwood number of the first *i* particles. From each value of $\langle Sh \rangle_{L,i}$, the Sherwood number for a fully developed mass transfer boundary layer (*i.e.* Sh_{∞}) was estimated, using Eq. (3-15). It is seen that no matter over which length (or number of particles) the average Sherwood number was measured, a value of Sh_{∞} of *ca.* 19 is estimated. The fact that the estimated value of Sh_{∞} does not significantly depend on *i*, justifies the use of Eq. (3-15) to predict the change of Sh in the mass transfer entrance zone.

This can also be shown in another way. Based on a value of Sh_{∞} of 19, the value of $\langle Sh \rangle_{L,i}$ as a function of *i* was predicted with Eq. (3-15). Fig. 3-10 shows that the

predicted change of $\langle Sh \rangle_{L,i}$ with i agrees quite well with the experimentally determined curve.

From experiments like the one discussed in this section, it was concluded that it is possible to study the mass transfer characteristics of a BSR in the following way:

1. Experimentally find the Sherwood number of a single particle on a string, without using any leading naphthalene particles to obtain a fully developed mass transfer boundary layer.
2. Use the experimentally determined value of Sh to estimate Sh_∞ using Eq. (3-15).

This procedure was followed in all experiments reported in Sections 4.6 and 4.7. The Sherwood numbers that are mentioned in those sections, are always the estimated Sh_∞ values. Out of convenience, however, the index ∞ has been dropped. Note that for turbulent flow (and for laminar flow with $s/d > 1.1$), only Sh_∞ is important the design of a BSR: the difference between the length averaged Sherwood number in a BSR module of 50 cm long, will typically be only a few percent higher than Sh_∞ .

4.6 Dependence of Sh on the lateral position

Based on the momentum transport phenomena discussed in Chapter 2, it can be predicted that there will be no significant difference between the Sherwood numbers of particles in different central subchannels of the same bundle; furthermore it can be predicted that there may be significant differences between Sherwood numbers of particles facing four central subchannels on one hand, and particles facing wall and/or corner subchannels on the other hand. Whether the mass transfer coefficient in a corner or wall subchannel is higher or lower than in the central subchannels, is expected to depend on the ratios of the gas velocities in the different subchannels. Based on the relations discussed in Chapter 2, those ratios were estimated for the four reactor geometries used in the present study; see Table 3-2. Based on these estimations one would expect that the most significant influence of the lateral position on the Sherwood number is seen for the corner position of the geometry with $d_p = 6.5$ mm and $s/d_p = 1.1$. The various positions are identified in Fig. 3-6.

Table 3-2 Expected gas velocities in the subchannels, relative to the average velocity.

d_p [mm]	s/d [-]	velocity in subchannel / average velocity in bundle; turbulent flow (laminar flow)		
		central subchannel	wall subchannel	corner subchannel
6.5	1.1	0.82 (0.99)	1.21 (1.41)	1.26 (1.55)
6.5	1.4	0.92 (0.94)	1.10 (1.24)	1.05 (1.25)
6.5	1.8	0.97 (0.82)	1.05 (1.13)	0.92 (1.10)
4.6	1.4	1.01 (1.00)	1.01 (1.00)	0.92 (0.93)

The simplest way to check for any influence of the lateral position is to plot the Sherwood numbers of the particles on different positions in one run, as a function of their position. This was done in Fig. 3-11; different symbols represent different runs. At none of the positions the Sherwood numbers seem significantly higher or lower than the average of a specific run. Even at the highest Reynolds number, where (as was known from pressure drop measurements) the flow is turbulent, no significant difference is seen, in spite of the fact that the gas velocity in the corner subchannels (position 3) is estimated to be *ca.* 13% lower than in the wall subchannels (positions 4 and 6).

Another way to check for a significant influence of the lateral position is presented in Fig. 3-12. In this experiment an estimate was obtained of the variance of the Sherwood number found for a certain lateral position, by arranging active strings in symmetrical pairs; based on symmetry considerations, the Sherwood number obtained for position 2 should be identical with the value obtained for position 2', except for random errors. From Fig. 3-12 it is seen that for this run, the differences between the average Sherwood numbers for the various positions cannot be distinguished from experimental noise. This is in spite of the fact that according to the estimated flow distribution, the gas velocity through the wall and corner subchannels is about 10 to 15% higher than through the central subchannels.

The last way to check for a significant influence of the lateral position is by replicating one run several times, and see whether the Sherwood numbers of one position are systematically higher or lower than the others. To compare the Sherwood numbers of several runs, however, one should account for small so-called 'block' differences between different runs (*cf.*, *e.g.*, Box *et al.*, 1978). This was done by dividing the individual Sherwood numbers of each run by the run average, yielding 'normalized' Sherwood numbers. The results for the geometry where the most significant influence was expected, are presented in Fig. 3-13. It is seen that for all positions but position

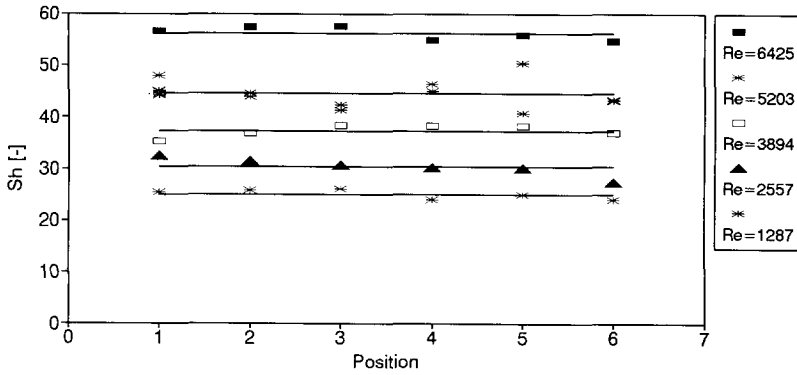


Figure 3-11 Check for influence of the lateral position. $s/d = 1.8$, $d = 6.5$ mm. Symbols = experimental data; solid lines = run averages.

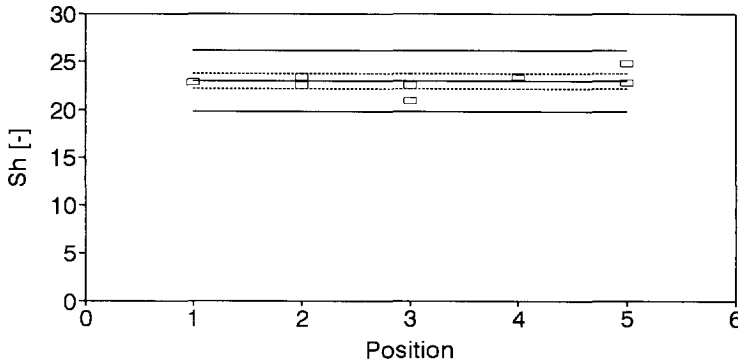


Figure 3-12 Check for influence of the lateral position; two data points at one position represent one particle at position n and the other at position n' . $s/d = 1.4$, $d = 6.5$ mm. \square = experimental data; solid lines = 95% confidence interval of a new data point; dotted lines = 95% confidence interval of a new run average.

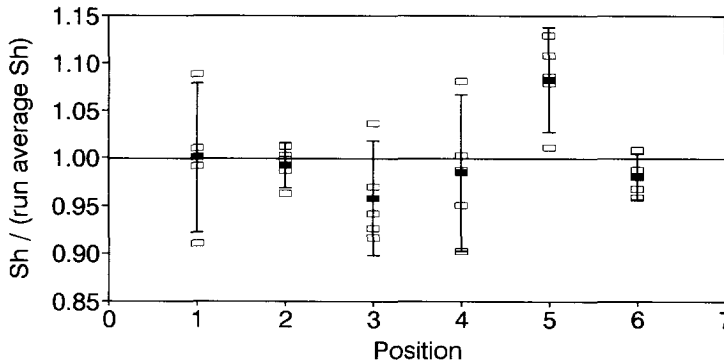


Figure 3-13 Check for influence of the lateral position. $s/d = 1.1$, $d = 6.5$ mm. \square = experimental data; \blacksquare = position average; | = 95% confidence interval of a new position average.

5 (the corner position), the 95% confidence intervals of the position average includes 1.0; this shows that for those positions the effect of the lateral position is insignificant. Only for the corner position the Sherwood number seems significantly higher than for the other positions. However, the difference, *ca.* 8%, is much smaller than the difference between the estimated gas velocity through the corner channel and the average gas velocity in the complete bundle (*ca.* 26%).

Based on a meticulous statistical analysis of the observations, that is not described here because of space limitations, it was concluded that under the tested conditions the influence of the lateral position on the Sherwood number was insignificant except for the corner position that was just discussed. The term 'insignificant' in this respect means that the differences between the experimental Sherwood numbers were smaller than (*ca.*) two times the standard deviation of the observations.

The conclusion of these experiments is, that for typical BSR geometries the difference between Sherwood numbers of particles facing the various subchannels, is smaller than the predicted difference between gas velocities through the various subchannels. Two explanations can be given for this. The first is that (except for the particles in the corner position) particles facing the reactor shell are only for one half facing a wall channel; the other half is facing the first ring of central subchannels (see Fig. 2-1). This dampens the effect of the effect of the higher (or lower) velocity through the wall subchannels compared to the central subchannels. The other explanation is that the turbulence is expected to cause transfer of momentum through the boundaries between the subchannels (which is not accounted for in the flow distribution model discussed in Chapter 2), resulting in a less pronounced flow distribution. Considering the small effect of the lateral position on the Sherwood numbers, and the relatively small fraction of the total catalyst surface facing wall or corner subchannels (especially in practical situations), it can be concluded that only negligible errors are introduced when the mass transfer in a BSR is described with only one Sherwood number rather than three different values for the three types of subchannels.

4.7 Dependence of Sh on Re

The experimentally determined Sherwood numbers in all four tested geometries are plotted as a function of Re in Figs. 3-14a to d. Note that at each Reynolds number, the different data points correspond to different lateral positions. The values of all but one of the different lateral positions could be pooled because the effect of the lateral position had been found insignificant. The points for which the lateral position did have a significant effect, have been left out of the plot.

In the figures three predicted curves are plotted. The dashed line represents Sherwood numbers calculated with the Chilton-Colburn analogy (Eq. (3-13)), based on the friction factor for smooth rods (predicted with the procedures described in Chapter 2). The solid line also represents Sherwood numbers calculated with the Chilton-Colburn analogy, but then based on the experimentally determined values of the friction factor.

For two geometries this line could not be calculated, for lack of reliable pressure drop data. The dotted line represents the prediction based on the equivalent ringzone approximation for smooth rod bundles (Eqs. (3-11) and (3-12)).

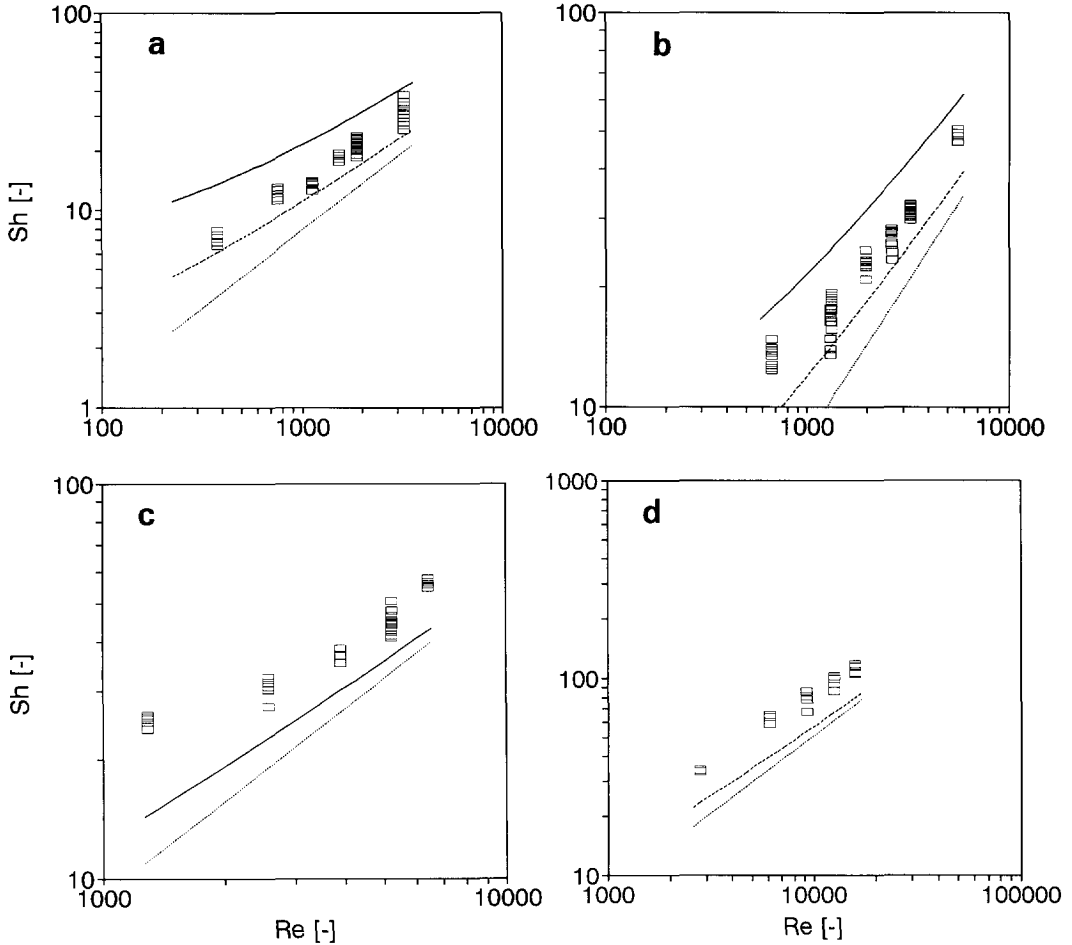


Figure 3-14 Sherwood as a function of the Reynolds number. (a) $s/d = 1.1$, $d = 6.5$ mm; (b) $s/d = 1.4$, $d = 6.5$ mm; (c) $s/d = 1.8$, $d = 6.5$ mm; (d) $s/d = 1.4$, $d = 4.6$ mm.
 □ = experimental data; dotted line = prediction from ringzone approximation (Eqs. (3-11) and (3-12)); dashed line = Chilton-Colburn prediction based on predicted friction factor for smooth rods; solid line = Chilton-Colburn prediction based on experimental friction factor.

It appears that for the conditions tested, the Chilton-Colburn prediction procedure proposed in Section 2.4.2 correctly predicts the range within which the Sherwood numbers fall. In case of hydraulically rough strings or rods, the Sherwood numbers are higher than predicted from the friction factor of smooth rods bundles; on the other hand the roughness has a stronger influence on the hydrodynamic boundary layer than on the mass transfer boundary layer, because of which the experimentally determined friction factor leads to a too high prediction of the Sherwood number. These results show that when an error of *ca.* 30% in the predicted Sherwood number is acceptable (as is often true), pressure drop measurements are an easy means to obtain estimates of the mass transfer characteristics, in case of turbulent flow.

At higher Reynolds numbers the experimental data can be adequately fitted with a power in Re of approximately 0.8. Apart from the pressure drop characteristics, it can therefore be concluded from the mass transfer characteristics that in the higher Re range of the tested conditions, the flow is turbulent.

With the technique discussed in Section 2.3, the Sherwood numbers for laminar flow can be predicted. For the geometries of the present study, the Sherwood numbers for laminar flow with the $\langle T \rangle$ boundary condition pertaining to Figs. 4.7a to d, are 2.2, 6, 10, and 6, respectively. These values are expected to be approached asymptotically when going to lower Reynolds numbers. Consequently, the straight line with slope 0.8 that could be drawn through the clouds of data points at the highest Reynolds numbers, is expected to start to curve when going from turbulent to laminar flow. Based on pressure drop characteristics, the flow in the geometry to which Fig. 3-14c pertains was known to be in the transition regime at the lowest Reynolds numbers; the data points indeed seem to start to deviate from the imaginary line with slope 0.8 that could be drawn through the points at the highest Reynolds numbers.

5 Conclusions

The large amount of literature on heat transfer in rod bundles allows a reasonably accurate prediction of the mass transfer characteristics of a BSR.

Deviations from predictions based on literature correlations may occur because of two facts:

1. The boundary condition of the governing partial differential equation that describe mass transfer in a reactor with catalytic walls, differs from the standard boundary conditions assumed in most texts on heat transfer in rod bundles; however, the Sherwood number of a reactor with catalytic walls will lie between the values obtained for these two standard boundary conditions.
2. The literature usually deals with hydraulically smooth rod bundles; the type of artificial roughness of the BSR strings seems unique.

For the laminar flow regime the effect of the boundary condition is relatively unimportant, except for relative pitches smaller than 1.1. Furthermore, for relative pitches smaller than 1.1, the mass transfer entrance length becomes of the same order of magnitude as the length of a typical BSR module (*ca.* 0.5 m). The Sherwood number averaged over the length of the reactor may then be more than 25% higher than the Sherwood number for a fully developed concentration profile. However, the effect of the enhanced mass transfer in the mass transfer entrance zone will usually only have a small effect on the overall reactor performance.

Based on the experimental study it is concluded that for any Reynolds number in the turbulent flow regime the experimental Sherwood number falls between the two values predicted from (A) the experimentally determined friction factor for the tested reactor, and (B) the theoretical friction factor for a smooth rod bundle with the same relative pitch. Using these two predictions as the limiting values, the experimental Sherwood numbers can be predicted with an accuracy of *ca.* 30%, which is acceptable in most cases.

Finally it can be concluded that for all practical situations, the dependence of the Sherwood number on the axial or lateral position in the reactor may be neglected in case of turbulent flow.

Acknowledgement

Joeri Arnouts, Joke Droogh, Sico Waagmeester, Frank Ouwerkerk, Martin Furth and Kálmán Takács are gratefully acknowledged for their substantial contribution to the work reported in this chapter.

Notation

A_p	mass transfer surface area	$[\text{m}^2_{\text{part}}]$
c_A	concentration of reactant A	$[\text{mol}_A/\text{m}^3_{\text{fluid}}]$
c_A^+	dimensionless concentration of reactant A	$[-]$
$c_{A,b}$	concentration of A in the bulk phase (cup mixing average of the fluid domain)	$[\text{mol}_A/\text{m}^3_{\text{fluid}}]$
$c_{A,in}$	concentration of A at the reactor inlet	$[\text{mol}_A/\text{m}^3_{\text{fluid}}]$
$c_{A,s}$	concentration of A at the external catalyst particle surface	$[\text{mol}_A/\text{m}^3_{\text{fluid}}]$
${}^\circ c_{A,s}$	circumferentially averaged surface concentration	$[\text{mol}_A/\text{m}^3_{\text{fluid}}]$
$c_{N,b}$	bulk concentration of naphthalene	$[\text{mol}_N/\text{m}^3_{\text{fluid}}]$
$c_{N,s}$	surface concentration of naphthalene	$[\text{mol}_N/\text{m}^3_{\text{fluid}}]$
D	diffusivity (free molecular or turbulent)	$[\text{m}^2/\text{s}]$
D_e	effective pore diffusion constant	$[\text{m}^2/\text{s}]$
D_{free}	free molecular diffusion constant	$[\text{m}^2/\text{s}]$
Da_{II}	second Damköhler number	$[-]$
d	rod or particle diameter in a rod bundle or BSR	$[\text{m}_{\text{part}}]$
d_h	hydraulic channel diameter (for rod bundles it normally includes the perimeter of the reactor shell)	$[\text{m}]$
d_p	particle diameter	$[\text{r}_{\text{part}}]$
$\langle H1 \rangle$	boundary condition of constant axial wall heat flux with constant circumferential wall temperature	
$\langle H2 \rangle$	boundary condition of constant axial and circumferential wall heat flux	
k_g	mass transfer coefficient	$[\text{rn}/\text{s}]$
$k_{g,\alpha}$	angularly local mass transfer coefficient	$[\text{rn}/\text{s}]$
${}^\circ k_g$	circumferentially averaged mass transfer coefficient	$[\text{rn}/\text{s}]$
$k_{r,v}$	first order rate constant, volume basis	$[\text{m}^3_{\text{fluid}}/(\text{m}^3_{\text{ca}} \cdot \text{s})]$
L	distance from the leading edge of a mass or heat transfer surface	$[\text{m}]$
L	length of a particle	$[\text{m}]$

ℓ_c, ℓ_T	mass and heat transfer entrance lengths	[m]
$M_{w,N}$	molecular weight of naphthalene	[kg _N /mol _N]
Nu	Nusselt number	[-]
$Nu(\langle H2 \rangle)$	Nusselt number for the $\langle H2 \rangle$ boundary condition	[-]
Nu_t	Nusselt number for a circular tube	[-]
Nu_∞	Nusselt number for a fully developed temperature profile or boundary layer	[-]
$\langle Nu \rangle_L$	Nusselt number averaged over a length L from the leading edge of the heat transfer surface	[-]
p_N^{sat}	saturated vapor pressure of naphthalene	[Pa]
r	radial coordinate	[m]
r^+	dimensionless radial coordinate	[-]
R	(outer) radius of a cylindrical or ring-shaped particle	[m]
\mathcal{R}_A	reaction rate of A expressed per unit catalyst volume	[mol _A /(m ³ _{cat} ·s)]
R_g	gas constant (8.31)	[J/(mol·K)]
Re	Reynolds number, based on the hydraulic diameter of the complete bundle (incl. the perimeter of the reactor shell)	[-]
s	pitch of strings in a BSR or rods in a rod bundle, <i>i.e.</i> the heart-to-heart distance	[m]
Sc	Schmidt number	[-]
Sh	Sherwood number ($k_g a_p / D_{free}$)	[-]
$Sh(\langle H2 \rangle)$	Sherwood number for the $\langle H2 \rangle$ boundary condition	[-]
Sh_∞	Sherwood number for a fully developed concentration profile or boundary layer	[-]
Sh_x	axially local Sherwood number	[-]
$\langle Sh \rangle_L$	Sherwood number averaged over a length L from the leading edge of the mass transfer surface	[-]
T_b	bulk fluid temperature (cup mixing average)	[K]
$\langle T \rangle$	boundary condition of constant axial and circumferential wall temperature	
u_z	linear axial gas velocity	[m/s]
z	axial coordinate	[m]
<i>Greek letters</i>		
Δm	mass decrease of a naphthalene particle	[kg _N]
Δt	run time of an experiment	[s]
$\delta_c, \delta_h, \delta_T$	concentration, hydrodynamic and temperature boundary layer thickness	[m]
η_p	effectiveness factor of a catalyst particle	[-]
$\phi^{mol,A}$	molar flux of component A	[mol _A /(m ² ·s)]
$\phi_{mol,N}$	molar flow of naphthalene	[mol _N /s]

References

- Bird, R.B., Stewart, W.E. and Lightfoot, E.N., 1960, *Transport Phenomena*. John Wiley & Sons, New York. p. 200.
- Box, G.E.P., Hunter, W.G. and Hunter, J.S., 1978, *Statistics for Experimenters*. John Wiley & Sons, New York.
- Bräuer, H.W. and Fetting, F., 1966, Stofftransport bei Wandreaktion im Einlaufgebiet eines Strömungsrohres. *Chem. Ing. Tech.* **38-1**, 30-35.
- Brauer, H. and Schlüter, H., 1965, Konvektiver Stoffaustausch mit heterogener chemischer Reaktion. *Chem. Ing. Techn.* **37-11**, 1107-1117.
- Kim, J.H., 1979, Heat Transfer in Longitudinal Laminar Flow Along Circular Cylinders in a Square Array, in *Fluid Flow and Heat Transfer Over Rod or Tube Bundles*, (Edited by S.C. Yao and P.A. Pfund). Winter Annual Meeting of the American Society of Mechanical Engineers, December 2-7, New York, pp. 155-161.
- Perry, R.H. and Green, D. (Eds.), 1987, *Perry's Chemical Engineers' Handbook*, 6th ed., 3rd printing, p. 10-17. McGraw-Hill Book Company, New York.
- Petukhov, B.S. and Roizen, L.I., 1974, Generalized Dependences for Heat Transfer in Tubes of annular Cross Section, *Teplofiz. Vysokikh Temp.*, Vol. 12, pp. 565-569; as quoted in Rehme (1987), p. 7-37.
- Presser, K.H., 1971, Stoffübergang und Druckverlust an Parallel angeströmten Stabbüdeln in einem grossen Bereich von Reynolds-Zahlen und Teilungsverhältnissen. *Int. J. Heat Mass Transfer* **14**, 1235-1259.
- Rehme, K., 1987, Convective Heat Transfer over Rod Bundles, in *Handbook of Single-Phase Convective Heat Transfer* (Edited by S. Kakaç, R.K. Shah and W. Aung), pp. 7.1-7.62. John Wiley & Sons, New York.
- Smith, J.M., Stammers, E., Janssen, L.P.B.M., 1984, *Fysische Transportverschijnselen I*, p. 109. Delfts Uitgeversmaatschappij, Delft, The Netherlands.
- Sparrow, E.M. and Loeffler Jr., A.L., 1959, Longitudinal Laminar Flow Between Cylinders Arranged in Regular Array. *AIChE J.* **5**(3), 325-330.
- Takács, K., 1994, *Mathematical modelling of the Bead String Reactor* (internal report). Faculty of Chemical Engineering and Materials Science, Delft University of Technology, Delft, The Netherlands.
- Toenes, D., 1957, *Stofoverdracht bij stroming door een vast bed van korrelig materiaal*. PhD thesis, Technische Hogeschool Delft, Delft, The Netherlands.
- Tronconi, E. and Forzatti, P., 1992, Adequacy of Lumped Parameter Models for SCR Reactors with Monolith Structure. *AIChE J.* **38-2**, 201-210.

Chapter 4

**Kinetic study of the test reaction—
SCR of NO with excess NH₃**

Contents

Summary	101
1 Introduction	102
2 Starting points for the kinetic study	103
3 Catalytic reactor engineering aspects of studying kinetics in a recycle reactor	105
3.1 Introduction	105
3.2 Criteria for ideal mixing in the recycle reactor	106
3.3 Criteria for absence of film layer gradients	114
3.4 Criteria for absence of intraparticle gradients	116
4 Experimental work	118
4.1 Introduction	118
4.2 Creation of the experimental designs	118
4.3 Experimental set-up and experimental procedure	119
4.4 Checks on the occurrence of side reactions	122
4.5 Implementation of the experimental designs	122
5 Results and discussion	123
5.1 Introduction	123
5.2 Checks on falsification of the observations	123
5.3 Modeling of the intrinsic kinetics	124
5.4 Modeling of the particle kinetics	129
6 Conclusions	137
Acknowledgements	138
Notation	138
References	141

Summary

To enable experimental validation of the mathematical BSR model, the intrinsic kinetics of a test reaction were needed, as well as a model to describe pore diffusion in the catalyst. To obtain these, both the intrinsic and particle kinetics of the selective catalytic reduction (SCR) of NO with NH₃ over a commercial deNO_x catalyst were studied in an internal recycle reactor of the Berty type. The conditions were: 413-453 K, atmospheric pressure, 20-120 ppmv NO, 1000 ppmv NH₃, 3-7 vol. % O₂, 10-20 vol. % H₂O, balance nitrogen. The catalyst was shaped as cylindrical extrudates (Ø 1.6 or 3.2 mm), with an axial hole (Ø 0.4 mm) to allow stringing of the particles for application in the BSR.

The intrinsic kinetics were studied after powdering the extrudates, using the sieve fraction 425-500 µm. It was verified that under the experimental conditions the axial, film layer and intraparticle concentration and temperature gradients in the catalyst bed of the recycle reactor were negligible. In all accepted runs the falsification of the observed reaction rate due to the finite recycle ratio was less than 5%. The effect of side reactions (NO → NO₂, NO → N₂O, NH₃ → NO, NH₃ → N₂) was negligible.

The intrinsic reaction rate could be adequately described (significance level 18%) by a power law rate expression, with only one set of parameters (per catalyst) for the complete range of conditions:

$$-r_{\text{NO}} = k_0 e^{\frac{-E_A}{R_g T}} c_{\text{NO}}^n c_{\text{O}_2}^m c_{\text{H}_2\text{O}}^p \quad (4-1)$$

The estimated activation energy (*ca.* 6·10⁴ J/mol) lies within the range reported in the literature for various catalysts resembling the one used in this study. Also the values of the orders in NO (*ca.* 0.7), O₂ (*ca.* 0.3) and H₂O (*ca.* -0.4) are in agreement with the literature. The trend of the parameters *n*, *m* and *p* with temperature is barely significant. No activation or deactivation of the catalyst was observed. The uncertainty in a reaction rate predicted by the regression model, within the studied range of conditions, it is smaller than 3%.

Also in the study of the particle kinetics it was verified that under the experimental conditions the axial and film layer concentration and temperature gradients in the catalyst bed of the recycle reactor were negligible. For each run with the extrudates, the effectiveness factor of the particles was calculated using the intrinsic kinetic model. The experimentally determined effectiveness factors were used to fit a single parameter in a simple pore diffusion model. With this model and the intrinsic kinetic model, the particle kinetics could be adequately described (significance level 9%).

1 Introduction

One of the goals of this thesis work is the development of a mathematical model of the Bead String Reactor (BSR), that can be used to do case studies. This reactor model should be validated experimentally, by running a suitable, heterogeneously catalyzed 'test' reaction in the BSR and comparing the observed performance to the performance predicted by the reactor model. To enable such experimental validation, the intrinsic kinetics of the test reaction should be known, as well as a pore diffusion model for the catalyst, since these are inputs to the reactor model.

The kinetic study reported in this chapter consists of two stages. First, the intrinsic kinetics of the test reaction are studied, after crushing a sample of the catalyst to obtain particles small enough to exclude intraparticle gradients. Secondly, the effectiveness factor of the original catalyst particles is studied, by comparing observed reaction rates over these particles with the predicted intrinsic reaction rates. From the effectiveness factors found in this way, a fit parameter in a catalyst pore diffusion model is estimated. On the basis of the intrinsic kinetics and the pore diffusion model, it should be possible to predict the intrinsic and particle kinetics in the BSR within the studied range of conditions.

The structure of this chapter is as follows:

In Section 2 the starting points of the kinetic study are discussed: which type of reactor is chosen for the kinetic study, which reaction is going to serve as the 'test' reaction, which rate expression is going to be used to describe the intrinsic reaction rate, and which pore diffusion model will be used?

In Section 3 the criteria will be presented that will be used to design kinetic experiments in a recycle reactor in such a way that the observations are only negligibly falsified by insufficient recycle ratio, or insufficient film layer mass and heat transfer, or (with the powdered catalyst) intraparticle mass and heat transfer.

In Section 4 the experimental work is described. It includes a description of the creation of experimental designs, the experimental set-up, the experimental procedure, and the experiments to check for the occurrence of side reactions.

In Section 5 the results of the experimental work are discussed. It includes checks on the falsification of observations as a consequence of insufficient recycle and insufficient mass or heat transfer. Furthermore the estimation of the intrinsic kinetic parameters is discussed, as well as various statistical checks. Finally the estimation of the pore diffusion fit parameter is discussed.

2 Starting points for the kinetic study

For reasons of convenience, the reactor that is used to perform the kinetic study should have specific characteristics: the hydrodynamics should be well known and should allow for easy interpretation of the observations. The reactor used in this kinetic study is an Internal Recycle Reactor (IRR) of the Berty type (see, *e.g.*, Berty, 1984). It was chosen because of its commercial availability and because it had already proven all over the world to be a convenient piece of equipment. Details of the reactor are discussed in Section 4.3.

Like the reactor used for the kinetic study, also the catalytic reaction serving as a 'test reaction' is required to have specific characteristics: it should have a high selectivity, there should be no appreciable catalyst deactivation, and the key component should be easy to analyze. In this work, the Selective Catalytic Reduction (SCR) of nitric oxide with excess ammonia, oxygen and water was chosen to serve as the test reaction. The catalyst is a commercial deNO_x catalyst in the form of extrudates of 1.6 or 3.2 mm diameter and *ca.* 6.5 mm long, with a small axial hole (0.4 mm diameter); the hole is necessary to allow stringing of the particles for application in a BSR. Samples of the extrudates are powdered and sieved for the study of the intrinsic kinetics. The conditions of the kinetic study were chosen such, that based on literature data, specifications of the catalyst manufacturer and preliminary experimental data, the SCR reaction could be expected to meet the criteria described above. It is out of the scope of this thesis to discuss the considerations behind this choice. The chosen range of conditions is listed in Table 4-1.

In the experimental validation of the BSR model, the independent variables are the relative pitch, catalyst particle diameter, gas velocity, temperature and NO feed concentration; the feed concentrations of ammonia, water and oxygen will be kept constant. However, in practice small deviations from the set points are inevitable, and from literature and preliminary experiments it was known that in the experimental range of conditions, the oxygen and water concentrations do influence the SCR reaction rate, whereas the ammonia concentration does not. For this reason it was decided to include not only T and c_{NO} in the kinetic model, but also c_{O_2} and $c_{\text{H}_2\text{O}}$. Furthermore the space velocity was included as an independent variable in the study of the intrinsic kinetics, to verify that it did not influence the values of the estimated kinetic parameters.

Table 4-1 Experimental range of conditions

T	413 - 453	K
p	0.11	MPa
c_{NO}	10 - 100 $\approx 3.0 \cdot 10^{-4} - 3.0 \cdot 10^{-3}$	ppmv mol/m ³
c_{O_2}	2 - 8 $\approx 0.6 - 2.4$	vol. % mol/m ³
$c_{\text{H}_2\text{O}}$	10 - 20 $\approx 3.0 - 6.0$	vol. % mol/m ³
c_{NH_3}	1000 $\approx 3.0 \cdot 10^{-2}$	ppmv mol/m ³

Based on SCR literature, it was decided to describe the intrinsic kinetics with the simple power law rate expression of Eq. (4-1). In the limited range of conditions of this study, the power law expression was expected to enable adequate description of the reaction rate not less than more complex rate equations derived (through many extreme assumptions and simplifications) from assumed (and often disputed) mechanistic models. Furthermore the power law rate expression enables simple statistical manipulation, because it can be easily linearized:

$$-r_{\text{NO}} = k_0 e^{\frac{-E_A}{R_g T}} c_{\text{NO}}^n c_{\text{O}_2}^m c_{\text{H}_2\text{O}}^p \Rightarrow \quad (4-2)$$

$$\ln(-r_{\text{NO}}) = \ln(k_0) - \frac{E_A}{R_g} \frac{1}{T} + n \ln(c_{\text{NO}}) + m \ln(c_{\text{O}_2}) + p \ln(c_{\text{H}_2\text{O}})$$

Note that from the point of view of statistical data analysis, this linearization is only allowed if the stochastic error in the observations is proportional to the observations, rather than independent. It will be made plausible in Section 5.3.1 that this condition is indeed met in the present study.

The effectiveness factor of the extrudates will be modeled using the generalized formulae derived by Wijngaarden and Westerterp (1994). This method, which will be called 'Aris method' in this thesis, is an extension of the well-known method based on the Thiele modulus. It will be shown that for the tested reaction and catalyst geometry, the deviation of the effectiveness factor estimated by the Aris method from the effectiveness factor obtained from time-consuming numerical solution of the balance equations, is considerably smaller than the error of the kinetic experiments.

A critical parameter in the calculation of the particle kinetics from an intrinsic kinetic model, is the effective pore diffusivity D_e . In this study the following well-known, simple pore diffusion model will be used:

$$D_e = \frac{\varepsilon}{\tau} \left(\frac{1}{D_{free}} + \frac{1}{D_{Kn}} \right)^{-1}$$

The Knudsen diffusion coefficient is calculated from the median pore radius, which is known from mercury intrusion analysis. Because this model is very crude, and because the pore tortuosity cannot be determined from independent physical analysis, it was decided to replace the physical parameter ε/τ by a fit parameter Ω . Ω will be fitted from experimentally determined effectiveness factors of the extrudates, obtained by comparing the observed particle kinetics with the intrinsic kinetics. On the basis of the intrinsic kinetic model and the pore diffusion model with the fitted Ω , it should then be possible to predict the particle kinetics within the studied range of conditions.

3 Catalytic reactor engineering aspects of studying kinetics in a recycle reactor

3.1 Introduction

This section discusses criteria used to design the experiments in such a way that the observations are not falsified by insufficient recycle ratio (Section 3.2), or insufficient film layer or intraparticle mass and heat transfer (Sections 3.3 and 3.4). In the normal routine, the methods presented in this section are used twice. The first time is prior to the experimental work, to calculate experimental conditions under which falsification of the experiments is expected to be negligible; the calculations are then based on estimations of reaction rates, equipment performance etcetera. The second time is after the experiments have been carried out, when the experimental conditions are known with a higher accuracy and the observations are available. The criteria are then used to select the experiments that should be rejected. The latter will be discussed in Section 5.2.

3.2 Criteria for ideal mixing in the recycle reactor

The incentive for using a recycle reactor is that it allows analysis of the observations using the reactor equations pertaining to an ideal CSTR, thereby neglecting gradients in the bulk fluid phase; it therefore allows direct measurement of the reaction rate, without the need to assume a rate expression first. Obviously it must be checked that the deviation from CSTR behavior is indeed negligible, i.e., that there is virtually instantaneous mixing of the fresh feed with all the fluid in the reactor and that there is practically no concentration or temperature gradient across the catalyst bed.

Instantaneous mixing of the fresh feed with the fluid in the reactor can be checked with residence time distribution (RTD) measurements. However, in the present study it has been assumed that the effect of deviations from instantaneous mixing are negligible. This assumption is mainly based on RTD measurements reported by Bennett *et al.* (1972), performed with a reactor similar to the one used in this study. The results by Bennett *et al.* indicated that due to the shape of the internal recycle reactor, the RTD curves resemble those of an ideal CSTR even at low rotor speeds. Furthermore effects of deviations from instantaneous mixing are most pronounced for high conversions and high reaction orders, whereas in our study the conversion was normally less than 80% and the reaction order in the key component (NO) is only about 0.7.

The check for absence of important concentration or temperature gradients across the catalyst bed consists of two parts: 1) the estimation of the recycle ratio obtained in the experiments, and 2) the estimation of the effect of the recycle ratio on the falsification of the observations. Both subjects are treated in the following two sections.

3.2.1 Estimation of the recycle ratio in the RotoBerty reactor

A drawing of the RotoBerty recycle reactor used in this study, is shown in Figure 4-1. The basis of the estimation of the recycle ratio in the RotoBerty reactor is the actual calibration of the gas flow through the catalyst bed as a function of the rotor speed. After charging a portion of catalyst in the catalyst basket and inserting the basket in the reactor, a tube is placed on top of the basket. Using a hot-wire anemometer, the air velocity through the tube is measured as a function of the rotor speed (see Figure 4-2). From this the volumetric flow rate through the catalyst bed under ambient conditions can be related to the rotor speed. Using a simple hydrodynamic model, discussed briefly in the next paragraph, this flow rate can be translated to the actual volumetric flow rate through the catalyst bed under process conditions.

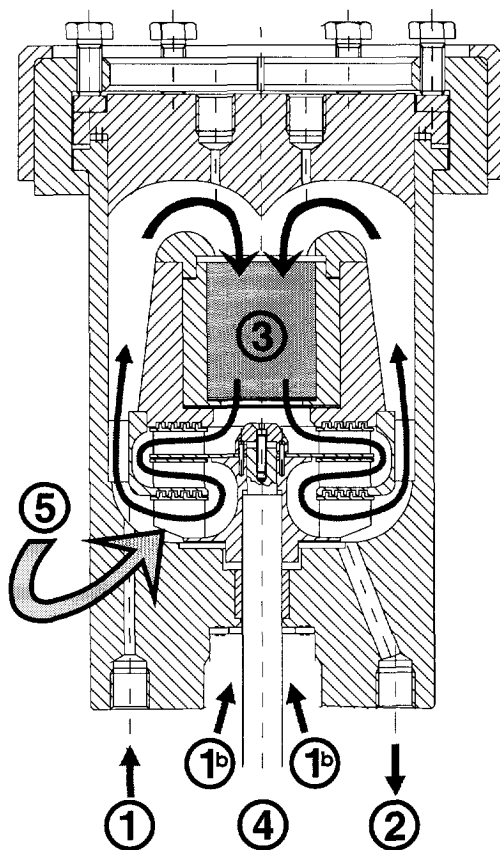


Figure 4-1 The RotoBerty internal recycle reactor

1) Main inlet; 1^b) Second 'inlet'; the gas flows along the shaft, through a slot (not drawn) in the the top-bushing; 2) Outlet; 3) Catalyst basket; 4) Shaft; 5) Two-stage rotor.

Note: the motor housing and the motor, below the reactor, are not drawn.

The reactor contains a basket (3) in which the catalyst is placed. This construction allows any shape or amount of catalyst packing, provided it fits in the basket. The basket is placed just above (but is not fixed to) a two-stage rotor that is fixed to a permanent magnetic shaft. The shaft, supported by a trust-bearing at the bottom (not drawn) and a top-bushing, is driven by a rotating magnetic field induced by a static motor (not drawn) outside the reactor space. Thanks to this construction, the only moving parts (rotor + shaft) are fully contained inside the reactor space, which avoids leaking problems often reported for other types of recycle reactors.

The rotor is usually driven to a speed of 5,000 rpm, which generates a pressure difference across the rotor. The direction of rotation is such that the fluid flows downward through the catalyst basket and rotor. Because the rotor generates pressure and not flow, the flowrate through the catalyst basket (ergo, the recycle ratio) depends on the resistance to flow in the catalyst basket, *i.e.*, the pressure drop across the catalyst packing.

The ratio of this flow rate to the flow rate of the fresh feed finally yields the recycle ratio, in this thesis defined as:

$$R \equiv \frac{\phi_{V,bed}}{\phi_{V,feed}} \quad (4-4)$$

The hydrodynamic model that links the recycle flow to the rotor speed is based on the fact that the pressure difference generated by the rotor, equals the pressure drop across the pathway from the rotor exit to the rotor entrance (see Figure 4-1). Since the catalyst bed forms the main flow restriction in this pathway, unless a 'very small' amount of catalyst is used, it is safe to assume that the pressure difference generated by the rotor equals the pressure drop across the catalyst bed. Given the fact that the pressure difference generated by a rotor is proportional to the square of the rotor speed (*RPM*), and using Ergun's relation (Bird *et al.*, 1960) to describe the pressure drop across the catalyst bed, the following implicit expression for the superficial fluid velocity through the bed as a function of the rotor speed, can be easily derived:

$$RPM = \sqrt{\frac{a \psi u^2 + bu / \rho_f}{cg}} \quad (4-5)$$

The parameters *a* and *b* in this equation result from the Ergun relation, and are known functions of the catalyst bed voidage, the bed height, the equivalent catalyst particle diameter and the dynamic fluid viscosity. The constant ψ accounts for the influence of the roughness of the particles on the pressure drop. The constant *c* is the proportionality constant of the rotor, that links the generated pressure difference to the rotor speed.

The values of ψ and *c* are found experimentally by fitting pressure drop measurements, through calibration measurements described in the beginning of this section. Equation (4-5) shows that when the flow is not fully turbulent, the rotor speed required for a certain gas velocity through the catalyst bed depends on the gas temperature. This is because the temperature influences both the dynamic viscosity and the gas density. Since the viscosity of a gas generally increases with increasing

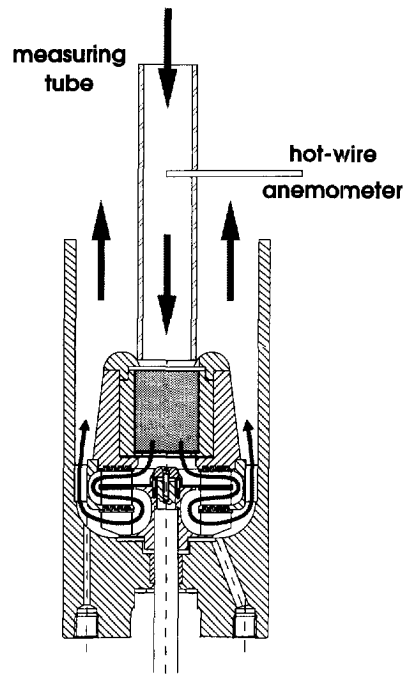


Figure 4-2 Calibration of the recycle flow in the RotoBerty reactor.

temperature, and the gas density decreases, the gas velocity through the bed (at constant rotor speed) decreases with increasing temperature.

Even more important, for a given gas velocity through the bed, the flowrate expressed in m³ (NTP)/s is inversely proportional to the gas density, ergo, inversely proportional to the temperature. It then follows from Equation (4-4) that also the recycle ratio is inversely proportional to the gas temperature.

Under conditions used in our study, for a given catalyst bed the recycle ratio at 180°C can be almost 50% lower than at 25°C, at a constant fresh feed flow rate and a constant rotor speed. This underlines the importance of calculating the recycle flow under process conditions, using Equation (4-5) with fitted values of ψ and c , rather than assuming that the recycle flow under process conditions equals the flow measured under ambient conditions.

Using the fitted constant c , the pressure drop across the catalyst bed can be estimated as a function of the rotor speed. Since for a gas the pressure drop entails a proportional axial concentration drop across the bed, it adds to the concentration drop of the reactants resulting from the chemical reaction. Therefore it is important to estimate the concentration drop across the bed due to the pressure drop, and to check whether its effect on the estimation of the kinetic parameters is negligible.

3.2.2 Effect of recycle ratio on falsification of observations

Only when the recycle ratio approaches infinity, the behavior of the recycle reactor becomes truly identical to that of an ideal CSTR. An important question is to what extent the experimentally determined kinetic parameters deviate from the 'true' parameters at finite recycle ratios. From a practical point of view this question could be rephrased as the question what recycle ratio is sufficient to obtain negligible deviation from ideal CSTR behavior.

As far as concentration gradients are concerned, this question can be answered using the method proposed by Wedel and Villadsen (1983). For a given experiment with a recycle reactor, they distinguish two reaction rates. The first is the 'true' reaction rate that could be calculated from the measured reactor outlet conditions, if the 'true' kinetics were known; *e.g.*, for n -th order kinetics:

$$-r_{A,true} = kc_A^n \quad (4-6)$$

The second is the apparent reaction rate, that is calculated from the difference in molar flows of the reactants between the feed and product stream, using the ideal CSTR equations:

$$-r_{A,app} = \frac{\phi_{mol,A,in} - \phi_{mol,A,out}}{M_{cat}} \quad (4-7)$$

Wedel and Villadsen (1983) defined the so-called 'falsification ratio' as the ratio of these two reaction rates:

$$\rho \equiv \frac{-r_{A,app}}{-r_{A,true}} \quad (4-8)$$

A falsification ratio higher than 1 implies that the catalyst activity, or, consequently, the rate constant, is overestimated, and vice versa. In the remainder of this report, ρ will be referred to as the 'rate falsification ratio', to distinguish it from the 'order falsification ratio' that will be defined later in this section.

For an ideal CSTR, the difference in molar flows of the reactants between the feed and product stream follows from a mole balance, and is given by:

$$\phi_{mol,A,in} - \phi_{mol,A,out} = -r_{A,true} M_{cat} \quad (4-9)$$

Substitution of Equation (4-9) into Equation (4-7) shows that for an ideal CSTR, the apparent reaction rate equals the true reaction rate. Consequently, the rate falsification ratio of an ideal CSTR equals 1.

In the following discussion on the falsification ratio of recycle reactors, it is important to distinguish two fundamentally different recycle reactor configurations, depicted in Figures 4-3a and b. The first one is the 'classical' so-called 'reverse flow configuration', that corresponds to most external recycle reactors. Because this configuration is in fact a plug flow reactor with recycle, the rate falsification ratio will be bigger than one. The second configuration, the so-called 'forward flow configuration', is obtained by exchanging the feed and exit of the external recycle reactor. This configuration is in fact a plug flow reactor with by-pass; the by-pass causes the rate falsification ratio to be smaller than one.

Internal recycle reactors may resemble either the reverse or the forward flow configuration. For internal recycle reactors characterized by a static catalyst basket and an impeller to drive the recycle flow, this is shown in Figures 4-3c and d. Which of these two basic configurations the RotoBerty reactor resembles, is discussed at the end of this section.

Wedel and Villadsen only discussed the reverse flow configuration; for the present study relations were derived for the forward flow configuration as well. It can be shown that for a recycle reactor of the forward flow configuration, the rate falsification ratio is given by:

$$\rho = \frac{(1-n)S}{1-(1-S)^{1-n}} \quad (4-10)$$

in which S is defined as:

$$S = \frac{\xi}{R(1-\xi)} \quad (4-11)$$

in which ξ is defined as:

$$\xi_A \equiv \frac{\phi_{mol,A,in} - \phi_{mol,A,out}}{\phi_{mol,A,in}} \quad (4-12)$$

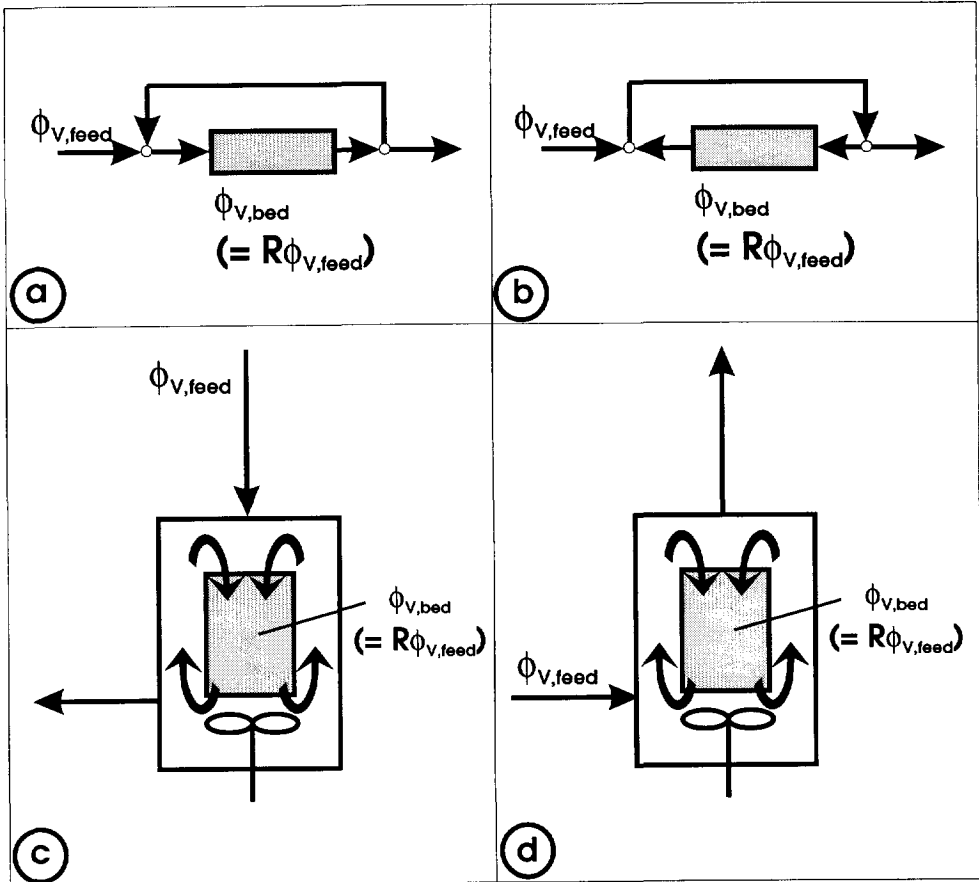


Figure 4-3 Two recycle reactor configurations:

- a) reverse flow (external);
- b) forward flow (external);
- c) 'reverse flow' (internal);
- d) 'forward flow' (internal).

A graphical representation of the forward flow rate falsification ratio as a function of ξ and R , for a (true) reaction order of 0.75, is given in Figure 4-4. It can be seen, for example, that acceptable rate falsification ratios higher than 0.95 can be obtained with a recycle ratio as low as 10, by making sure that the conversion is lower than 50%. Obviously, the lower the reaction order is, the closer to 1 the rate falsification ratio is, at a given recycle ratio and conversion.

A finite recycle ratio not only results in underestimation (forward flow) or overestimation (reverse flow) of the catalyst activity or rate constant, but also in overestimation (forward flow) or underestimation (reverse flow) of the reaction order. For n -th order kinetics, the apparent order is usually estimated from the observed reaction rates by:

$$n_{app} = \frac{\partial \ln(-r_{A,app})}{\partial \ln(c_A)} \quad (4-13)$$

It can be shown that for a recycle reactor of the forward flow configuration, the apparent reaction order is given by:

$$n_{app} = -\frac{1-\xi}{\xi} - \frac{(1-n) \left[R^{1-n} - (R+1) \left(\frac{1-\xi}{R(1-\xi)-\xi} \right)^n \right]}{R^{1-n} - \left(\frac{R(1-\xi)-\xi}{1-\xi} \right)^{1-n}} \quad (4-14)$$

The 'order falsification ratio' is defined as the ratio of the apparent reaction order to the true order:

$$v = \frac{n_{app}}{n} \quad (4-15)$$

Graphical representations of the forward flow apparent reaction order and order falsification ratio, both as functions of ξ and R , for a true reaction order of 0.75, are given in Figures 4-5 and 4-6. Comparing Figures 4-4 and 4-6 it can be seen, that the order falsification ratio depends stronger on ξ and R than the rate falsification ratio

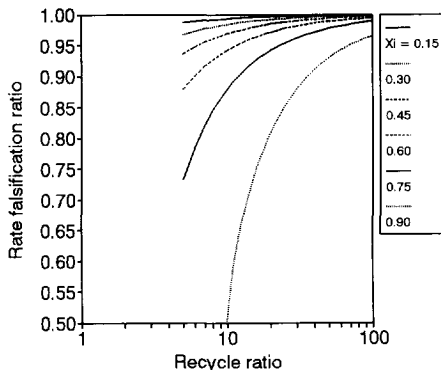


Figure 4-4 Rate falsification factor for the forward flow configuration. True reaction order: 0.75.

does. However, for many reactor design purposes the catalyst activity is far more important than the reaction order.

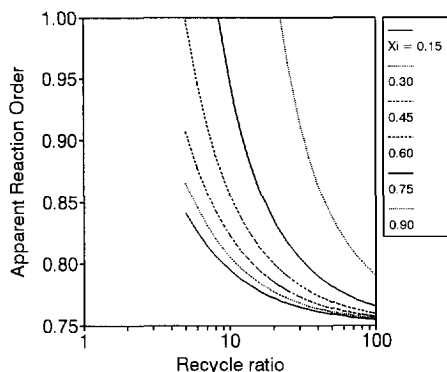


Figure 4-5 Apparent reaction order for the forward flow configuration. True reaction order: 0.75.

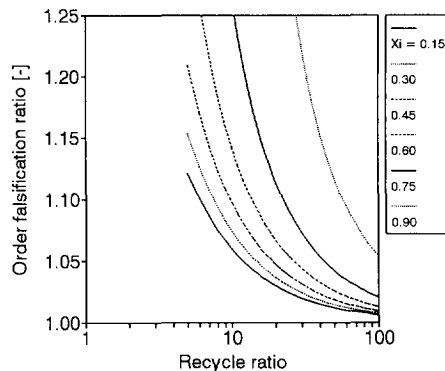


Figure 4-6 Order falsification factor for the forward flow configuration. True reaction order: 0.75.

The question remains which of the two basic recycle reactor configurations the RotoBerty reactor used in this study resembles. In fact it is a hybrid between the two basic configurations. The key point is that there are two inlets (see Figure 4-1). The main inlet is located 'downstream' of the outlet. Therefore even at low rotor speeds the molecules of the fresh feed entering through the main inlet cannot be transported directly from the inlet to the outlet by diffusion or even dispersion, and consequently have to pass at least once through the catalyst bed. The second inlet is located at the bottom end of the shaft; it is used to bleed the otherwise dead space between the shaft and the housing. Since the second inlet is 'upstream' of the outlet, part of the fresh feed molecules entering through the second inlet will directly leave the reactor without passing through the catalyst bed.

Which of the two basic configurations the RotoBerty reactor resembles most, depends on the ratio of the fresh feed flow rates entering through the main inlet and the second inlet. The flow through the main inlet contributes to a rate falsification ratio bigger than one, whereas the flow through the second inlet contributes to a falsification ratio smaller than one. Consequently, when the two flows are approximately equal or when they are not measured separately, it is difficult to tell whether the rate falsification ratio is bigger or smaller than one. To make sure that its absolute value is close to one, it is therefore best to calculate both the rate falsification ratio for the reverse and the forward flow configuration and make sure that both are sufficiently close to one. The real effect will most probably be smaller, as the two inlet flows have opposite effects.

The result of a finite recycle ratio is not only a concentration drop across the catalyst bed, but also a temperature increase (in case of an exothermic reaction like SCR of

NO). An estimate of the maximum temperature increase across the catalyst bed is given by:

$$\Delta T_b = \frac{\Delta T_{ad} \xi}{R} \quad (4-1.6)$$

Whether the maximum temperature difference is attained, depends on the rate of heat transfer from the catalyst bed to the wall.

When the reaction rate constant is modelled with an Arrhenius expression, the ratio of rate constants at the outlet and inlet of the catalyst bed is given by:

$$\frac{k_{outlet}}{k_{inlet}} = \exp\left(-\frac{E_A}{R_g} \left[\frac{1}{T_{outlet}} - \frac{1}{T_{inlet}}\right]\right) \approx \exp\left(\frac{E_A}{R_g} \frac{\Delta T_{ad} \xi}{T_{inlet}^2 R}\right) \quad (4-1.7)$$

Often a ratio between 0.95 and 1.05 is deemed acceptable. Since the average temperature in the catalyst bed will normally be between T_{inlet} and T_{outlet} , the error in the estimation of the rate constant, due to the axial temperature difference, will then be smaller than 5%. In the present study the ratio of the rate constants is always lower than 1.005, due to the low concentrations; furthermore, the temperature increase across the bed counteracts the effect of the concentration drop. Therefore the axial temperature gradient is not further discussed here.

3.3 Criteria for absence of film layer gradients

To measure intrinsic kinetics, not influenced by mass and heat transfer phenomena, it must be checked that there are neither gradients in the film layer around the catalyst particles, nor in the particles themselves. From the fact that the free gas diffusivity in the film layer is always bigger than the effective diffusivity in the pores of the catalyst, it can be made plausible that concentration gradients in the film layer are normally smaller than in the catalyst pores. Conversely, from the fact that the heat conductivity of a gas film layer is usually smaller than the effective conductivity of a catalyst particle, it follows that the temperature gradient in the film layer can be bigger than in the particles, especially at low Reynolds numbers. Note that in case of an exothermic reaction like SCR of NO, the effects of concentration and temperature gradients on the overall effectiveness factor counteract.

In this section estimations are made of the film layer gradients and their effect on the observations. In Section 3.4 intraparticle gradients are discussed.

Values of mass and heat transfer coefficients needed in the estimation of the film layer gradients, can be obtained from empirical relations for Sherwood and Nusselt numbers in packed beds of particles. Since such relations depend on the Reynolds number of the flow through the bed, reliable estimates are needed of the gas velocity through the catalyst bed. These can be obtained from the relations presented in Section 3.2.1, after the experimental calibration of the recycle flow.

It is important to realize that the velocities predicted by those relations are average values. There may be significant variations in local velocities, due to uneven distribution of the catalyst particles in the bed. Especially when small amounts of catalyst are charged, the relative variation in bed height may be considerable. Since the axial pressure drop is fixed for a given rotor speed, and constant across the bed surface, the axial pressure gradients vary inversely proportional to the local bed height. Consequently the local gas velocity normally varies less than inversely proportional to the bed height, as the gas velocity depends on the pressure gradient to the power 0.5 to 1.0. The safest procedure is of course to use the lowest local fluid velocity in the estimation of the mass and heat transfer coefficients.

Wall effects are not expected to influence the flow distribution in this study, since the ratio of the catalyst bed diameter to the particle diameter was about 60. According to Schwartz and Smith (1953), this is sufficient to neglect wall effects on the flow distribution.

A suitable measure of the effect of concentration and temperature gradients in the film layer is the 'film layer effectiveness factor'. It is defined as the ratio of *a*) the reaction rate at the concentration and temperature existing at the particle surface, and *b*) the reaction rate at the bulk concentration and temperature:

$$\eta_f \equiv \frac{-r_A|_{c_{A,s}, T_s}}{-r_A|_{c_{A,b}, T_b}} \quad (4-18)$$

For an *n*-th order reaction, of which the temperature dependence is modeled with an Arrhenius expression, the film layer effectiveness factor is given by:

$$\eta_f = \left(\frac{c_{A,s}}{c_{A,b}} \right)^n \exp \left(\frac{-E_A}{R_g} \left[\frac{1}{T_s} - \frac{1}{T_b} \right] \right) \quad (4-19)$$

It can be easily derived that this is equivalent to:

$$\eta_f = (1 - Ca_A)^n \exp \left(\frac{E_A}{R_g T_b} \frac{Da_V}{Da_V + 1} \right) \quad (4-20)$$

In this equation, the Carberry number and Damköhler number are defined as:

$$Ca_A \equiv \frac{c_{A,b} - c_{A,s}}{c_{A,b}} ; \quad Da_V \equiv \frac{T_s - T_b}{T_b} \quad (4-21)$$

These numbers can be calculated more or less directly from the observed reaction rate: When an experimental design is being made, one needs to estimate the expected reaction rate, for example using preliminary experiments.

$$Ca_A = \frac{-r_{A,app}}{k_g a_w c_{A,b}} ; \quad Da_V = \frac{-r_{A,app}(-\Delta_r H)}{h a_w T_b} \quad (4-22)$$

Many closely resembling relations are available for estimating mass and heat transfer coefficients pertaining to flow through packed beds, which are needed to evaluate the Carberry and Damköhler numbers of Eq. (4-22). A relation suitable for the conditions in our study, based on correlation of literature data on mass transfer coefficients, was proposed by Beek (1967).

3.4 Criteria for absence of intraparticle gradients

The effect of intraparticle gradients can also be expressed in an effectiveness factor, η_p . η_p is the ratio of *a*) the actual average reaction rate in a catalyst particle, to *b*) the reaction rate at the conditions existing at the particle surface. In Section 3.4.1 intraparticle concentration gradients are discussed for isothermal conditions. In Section 3.4.2 intraparticle concentration gradients in combination with intraparticle temperature gradients are discussed.

3.4.1 Intraparticle concentration gradients for isothermal conditions

The 'effectiveness factor for intraparticle mass transfer' for isothermal conditions is defined as the ratio of the actual average reaction rate in a catalyst particle, to the reaction rate at surface concentrations, under isothermal conditions:

$$\eta_{p,m} \equiv \frac{-r_A|_{C_{A,p}}}{-r_A|_{C_{A,s}}} \quad (4-23)$$

When the kinetics (*i.e.*, both rate expression and parameter values) are known, several methods can be used to estimate $\eta_{p,m}$. For irreversible *n*-th order kinetics, the simplest method is based on the Thiele modulus and a relation between the Thiele modulus and $\eta_{p,m}$ for general particle geometry. This procedure is well-known, and will not be discussed here.

When, for an irreversible n-th order reaction, the rate constant is not known but the order *is* (e.g., from literature data), $\eta_{p,m}$ can be estimated from the observed reaction rate, using the Weisz modulus (Mears, 1971). The Weisz modulus is defined as:

$$\Phi \equiv \eta_{p,m} \phi_m^2; \quad \phi_m \equiv \frac{\frac{V_p}{A_p} -r_A|_{c_{A,s}} \rho_p}{\sqrt{2D_e \int_0^{c_{A,s}} -r_A \rho_p dc_A}} \quad (4-24)$$

From the relations mentioned in the previous paragraph, it follows that an effectiveness factor of 0.975 or higher corresponds to a Weisz modulus of 0.075 or lower. If acceptable estimations can be made of the order of the reaction and the effective pore diffusion coefficient in the particle, the Weisz modulus can be calculated more or less directly from the observed reaction rate:

$$\Phi = \frac{n+1}{2} \frac{(-r_{A,app}) \rho_p}{D_e c_{A,s}} \left(\frac{V_p}{A_p} \right)^2 \quad (4-25)$$

3.4.2 Intraparticle concentration gradients in combination with intraparticle temperature gradients

When heat effects are not negligible, the 'effectiveness factor for intraparticle heat transfer' is defined as:

$$\eta_{p,h} \equiv \frac{-r_A|_{c_{A,p},T_p}}{-r_A|_{c_{A,p},T_s}} \quad (4-26)$$

The definition of $\eta_{p,h}$ shows that it gives the deviation from isothermal behavior, no matter whether or not there are significant intraparticle concentration gradients.

The effect of the intraparticle temperature gradient on $\eta_{p,h}$ depends on the activation energy of the rate determining step. It can be shown that $\eta_{p,h}$ lies between 0.95 and 1.05, when the following criterion is met (Mears, 1971):

$$|\gamma \beta_i| < 0.05n \quad (4-27)$$

In this equation, β_i and γ are defined as:

$$\beta_i \equiv \frac{(T_s - T^*)_{\max}}{T_s}; \quad \gamma \equiv \frac{E_A}{R_g T_s} \quad (4-28)$$

The internal Prater number β_i is defined as the maximum attainable relative temperature difference between the hottest (or coldest) spot in the particle and the particle surface. This maximum temperature difference will only be attained when the

conditions are such that somewhere in the catalyst particle the reactant concentration becomes zero, i.e., when the Thiele modulus is (much) bigger than 1. The internal Prater number can be calculated with:

$$\beta_i = \frac{D_e \Delta_r H c_{A,s}}{\lambda_e T_s} \quad (4-29)$$

It should be noted that this analysis gives an indication of the maximum possible effect; even if the criterion of Equation (4-27) is not met, the particle might be very well practically isothermal if the Thiele modulus is small.

4 Experimental work

4.1 Introduction

In this section the experimental work is described. It includes a description of the experimental designs, the experimental set-up, the experimental procedure, experiments to check for the occurrence of side reactions, and the implementation of the experimental designs. Because two lots of catalyst (\varnothing 1.6 and \varnothing 3.2 mm) were used in the experimental validation of the BSR model, the intrinsic and particle kinetics of both lots had to be found. To keep the discussion concise, however, not all experiments are discussed.

4.2 Creation of the experimental designs

The experimental designs were created according to the guidelines recommended by Box *et al.* (1978) and Box and Draper (1987). Using the software package *ECHIP* (ECHIP, Inc., 1994), G_n -optimal design matrices were created. In the study of the intrinsic kinetics, the independent variables were c_{NO} , c_{O_2} , c_{H_2O} , T and *WHSV*; in the study of the particle kinetics, the *WHSV* was left out as a independent variable, because the former study had confirmed the expectation that the *WHSV* in itself did not influence the observations.

Because the chosen rate expression can be linearized (Eq. (4-2)), it would have been possible to test the independent variables on two levels only. However, to check for curvature of the response surface (*i.e.* $\ln(-r_{NO})$ as a function of $1/T$, $\ln(c_{NO})$, $\ln(c_{O_2})$ and $\ln(c_{H_2O})$), it was decided to test all independent variables on three levels.

Note that also a two-level design with center points would have been possible, which would have required less runs. The three-level design was preferred because the extra runs resulted in increased resolution of the regression model. The experimental design for the intrinsic kinetics contained 82 runs, the design for the apparent kinetics only 25, because it contained one independent variable less.

Whereas the experimental design tells at which values of c_{NO} , c_{O_2} , $c_{\text{H}_2\text{O}}$, T (and $WHSV$) the experiments should be done, it does not tell how much catalyst should be used, how big the particles should be (in the study of the intrinsic kinetics), or which rotor speed should be used. From preliminary experiments, using the criteria mentioned in Section 3.4, it was learnt that intraparticle gradients would be negligible if particles smaller than 500 μm were used. The amount of catalyst to be used and the minimum rotor speed depend on constraints such as:

- the minimum gas velocity through the catalyst bed to eliminate film layer gradients;
 - the minimum recycle ratio and maximum reactant conversion to obtain practically ideal CSTR behavior;
 - the minimum mass flow controller settings that give an accurate flow;
 - the minimum and maximum reactant conversion that allow sufficiently accurate analysis;
 - the minimum catalyst sample size that can be considered representative for the lot.
- Suitable values were calculated using the criteria mentioned in Section 3 in combination with the results of preliminary experiments. Of course these calculations were double-checked afterwards, when all experimental data were available; see Section 5.2.

4.3 Experimental set-up and experimental procedure

A flow sheet of the experimental set-up is given in Figure 4-7. Nitrogen, air, nitric oxide and ammonia were dosed using mass flow controllers. Water was dosed using a peristaltic pump; the water flow rate was checked by means of an electronic balance holding the feed water container. The gases and water were heated, mixed, and either led through the reactor or by-passed.

The experiments were performed in a RotoBerty[®] internal recycle reactor (Berty Reactor Engineers, Ltd., Fogelsville (PA), USA), depicted and described in Figure 4-1. Apart from the graphite bearings, bushings and gaskets, all parts of the reactor in contact with the reactants, are made of 316 stainless steel. The free volume of the reactor is 0.7 ℓ , and the surface area of all metal parts exposed to the reactants is 0.13 m^2 .

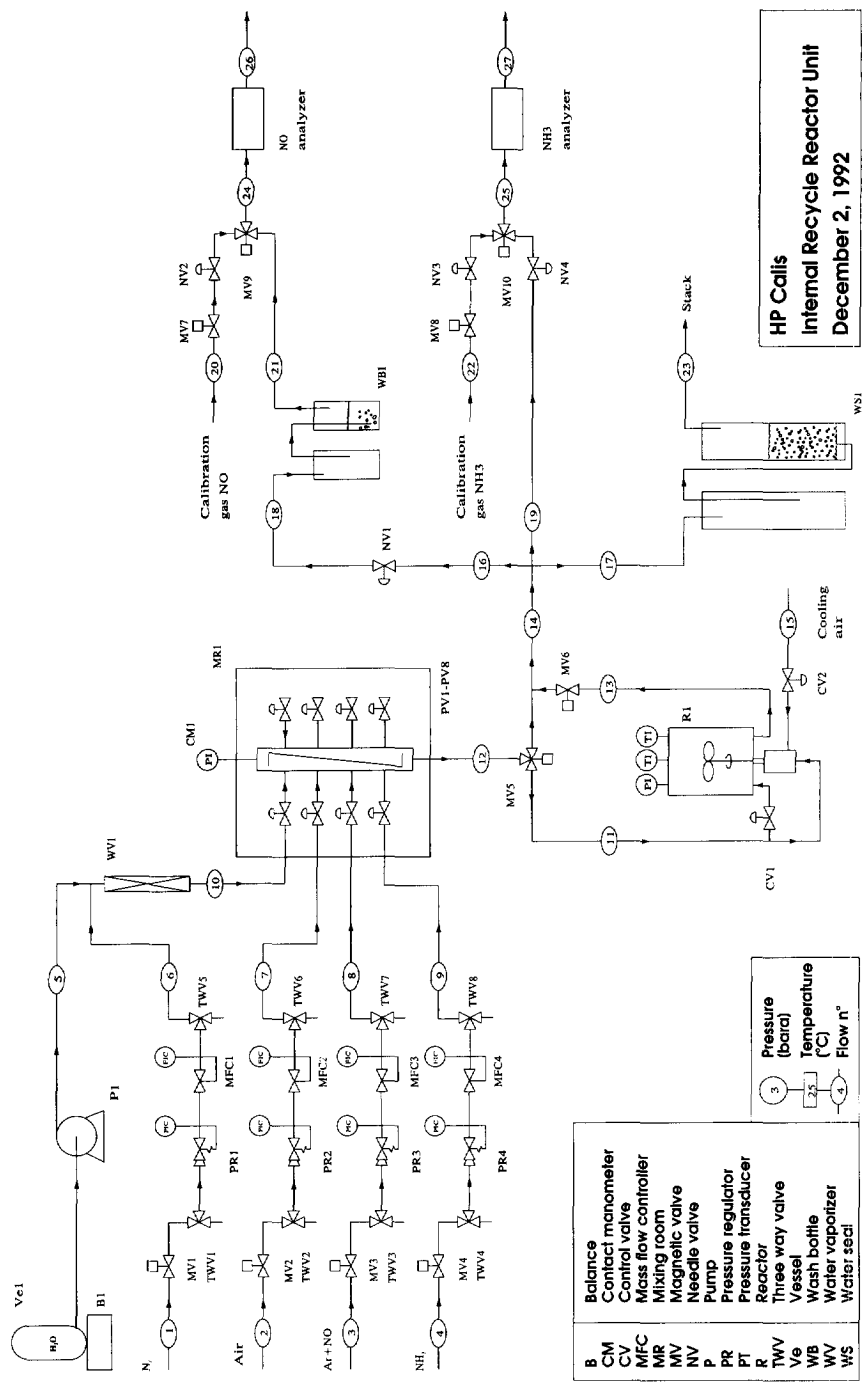


Figure 4-7 Experimental set up.

Constant pressure in the system was obtained by using a water seal, generating a static pressure of 100 mbar gauge. The constant pressure in the system ensured a constant gas flow to the analyzing equipment.

Water and ammonia were stripped from part of the by-pass flow or the product stream, using gas-washbottles filled with 85 mass % phosphoric acid. The gas was analyzed on nitrogen oxides content using a chemiluminescence meter, equipped with a thermal convertor, which allowed analysis of either NO only or the sum of NO and NO₂. Removal of water is necessary because it has a significant quenching effect on the NO-signal in the chemiluminescence equipment. Removal of ammonia is necessary because it is converted to NO and NO₂ in the thermal convertor, leading to erroneous NO_x readings.

The experimental set-up operated fully automatically, controlled by a personal computer. The process control hardware *Transport System* was from Transition Technology Inc. (Amesbury, MA, USA). The software *The FIX* was from Intellution, Inc (Norwood, MA, USA).

Each run consisted of three stages. First, the system was flushed with nitrogen for 20 min. Secondly, the test gas was passed through the reactor for 80 min and the product stream was analyzed on NO_x (i.e., NO + NO₂) content. Thirdly, the reactor was bypassed for 80 min and the test gas was analyzed on NO_x content. The chemiluminescence meter was calibrated (span) twice per experiment, during the first 20 minutes of stages 2 and 3. The experimental cycle is shown graphically in Figure 4-8.

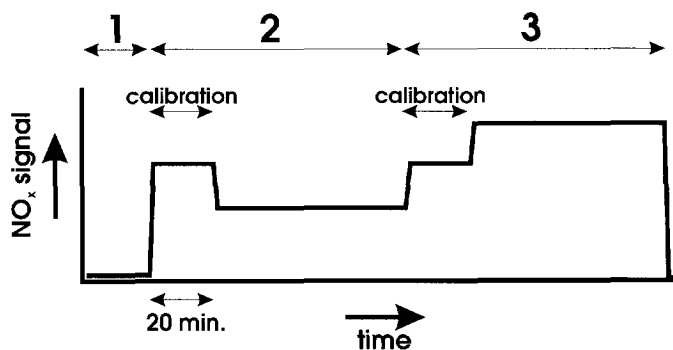


Figure 4-8 Expected signal from the chemiluminescence meter during a run.
Phase 1: Nitrogen flush;
Phase 2: Test gas through reactor; during the first 20 minutes of this phase, not the product stream but a calibration gas is led to the chemiluminescence meter;
Phase 3: Test gas by-passes reactor; during the first 20 minutes of this phase, not the feed gas but a calibration gas is led to the chemiluminescence meter;

The catalyst that was used in this study consisted of 'hollow' cylindrical extrudates. Two lots of catalyst were used, with outer diameters of approximately 1.6 mm and 3.2 mm. The diameter of the hole was approximately 0.4 mm for both lots. For the study of the intrinsic kinetics, samples of the extrudates were powdered and sieved. The sieve fraction from 425 to 500 μm was used.

No catalyst pretreatment prior to use was prescribed by the manufacturer. The only pretreatment consisted of drying the catalyst overnight in air at 80°C, after which the dry weight was measured.

4.4 Checks on the occurrence of side reactions

According to the catalyst manufacturer, at temperatures lower than 350°C the catalyst does not oxidize NH_3 to NO , neither does it decompose NH_3 to N_2 (and H_2O). This was not checked experimentally in this study.

The occurrence of four possible 'side reactions' was investigated experimentally:

- 1) Oxidation of nitric oxide to NO_2 in the reactor, either thermally or catalyzed by the catalyst or the reactor wall.
- 2) Reduction of nitric oxide by ammonia, or oxidation of ammonia to nitric oxide, otherwise than over the catalyst — i.e., thermally, or catalyzed by the steel surface of the reactor, or the graphite bearings of the shaft.
- 3) The production of N_2O by the catalyst.
- 4) The stripping of nitrogen oxides by phosphoric acid in the gas-washbottles during NO_x -analysis.

None of these side reactions turned out to have a significant effect on the observations. For details, reference is made to Boutkan (1992, 1993).

4.5 Implementation of the experimental designs

Including the useable preliminary experiments, a total of 200 experiments were done with the powdered catalyst obtained from the 1.6 mm \varnothing extrudates. Fourteen runs, at different settings, were duplicated to obtain an extra measure of the experimental variance and to allow a test for the 'goodness of fit' of the regression model. Replicated trials were done at the two extreme temperature levels (413 and 453 K). Since the reaction rate at 453 K is about 4 times higher than at 413 K, an indication is obtained whether the variance is an absolute value ($\dots \text{mol}_{\text{NO}}/(\text{kg}_{\text{cat}}\cdot\text{s})$) or whether it is proportional to the response value ($\dots \%$ of $-r_{\text{NO}}$). This distinction is important, because the estimation of the model parameter depends on the correlation between the variance and the response value.

In the study of the particles kinetics, using the original extrudates, a considerable part of the experimental design was replicated. This was done to increase the accuracy of the estimation of the fit parameter in the pore diffusion model.

5 Results and discussion

5.1 Introduction

In Section 5.2 the falsification of the observations, due to insufficient recycle ratio or insufficient mass and heat transfer, is assessed. In Section 5.3 the results of the study of the intrinsic kinetics, using the powdered catalyst, is discussed. It includes the procedure of estimating the kinetic parameters of the regression model, as well as several statistical tests that were used to check the validity of the parameter estimation. In Section 5.4 the results of the study of the particle kinetics, using the original hollow extrudates, is discussed. It includes a discussion of the concentration profile in the holes of the extrudates, a description of the semi-analytical method that was used to predict the catalyst particle effectiveness factor, and a description of the procedure that was followed to estimate the fit parameter Ω in the pore diffusion model.

5.2 Checks on falsification of the observations

recycle ratio

For each kinetic trial, the gas velocity through the catalyst bed and the recycle ratio R were estimated, using the relations presented in Section 3.2.1 in combination with experimental calibration curves of the gas velocity through the catalyst beds as a function of the rotor speed. Based on the estimated recycle ratio and the other experimental data, the rate falsification ratio ρ and the order falsification ratio ν were calculated, both for the reverse and forward flow configuration.

Runs for which $|1-\rho|$ is bigger than 0.05 and/or $|1-\nu|$ is bigger than 0.15, were rejected. This was the case for 11 runs out of 200.

film layer gradients

Using the estimated gas velocity through the catalyst bed to estimate mass and heat transfer coefficients, the effectiveness factors for mass and heat transfer in the film layer were calculated for all trials. For all experiments in our study, $|1-\eta_f|$ was

smaller than 0.015, allowing negligence of concentration and temperature gradients in the film layer.

intraparticle gradients

Obviously this paragraph only pertains to the experiments with the powdered catalyst. Using the criteria of Section 3.4, it was verified that the catalyst particles can be considered to be isothermal in the range of conditions studied here.

To check the absence of intraparticle concentration gradients, the experimental Weisz modulus was calculated for all trials, according to Equation (4-25). For all experiments with the powdered catalyst, the Weisz modulus was lower than 0.058, corresponding to an effectiveness factor of 0.980. The average value of the Weisz modulus is 0.019, corresponding to an effectiveness factor of more than 0.993.

From these checks it was concluded that the observations were not significantly falsified by insufficient recycle ratio, insufficient film layer mass and heat transfer, or (for the powdered catalyst) insufficient intraparticle mass and heat transfer. Consequently, for the powdered catalyst the true intrinsic kinetics were observed, and for the extrudates the true particle kinetics were observed.

5.3 Modeling of the intrinsic kinetics

In this section the estimation of the parameters in the rate expression (Eq. (4-2)) is discussed; because of space limitations, only the results obtained with the powdered 1.6 mm \varnothing extrudates are reported.

In the regression procedure it is important to weigh all data points according to their respective variances. Therefore in Section 5.3.1 first the variance of the data is discussed, based on the replicated runs. To obtain a small confidence region of the estimated parameters, it is useful to transform the data; this topic is touched upon in Section 5.3.2. The parameter estimation is discussed in Section 5.3.3; in this section also the normality of the residuals is checked, without which the 'goodness of fit' test discussed in Section 5.3.4 would not be valid. Using the conclusion on model adequacy, deactivation of the catalyst and difference in activity between the catalyst samples are discussed in Sections 5.3.5 and 5.3.6. Finally, the accuracy of reaction rate predictions is discussed in Section 5.3.7.

5.3.1 Estimation of the experimental variance

As was mentioned in Section 4.5, with the powdered catalyst 14 runs were duplicated, yielding 14 pairs of 'twin' runs. For each pair, the observations were corrected for measured variations (between the two runs) in the settings of the independent variables. After this the variance of $\ln(-r_{NO})$ was found to be $8.0 \cdot 10^{-3}$, approximately independent of the value of the reaction rate. This variance corresponds to a standard deviation of $\ln(-r_{NO})$ of $8.9 \cdot 10^{-2}$, which means that the standard deviation of $-r_{NO}$ equals

8.9%. This might seem a rather high value; however, it should be noted that the runs of every pair of duplicates were usually done with different catalyst samples, which implies that between the two runs the reactor has been opened to replace the catalyst. Also the complete reactor has been disassembled and reassembled between many of the two runs of a pair. Consequently it can be expected that the short term variance of trials with the same sample of catalyst, is much smaller. However, this short term variance is obviously not the best measure to assess the adequacy of the regression model.

5.3.2 Correlation of parameters

From the linearized rate expression (Eq. (4-2)) it can be seen (with a little knowledge of statistics) that the estimated parameter $-E_A/R_g$ will be strongly correlated with the estimated parameter $\ln(k_0)$, unless the values of $1/T$ in the total set of runs are evenly distributed around 0. Obviously, the latter requirement will not be met. The resulting correlation implies that a small change in the estimation of $-E_A/R_g$ results in a large change in the estimation of $\ln(k_0)$, which in turn results in an inflated confidence region of $\ln(k_0)$.

In the same way, the estimated parameters n , m and p will be strongly correlated with $\ln(k_0)$ if the values of $\ln(c_{\text{NO}})$, $\ln(c_{\text{O}_2})$ or $\ln(c_{\text{H}_2\text{O}})$, respectively, in the total set of runs, are not evenly distributed around 0.

Such parameter correlation was circumvented, and a smaller confidence region of $\ln(k_0)$ was thus obtained, by transforming the values of $1/T$, $\ln(c_{\text{NO}})$, $\ln(c_{\text{O}_2})$ and $\ln(c_{\text{H}_2\text{O}})$, respectively. This transformation, which is commonly used by statisticians and is therefore not discussed here, comes down to translating the values of $1/T$, $\ln(c_{\text{NO}})$, $\ln(c_{\text{O}_2})$ and $\ln(c_{\text{H}_2\text{O}})$ by their respective averages over the total set of runs; the transformed values then are usually quite evenly distributed around 0. The parameter estimation described in the next section was done with data transformed in this way.

5.3.3 Parameter estimation and normality of the residues

The software used for the parameter estimation was *Pastifit*, a general non-linear regression program (Verheijen, 1994). It can be used (a.o.) to estimate parameters, to produce residuals plots and residuals histograms, and to calculate variance-covariance and correlation matrices.

Regression was done first for the whole set of data, covering the complete temperature range from 413 K to 453 K. Using the obtained estimation of the activation energy, regression was done separately for the three subsets of data at 413, 433 and 453 K. Consequently, four regression models were obtained. Runs with a residual bigger than $t_{0.95}$ times the standard deviation were considered to be outliers, and were removed from the data set. This reduced the total number of useable runs from 189 to 175. A parity plot of the regression model covering 413-453 K is presented in Fig. 4-9.

In Table 4-2 the estimated parameters are given \pm their standard deviation. To obtain the 95% confidence interval, the standard deviation should be multiplied by the listed

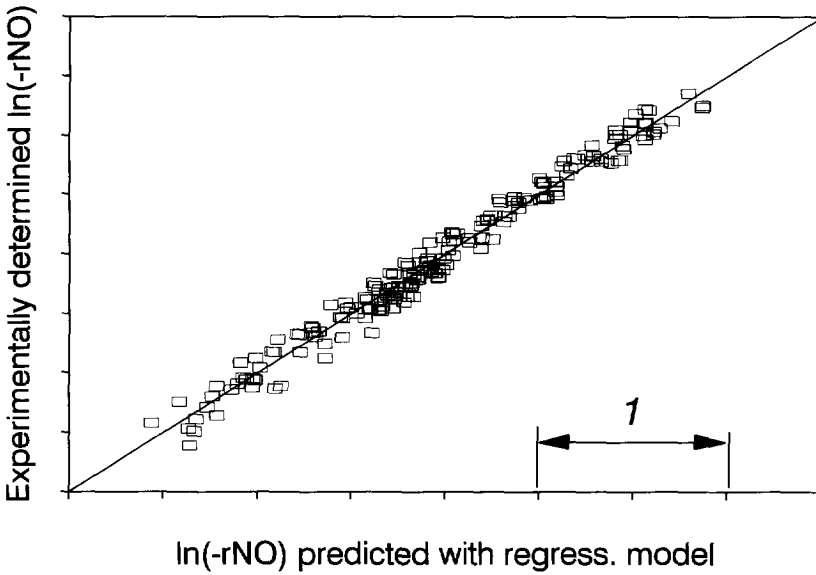


Figure 4-9 Parity plot of the kinetic experiments with the powdered catalyst.

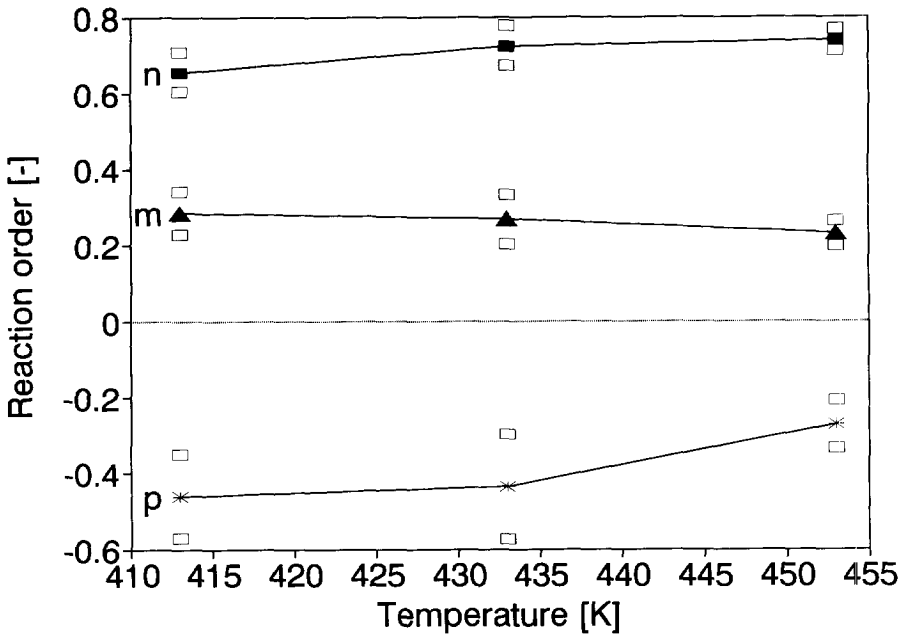


Figure 4-10 Parameter values of the regression models vs the temperature.

t -factor. The activation energy is *ca.* $6 \cdot 10^4$ J/mol.

Table 4-2 Estimated intrinsic kinetic parameters \pm standard deviation. On request of the catalyst manufacturer, the numeric values of k_0 are not listed. $t_{0.95}$ value: 2.0.

T [K]	k_0 [$10^3 \text{ mol}_{\text{NO}}/(\text{kg}_{\text{cat}} \cdot \text{s})$]	n	m	p
413-453	$k_{0,413-453} \pm 0.8\%$	0.71 ± 0.01	0.26 ± 0.01	-0.36 ± 0.03
413	$k_{0,413} \pm 1.7\%$	0.66 ± 0.03	0.29 ± 0.03	-0.46 ± 0.05
433	$k_{0,433} \pm 1.3\%$	0.73 ± 0.03	0.27 ± 0.03	-0.44 ± 0.07
453	$k_{0,453} \pm 1.1\%$	0.74 ± 0.01	0.23 ± 0.02	-0.27 ± 0.03

The parameter values listed in Table 4-2 are presented graphically as a function of temperature in Figure 4-10. From the overlap of the 95% confidence intervals it follows that the significance of temperature dependence of the parameters is very small. It is also seen that the model covering the complete temperature range does not contradict with the three fixed-temperature models.

Residuals plots indicated random distributions of the residuals as a function of all variables. This was supported by straight lines in the cumulative residual histograms. From the so-called Cramér-Von Mises test for normality (Van Soest, 1985), it can be concluded that the residuals are normally distributed, with significance levels larger than 10%, 10%, 5% and 1%, for the models covering all temperatures, 413 K, 433 K and 453 K, respectively. These results allow the use of the F test for adequacy of the regression models, described in Section 5.3.4.

5.3.4 F test for adequacy of the model

From the so-called F test for goodness of fit (Box *et al.*), it was concluded that both the model covering all temperatures and the three models covering one of the three temperature levels, describe the observations adequately. Though the significance level of the regression model covering all temperatures (0.18) is much lower than those of the fixed-temperature

Table 4-3 Variance of experiments.

T [K]	$SS_{res}/(n-p)$ [-]	st.dev. of $\ln(-r_{\text{NO}})$ [-]	st.dev. of $-r_{\text{NO}}$ [%]
413	$1.39 \cdot 10^{-2}$	$1.12 \cdot 10^{-1}$	11
433	$8.67 \cdot 10^{-2}$	$9.47 \cdot 10^{-2}$	9.5
453	$6.86 \cdot 10^{-3}$	$8.28 \cdot 10^{-2}$	8.3
413-453	$1.21 \cdot 10^{-2}$	$1.10 \cdot 10^{-1}$	11

models (0.55, 0.43 and 0.28 for the models at 413 K, 433 K and 453 K, respectively), it is still very high compared to the often used critical value of 0.05.

From the fact that the models are found to be adequate it follows that the residual sum of squares divided by the number of degrees of freedom, is an estimation of the variance of the observations. The estimates that are thus obtained are listed in Table 4-3, together with the standard deviation in $\ln(-r_{\text{NO}})$ and in $-r_{\text{NO}}$. These values compare well to the estimates based on replicated runs (8.9%), supporting the assumption that the replicates give a true reflection of the experimental variance.

5.3.5 Check for deactivation of the catalyst

Because the regression models were found to be adequate, they can be used to check for deactivation of the catalyst during the experiments. Indeed, if deactivation (or activation) would be significant, it would show as a significant trend in plots of residuals as a function of time. In this study, apparent trends seem to be insignificant when compared with the scatter of the points. Without any further analysis it was concluded that there is no significant deactivation (or activation) of the catalyst.

5.3.6 Check for activity differences between catalyst samples

In the study with the powdered catalyst, four different samples from the same stock of powdered catalyst were used. Significant differences in activity of the four catalyst samples would show up as significant differences between the four averages of the residuals. Differences up to 12% were seen, but the 95% confidence interval of each value included 0. Even though the averages were thus found to be statistically insignificant, it is estimated that in the present study insufficient attention for proper sampling may have lead to activity differences of *ca.* 10% between the various samples. This is a quite serious error, because the experiments with the extrudates were done with only one sample of each lot. As a result the experimentally determined effectiveness factors of the extrudates might be systematically off by 10%. Fortunately, however, a careful inspection of the residuals plots of the effectiveness factor as a function of the Thiele modulus would reveal such a systematic error.

5.3.7 Accuracy of the model predictions

The variance of the reaction rate prediction calculated with the regression model, depends on the variance, number and settings of the experiments on which the regression model is based, and on the conditions for which the reaction rate is predicted. Using the variance of the prediction, a 95% confidence interval can be calculated; the chance that the calculated confidence interval includes the mean response of new runs at the specified conditions, is 95%.

For several cross-sections of the studied variable space, plots were made of the variance of the expected response as a function of the conditions. From these plots it was estimated that for the model covering all temperatures, the maximum variance within the range of conditions tested in this study is about $0.9 \cdot 10^{-3}$, corresponding to a standard deviation of 3%. For the three fixed-temperature models the maximum

variance is estimated to be about $2.5 \cdot 10^{-3}$, corresponding to a standard deviation of 5%. The higher variance of the fixed-temperature is caused by the smaller number of trials upon which the models are based, in comparison with the all-temperature model. The variance of a new observation is the sum of the variance of the expected response and the trial-to-trial variance discussed in Section 5.3.1. The latter one was estimated to be $8 \cdot 10^{-3}$, yielding an estimated maximum variance of one new observation of about 10^{-2} , corresponding to a standard deviation of about 10%.

5.4 Modeling of the particle kinetics

In order to translate intrinsic kinetics into particle kinetics, one should consider possible concentration and temperature gradients in the particles. Due to the low concentrations that were used in the present study, temperature gradients could safely be neglected. Concentration gradients, however, were not negligible, which resulted in effectiveness factors smaller than unity for the extrudates.

One way to predict the effectiveness factor of a catalyst particle on the basis of the intrinsic kinetics and the particle geometry and characteristics, is to numerically solve the differential equations that arise from the mole balance(s) over an element of the particle. However, in many cases sufficiently accurate estimates can be obtained using less time-consuming semi-analytical methods, like the well-known method based on the Thiele modulus:

$$\phi_m \equiv \frac{\frac{V_p}{A_p} \mathfrak{R}_A|_{c_{A,s}}}{\sqrt{2D_e \int_0^{c_{A,s}} \mathfrak{R}_A dc_A}}; \quad \hat{\eta}_{p,m} = \frac{\tanh(\phi_m)}{\phi_m} \quad (4-30)$$

The hat ($\hat{\ }$) over $\eta_{p,m}$ indicates that it is an approximation.

Literature surveys of proposed semi-analytical, approximative methods are given by Wijngaarden and Westerterp (1994) and IJselendoorn (1994). All methods have in common that the reactant concentration at the surface of the particle, $c_{A,s}$, is assumed to be constant, *i.e.* independent of the location on the particle surface. Unfortunately this assumption might not always be justified in the case of the hollow extrudates used in the present study: it is conceivable that during the kinetic experiments in the recycle reactor, the mass transfer in the axial direction in the hole of the extrudates is relatively slow (compared to the reaction rate). In that case there is an axial concentration gradient in the hole, and in $c_{A,s}$ in the hole is lower than at the outer surface of the particle. This results in an effectiveness factor that is lower than predicted by the semi-analytical methods. The use of such methods in the present study of the particle kinetics is therefore only justified if it can be made plausible that

the assumption of constant surface concentration results in only small errors in the predicted particle effectiveness factors.

It will be shown in Section 5.4.1 that for the experiments with the extrudates in the RotoBerty recycle reactor, this assumption is indeed plausible, and that the use of semi-analytical methods to predict the effectiveness factor is therefore justified. In Section 5.4.2 the semi-analytical method will be discussed that was used in the present study. A critical parameter in the prediction of the effectiveness factor is the effective pore diffusion coefficient. In Section 5.4.3 the estimation of the pore diffusion fit parameter Ω , based on the experimentally observed effectiveness factors, is discussed. To keep the discussion concise, only the results obtained with the 3.2 mm \varnothing extrudates are reported. These are most interesting, because of the lower effectiveness factors than the 1.6 mm \varnothing extrudates.

5.4.1 Concentration gradients in the axial hole of the extrudates

To assess the error made in the calculation of the effectiveness factor of the hollow extrudates when a constant surface concentration is assumed, the effectiveness factors in four situations were calculated from numerical solutions of the partial differential equations (PDE's) that arise from mole balances across infinitesimally small volume elements of the hole and the catalyst material. As shown in Fig. 4-11, two domains can be identified in this problem, representing the axial hole and the catalyst material.

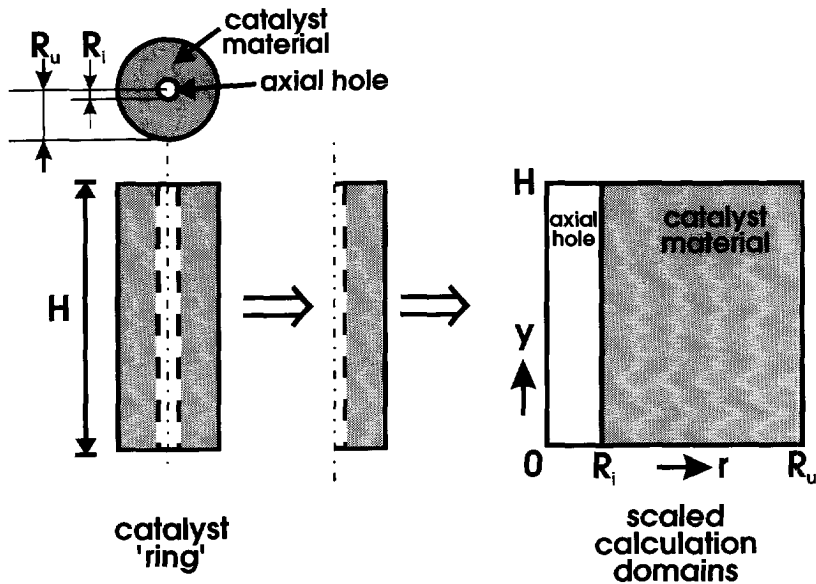


Figure 4-11 Mathematical domains in a hollow extrudate.

The four investigated situations are:

- a** There is no transport of reactants at all in the hole. Obviously this situation will not exist with separate particles charged in the recycle reactor; nevertheless this situation interesting, because it may arise in the BSR, if the hole is completely occupied by the metal wire on which the bead is stringed.
- b** The transport of reactants in the hole is only due to molecular diffusion. This situation might arise if in the recycle reactor a catalyst particle lies perfectly horizontally, *i.e.* perpendicular to the pressure gradient generated by the rotor.
- c** The transport of reactants in the hole is due to convection (and molecular diffusion). This situation is most likely to arise in the recycle reactor, because the pressure gradient across the particle (in the direction of the hole) causes convection in the hole.
- d** The transport of reactants in the hole is infinitely fast. This would be the preferred situation in the recycle reactor, because then a constant surface concentration could be assumed.

Equations for the catalyst domain

In all four situations the reactant concentration in the catalyst domain is described (in steady state) by the following PDE:

$$\frac{1}{r} \frac{\partial}{\partial r} \left[D_e r \frac{\partial c_A}{\partial r} \right] + \frac{\partial}{\partial y} \left[D_e \frac{\partial c_A}{\partial y} \right] - \mathfrak{R}_A = 0 \quad (4-31)$$

On the north, east, and south boundaries of the catalyst domain (see Fig. 4-11), the boundary condition is that the concentration equals a given, constant surface concentration $c_{A,s}$. On the west boundary of the catalyst domain the boundary conditions are different for the four situations. In situation **a** the condition is that there is no flux through the west boundary, so that the radial concentration gradient should equal zero. In situations **b** and **c** the flux through the west boundary couples the catalyst domain with the hole domain:

$$D_e \frac{\partial c_A}{\partial r} \Big|_{\text{catalyst domain}} = D_{free} \frac{\partial c_A}{\partial r} \Big|_{\text{hole domain}} \quad (4-32)$$

In situation **d** the west boundary condition is that the concentration equals $c_{A,s}$.

Equations for the hole domain

In situation **a** the concentration in the hole is not defined, in situation **d** it is assumed to equal $c_{A,s}$ everywhere. In situations **b** and **c** it is described (in steady state) by the

following PDE, albeit that in situation **b** the gas velocity in the axial direction (u_y) equals zero:

$$\frac{1}{r} \frac{\partial}{\partial r} \left[D_{free} r \frac{\partial c_A}{\partial r} \right] + \frac{\partial}{\partial y} \left[D_{free} \frac{\partial c_A}{\partial y} \right] - u_y \frac{\partial c_A}{\partial y} = 0 \quad (4-33)$$

Out of convenience, the gas velocity in the hole in situation **c** was assumed to be uniform. On the north and south boundaries of the hole, the boundary condition is assumed to be that the concentration equals $c_{A,s}$. On the east boundary the condition is given by Eq. (4-32); the west boundary is the axis of the hole, so that because of symmetry the radial concentration gradient should be zero.

When the PDE's of Eq. (4-31) and (4-33) are made dimensionless, it is found that the situation is characterized by the following dimensionless groups:

$$R_u^2 \frac{\mathfrak{R}_A |_{c_{A,s}}}{D_e c_{A,s}} \equiv \phi^2; \quad \frac{u_y H}{D_{free}} \equiv Pe \quad (4-34)$$

$$\frac{D_{free}}{D_e}; \quad \frac{R_i}{R_u} \equiv \ell; \quad \frac{H}{R_u} \equiv \lambda$$

The PDE's were solved using the Finite Element program *SPDE* (SPDE Inc., 1992). From the concentration field, the effectiveness factor was calculated by numerically calculating the volume-averaged reaction rate in the catalyst domain and comparing it to the reaction rate at $c_A = c_{A,s}$ (Takács, 1994). The error of the effectiveness factor thus obtained was less than 0.1%, which was checked by comparing *SPDE* solutions for simple geometries and first order reactions with analytical solutions.

To give an impression of the results, contour plots of the concentration in the catalyst domain and (for situations **b** and **c**) the hole are presented in Fig. 4-12; the plots pertain to a first order reaction and the following, more or less arbitrarily chosen, values of the dimensionless groups: $\phi^2 = 5$, $Pe = 5$, $D_{free}/D_e = 100$, $\ell = 0.2$ and $\lambda = 5$. In the plots the value of the concentration at each contour line is not printed, as it is trivial that the concentration drops monotonously from the boundaries toward the minimum (indicated by an asterisk), and that the effectiveness factor increases going from a to b to c to d.

Unfortunately the actual value of Pe of the hollow extrudates during the kinetic experiments cannot be calculated directly, because the gas velocity in the holes of the particles is unknown. However, it can be estimated using the performance data of the recycle reactor rotor (which allow calculation of the pressure drop across the catalyst bed), and assuming developed, laminar flow in the holes of the extrudates. The axial gas velocity in the holes is then expected to be $ca. 12.5 \cos(\alpha)$ [m/s], where α is the angle between the longitudinal axis of the particle and the vertical direction (which is

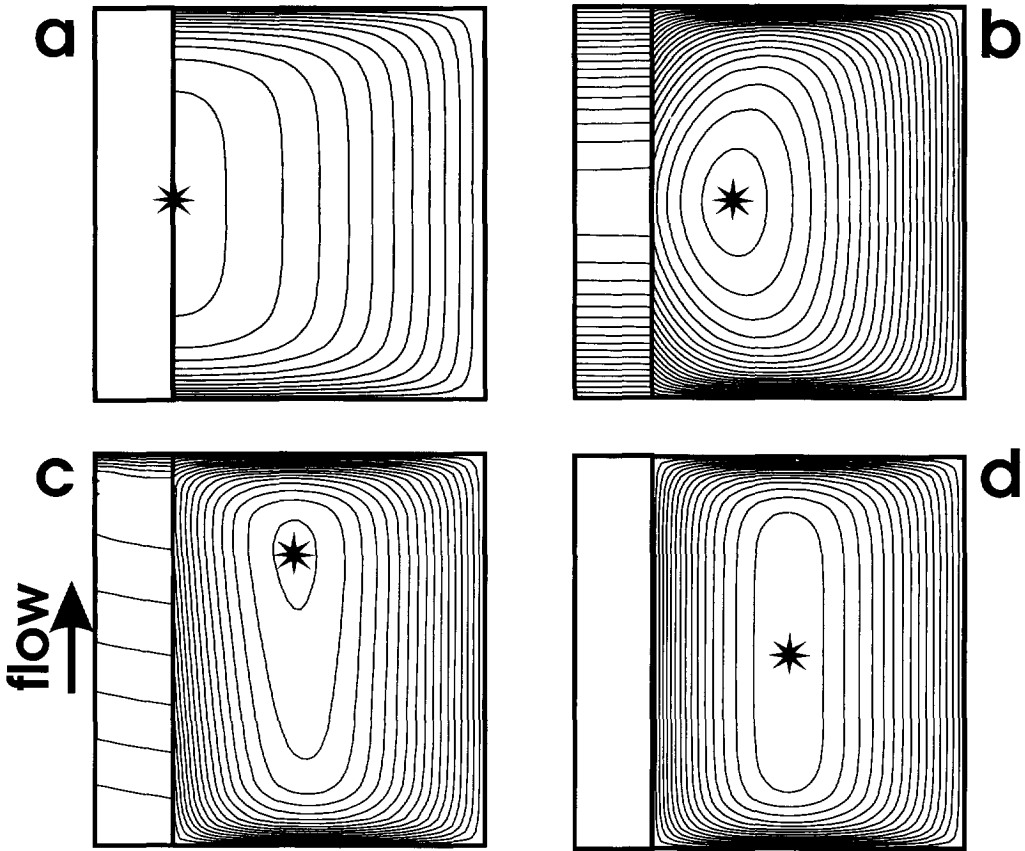


Figure 4-12 Concentration contour plots in a hollow extrudate, for four different situations in the hole.

the direction of the main flow through the catalyst bed). For practically all particles in the catalyst bed α is bigger than 85° , so that a safe minimum value of u_p is 1 m/s.

In Table 4-4 the relative deviations are listed of the effectiveness factors of situations **a**, **b** and **c** (the latter for $\alpha = 85^\circ$), from the effectiveness factor of situation **d**. The values pertain to the kinetic experiments in the recycle reactor under worst case conditions, *i.e.* at the highest temperature and oxygen concentration, and the lowest water and nitric oxide bulk concentration. It is seen that when a constant surface concentration in the holes is assumed for the experiments in the recycle reactor (*i.e.* situation **c**), the maximum error in the effectiveness factor is only 1.6%. Realizing that in the catalyst bed of the recycle reactor for most particles α is smaller than 85° , it is concluded that the error is negligible. This conclusion justifies the use of semi-analytical methods that assume a constant surface concentration, to predict the

effectiveness factor in the case of the kinetic experiments with the hollow extrudates in the recycle reactor.

It is also seen from Table 4-4 that if the hollow extrudates are strung on a tightly fitting impermeable wire in the BSR (*i.e.* situation a), this assumption may lead to errors as big as 15%. Consequently, special attention should be given to this situation; this will be done in Chapter 5 (*Experimental validation of the mathematical BSR model*).

Table 4-4 Relative deviations of the effectiveness factors of situations a, b, and c.

Particle diameter [mm]	$\eta_p(\mathbf{a})/\eta_p(\mathbf{d}) - 1$ [-]	$\eta_p(\mathbf{b})/\eta_p(\mathbf{d}) - 1$ [-]	$\eta_p(\mathbf{c})/\eta_p(\mathbf{d}) - 1$ [-]
1.6	-0.15	-0.13	-0.016
3.2	-0.13	-0.12	-0.0059

5.4.2 Approximation of the effectiveness factor using the Aris method

Wijngaarden and Westerterp (1994) presented an elegant new semi-analytical method to approximate the effectiveness factor for general catalyst geometry and kinetics (assuming a constant surface concentration), based on two dimensionless numbers called Aris numbers. This method, called 'Aris method' in this thesis, was used to model the effectiveness factor of the extrudates used in the present study, and will therefore be briefly discussed.

The 'zeroth Aris number' An_0 is defined as the number which becomes equivalent to $1/\eta_p^2$ when the effectiveness factor η_p goes to zero; obviously, this number is most important at low effectiveness factors. For simple reactions, An_0 turns out to be equivalent to the square of the Thiele modulus ϕ_m (see Eq. (4-30)). The 'first Aris number' An_1 is defined as the number which becomes equivalent to $1-\eta_p^2$ when An_0 goes to zero; this number is most important at high effectiveness factors. For simple reactions, An_1 can be expressed as:

$$An_1 = \left(\frac{V_p}{A_p} \right)^2 \frac{\Gamma}{D_e} \frac{\partial \mathfrak{R}_A}{\partial c_A} \Big|_{c_{A,s}} \quad (4-35)$$

The parameter Γ is a geometry factor that is independent of the particle size and the kinetics; expressions for Γ for various geometries can be derived from the definition of An_1 . Values of Γ are claimed to always lie in the range of 2/3 to 6/5; the extremes pertain to an infinitely long slab and a sphere, respectively.

After calculation of the Aris numbers, the effectiveness factor can be estimated with the following implicit relation:

$$\hat{\eta}_p = \frac{1}{\sqrt{1 + \hat{\eta}_p An_1 + (1 - \hat{\eta}_p) An_0}} \quad (4-36)$$

The usefulness of this method for the present study depends on the availability of values for the geometry factor of the hollow, cylindrical extrudates, and the error in the effectiveness factor of such particles that is made with this method, for the case of a reaction order of *ca.* 0.7.

For so-called ring-shaped catalysts particles, which the hollow extrudates used in the present study are, Wijngaarden and Westerterp present an analytical expression for Γ , as well as a graphical correlation. The parameters that tie down the geometry of a ring-shaped particle are ℓ and λ , defined in Eq. (4-34). For the 1.2 mm \emptyset extrudates Γ equals 0.76, for the 3.2 mm \emptyset extrudates it equals 0.9.

The authors claim that for first order kinetics, the effectiveness factor of ring-shaped particles can be estimated with Eq. (4-36) with a maximum error of 4.4%. The actual error depends on η_p , ℓ and λ . For reaction orders lower than one, as in the present study, the maximum error is somewhat higher; for an order of 0.7, the maximum error is estimated to be 5.7%. However, for the geometry of the hollow extrudates used in the present study, and the tested conditions, the error is estimated to be only *ca.* 1%. This estimate was obtained by comparing the effectiveness factors obtained with the Aris method, to the value obtained from the numerical solution of Eq. (4-31) (situation **d**). The error of *ca.* 1% made by using the Aris method is considerably smaller than the error in the experimentally determined effectiveness factors, which is a combination of the inaccuracy of the intrinsic kinetic model (1 to 3%) and the standard deviation of the kinetic experiments with the extrudates (*ca.* 5%). This justifies use of the Aris method instead of the more precise, but also much more time-consuming, numerical method using *SPDE*.

5.4.3 Estimation of the pore diffusion fit parameter Ω

For each experiment with the extrudates in the recycle reactor, the apparent reaction rate was divided by the reaction rate predicted with the intrinsic kinetic model pertaining to the same catalyst lot (*i.e.* either the 1.6 mm \emptyset or the 3.2 mm \emptyset extrudates). This yielded an experimentally determined effectiveness factor for each run. The standard deviation of these factors was estimated on the basis of replicated experiments, after correction for measured differences in the conditions. The standard deviation was estimated to be 4%; the $t_{0.95}$ value is 2.1. The variance appeared to be proportional to the effectiveness factor. After removal of outliers, 42 experimentally determined effectiveness factors were left over for the 3.2 mm \emptyset extrudates.

A critical parameter in the prediction of the effectiveness factor is the effective pore diffusion coefficient. As was mentioned in Section 2, a simple pore diffusion model was used (see Eq. (4-3)), in which the catalyst characteristic ratio of ε and τ was

replaced by a single fit parameter Ω . Using a least-squares regression method (*PastiFit*, Verheijen, 1994), the value of Ω was optimized with respect to the experimentally determined effectiveness factors. In the optimization procedure the regression values of the effectiveness factor were calculated with the Aris method discussed in the previous section.

The value of Ω was thus found to be 0.66 ± 0.02 ($t_{0.95}$ value: 2.0). This value seems to be plausible, when it is compared to the range of values that might be expected for the catalyst-characteristic ratio ε/τ : values of ε are typically in the range of 0.55-0.75, whereas values of τ ranging from 1 (!) to 6 have been reported in the literature. Furthermore it must be kept in mind that the pore diffusion model is very simple; for example, it only takes into account one median pore radius, even though the pore radius distribution and possible anisotropy (especially with extruded catalysts) are expected to have a considerable influence on the pore diffusion characteristics.

Careful inspection of the residuals plots of the effectiveness factors as a function of all independent and dependent variables revealed no systematic trends. A parity plot of the results is presented in Fig. 4-13. An F -test for goodness of fit showed that the fitted pore diffusion model, in combination with the Aris method, adequately describes the experimentally determined effectiveness factors (significance level 9%).

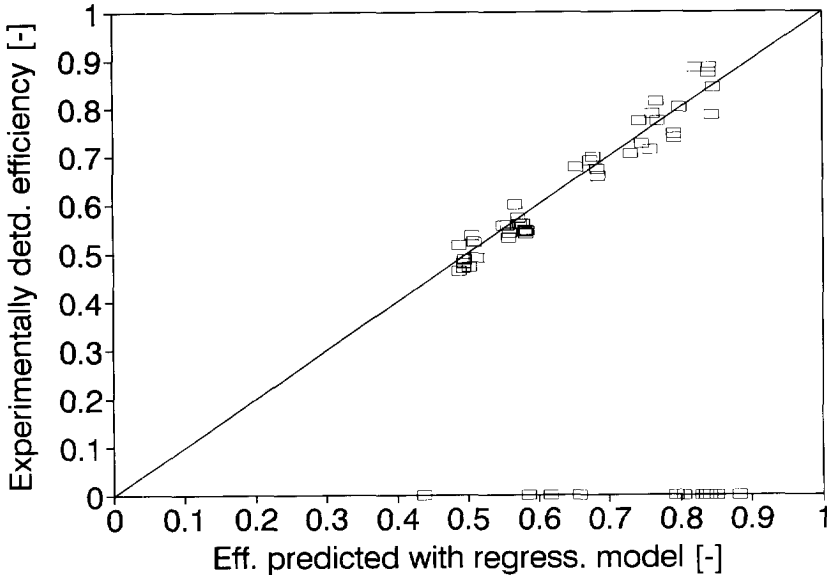


Figure 4-13 Parity plot of the effectiveness factor of the 3.2 mm \varnothing extrudates.

6 Conclusions

The SCR of NO with excess NH₃ over a commercial deNO_x catalyst, in the presence of high concentrations of O₂ and H₂O and between 140-180°C, is a suitable test reaction to validate the reactor model of the Bead String Reactor. This is because side reactions are insignificant and deactivation has not been observed on a time scale of months.

The kinetics of the test reaction between 140 and 180°C can be described adequately with a power law rate expression with powers in the NO, O₂ and H₂O concentrations. For this purpose a power law rate expression is preferred over rate expressions based on mechanistic models. The latter are based on so many simplifying assumptions, that it is hardly conceivable that they allow more accurate extrapolation outside the experimentally investigated range of conditions than the power law expression.

The standard deviation of the experiments with the powdered catalyst is about 10%. This value is acceptable, taking into account that the experiments have been performed in a time span of several months, that the reactor has been disassembled and reassembled in the course of the experiments, and that no special attention was given to proper catalyst sampling. Thanks to the rather high number of (successful) trials, 175, the standard deviation of the reaction rate predictions made by the regression model covering all temperatures, is smaller than 3% in the complete experimental range of conditions. This is sufficiently small for the purpose of this study.

For the tested reaction and catalyst geometry, the error in the prediction of the effectiveness factor due to the use of the Aris method, is at least five times smaller than the experimental error. This justifies the use of the simple Aris method instead of time-consuming numerical solution of the balance equations.

The particle kinetics can be adequately predicted from the intrinsic kinetic model, using the extra fit parameter Ω in the simple pore diffusion model. Because the value of the fit parameter agrees reasonably well with the range of values expected from physical considerations, the statement that the effectiveness factor modeling is physically sound, cannot be rejected.

Acknowledgements

Arie de Niet, Marco Eykelenboom, Ben Leung, Else Boutkan, Henk IJselendoren, Åsa Granquist and Kálmán Takács are gratefully acknowledged for their substantial contribution to the work reported in this chapter.

Notation

A_p	external catalyst particle surface area	$[\text{m}^2_{\text{part}}]$
An_0, An_1	zeroth and first Aris number	[-]
a_w	specific external surface area of the catalyst	$[\text{m}^2_{\text{part}}/\text{kg}_{\text{cat}}]$
c	rotor proportionality constant	$[(\text{Pa} \cdot \text{min}^2 \cdot \text{m}^3_{\text{fluid}} \cdot \text{s}^2)/(\text{kg}_{\text{fluid}} \cdot \text{m})]$
c_A	outlet concentration of reactant A	$[\text{mol}_A/\text{m}^3_{\text{fluid}}]$
Ca_A	Carberry number for reactant A	[-]
$c_{A,b}$	concentration of A in the bulk phase	$[\text{mol}_A/\text{m}^3_{\text{fluid}}]$
$c_{A,p}$	concentration of A in the catalyst particle	$[\text{mol}_A/\text{m}^3_{\text{fluid}}]$
$c_{A,s}$	concentration of A at the external catalyst particle surface	$[\text{mol}_A/\text{m}^3_{\text{fluid}}]$
C_p	fluid heat capacity	$[\text{J}/(\text{kg}_{\text{fluid}} \cdot \text{K})]$
Da_v	Fifth Damköhler number	[-]
D_e	effective pore diffusion constant	$[\text{m}^2/\text{s}]$
D_{free}	free molecular diffusion constant	$[\text{m}^2/\text{s}]$
D_{Kn}	Knudsen diffusion constant	$[\text{m}^2/\text{s}]$
d_{eq}	equivalent particle diameter	$[\text{m}_p]$
d_p	particle diameter	$[\text{m}_{\text{part}}]$
E_A	activation energy	$[\text{J}/(\text{mol} \cdot \text{K})]$
g	gravitational constant (9.81)	$[\text{m}/\text{s}^2]$
h	heat transfer coefficient	$[\text{W}/(\text{m}^2 \cdot \text{K})]$
H	height (length) of a catalyst particle	$[\text{m}]$
k	n-th order rate constant	$[\text{mol}_A/(\text{kg}_{\text{cat}} \cdot \text{s})/(\text{mol}_A/\text{m}^3_{\text{fluid}})^n]$
k_g	mass transfer coefficient	$[\text{m}/\text{s}]$
k_g	mass transfer coefficient	$[\text{m}/\text{s}]$
k_{inlet}	reaction rate constant at inlet temperature of catalyst bed	[..]
k_{outlet}	reaction rate constant at outlet temperature of catalyst bed	[..]

k_s	reaction rate constant based on internal catalyst surface	$[(\text{m/s}) \cdot (\text{mol}/\text{m}^3_{\text{fluid}})^{1-n}]$
ℓ	geometry defining parameter	[m]
L	bed height	$[\text{m}_{\text{bed}}]$
M_{cat}	mass of catalyst in reactor	$[\text{kg}_{\text{cat}}]$
m	reaction order (in O ₂)	[-]
n	reaction order (in NO)	[-]
n_{app}	apparent reaction order	[-]
p	reaction order (in H ₂ O)	[-]
Pe	Péclet number	[-]
r	radial coordinate	[m]
R	recycle ratio	[-]
R_i	inner radius of a ring-shaped particle	[m]
R_u	outer radius of a ring-shaped particle	[m]
$-r_A$	molar reaction rate (=rate of consumption) of reactant A, per unit catalyst mass	$[\text{mol}_A/(\text{kg}_{\text{cat}} \cdot \text{s})]$
$-r_{A,\text{app}}$	apparent reaction rate of reactant A observed in a non-ideal reactor	$[\text{mol}_A/(\text{kg}_{\text{cat}} \cdot \text{s})]$
$-r_{A,\text{true}}$	true reaction rate of reactant A under reactor outlet conditions	$[\text{mol}_A/(\text{kg}_{\text{cat}} \cdot \text{s})]$
\mathcal{R}_A	molar reaction rate (=rate of consumption) of reactant A, per unit catalyst volume	$[\text{mol}_A/(\text{m}^3_{\text{cat}} \cdot \text{s})]$
R_g	gas constant (8.31)	$[\text{J}/(\text{mol} \cdot \text{K})]$
RPM	rotor speed	[1/min]
Sc	Schmidt number	[-]
S_g	specific internal catalyst surface	$[\text{m}^2_{\text{cat}}/\text{kg}_{\text{cat}}]$
$t_{0.95}$	Student-t value for a 95% confidence interval	[-]
T^*	local temperature at the hottest or coldest spot in the particle	[K]
T_b	bulk fluid temperature	[K]
T_{inlet}	temperature at the inlet of the catalyst bed	[K]
T_{outlet}	temperature at the outlet of the catalyst bed	[K]
T_s	external catalyst surface temperature	[K]
u	superficial gas velocity through the bed	$[\text{m}_{\text{bed}}/\text{s}]$
u_y	gas velocity in the axial hole of the hollow extrudates, in the axial direction of the particle	[m/s]
V_p	catalyst particle volume	$[\text{m}^3_{\text{part}}]$
WHSV	Weight Hourly Space Velocity (ratio of fresh feed mass flow rate to dry catalyst mass)	$[\text{kg}_{\text{gas}}/(\text{kg}_{\text{cat}} \cdot \text{h})]$

Greek letters

α	significance level of a regression model	[-]
β_i	internal Prater number	[-]
Γ	geometry parameter of a catalyst particle	[-]
$\Delta_r H$	reaction enthalpy	[J/mol]
ΔT_{ad}	adiabatic temperature increase	[K]
ΔT_b	temperature difference across the catalyst bed	[K]
ε	catalyst particle voidage	$[\text{m}^3_{\text{void}}/\text{m}^3_{\text{part}}]$
ε_b	bed voidage	$[\text{m}^3_{\text{void}}/\text{m}^3_{\text{bed}}]$
η_f	film effectiveness factor	[-]
$\eta_{f,h}$	effectiveness factor for heat transfer in the film layer	[-]
$\eta_{f,m}$	effectiveness factor for mass transfer in the film layer	[-]
η_p	effectiveness factor for intraparticle mass (and heat) transfer	[-]
$\eta_{p,h}$	effectiveness factor for intraparticle heat transfer	[-]
$\eta_{p,m}$	effectiveness factor for intraparticle mass transfer	[-]
λ	geometry defining parameter	[m]
λ_e	effective conductivity of the catalyst particle	[W/(m·K)]
μ	dynamic viscosity of the fluid	[Pa·s]
ν	order falsification ratio	[-]
ξ_A	conversion of reactant A	[-]
ρ	rate falsification ratio	[-]
ρ_f	density of the transported fluid	$[\text{kg}_{\text{fluid}}/\text{m}^3_{\text{fluid}}]$
ρ_p	catalyst particle density	$[\text{kg}_{\text{cat}}/\text{m}^3_{\text{part}}]$
τ	catalyst particle tortuosity factor	[-]
Φ	Weisz modulus	[-]
ϕ, ϕ_m	Thiele moduli	[-]
$\phi_{\text{mol},A,\text{in}}$	molar flowrate of A in feed stream	$[\text{mol}_A/\text{s}]$
$\phi_{\text{mol},A,\text{out}}$	molar flowrate of A in product stream	$[\text{mol}_A/\text{s}]$
ψ	particle roughness parameter	[-]
$\phi_{V,\text{bed}}$	flowrate through the catalyst bed	$[\text{m}^3 \text{ (NTP) } / \text{s} \text{ or } \text{m}^3/\text{s}]$
$\phi_{V,\text{feed}}$	fresh feed flow rate	[same units as $\phi_{V,\text{bed}}$]
Ω	pore diffusion fit parameter	[-]

References

- Beek, W.J., 1967, in *Proc.Int.Symp.Fluidization* (Edited by A.A.H. Drinkenburg), p. 507. Neth.Univ.Press, Amsterdam.
- Bennett, C.O., Cutlip, M.B. and Yang, C.C., 1972, Gradientless Reactors and Transient Methods in Heterogeneous Catalysis. *Chem. Engng. Sci* **27**, 2255-2264.
- Berty, J.M., 1984, 20 Years of Recycle Reactors in Reaction Engineering. *Plant/Operations Progress* **3/3**, p. 163-168.
- Bird, R.B., Stewart, W.E. and Lightfoot, E.N., 1960, *Transport Phenomena*. John Wiley & Sons, New York. p. 200.
- Boutkan, E.J.M., 1992, *Pitfalls in the study of SCR kinetics* (literature survey). Faculty of Chemical Engineering and Materials Science, Delft University of Technology, Delft, The Netherlands.
- Boutkan, E.J.M., 1993, *Study of the kinetics of the SCR of NO with excess NH₃* (MSc. thesis). Faculty of Chemical Engineering and Materials Science, Delft University of Technology, Delft, The Netherlands.
- Box, G.E.P. and Draper, N.R., 1987, *Empirical Model-Building and Response Surfaces*. John Wiley & Sons, New York.
- Box, G.E.P., Hunter, W.G. and Hunter, J.S., 1978, *Statistics for Experimenters*. John Wiley & Sons, New York.
- ECHIP, Inc., 1994, *ECHIP* (software package, version 5), Hockessin (DE), USA.
- IJselendoorn, 1994, *Approximate Expressions for the Effectiveness Factor of Catalyst Particles* (literature survey). Faculty of Chemical Engineering and Materials Science, Delft University of Technology, Delft, The Netherlands.
- Mears, D.A., 1971. *Ind.Eng.Chem.,Process Des. Dev.* **10**, 541.
- Schwartz, C.E. and Smith, J.M., 1953, Flow Distribution in Packed Beds. *Ind.Eng.Chem.* **45**, 1209-1218.
- SPDE, Inc, 1992, *SPDE* (software package, version 1.2). SPDE, Inc., Bass Lake, CA, USA.
- Van Soest, J., 1985, *Elementaire Statistiek*. Delftse Uitgevers Maatschappij, Delft, The Netherlands.
- Takács, K., 1994, *SPDI5* (private software). Faculty of Chemical Engineering and Materials Science, Delft University of Technology, Delft, The Netherlands.
- Verheijen, P.J.T., 1994, *PastiFit* (software package, version 2.30). Faculty of Chemical Engineering and Materials Science, Delft University of Technology, Delft, The Netherlands.
- Wedel, S. and Villadsen, J., 1983, Falsification of Kinetic Parameters by Incorrect Treatment of Recirculation Reactor Data. *Chem. Engng. Sci* **38**(8), 1346-1349.
- Wijngaarden, R.J. and Westerterp, K.R., 1994, *Generalized Formulae for the Calculation of the Effectiveness Factor*. University of Twente, Enschede, The Netherlands.

Chapter 5

Modeling of the Bead String Reactor and experimental validation of the models

Contents

Summary	145
1 Introduction	146
2 Description of the mathematical BSR models	147
2.1 Introduction	147
2.2 General assumptions	147
2.3 Governing equations	149
2.3.1 Momentum balance	149
2.3.2 Reactant mole balance for the fluid phase	150
2.3.3 Reactant mole balance for the catalyst phase	151
2.3.4 Reaction kinetics	151
2.4 Five models	151
2.4.1 The 'Infinitely Long Cylinder Elementary Cell' (ILCEC) model	153
2.4.2 The 'Infinitely Long Cylinder Ringzone' (ILCR) model	155
2.4.3 The 'Infinitely Long Cylinder Film' (ILCF) model	155
2.4.4 The 'Catalyst Bead Equiflow Film' (CBEF) model	157
2.4.5 The 'Catalyst Bead Subflow Film' (CBSF) model	158
2.4.6 Estimation of the errors introduced by the model assumptions	159
3 Experimental work	162
3.1 Introduction	162
3.2 Experimental set-up and procedures, and materials used	162
3.3 Experiments conducted	164
4 Results and discussion	165
4.1 Pressure drop experiments	165
4.2 Validation of the mathematical reactor models	166
5 Conclusions	170
Acknowledgements	171
Notation	171
References	173

Summary

To allow assessment of the feasibility of the BSR, a simple mathematical reactor model enabling case studies is required. The model should be accurate enough to predict adequately the performance of a given BSR configuration, for a reaction with given kinetics, under given conditions. Five reactor models describing gas/solid (or liquid/solid) reactions in a BSR with strings of cylindrical catalyst particles were developed and validated experimentally. The complexity of the five models varies from a system of three second order, two- or three-dimensional partial differential equations (PDE's) to a system of one ordinary differential equation coupled with two algebraic equations. The most important differences between the models are the way in which they account for the reactant flux through the 'top' and 'bottom' surface of the catalyst particles on a string, whether axial symmetry in and/or around each string is assumed, and whether the flow distribution over the various types of subchannels is taken into account. The models contain no parameters to be estimated from the validation experiments: all model parameters have been estimated from theoretical relations or independent measurements on momentum and mass transfer and reaction kinetics. Except the most complex one, the models can be solved numerically on a personal computer within one minute. The most complex model was only tested marginally, and found to give approximately the same predictions as a simpler model derived from it.

The selective catalytic reduction (SCR) of NO with excess ammonia at low temperatures (140-180°C) served as the test reaction to validate the mathematical models. Experiments were done with lab-scale BSR modules filled with strings of deNO_x catalyst extrudates of 1.6 and 3.2 mm diameter. The strings were arranged in regular square arrays, with relative pitches between 1.00 and 2.75. All experiments were performed in the laminar flow regime, where the influence of the mass transfer rate on the reactant conversion is significant.

The difference between the experimentally observed NO conversions and the conversions predicted by the mathematical models, was *ca.* ten percent (relative) on the average. For three models the differences between experiments and predictions were systematic, and could be explained from the model assumptions. For the fourth model the differences were spread evenly around zero. For this model the average difference between the experimentally determined and the predicted conversion was *ca.* five percent (relative); this difference can be attributed to stochastic variations in the observations.

All models satisfactorily describe the trends of the conversion with the most important reactor geometry variables and process condition variables.

1 Introduction

To assess the feasibility of the BSR as a competitor of the monolithic reactor, Parallel Passage Reactor and Lateral Flow Reactor, it is necessary to do case studies in which the performance and price of these reactors is compared, for certain applications. To allow such case studies, two tools are needed: 1) mathematical models of the reactors, and 2) an optimization routine that, given a mathematical reactor model and a set of process specifications, finds the optimum reactor configuration. Furthermore, data are needed on costs, safety, availability, *etc.* In this chapter the development of mathematical models for the Bead String Reactor (BSR) is discussed. The implementation of the reactor models in an optimization routine, and detailed cost analyses of the reactor are beyond the scope of this thesis work.

Obviously the most accurate results are obtained with the most accurate reactor models. However, more accurate models are usually more complex, and therefore consume more computer time. This puts a limit on the accuracy of the reactor models that should be pursued. In this chapter a model is considered sufficiently accurate when it adequately describes the experimental data, the word 'adequate' being used in its statistical meaning.

The aim of the work reported in this chapter is to develop mathematical models (varying in complexity) describing a gas/solid (or liquid/solid) reaction in a BSR, that can be numerically solved on a personal computer within a few hours time or less, and to validate these models experimentally. As has been mentioned in the previous three chapters, the reactor models need at least three ingredients: a model describing momentum transfer (pressure drop), a model describing mass (and heat) transfer, and a model describing the intrinsic and particle kinetics of the chemical reaction. Therefore the results of the previous three chapters will be integrated in this chapter. The reactor models will contain no extra fit parameters to be estimated from the validation experiments; all parameters used in the models have been derived theoretically or from independent experiments on pressure drop, mass transfer and kinetics.

The selective catalytic reduction (SCR) of nitric oxide with excess ammonia will serve as the test reaction, using a BSR filled with strings of a commercial deNO_x catalyst shaped as hollow extrudates. The reaction temperature, gas velocity, particle diameter and relative pitch will be varied.

The structure of this chapter is as follows. In Section 2 the five mathematical BSR models will be discussed that were developed and experimentally validated. This includes a discussion of the assumptions made in the development of the models, and of the relations that were used to describe momentum and mass transfer and the

kinetics. In Section 3 a description is given of the experimental set-up and procedures used to perform the SCR reaction in lab-scale BSR modules, and of the experimental design. In Section 4 the results of the experimental study are compared with predictions based on the different models.

2 Description of the mathematical BSR models

2.1 Introduction

In this section the five mathematical BSR models that were developed and validated experimentally, will be discussed. The assumptions that all models have in common, are discussed in Section 2.2. The governing equations that describe the performance of a BSR are summarized in Section 2.3. Although those equations have already been discussed separately in Chapters 2, 3 and 4, they are summarized here for the reader's convenience. Finally, the mathematical models are presented in Section 2.4.

2.2 General assumptions

The mathematical BSR models presented in Section 2.4 share the following assumptions:

1. The flow is incompressible (in other words, the pressure drop across the reactor is small compared to the absolute pressure).
2. There is a steady state situation.
3. The flow is hydrodynamically fully developed at the entrance of the reactor. It was shown in Chapter 2 that this assumption results in a negligibly small error in the prediction of the pressure drop, and it is therefore expected that the influence of the flow development on the mass transfer rate is also negligible. Because the flow is assumed to be fully developed, the gas velocity vector will only have one component, namely in the axial (z -) direction, u_z .
4. The pressure gradient has only one component, namely in the z -direction; in other words, there are no lateral pressure gradients. Because the flow is incompressible, the pressure gradient is independent of the axial position (z) in the reactor.
5. There is no interaction between the various subchannels, *i.e.* no net exchange of momentum or reactants. This assumption will usually be valid in laminar flow, but not in turbulent flow, where lateral flows are known to occur between

neighboring subchannels. However, no significant effect of lateral flows on the pressure drop has been observed (see Chapter 2). Furthermore the lateral flows are expected to have a negligible effect on the reactor performance as long as the reactant concentrations in the various subchannels are approximately the same at each lateral plane.

6. The enhancement of the mass transfer rate in the first part of the reactor, resulting from the developing concentration profile, is negligible. It was shown in Chapter 3 that for relative pitches larger than 1.1 this assumption is valid, and that even for smaller relative pitches the effect of the enhanced mass transfer rate is small, except for the unlikely situation that film layer mass transfer is the limiting factor in the reactor performance.
7. Axial dispersion is negligible. Whether this assumption is valid, can be seen from the Péclet number ($u_z L/D$); for typical conditions ($u_z = 1$ m/s, $L = 0.5$ m) and laminar flow, the Péclet number is larger than 1000, and even for turbulent flow it will be much larger than 10. Note that in laminar flow, the radial flow profile within a subchannel will also result in deviation from plug flow. The effect of this deviation can be estimated by comparing the predictions from different mathematical models, one of which taking the flow profile into account and the other assuming plug flow.
8. The system is isothermal. This assumption is valid because very low reactant concentrations (*ca.* 100 ppmv) are used in the present study, resulting in an adiabatic temperature rise of only *ca.* 1.5 K for the SCR of NO.
9. The chemical reaction has no effect on the flow profile. This assumption is valid for the conditions of the present study, because of the low reactant concentrations.
10. Diffusion in the gas phase (in laminar flow) can be described with the Fick diffusion model; in the catalyst phase it can be described with a combination of Fick and Knudsen diffusion. These assumptions are expected to be valid, because of the low reactant concentrations, the small size of the reactant molecules (NO) and the low affinity of the reactant toward the catalyst material.
11. The diameter of the wire (or 'kernel') on which the catalyst particles are stringed, exactly equals the inner diameter of the hollow catalyst particles (or 'rings'). In the present study this situation was closely approximated.

In a properly designed BSR, the influence of the reactor wall on the flow distribution is negligible, even in lab-scale modules (see Chapter 2). A BSR will usually be designed to have a uniform flow profile, *i.e.* to have the same average velocity all subchannels. Therefore, in four of the five mathematical models presented in this chapter, it is assumed that all subchannels are identical. To estimate the effect of the wall in the validation experiments, a fifth model was developed that takes into account the flow distribution over the various subchannels.

2.3 Governing equations

The equations that describe the performance of a BSR, arise from the momentum balance and reactant mole balances and from the reaction kinetics. All equations are summarized in the following four sections.

2.3.1 Momentum balance

The momentum balance over a small element of the fluid domain (see Fig. 5-1), for incompressible, steady state, fully developed flow in the z -direction, results in the following partial differential equation (PDE):

$$\nabla \cdot (\mu \nabla u_z) = \frac{dp}{dz} \quad (5-1)$$

Note that the Nabla operator (∇) is in fact two-dimensional in Eq. (5-1), because u_z is constant in the z -direction (as the flow was assumed to be fully developed). The pressure gradient dp/dz is a constant, *i.e.* place independent.

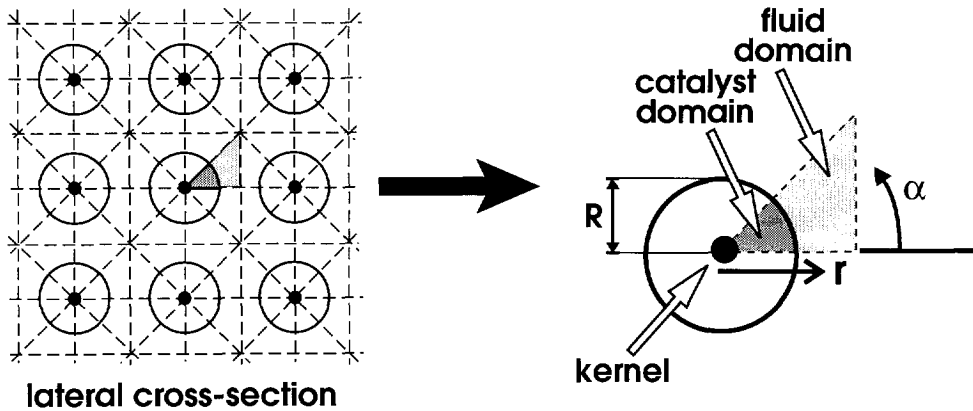


Figure 5-1 Unit or elementary cell of a central subchannel in a regular square array.

In laminar flow μ is the molecular diffusivity constant; in that case Eq. (5-1) is a second order, linear, two-dimensional PDE. In turbulent flow μ also depends on the velocity gradients (hence on the lateral position), and Eq. (5-1) then is quasilinear or non-linear. In either case Eq. (5-1) can be solved independently from the equations discussed in Sections 2.3.2 and 2.3.3.

On the dashed boundaries of the fluid domain indicated in Fig. 5-1, the boundary condition of Eq. (5-1) follows from the symmetry requirement, and the velocity gradient normal to the boundary should be zero. At the catalyst surface, the boundary condition follows from the 'no slip' condition, and the velocity should be zero. In the modeling of the momentum transfer, the strings of catalyst particles are treated as rods with an artificial roughness. In non-laminar flow the roughness may affect the

momentum transfer, which can be modeled with an empirical roughness parameter (see Chapter 2).

2.3.2 Reactant mole balance for the fluid phase

The reactant mole balance over a small element of the fluid domain, for incompressible, steady state, fully developed flow in the z -direction, results in:

$$\nabla \cdot (D \nabla c_A) = u_z \frac{\partial c_A}{\partial z} \quad (5-2)$$

The axial gas velocity u_z follows from Eq. (5-1). In laminar flow D is the free molecular diffusivity constant D_{free} , and Eq. (5-2) is a second order, linear, three-dimensional PDE. In turbulent flow the diffusivity is a function of the velocity gradients (hence of the lateral position), and Eq. (5-2) then is quasilinear or non-linear.

On the dashed boundaries of the fluid domain indicated in Fig. 5-1, the boundary condition of Eq. (5-2) follows from the symmetry requirement, and the concentration gradient normal to the boundary should be zero. The boundary condition at the external catalyst side surface (see Fig. 5-2) is the relation that couples the fluid domain with the catalyst domain:

$$D_e \left. \frac{\partial c_A}{\partial r} \right|_{r=R}^{\text{catalyst domain}} = D_{free} \left. \frac{\partial c_A}{\partial r} \right|_{r=R}^{\text{fluid domain}} \quad (5-3)$$

The boundary condition at the top and bottom surface of each catalyst particle is analogous:

$$D_e \left. \frac{\partial c_A}{\partial z} \right|_{\text{top/bottom}}^{\text{catalyst domain}} = D_{free} \left. \frac{\partial c_A}{\partial z} \right|_{\text{top/bottom}}^{\text{fluid domain}} \quad (5-4)$$

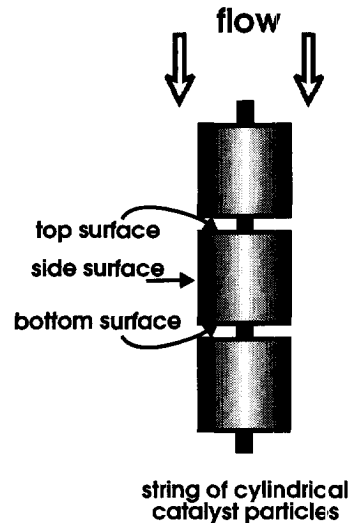


Figure 5-2 Three 'types' of external particle surface in a string of cylindrical catalyst particles.

2.3.3 Reactant mole balance for the catalyst phase

The reactant mole balance over a small element the catalyst domain yields:

$$\nabla^2 c_A = \frac{1}{D_e} \mathfrak{R}_A \quad (5-5)$$

This is a second order, quasilinear three-dimensional PDE. The boundary condition of Eq. (5-5) at the external catalyst surface is given by Eq. (5-3); the boundary condition at the symmetry lines and at the boundary with the inert kernel, is that the derivative of c_A with respect to the normal vector should equal zero.

2.3.4 Reaction kinetics

For the validation experiments with the SCR of NO as the test reaction, the reaction rate in Eq. (5-5) is described with a power law rate expression:

$$-r_{\text{NO}} \equiv \frac{\mathfrak{R}_{\text{NO}}}{\rho_{\text{cat}}} = k_0 e^{\frac{-E_A}{R_s T}} c_{\text{NO}}^n c_{\text{O}_2}^m c_{\text{H}_2\text{O}}^p \quad (5-6)$$

Under the conditions used in the present study (see Section 3), the reactants oxygen and ammonia, and the product water are present in large excess, and their concentrations will be place independent in the reactor. (Note that the diffusivities of these components are approximately equal to the diffusivity of NO). Furthermore, also the temperature will be place independent, as the system is assumed to be isothermal. Therefore the reaction rate can be written as:

$$\mathfrak{R}_{\text{NO}} = k c_{\text{NO}}^n \quad (5-7)$$

in which the value of the rate constant k in each experiment depends on the reaction conditions.

The effective diffusion constant in Eq. (5-5) is described with the following simple, well-known model:

$$D_e = \Omega \left(\frac{1}{D_{\text{free}}} + \frac{1}{D_{\text{Kn}}} \right)^{-1} \quad (5-8)$$

in which Ω is a catalyst characteristic parameter that could be associated with the physical parameter ε/τ . The Ω values of the two catalysts used in the present study, were fitted from independent kinetic experiments (see Chapter 4).

2.4 Five models

In spite of the eleven assumptions made in Section 2.2, numerical solution of the mathematical system presented in Section 2.3 is still very time consuming. Various simplifications can be made to obtain simpler mathematical systems or models. Below

five models are presented that can be expected to allow adequate description of the BSR in a limited range of conditions (that will be indicated for each model). The errors introduced by the extra assumptions in each model, will be quantified in Section (2.4.6). To illustrate the different models, their distinguishing features are explained graphically in Fig. 5-3.

Because the pressure drop across the BSR can be calculated independently from the concentration profile, the modeling of the momentum transfer could be the same for all five models, and will therefore not be discussed any further; see Chapter 2 for details on the modeling of the momentum transfer.

model	axial plane	lateral plane			wall effects	
		angular gradients in catalyst	angular gradients in bulk fluid	lateral gradients in bulk fluid		
ILCEC			+	+	+	-
ILCR			-	-	+	-
ILCF						-
CBEF			-	-	-	-
CBSF						+

Figure 5-3 Illustration of the five BSR models.

2.4.1 The 'Infinitely Long Cylinder Elementary Cell' (ILCEC) model

If the (axial) length of the catalyst beads is much larger than the outer particle radius, the molar flow of reactants entering a particle through its top and bottom surface, is small compared to the flow entering through the side surface. A string of catalyst particles can then be modeled as an infinitely long 'catalyst rod' with blocked top and bottom ends; see Fig. 5-4. This is a useful simplification, because it allows reduction of the three-dimensional PDE of Eq. (5-5) to two dimensions. The justification for this reduction is that in an 'infinitely long' catalyst cylinder (where 'infinitely long' should be interpreted as the length of the reactor), the axial concentration gradients will be very small compared to the radial gradients; hence the axial reactant flux is negligible compared to the radial flux. (The situation where the angular gradients are also small compared to the radial gradients, is treated in Section 2.4.2).

The 'infinitely long cylinder' approximation could also be expected to be valid if the catalyst particles are tightly packed on the string (*i.e.* with only a very narrow gap between two consecutive particles); see Fig. 5-5. This is illustrated in Fig. 5-6, in which four contour plots are presented of the reactant concentration in and around cylindrical catalyst particles on a string, with different spacings of the particles. It is assumed that outside (and inside) the particles there is only reactant transport due to diffusion, and the concentration is taken constant at the outer side boundary of the annularly shaped fluid domain. It can be seen that even when the gap between the particles is small relative to the length of the particles, the concentration profile deviates considerably from the profile in an infinitely long cylinder. In practice the deviation will be even bigger, because of extra convective reactant transport in the fluid phase. Consequently, the 'infinitely long cylinder' approximation can usually not be justified by assuming that the transport of reactants is negligible in the 'gap' between consecutive particles on a string. The approximation is therefore only justified for particles with a relatively large length over diameter ratio.

The model that results from the relations presented in Section 2.3 and the extra assumption of negligible axial reactant flux within the catalyst particles, will be called the 'infinitely long cylinder elementary cell' (ILCEC) model. The 'elementary cell' part of the name refers to the fact that in this model the effect of the reactor wall is neglected, *i.e.* it is assumed that the reactor is built up solely of elementary cells as the one depicted in Fig. 5-1.

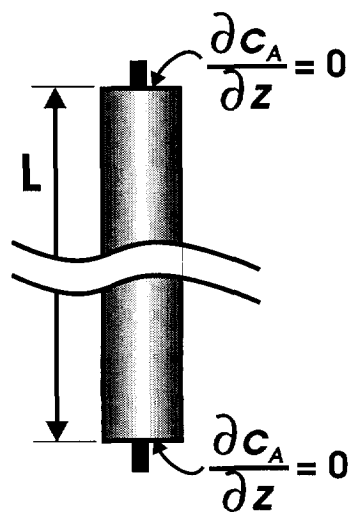


Figure 5-4 Model of a string of catalyst particles, with the 'infinitely long cylinder' approximation.

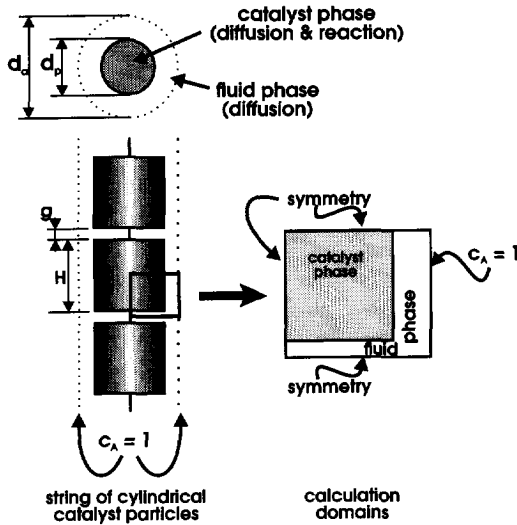


Figure 5-5 Model for studying the effect of the 'gap' between stringed particles on the concentration profile in the particles. Left: top view and side view of a string in an annular space; right: mathematical domains.

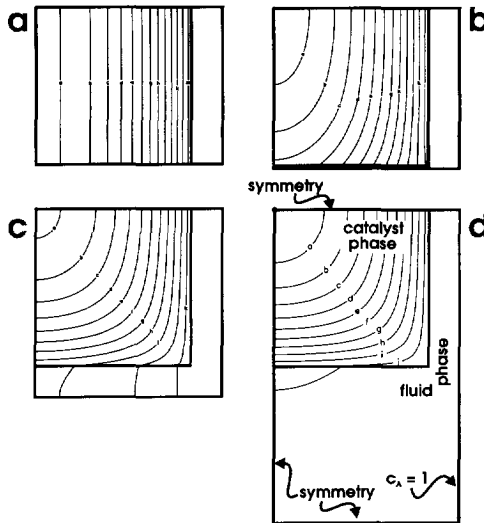


Figure 5-6 Concentration profiles in the calculation domains indicated in Fig. 5-5, for different values of g/H . At the east boundaries $c_A = 1$; the concentration difference between consecutive contour lines is 0.05. Conditions: (a) $g/H = 0$ (infinitely long cylinder); (b) $g/H = 1/50$; (c) $g/H = 1/5$; (d) $g/H = 1$. In all cases: $d_e/d_p = 1.2$; $H/d_p = 1$; $D_e/D_{free} = 1/20$; first order reaction; $d_p^2 k/D_p = 12$.

When the length over diameter ratio of the catalyst beads is *not* much larger than 0.5 (and the particles are not very tightly packed on the string), the **ILCEC** model is obviously expected to underestimate the reactant conversion in the BSR.

2.4.2 The 'Infinitely Long Cylinder Ringzone' (ILCR) model

Upon increasing the relative pitch, the velocity and concentration profiles around each rod become more axisymmetric. For relative pitches higher than *ca.* 2.5, only a negligible error is introduced when the lateral plane is described by one coordinate (r) instead of two (r and α); see the discussion on the so-called 'equivalent ringzone approximation', in Chapter 2, Section 2.2. The **ILCR** model is derived from the **ILCEC** model by assuming axial symmetry in and around each rod. This assumption reduces Eq. (5-1) to a second order, linear or (in turbulent flow) non-linear, ordinary differential equation (ODE), Eq. (5-2) to a second order, linear, quasilinear or non-linear, two-dimensional PDE, and Eq. (5-5) to a second order, linear or non-linear (depending on the reaction rate expression) ODE:

$$\frac{1}{r} \frac{d}{dr} \left[\mu r \frac{du_z}{dr} \right] = \frac{1}{\mu} \frac{dp}{dz} \quad (5-9)$$

$$\frac{1}{r} \frac{\partial}{\partial r} \left[D r \frac{\partial c_A}{\partial r} \right] = u_z \frac{\partial c_A}{\partial z} \quad (5-10)$$

$$\frac{d^2 c_A}{dr^2} + \frac{1}{r} \frac{dc_A}{dr} = \frac{1}{D_e} \mathfrak{R}_A \quad (5-11)$$

Obviously this drastically reduces the computation time needed to solve the model numerically.

It is expected that for relative pitches smaller than 2.5, the **ILCR** predicts higher conversions than the **ILCEC** model. This is because the equivalent ringzone approximation then overestimates the transfer of momentum and mass (see Chapters 2 and 3).

2.4.3 The 'Infinitely Long Cylinder Film' (ILCF) model

The calculation of the reactant concentrations in the fluid phase can be simplified significantly by adopting the film model, according to which the fluid phase is perfectly mixed in the lateral plane, except for a small layer at the surface of the catalyst. The model that is obtained by combining the 'infinitely long cylinder' approximation discussed in the previous two sections, and the film model, is called the 'infinitely long cylinder film' (**ILCF**) model.

According to the film model, the rate of mass transfer from the bulk fluid phase to the catalyst surface is described by a mass transfer coefficient, and boundary condition (5-3) changes into:

$$D_e \left. \frac{\partial c_A}{\partial r} \right|_{r=R, \text{catalyst domain}} = k_g (c_{A,b} - c_{A,s}) \quad (5-12)$$

Because the bulk fluid phase is assumed to be perfectly laterally mixed, a mass balance over a thin lateral slice of a unit cell leads to the following ODE:

$$\frac{dc_{A,b}}{dz} = - \frac{4}{\langle u_z \rangle d_{h,c}} k_g (c_{A,b} - c_{A,s}) \quad (5-13)$$

This ODE replaces the PDE of Eq. (5-2).

The **ILCF** model allows another (trivial) simplification. Because the bulk fluid phase is assumed to be perfectly mixed, it will also be axisymmetric; consequently, also the concentration profile in the catalyst particles will be axisymmetric. As a result the three-dimensional PDE of Eq. (5-5), which could be reduced to a two-dimensional PDE due to the 'infinitely long cylinder' approximation, can be further reduced to the second order linear or non-linear ODE of Eq. (5-11), as the angular coordinate drops out.

From this it follows that the **ILCF** model consists (besides of the momentum transfer model) of one first and one second order ODE, and the numerical solution of this model therefore consumes considerably less time than of the previous two models. However, there is a complication in the **ILCF** model. As was discussed in Chapter 3, the value of the mass transfer coefficient depends on the second Damköhler number, which represents the ratio of the reaction rate to the diffusion rate in the fluid phase. Fortunately the dependence is only weak (at least for relative pitches larger than 1.1), and the difference between the Sherwood numbers for $Da_{II} = 0$ and $Da_{II} = \infty$ is smaller than 30% ($s/d > 1.1$). It was also shown in Chapter 3 that, depending on Da_{II} , the Sherwood number may vary significantly along the perimeter of a particle or 'rod', which can be accounted for by using a circumferentially averaged Sherwood number. A suitable value for the Sherwood number to be used in the **ILCF** model can therefore be obtained from Fig. 3-2 (Chapter 3); whether to use the value for constant surface concentration or for constant flux, can be assessed from the (estimated) second Damköhler number.

The **ILCF** model is expected to underestimate the conversion obtained in a BSR, because of the 'infinitely long cylinder' approximation.

2.4.4 The 'Catalyst Bead Equiflow Film' (CBEF) model

If the length over diameter ratio of the catalyst particles is not much larger than 0.5 (and the particles are not very tightly packed on the string), it is necessary to account for the reactant flux entering the particles through the top and bottom surfaces. A model that does not require much computing time to solve, is obtained when an approximative, algebraic method is used to estimate the effectiveness factor of each catalyst particle (*e.g.* the Aris method discussed in Chapter 4, Section 5.4.2), and to treat each particle as if it were homogeneous, at the conditions existing at the particle surface. It is then no longer necessary to solve Eq. (5-5) to obtain the concentration field in the catalyst particle. (Note that according to the governing equations discussed in Section 2.3, the concentration profile in the particle was necessary to calculate the reactant flux from the fluid phase into the particle, using Eqs. (5-3) and (5-4)).

An important assumption must be made to justify the use of an approximative method for calculating the particle effectiveness factor. As was discussed in Chapter 4, Section 5.4, all approximative methods share the prerequisite that the reactant concentration at the particle surface has one and the same value over the complete surface. Consequently it must be assumed that (1) there is axial symmetry for each string, and (2) the top and bottom surfaces of the particles are exposed to the same surface concentration as the side surface; see Fig. 5-7. Therefore it seems logical to adopt the film model in this procedure (another possibility would be to adopt the 'equivalent ringzone' model), and to assume that the mass transfer coefficient at the top and bottom surfaces equals the (circumferentially averaged) mass transfer coefficient at the side surface; the latter can be obtained as discussed in the previous section.

The mathematical system that remains, consists (besides the momentum transfer equation) of only one ODE, namely Eq. (5-13), in which the concentration at the particle surface follows from:

$$A_p k_g (c_{A,b} - c_{A,s}) = V_p \eta \mathcal{R}_A|_{c_{A,s}} \quad (5-14)$$

In this equation A_p , the external particle surface area through which mass transfer takes place, is the sum of top, bottom and side surface areas. Note that in this approach it has been assumed that the external particle surface area is distributed homogeneously along the length of the string, which is only true on a length scale of

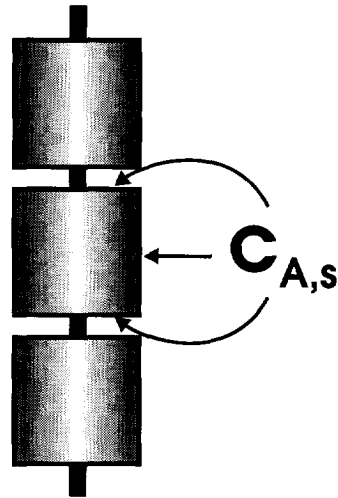


Figure 5-7 Assumption made in the 'catalyst bead' models: the surface concentration is the same everywhere on one bead.

at least one particle. However, the error introduced through this assumption can be expected to be negligible in practical situations.

The model that is formed by Eqs. (5-13) and (5-14), with the extra assumption that the flow through all subchannels is equal (*i.e.* that the reactor is built up solely of elementary cells as the one depicted in Fig. 5-1, so that wall effects can be neglected), is called the 'catalyst bead equiflow film' (CBEF) model. Because of the assumption in the CBEF model that the mass transfer coefficient value at the top and bottom surface of the particle equals the value at the side surface, it can be expected that this model overestimates the conversion obtained in a BSR, especially when the particle length over diameter ratio is much smaller than 0.5 and when the 'gap' between consecutive particles on a string is very small compared to the particle diameter. However whether the CBEF model over- or underestimates the BSR performance, also depends on the error made in the approximation of the particle effectiveness factor.

In the present study the particle effectiveness factor was estimated with the Aris method discussed in Chapter 4. In the estimation, the particles were modeled as normal cylindrical catalyst particles, *i.e.* finite cylinders with no inert kernel. This was necessary because approximative methods to estimate an effectiveness factor cannot account for an inert kernel in a catalyst particle such as the metal wire in the axial hole of the BSR beads. The cylinder diameter used in the calculations was $d_{p,s}$, defined in Fig. 5-8 (the subscript *s* stands for 'shrunk cylinder'). In this way the active catalyst volume of the 'shrunk' cylinder equals that of the real catalyst particles, and the particle volume to surface area ratio of the 'shrunk' cylinder approximately equals that of the real, stringed particles. The error that is made in the estimation of the effectiveness factor by using the Aris method with the 'shrunk particle' modeling, is quantified in Section 2.4.6.

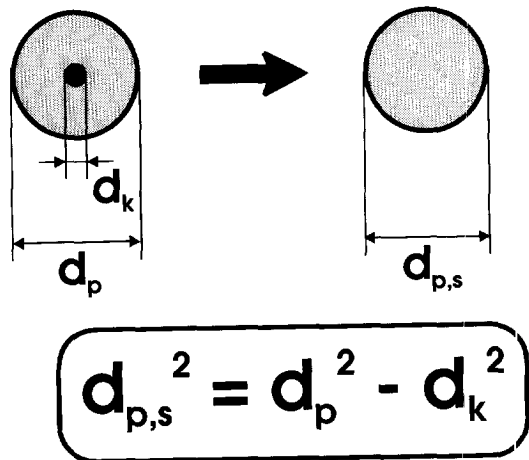


Figure 5-8 Transformation of a cylindrical particle with an inert kernel to an equivalent particle with no inert kernel.

2.4.5 The 'Catalyst Bead Subflow Film' (CBSF) model

The 'catalyst bead subflow film' (CBSF) model is a refinement of the CBEF model, in the sense that does not contain the assumption that the reactor solely contains central subchannels. Instead, in the CBSF model the flow distribution over the central, wall and corner subchannels is calculated following the procedures outlined in Chapter 2. The reactant conversion is then calculated for each type of subchannel,

under the assumption that there is no exchange of reactants between the subchannels. The overall outlet concentration is calculated as the cup mixing average of the outlet concentrations of all subchannels.

Obviously the assumption of no lateral exchange between the subchannels is strictly spoken only (approximately) valid for a relative pitch of one; however, for higher relative pitches it might be valid if the ratio of the residence time in the reactor to the time constant for lateral diffusion/dispersion is much smaller than one. For lateral diffusion/dispersion over a distance equal to the pitch (s) or the width of the reactor (d_r), these ratios or Fourier numbers are, respectively:

$$Fo_s = \frac{D_{lat}L}{u_z s^2}; \quad Fo_d = \frac{D_{lat}L}{u_z d_r^2} \quad (5-15)$$

The symbol D_{lat} represents the effective lateral diffusion/dispersion constant; for laminar flow a value equal to *ca.* $0.5\epsilon_r D_{free}$ is expected to be suitable, for turbulent flow the molecular diffusion coefficient in this expression should be replaced by the turbulent diffusion coefficient. Based on these simple relations it can be calculated that under typical conditions, lateral reactant transport takes only place over distances of a few subchannels. In other words, if the gas velocity through the wall channels differs much from the velocity through the central subchannels, the non-uniform flow profile can have a significant effect on the overall reactant conversion. In these situations the **CBSF** model can be expected to give a better estimate of the reactor performance than the **CBEF** model.

2.4.6 Estimation of the errors introduced by the model assumptions

As was mentioned, the three models based on the 'infinitely long cylinder' approximation are expected to underestimate the reactant conversion, because in these models the transfer of reactants through the top and bottom surface of the catalyst particles is neglected. The 'catalyst bead' models might be expected to overestimate the conversion, because in these models the surface concentration at the top and bottom surface is assumed to equal the surface concentration at the side surface. However, in the 'catalyst bead' models an extra error is introduced because the catalyst effectiveness factor is calculated with an approximative method, in which the catalyst beads are modeled as 'shrunk' cylinders. In this section it is attempted to estimate the error resulting from the 'infinitely long cylinder' approximation and from the approximation of the effectiveness factor of 'shrunk' particles.

To this end the effectiveness factors were calculated for three representations of the catalyst particles used in the present study:

1. Cylindrical particles of a finite length, with an inert kernel. These particles are called the 'real' particles.
2. Cylinders of infinite length, of the same outer diameter as the 'real' particles, and with an inert kernel. These particles are called the 'infinitely long cylinders'.

3. Cylindrical particles with the same length and active catalyst volume as the 'real' particles, but with no inert kernel; these particles consequently have a smaller diameter than the 'real' particles (see Fig. 5-8). They are referred to as the 'shrunk' particles.

In the calculations it was assumed that the surface concentration was constant over the complete surface. Consequently, particle 2 represents the situation assumed in the 'infinitely long cylinder' models, and particle 3 the situation assumed in the 'catalyst bead' models.

The effectiveness factors of particles 1, 2 and 3 were estimated using *SPDE* (*SPDE Inc.*, 1992), software that solves the elliptic PDE's (like Eq. (5-5)) using a finite element technique. From the concentration field obtained with *SPDE*, the effectiveness factor was calculated by numerically calculating the volume-averaged reaction rate in the catalyst domain and comparing it to the reaction rate at $c_A = c_{A,s}$ (Takács, 1994). The error of the effectiveness factor thus obtained was less than 0.1%, which was checked by comparing *SPDE* solutions for simple geometries and first order reactions with analytical solutions. The effectiveness factor of particle 3 was also estimated using the Aris method.

The calculations were done for 'real' particles with a length of 6.4 mm, an inert kernel diameter of 0.4 mm and an outer particle diameter of either 1.6 mm or 3.2 mm, like the particles used in the present study. An n -th order reaction was assumed, n being 0.7; the experimentally determined rate intrinsic rate constants were used (see Chapter 4).

The 'error' of the effectiveness factor η_i obtained with a certain particle model i (i is 2 or 3) and/or the approximative Aris method, was defined as:

$$\varepsilon_i \equiv \frac{\eta_i - \eta_{1,SPDE}}{\eta_{1,SPDE}} \quad (5-16)$$

where $\eta_{1,SPDE}$ represents the effectiveness factor calculated with *SPDE* for the 'real' particle 1. The errors were calculated as a function of the rate constant (at a fixed surface concentration of 100 ppmv) and also as a function of the surface concentration (at a fixed reaction rate constant corresponding to a temperature of 160°C, the standard temperature in the present study).

The results are presented in Figs. 5-9a to d. The following comments can be made:
Ad $\varepsilon_{3,SPDE}$:

Modeling a particle with an inert kernel as a particle without an inert kernel but with a smaller diameter (such that the active catalyst volume equals that of the 'real' particle), is expected to result in a slight underestimation of the effectiveness factor, because the volume to external surface area ratio of the 'shrunk' particle is slightly larger. This effect will increase when the diameter of the inert kernel becomes larger relative to the outer diameter of the 'real' particle. This corresponds to what is observed in the graphs.

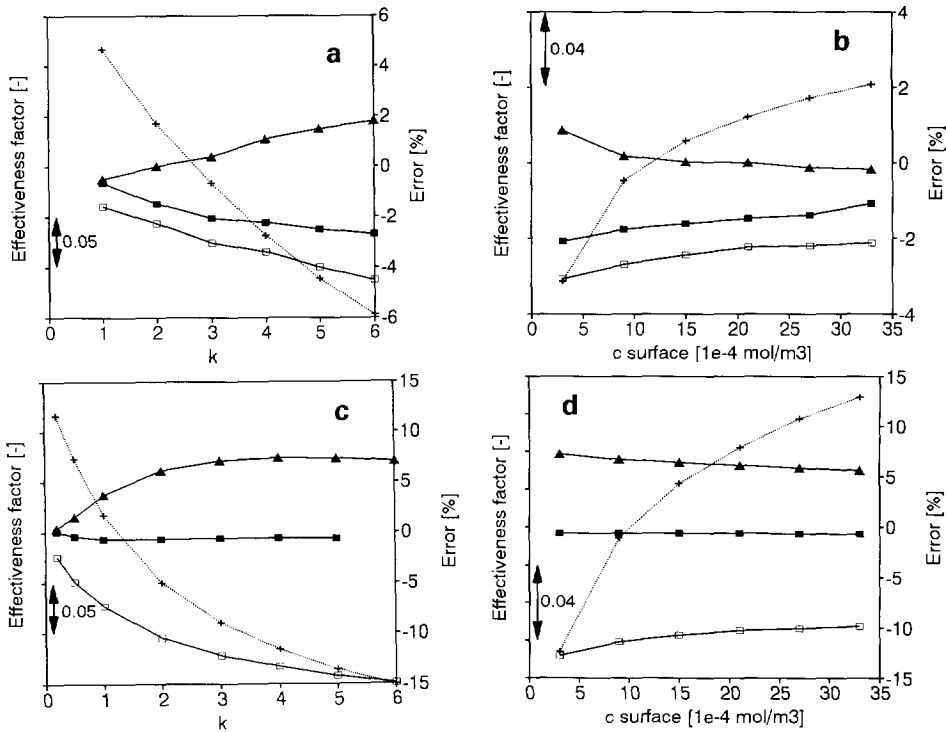


Figure 5-9 Assessment of the errors in the effectiveness factor due to modeling of the particles and the use of an approximative method. (a) and (b) 1.6 mm \varnothing particles; (c) and (d) 3.2 mm \varnothing particles. Symbols: + = $\eta_{1,SPDE}$; ■ = $\epsilon_{3,SPDE}$; ▲ = $\epsilon_{3,Aris}$; □ = $\epsilon_{2,SPDE}$.

Ad $\epsilon_{3,Aris}$:

The Aris method is seen to overestimate the effectiveness factor of the 'shrunk' particles, at higher temperatures even to such an extent that it overestimates the effectiveness factor of the 'real' particles. This implies that the **CBEF** and **CBSF** are expected to overestimate the conversion in the BSR in two ways: first because the surface concentration at the top and bottom surface of the cylinders is overestimated (see Sections 2.4.4 and 2.4.5) and second because of the error resulting from the Aris method. However, for the conditions and catalyst particles of the present study, the overestimation of the effective reaction rate constant is expected to be less than ten percent.

Ad $\epsilon_{2,SPDE}$:

Obviously, the effectiveness factor of the infinitely long cylinders is smaller than that of the 'real' cylinders, especially for the particles with the smallest length over diameter ratio. Consequently it is expected that the **ILCEC** model and the **ILCF** model underestimate the conversion in the BSR. The **ILCR** model is expected to underestimate the conversion at least at relative pitches higher than *ca.* 2.5 (when

the 'equivalent ringzone' approximation is valid); at lower relative pitches the error resulting from the 'equivalent ringzone' approximation counteracts the error resulting from the 'infinitely long cylinder' assumption (see Section 2.4.2), and the ILCR might even overestimate the conversion in the BSR.

3 Experimental work

3.1 Introduction

To test the ability of the mathematical BSR models to predict the reactant conversion for a given reactor geometry (*i.e.* particle size, pitch and wall distance), given reaction kinetics and given process conditions (pressure, temperature, reactant conditions, gas velocity), experiments were performed with lab-scale BSR modules. The test reaction was the selective catalytic reduction (SCR) of nitric oxide, in the presence of excess ammonia, oxygen and water; see Chapter 4. The BSR modules were filled with strings of hollow deNO_x catalyst extrudates. In Section 3.2 the experimental set-up and procedures are described, in Section 3.3 the experiments that were done are described.

3.2 Experimental set-up and procedures, and materials used

A flow sheet of the experimental set-up is presented in Fig. 5-10. Nitrogen, air, nitric oxide and ammonia were dosed using mass flow controllers. Water was dosed using a membrane pump; the water flow rate was checked by means of an electronic balance holding the feed water container. The gases and water were heated, mixed, and led through the reactor. The reactor shell was made of 316 stainless steel. The reactor module was 500 mm long, and had a square inner cross-section of 35 mm. Diffusors with a top angle of 8° were used to connect the reactor module with the supply and exhaust pipes, to prevent swirls in the first and last part of the reactor.

Sample flows were drawn just before the reactor entrance and downstream of the exit diffuser. Water and ammonia were stripped from the sample flow, using gas-washbottles filled with 85 mass % phosphoric acid. The gas was analyzed on nitrogen oxides content using a chemiluminescence meter, equipped with a thermal or a catalytic convertor, which allowed analysis of either NO only or both NO and NO₂. Removal of water is necessary because it has a significant quenching effect on the NO-signal in the chemiluminescence equipment. Removal of ammonia is necessary because it is converted to NO and NO₂ in the thermal convertor, leading to erroneous NO_x

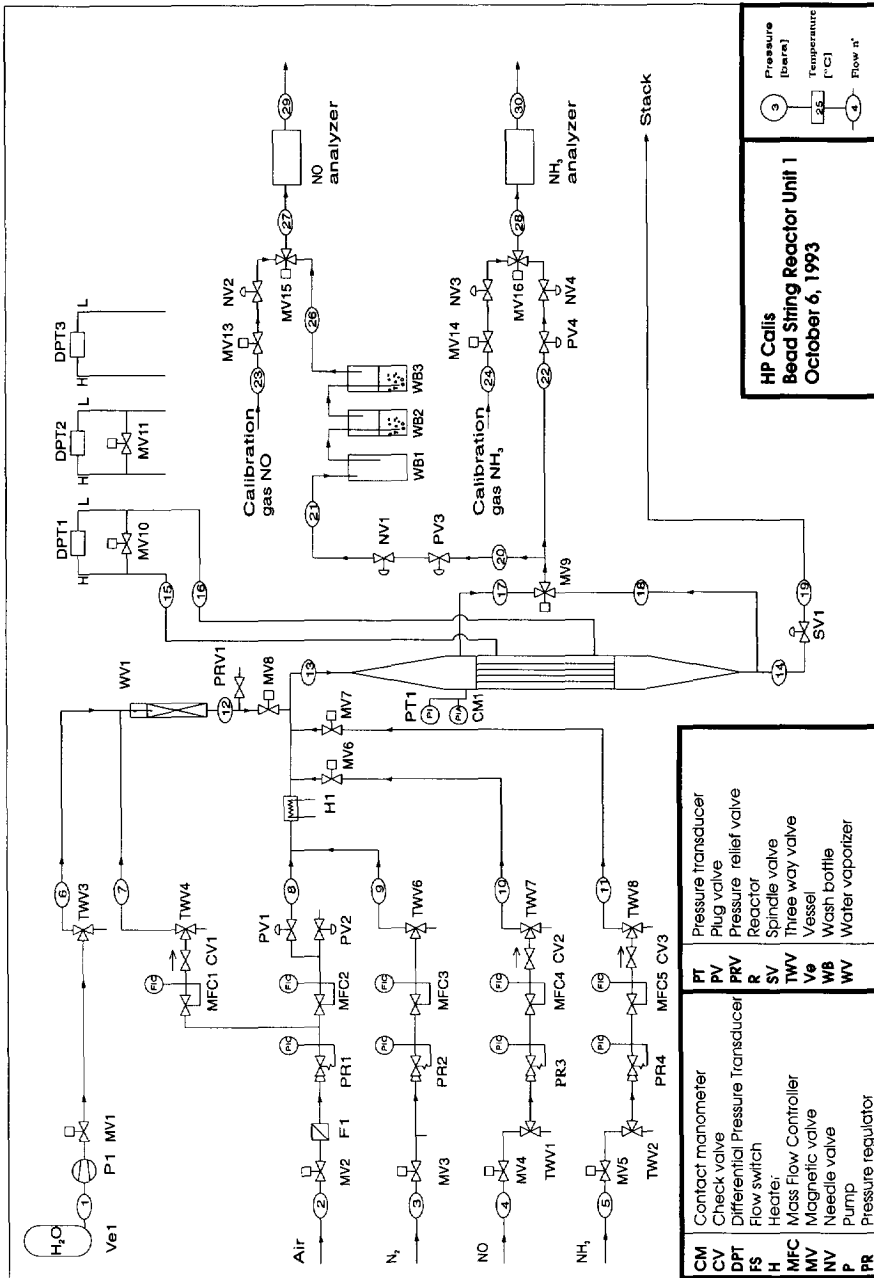


Figure 5-10 Flow sheet of the experimental set-up.

readings.

The experimental set-up operated fully automatically, controlled by a personal computer. The process control hardware *Transport System* was from Transition Technology Inc. [Amesbury (MA), USA]. The software *FIX DMACS* was from Intellution, Inc. [Norwood (MA), USA].

In each run the system was first flushed with nitrogen for 20 minutes, then the product stream was analyzed for one hour, and finally the feed was analyzed for one hour. The chemiluminescence meter was calibrated (span) twice per run.

SCR experiments were done with the two sizes of hollow cylindrical extrudates described in the previous chapter, with outer diameters of 1.6 mm and 3.2 mm and a weight averaged length of *ca.* 6.4 mm. For both particle sizes the diameter of the axial hole was 0.4 mm. The extrudates were stringed by hand, and the strings with a length of *ca.* 43 cm were arranged in the reactor in a regular square array, by fixing them to stainless steel wire meshes at the top and bottom of the reactor, using hooks and springs (see Fig. 2-14 in Chapter 2). The amount of catalyst in the reactor was estimated by weighing all strings before arranging them in the reactor, and correcting for the weight of the metal wires on which the particles are stringed, the weight of the springs and the amount of water on the catalyst under ambient conditions.

3.3 Experiments conducted

The most important variables to influence the reactant conversion in a BSR with a given type of catalyst, are the space velocity and the temperature. To a smaller extent the conversion is influenced by the relative pitch (on which the mass transfer coefficient depends), the nitric oxide concentration at the inlet (as the test reaction is non-first order), the catalyst particle diameter (which influences the effectiveness factor), and the oxygen and water concentrations (which influence the reaction rate constant). In turbulent flow the conversion is also influenced by the Reynolds number, through the mass transfer coefficient.

Except for the oxygen and water concentrations, all variables listed above were varied in the experiments, to check whether the various models adequately described the dependence of the NO conversion on those variables. It was unnecessary to vary the oxygen and water concentrations, because the rate constant can be varied much more effectively by varying the temperature.

Because the validation experiments were not intended to enable estimation of parameters in the reactor models, it was not necessary to create an experimental design like the one discussed in Chapter 4, Section 4.2. One would rather do series of runs in which one variable is varied at a time, to see how well the models predict the trends in the conversion; this procedure was followed in the validation experiments.

A point of practical concern in the choice of the experimental conditions is that the conversion should be in such a range that the relative error in the measured reactant

inlet and outlet concentrations is small, as well as the relative error in the difference between the inlet and outlet concentrations. This implies that the conversion is preferably between 20 to 80%. To obtain these conversions in the relatively short (0.5 m) lab-scale BSR modules, only relatively low linear gas velocities could be used, and as a result all validation experiments were done in the laminar flow regime. Fortunately this does not really affect the usefulness of the validation experiments; the only parameter that strongly depends on the flow regime (besides the friction factor) is the mass transfer coefficient, and the influence of the mass transfer rate will only decrease when going from laminar to turbulent flow.

The experimental range of conditions is listed in Table 5-1. For all three tested relative pitches, the wall subchannels made up *ca.* 20% of the total flow area. Using the methods described in Chapter 2, it was estimated that in all cases *ca.* 8% of the flow goes through wall subchannels. From this, only small effects of the wall on the reactant conversion were expected, hence small differences between the predictions made with the CBEF model and the CBSF model. In total, a number of 157 successful runs were done.

Table 5-1 Process conditions in the experimental validation of the BSR models

T	413 - 453	[K]
p	0.11	[MPa]
$c_{NO,in}$	50 - 150	[ppmv]
c_{O_2}	5	[vol. %]
c_{H_2O}	15	[vol. %]
$c_{NH_3,in}$	1000	[ppmv]
s/d	1.00, 1.38, 2.75	[-]
d	1.6, 3.2	[mm]

4 Results and discussion

4.1 Pressure drop experiments

In general the laminar friction factor was adequately predicted by the models described in Chapter 2. As an example, the experimental friction factors for the BSR with particles of 3.2 mm \varnothing and a relative pitch of 1.38 are compared with the predicted values in Fig. 5-11. The flow appears to become non-laminar at a Reynolds number of *ca.* 1000; in the turbulent flow regime the friction factor can be fitted with an empirical roughness function value of -1 (see Eq. 2-16 in Chapter 2).

Also for particles of 3.2 mm \varnothing and a relative pitch of 1.0 the laminar friction factor was predicted adequately; see Fig. 5-12. It can be seen that the deviation from laminar

flow already starts at a Reynolds number between 200 and 300 (corresponding to a linear gas velocity at ambient conditions of 3.7 to 5.5 m/s); this is in full agreement with the conclusions of Chapter 2. In the turbulent flow regime the experimental friction factors can be fitted with a roughness function of -5, which indicates considerable roughness; the high roughness is probably due to the non-uniformity of the catalyst extrudates.

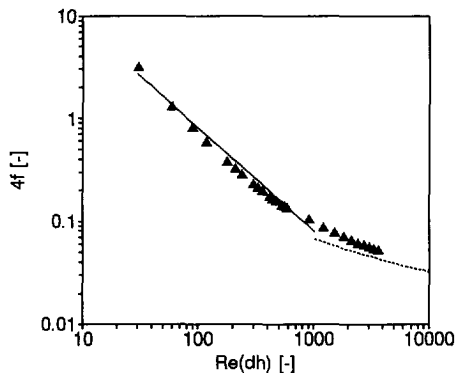


Figure 5-11

Friction factors for $s/d = 1.38$.

Triangles: experimental values; solid lines: prediction for laminar flow;

lower dashed line: prediction for turbulent flow in a hydraulically smooth rod bundle;

upper dashed line (Fig. 5-12 only): prediction for turbulent flow in a hydraulically rough rod bundle, with one fitted parameter.

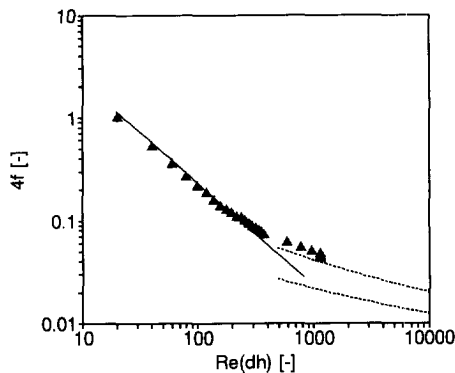


Figure 5-12

Friction factors for $s/d = 1.00$.

4.2 Validation of the mathematical reactor models

Turbo Pascal computer codes to numerically solve the models described in Section 2.4, were developed by Takács (1994), Aditia (1994) and De Vries (1994). The PDE's were solved using a finite difference method, with centered differencing discretization in the lateral direction and backward differencing in the axial direction. The ODE's were mostly solved with a Runge-Kutta method. The numerical error of the solutions was checked by changing the step size, and the step size was chosen small enough to keep the numerical error below half a percent.

Unfortunately, for the ILCEC model even the mild tolerance of half a percent led to computation times of several days per run (on an Intel 486 66 MHz processor). Therefore the adequacy of this model could not be fully tested. A few runs were calculated with the ILCEC model for the experiments with a relative pitch of 1.0, where the strongest angular gradients in the catalyst particle are expected (see

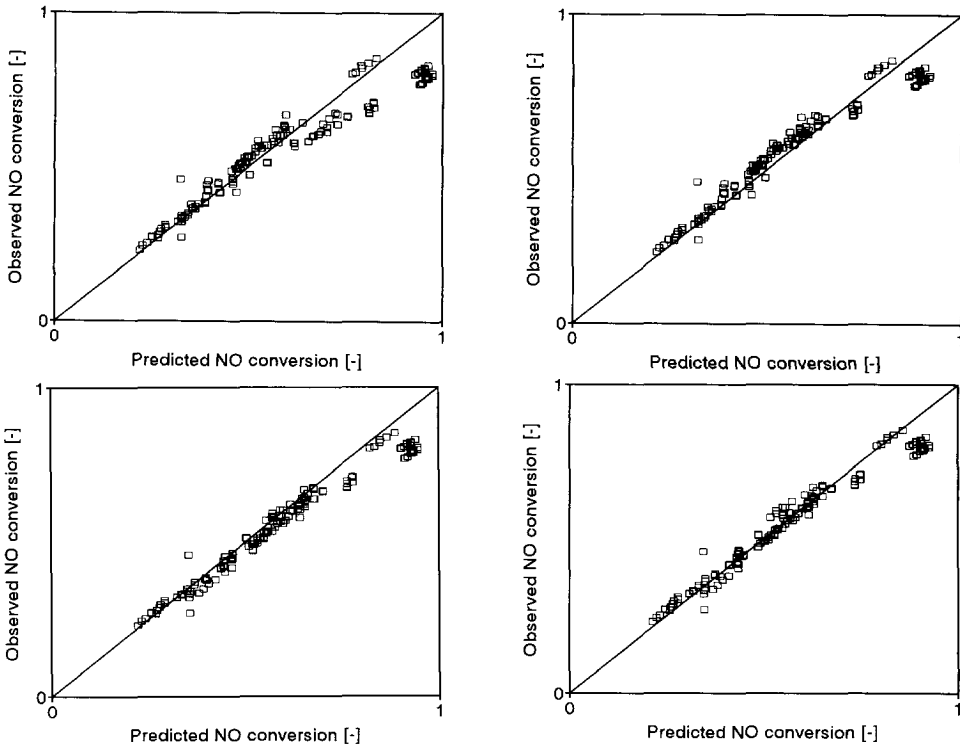


Figure 5-13 Parity plots of the NO conversion in the BSR.
 (a) **ILCR** model; (b) **ILCF** model; (c) **CBEF** model; (d) **CBSF** model.

Chapter 3, Section 2.3.1). The conversions calculated with the **ILCEC** model appeared to practically coincide with the values calculated with the **ILCF** model. The computation time needed to solve the **ILCF**, **ILCR**, **CBEF** and **CBSF** models is between 15 and 45 seconds (486 / 66 MHz). The performance of these models is presented in the form of parity plots in Figs. 5-13a to d. On the eye the plots show a satisfactory agreement between the predicted NO conversion and the experimental value, especially when it is taken into account that the models have **not** been fitted in any way to the experimental data. The deviations between the model predictions and the experimental observations are more or less in agreement with the expected deviations discussed in Section 2.4.6. The models based on the 'infinitely long cylinder' approximation (**ILCF** and **ILCR**) underestimate the conversion for most runs (except a few clusters of points at high conversions, which will be discussed below). Of the two models based on the 'catalyst bead' approximation (**CBEF** and **CBSF**), the first one generally overestimates the conversion, as expected. The second one, however, predicts the conversion correctly on the average, whereas a slight over-prediction was expected. This implies that the negative effect of the flow distribution on the conversion is smaller than predicted by the model; this is plausible, because the

CBSF gives a prediction for the extreme situation that there is no lateral exchange of reactants at all between the subchannels, which is obviously only approximately true. To see whether the models correctly predict trends of the conversion as a function of the important process variables, the experimental conversions were plotted together with the predicted values as a function of either the temperature, the linear gas velocity or the NO inlet concentration, for different relative pitches; see Figs. 5-14a to d. The following comments can be made:

Ad Fig. 5-14a:

It becomes apparent that with increasing temperature, the experimentally observed conversion in the BSR filled with the 1.6 mm \varnothing catalyst, increases less rapidly with temperature than predicted. Two explanations can be given; the first is that the activation energy is lower than estimated from the kinetic study, the second is that the effective diffusivity in the particles was overestimated. The latter explanation seems most likely, because 1) the estimation of the activation energy for this catalyst was based on many kinetic experiments (*ca.* 200) and was believed to be quite accurate, and 2) the estimation of the pore diffusion fit parameter Ω for this catalyst was based on less than 30 kinetic experiments, in many of which the experimentally determined effectiveness factor was close to one; obviously this causes a considerable uncertainty in the estimation of Ω .

Ad Fig. 5-14b:

All models excellently describe the trend of the conversion with the linear gas velocity.

Ad Fig. 5-14c:

The conversion seems to drop somewhat faster with increasing inlet NO concentration, than predicted by the models. Possible explanations are that the order in NO is somewhat smaller than the value of 0.713 assumed in the models, or that the pore diffusion parameter Ω is somewhat higher than the value of 0.67 assumed for this catalyst in the models. However, the trend of the difference between model and observation with inlet NO concentration is only marginal.

Ad Fig. 5-14d:

At low linear gas velocities (or high conversions) all models strongly overpredict the conversion. The **ILCR** model even overpredicts the conversion for all runs. The experiments that this figure pertains to, with a particle diameter of 3.2 mm and a relative pitch of 1.0, correspond to the clouds of points in Figs. 5-13a to d that significantly deviate from the $y=x$ line.

Only the overestimation by the **ILCR** model can be explained. In this model the assumption of axial symmetry around each string results of an overestimation of the mass (and momentum) transfer coefficient at low relative pitches (see Chapters 2 and 3). The cause of the strong overestimation by the other models of the conversion at low linear gas velocities, cannot be identified. A possible explanation is the fact that the high conversions correspond to relatively low NO concentrations, at which a relatively high inaccuracy is expected of the kinetic model and the measurement of the NO concentrations.

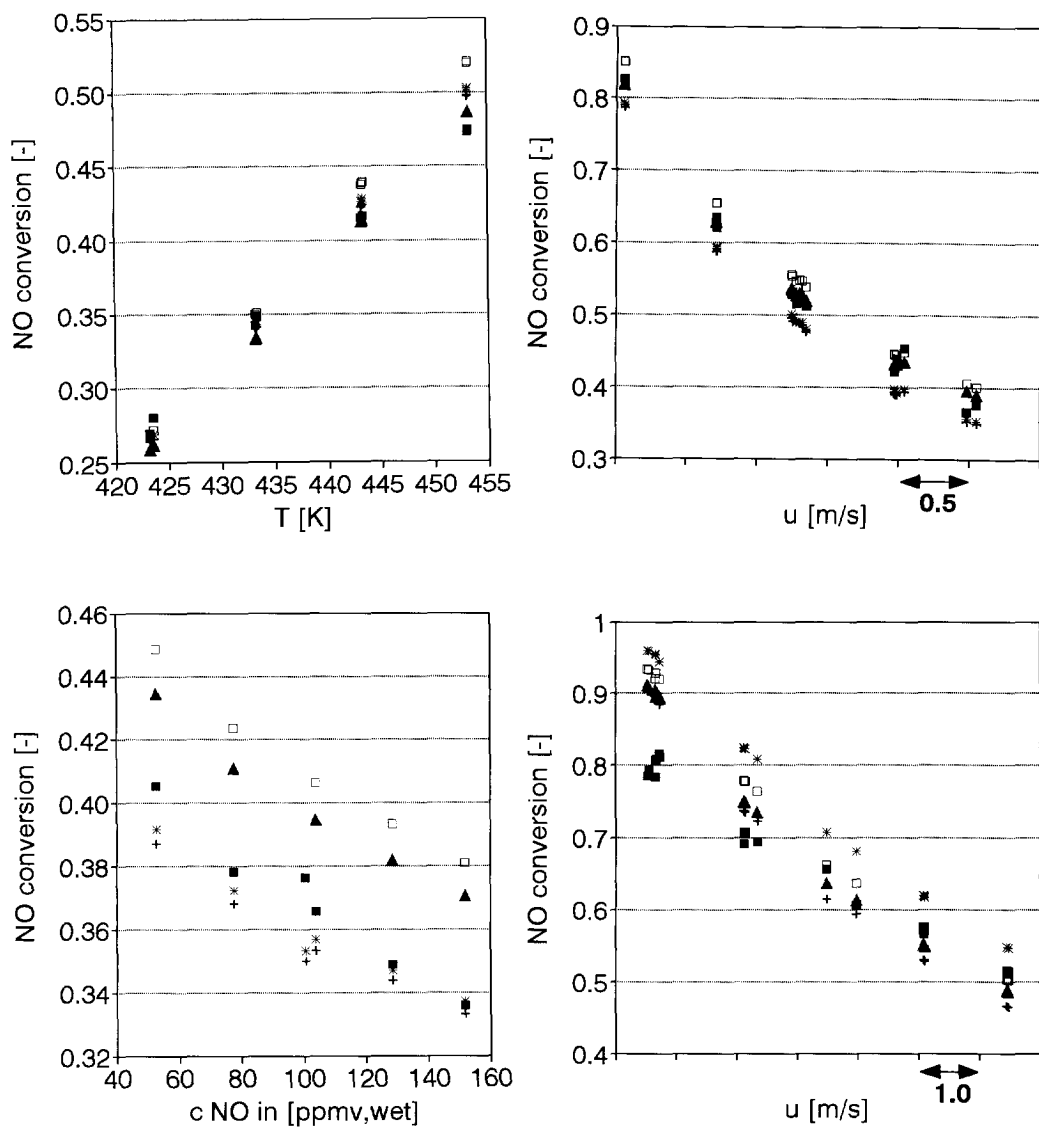


Figure 5-14 Trends of the NO conversion with various process variables. Conditions:
 (a) $d_p = 1.6$ mm, $s/d = 2.75$, $c_{NO,in} = 100$ ppmv, u_z constant.
 (b) $d_p = 3.2$ mm, $s/d = 1.38$, $c_{NO,in} = 100$ ppmv, $T = 433$ K.
 (c) $d_p = 3.2$ mm, $s/d = 1.38$, $T = 433$ K, u_z constant.
 (d) $d_p = 3.2$ mm, $s/d = 1.00$, $c_{NO,in} = 100$ ppmv, $T = 433$ K.
 Symbols: ■ = experimental; * = ILCR model; + = ILCF model;
 □ = CBEF model; ▲ = CBSF model.

Without any formal statistical test, it can be concluded from the parity plots that the **ILCF**, **ILCR** and **CBEF** model do not adequately describe the NO conversion. Indeed, for a model to be adequate the residuals (*i.e.* the deviations of the model predictions from the observations) should be normally distributed around zero, which is clearly not true for those models.

To test whether the **CBSF** model is adequate, the residuals should be compared to the standard deviation of the observations that is estimated from replicated runs. A total number of 15 replicated runs were done, at four different settings. Based on these, the standard deviation of the observed conversion (after correction for measured variations in settings) was estimated to be less than two percent. The corresponding *t* value for calculation of the 95% confidence interval is 2.2. Based on these values and the parity plot of the **CBSF** model, it was concluded that this model adequately describes the observations, except the runs described in the previous paragraph. It is likely, however, that the good predictions by the **CBSF** model partly result from the fact that two errors cancel each other (see the discussion of the parity plot of this model). If this is true, there is no reason those errors should also cancel at different conditions. It would therefore be useful to do more validation experiments, at different conditions (*e.g.* with relatively large wall distances).

5 Conclusions

The conversion of NO in lab-scale BSR modules can be predicted with an inaccuracy of *ca.* ten percent by four relatively simple mathematical models, of which the parameters were determined with independent experiments. All models satisfactorily describe the trends of the conversion with the most important reactor geometry variables and process condition variables. As expected, the **ILCF** and the **ILCR** model generally underpredict the conversion, whereas the **CBEF** model generally overestimates it. The **CBSF** model gives the most accurate prediction of the NO conversion: on the average, the predicted conversion deviates *ca.* five percent (relative) from the experimentally determined value. Such deviations can be attributed to stochastic variations in the experiments. However, possibly the good predictions by the **CBSF** model are caused by cancelling of two errors; to check this, more validation experiments should be done.

Acknowledgements

Sri Aditia (Adi), Niek de Vries and Kálmán Takács are acknowledged for their substantial contribution to the work reported in this chapter.

Notation

A_p	mass transfer surface area	$[\text{m}^2_{\text{part.}}]$
c_A	concentration of reactant A	$[\text{mol}_A/\text{m}^3_{\text{fluid.}}]$
$c_{A,b}$	concentration of A in the bulk phase (cup mixing average of the fluid domain)	$[\text{mol}_A/\text{m}^3_{\text{fluid.}}]$
$c_{A,in}$	concentration of a at the reactor inlet	$[\text{mol}_A/\text{m}^3_{\text{fluid.}}]$
$c_{A,s}$	concentration of A at the external catalyst particle surface	$[\text{mol}_A/\text{m}^3_{\text{fluid.}}]$
D	diffusivity (free molecular or turbulent)	$[\text{m}^2/\text{s}]$
D_e	effective pore diffusion constant	$[\text{m}^2/\text{s}]$
D_{free}	free molecular diffusion constant	$[\text{m}^2/\text{s}]$
D_{lat}	effective lateral diffusion/dispersion coefficient in a rod bundle	$[\text{m}^2/\text{s}]$
D_{Kn}	Knudsen diffusion constant	$[\text{m}^2/\text{s}]$
Da_{II}	second Damköhler number	[-]
d	rod or particle diameter in a rod bundle or BSR	$[\text{m}_{\text{part.}}]$
d_a	annulus diameter	$[\text{m}]$
d_h	hydraulic channel diameter (incl. reactor perimeter)	$[\text{m}]$
$d_{h,c}$	hydraulic central subchannel diameter	$[\text{m}]$
d_k	diameter of the inert kernel of a stringed bead	$[\text{m}]$
d_p	catalyst particle diameter	$[\text{m}_{\text{part.}}]$
$d_{p,s}$	diameter of a 'shrunk' cylinder	$[\text{m}_{\text{part.}}]$
d_r	reactor diameter	$[\text{m}_{\text{reactor.}}]$
E_A	activation energy	$[\text{J}/\text{mole}]$
FO	Fourier number	[-]
g	gap between two particles on a string	$[\text{m}]$
H	height (or length) of a catalyst particle	$[\text{m}_{\text{part.}}]$
k_g	mass transfer coefficient	$[\text{m}/\text{s}]$

k	n-th order rate constant, expressed per unit catalyst volume	$[(\text{m}^3_{\text{fluid}}/\text{mol}_A)^n \cdot \text{mol}_A / (\text{m}^3_{\text{cat}} \cdot \text{s})]$
k_0	q-th order rate expression pre-exponential factor, expressed per unit catalyst volume	$[(\text{m}^3_{\text{fluid}}/\text{mol}_A)^q \cdot \text{mol}_A / (\text{m}^3_{\text{cat}} \cdot \text{s})]$
L	reactor length	[m]
n, m, p	reaction orders in NO, O ₂ and H ₂ O	[-]
p	pressure in the reactor	[Pa]
r	radial coordinate	[m]
$-r_A$	reaction rate (= rate of consumption) of reactant A, expressed per unit catalyst mass	$[\text{mol}_A / (\text{kg}_{\text{cat}} \cdot \text{s})]$
R	(outer) radius of a cylindrical or ring-shaped particle	$[\text{m}_{\text{ran}}]$
\mathcal{R}_A	reaction rate (= rate of consumption of reactant A, expressed per unit catalyst volume	$[\text{mol}_A / (\text{m}^3_{\text{cat}} \cdot \text{s})]$
R_g	gas constant (8.31)	$[\text{J} / (\text{mol} \cdot \text{K})]$
Re	Reynolds number, based on the hydraulic diameter of the complete bundle (incl. the perimeter of the reactor shell)	[-]
s	pitch of strings in a BSR or rods in a rod bundle, <i>i.e.</i> the heart-to-heart distance	[m]
Sh	Sherwood number ($k_g d_h / D_{\text{free}}$)	[-]
T	temperature	[K]
u_z	linear axial gas velocity	[m/s]
$\langle u_z \rangle$	cup mixing average of the linear axial gas velocity in a subchannel	[m/s]
V_p	active catalyst particle volume	
z	axial coordinate	[m]
<i>Greek letters</i>		
α	angular coordinate	[rad] or [deg]
ε	catalyst material voidage	$[\text{m}^3_{\text{void}} / \text{m}^2_{\text{part}}]$
ε_i	error in the estimation of the effectiveness factor of catalyst particle i	[-]
ε_r	rod bundle reactor voidage	$[\text{m}^3_{\text{void}} / \text{m}^3_{\text{reactor}}]$
η	effectiveness factor of a catalyst particle	[-]
η_i	effectiveness factor of a catalyst particle, calculated for particle i	[-]
μ	dynamic fluid viscosity, molecular or turbulent	[Pa · s]
ρ_{cat}	catalyst particle density	$[\text{kg}_{\text{cat}} / \text{m}^3_{\text{cat}}]$
τ	catalyst material tortuosity	[-]
Ω	catalyst pore diffusion fit parameter	[-]

References

- Aditia, S., 1994, *Experimental validation of the mathematical model for the Bead String Reactor* (MSc. thesis). Faculty of Chemical Engineering and Materials Science, Delft University of Technology, Delft, The Netherlands.
- SPDE, Inc., 1992, *SPDE* (software package). SPDE, Inc., Bass Lake, CA, USA.
- Takács, K., 1994, *Mathematical modelling of the Bead String Reactor* (internal report). Faculty of Chemical Engineering and Materials Science, Delft University of Technology, Delft, The Netherlands.
- De Vries, N., 1994, *Validation of mathematical models for the Bead String Reactor* (MSc. thesis). Faculty of Chemical Engineering and Materials Science, Delft University of Technology, Delft, The Netherlands.

Chapter 6

Mass transfer in a Parallel Passage Reactor

published as:

H.P. Calis, T.S. Everwijn, A.W. Gerritsen, C.M. van den Bleek,
F.G. van Dongen and F. Goudriaan, 1994, Mass Transfer Characteristics of
Parallel Passage Reactors. *Chem. Engng Sci.* **49**, 4289-4297.

Contents

Summary	177
1 Introduction	177
2 Theory of mass transfer in a Parallel Passage Reactor	179
3 Efficiency of a catalyst bed in a Parallel Passage Reactor	182
4 Experimental work	183
4.1 Equipment and materials used	183
4.2 Experimental procedures	185
5 Results and discussion	186
5.1 Pressure drop	186
5.2 Catalyst bed efficiency	186
5.3 Estimation of the apparent bed dispersion coefficient	190
6 Conclusions	192
Acknowledgements	193
Notation	193
References	194

Summary

Relations were developed to describe mass transport phenomena in Parallel Passage Reactors (PPR), dustproof, low-pressure drop reactors consisting of shallow packed beds of catalyst particles confined between wire gauze screens. In a PPR, gas flows along the beds, and reactants are transferred through the screens to the catalyst particles by diffusion and dispersion. At low gas velocities along the beds, interparticle mass transfer in the beds is dominated by diffusion. At higher gas velocities it is significantly enhanced by dispersion, caused by a small gas flow through the catalyst beds. This flow, parallel to the bulk flow, results partly from the axial pressure gradient across the reactor. Up to a few particle diameters from the wire gauze screens, the gas flow through the beds is higher than would be expected from the pressure gradient. This is caused by the higher bed voidage near the wire gauze screen and by convective transfer of momentum from the gas channels, through the wire gauze screens, into the beds. The developed mass transfer relations were used to assess the feasibility of the PPR as a reactor for catalytic denoxing of industrial flue gases. At gas velocities normally encountered in industrial denoxing, dispersion in the catalyst beds of the PPR greatly enhances its efficiency. If the thickness of the catalyst slabs does not exceed six to ten catalyst particle diameters, the reactor performance is controlled more by intraparticle diffusion than by interparticle mass transfer. This holds true except for very low gas velocities. If this rule of thumb is obeyed, the PPR is an attractive alternative to the Honeycomb Reactor for full Selective Catalytic Reduction of nitric oxide, especially at low temperatures.

1 Introduction

Whenever pressure drop or fouling with dust is a cost determining factor in the operation of a gas/solid reactor, a Parallel Passage Reactor (PPR) is an interesting alternative to the traditional fixed bed reactor. The PPR is characterized by shallow packed beds of catalyst particles, confined between wire gauze screens (see Fig. 6-1). The gas flows along the beds and reactants are transferred, by diffusion and dispersion, through the screens to the catalyst particles. Because the channels through which the gas flows are straight, there is relatively little friction between the flowing gas and the catalyst packages, resulting in a low pressure drop. Furthermore, this reactor is essentially dustproof, since dust present in the gas can flow straight through the

reactor, without impinging upon obstacles on its way. These two characteristics make the PPR, in principle, suitable for end-of-pipe processes like catalytic removal of NO_x from industrial flue gases ("denoxing"). In this respect, the PPR should be compared to the monolithic reactor or Honeycomb Reactor, which is widely used for that purpose. An important advantage of the PPR compared to the Honeycomb Reactor is the fact that standard catalyst particles can be used in the PPR, as opposed to the complicated manufacture of the monolithic catalyst for the Honeycomb Reactor.

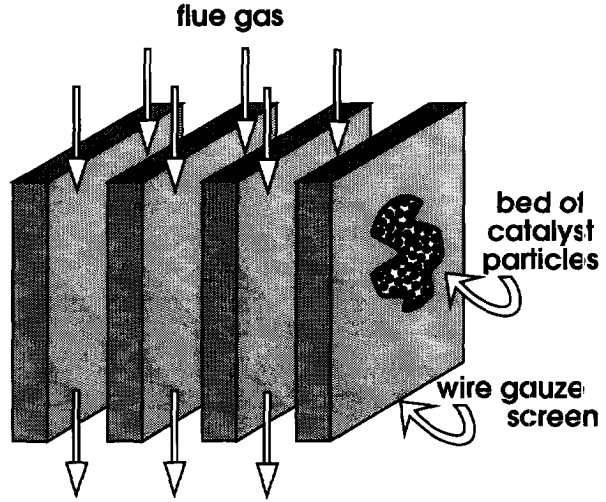


Figure 6-1 Principle of the Parallel Passage Reactor.

The concept of the PPR was used in the Shell Flue Gas Desulfurization Process (SFGD) in the early 1970s. In this process, a CuO/ γ -Al₂O₃ catalyst was used as a regenerative sorbent for SO₂ removal (Van Helden, 1969; Dautzenberg *et al.*, 1971; Conser, 1973; Ploeg *et al.*, 1974; Van der Linde, 1982). The PPR was also used in the Shell Flue Gas Treating Process, in which copper on alumina acts both as an acceptor for sulfur dioxide and as a catalyst for Selective Catalytic Reduction (SCR) of nitric oxide with ammonia (Siddiqi and Tenini, 1981). The latter process is still receiving attention at this moment (e.g. Centi *et al.*, 1992; Kiel *et al.*, 1992).

Application of an improved version of the PPR for SCR alone was described by Goudriaan *et al.* (1991). In 1990, a PPR filled with denox catalyst for SCR of NO with ammonia was successfully installed and put into operation at Rheinische Olefin Werke in Wesseling, Germany (a joint venture between BASF and Shell).

Like the design of a traditional fixed bed reactor and of a monolithic reactor, the design of a PPR is governed by pressure drop and mass transfer. The scope of this work is to present relations to describe mass transport phenomena in a PPR, and to use these relations to assess the feasibility of the PPR as a reactor for catalytic denoxing. To this end experiments were performed with several PPR modules, filled with denox catalyst. The various modules differ mainly in the shape and thickness of the catalyst beds, and the shape and activity of the catalyst particles. The influence of mass transfer on the performance of a module under certain process conditions is expressed in the quantity E_{bed} , the efficiency of the catalyst bed. E_{bed} is defined as the ratio of the space velocity in the PPR, for a specific experiment, to the space velocity

needed for the same chemical conversion if interparticle mass transfer limitation were absent.

2 Theory of mass transfer in a Parallel Passage Reactor

The key to understanding mass transport phenomena in a PPR is that the axial pressure gradient across the reactor, resulting from friction of the bulk flow with the wire gauze walls of the gas channels, induces a relatively small gas flow *through* the packed beds of catalyst particles, parallel to the bulk flow through the gas channels between the beds. The importance of the small gas flow through the catalyst beds stems from the lateral dispersion that it causes in the beds, which may significantly enhance the interparticle mass transfer rate. As a first approximation, the superficial gas velocity u through the bed may be estimated with common equations for flow through porous media, such as Ergun's equation (Ergun, 1952):

$$\nabla p = \frac{150 \mu u (1 - \epsilon)^2}{d_p^2 \epsilon^3} + \frac{1.75 \rho u^2 (1 - \epsilon)}{d_p \epsilon^3} \quad (6-1)$$

Based on this equation, a typical result for a realistic PPR would be that u is three orders of magnitude smaller than the velocity in the gas channels. However, it should be realized that Ergun's equation is only accurate for beds of a constant or average voidage, whereas in packed beds a significant voidage profile exists near the wall of the bed. This profile extends up to four or five particle diameters from the wall (Lerou and Froment, 1977). As a result, the gas flow through the catalyst beds is not uniform. In the case of solid walls, the interstitial gas velocity near the wall may well be twice as high as would be calculated from Ergun's relation for the densely packed bed (Schwartz and Smith, 1953; Schertz and Bischoff, 1969). This holds true, especially for narrow beds, i.e. beds not wider than ten particle diameters. In the case of wire gauze walls, as in a PPR, the velocity distribution may be more pronounced, because the pores of the gauze allow transport of momentum from the gas channel (where the gas velocity is much higher) into the catalyst beds. This phenomenon was described in detail by Hoebink *et al.* (1993), who studied mass transfer in a PPR designed for automotive exhaust cleaning. They measured gas velocities in the catalyst bed, and found that the velocity close to the gauze (0.5 mm, or 0.5 particle diameters) was five to ten times higher than far away from the gauze (20 mm). Only the latter velocity could be predicted by Ergun's equation.

Because in a PPR the gas flows mainly *along* the catalyst beds, the catalyst particles are not in direct contact with the main gas stream. As a result, interparticle mass

transfer limitation may significantly lower the apparent activity of a catalyst in a PPR. To gain insight into the design parameters determining the efficiency of the catalyst beds in a PPR, it is useful to identify six consecutive mass transfer steps to be taken by the reactants, before reaction at the catalytic sites can take place. These steps are depicted schematically in Fig. 6-2. Because the steps occur in series, the overall mass transfer rate is largely governed by the slowest one. The six mass transfer steps are:

- (1) from the bulk flow in the gas channels to the outside of the wire gauze screens;
- (2) through the wire gauze screen;
- (3) from the wire gauze screen to the edge of the bed of catalyst particles;
- (4) from the edge of the bed, through the interstitial space between the catalyst particles in the bed, to the film layer around a catalyst particle;
- (5) through the film layer around the catalyst particle to the outer surface of the particle; and
- (6) through the pores in the particle.

Distinction between steps 4 and 5 is impossible at the very low gas velocities encountered in the catalyst beds of a PPR, since the concept of a laminar film layer cannot be applied to particle beds in which the flow is laminar. Therefore, mass transfer steps 4 and 5 will be lumped together and described by an "effective lateral bed dispersion coefficient", which takes into account both diffusion and lateral dispersion effects.

It should be noted that, given

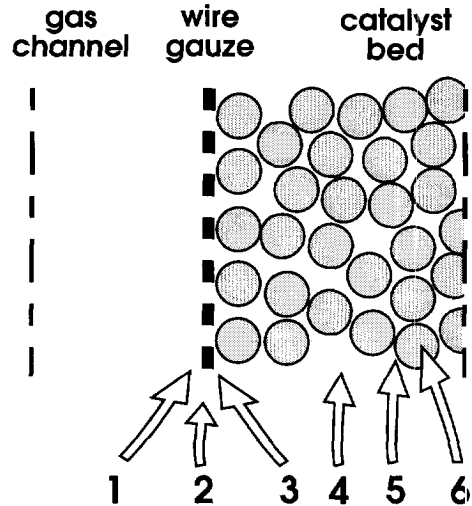


Figure 6-2 The six consecutive mass transfer steps in a PPR.

the catalyst particles, step 6 does not depend in any way on the type of reactor. Therefore, limitation of the reaction rate by intraparticle pore diffusion is not an issue when comparing the performance of different PPR configurations. Of course, it is important when comparing the PPR with, e.g., the Honeycomb Reactor.

In the study performed by Hoebink *et al.* (1993), it was found that steps 2 and 3 are much faster than the other steps. Furthermore, it was found that step 1 influences the overall mass transfer rates when the cross-sectional shape of the gas channel has sharp corners ($< 90^\circ$), as with triangular channels. With circular or narrow rectangular channels, step 1 is not rate limiting. In all cases, the overall mass transfer rate is

limited (except step 6) by steps 4/5. The conclusion is that to predict the performance of a PPR, one should at least be able to describe steps 4/5.

According to several authors (Schertz and Bischoff, 1969; Bauer, 1988; Kalthoff and Vortmeyer, 1980; Schrauwen, 1989; Van Dongen, 1989), lateral mass transfer in packed beds of catalyst particles can be described by an "effective lateral bed dispersion coefficient", D_{bed} . It is assumed that D_{bed} is made up of two contributions: a static contribution D_{stat} resulting from diffusion, and a convective contribution D_{conv} resulting from dispersion:

$$D_{bed} = D_{stat} + D_{conv} \quad (6-2)$$

Schrauwen (1989) and Van Dongen (1989) related D_{stat} to the bed voidage ϵ , the bed tortuosity τ and the free diffusion coefficient D_{free} :

$$D_{stat} = \frac{\epsilon}{\tau} D_{free} \quad (6-3)$$

Kalthoff and Vortmeyer (1980) derived an expression for D_{stat} from a theoretical relation for heat transfer in cylindrical packed beds, published by Zehner and Schlünder (1970, 1972) and Bauer and Schlünder (1978):

$$D_{stat} = (1 - \sqrt{1 - \epsilon}) D_{free} \quad (6-4)$$

For typical values of ϵ (0.40-0.45) and τ (1.5-2.0), eqs (6-3) and (6-4) yield the same results: D_{stat}/D_{free} equals 0.2-0.3.

Schrauwen (1989) and Van Dongen (1989) related D_{conv} to the superficial gas velocity in the bed, u , and a mixing length l_g :

$$D_{conv} = l_g u \quad (6-5)$$

The mixing length depends strongly on the size and shape of the particles, and can generally be expressed as the product of a shape factor and a characteristic particle size.

The relation proposed by Kalthoff and Vortmeyer (1980) takes into account the thickness of the bed (through the bed to particle diameter ratio d_b/d_p), but not the shape of the particles:

$$D_{conv} = \frac{d_p}{1.1K} u \quad (6-6)$$

in which K is given by:

$$K = 8 \left[2 - \left(1 - \frac{2}{d_b/d_p} \right)^2 \right] \quad (6-7)$$

Eq. (6-6) was generalized for particle shape by Schlünder and Tsotsas (1988):

$$D_{conv} = \frac{x_m}{K} u \quad (6-8)$$

in which K is given by Eq. (6-7); the mixing length x_m is related to a shape factor F_v and a characteristic particle size d_{char} :

$$x_m = F_v d_{char} \quad (6-9)$$

For spheres, a shape factor of 1.15 is reported and the characteristic particle size equals the sphere diameter. For cylinders, the shape factor is 1.75 and the characteristic particle size is given by:

$$d_{char} = \left(\frac{3l_c}{2d_c} \right)^{1/3} d_c \quad (6-10)$$

3 Efficiency of a catalyst bed in a Parallel Passage Reactor

The effect of interparticle mass transfer on the performance of a specific PPR type will be expressed as E_{bed} , the efficiency of a catalyst bed in a PPR. It is defined as the ratio of the space velocity in the PPR, for a specific experiment, to the space velocity that in an "ideal reactor", filled with exactly the same catalyst particles and under identical conditions, leads to the same chemical conversion. An "ideal reactor" is defined here as a classic fixed bed reactor operated under such conditions that deviations from ideal plug flow and interparticle mass transfer limitations are negligible.

As the comparison between the PPR and the "ideal reactor" is made based on the same catalyst particles, the efficiency of one catalyst particle as such (influenced by pore diffusion), is not important. Consequently, E_{bed} is a true measure of retardation of the overall rate in a PPR caused by the limited interparticle mass transfer rate.

4 Experimental work

4.1 Equipment and materials used

Six Parallel Passage Reactor configurations, described below and in Table 6-1 (A-F), were tested as modules with standard dimensions: 500 mm long in the direction of flow, and 160 mm × 60 mm in cross section.

Module A had corrugated wire gauze screens (Fig. 6-3). This module was constructed with gauze with a standard wire thickness of 0.30 mm. Fig. 6-3 shows that the catalyst beds are blinded perpendicular to the flow, both at the inlet and outlet of the module. These blinds provide mechanical strength to the structure; in the case of a dusty flue gas, they also prevent entrance of dust into the beds at the module inlet.

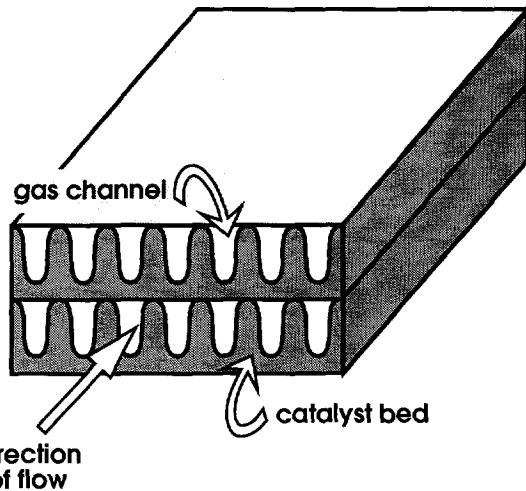


Figure 6-3 Schematic view of the laboratory PPR modules A, B and C.

Module B was the same as A but with large holes in the blinds of the catalyst beds at the module inlet. These holes were expected to increase the gas flow *through* the beds, thus increasing dispersion of reactants in the beds, resulting in a higher value of E_{bed} .

Module C was the same as A but constructed with thinner wire gauze than all the other modules, with a wire thickness of 0.20 mm. The thinner wire gauze was expected to reduce pressure drop across the reactor, resulting in a smaller convective gas flow through the catalyst beds.

Module D had flat catalyst beds, or envelopes. The envelopes were 7 mm thick, resulting in a hydraulic catalyst bed diameter equal to that of modules A, B and C. Module E had flat envelopes of 4 mm thickness. If interparticle mass transfer in the catalyst beds is indeed limiting E_{bed} , module E ought to have a significantly higher E_{bed} than module D.

Module F consisted of "wavy" flat envelopes of 6 mm thickness (Fig. 6-4). For this geometry, Bernoulli's law predicts a pressure profile along the direction of flow, which differs half a phase from the pressure profile in the two adjacent gas channels. This should lead to small convective gas flows laterally through the envelopes, expected to result in enhanced mass transfer in the catalyst beds.

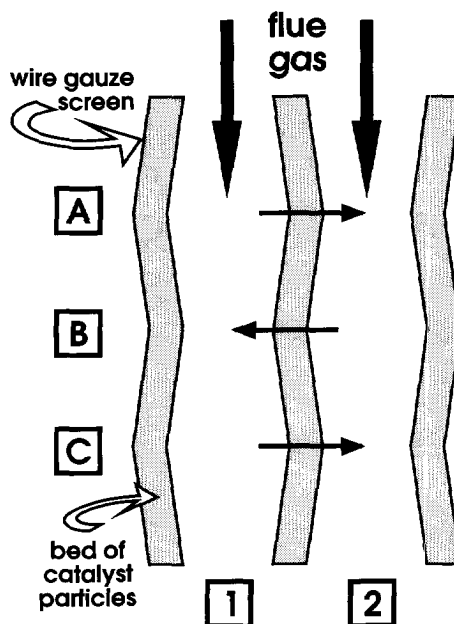


Figure 6-4 Vertical cross section of laboratory PPR module F.

Table 6-1 Dimensions and characteristics of the tested PPR configurations.

	Module				
	A, B	C	D	E	F
Hydraulic diameter catalyst bed [mm]	12.1	12.1	14.5	9.5	12.0
Hydraulic diameter gas channel [mm]	11.8	11.8	12.4	5.1	9.4
Number of catalyst beds	20	16	11	21	14
Number of gas channels	19	18	11	21	14
Wire mesh thickness [mm]	0.30	0.20	0.30	0.30	0.30

The "ideal" plug flow reactor that was used to measure the apparent catalyst activity, in the absence of interparticle mass transfer limitation, consisted of a cylindrical tube of 20 mm inner diameter, filled with 60 ml of the tested catalyst. Based on commonly used relations for axial and radial dispersion, and interparticle mass transfer in packed beds, it was concluded that the deviation from ideal behavior was within the experimental error.

Three denox catalysts were used, differing in activity and particle shape, so the effect of these variables on E_{bed} could be studied. The first catalyst, labeled A, consisted of irregularly shaped particles, a sieve fraction obtained from crushing bigger particles. The second catalyst, B, had the same morphology but a significantly lower activity than A (expressed per unit catalyst bed volume). The third catalyst, C, consisted of extrudates with the same activity as B. Because it was known (from independent measurements) that catalyst C had a significantly higher mixing length and bed voidage than A and B, C was expected to give a significantly higher value for E_{bed} .

4.2 Experimental procedures

The denox experiments with the PPR modules were performed under realistic flue gas conditions, based on a typical flue gas composition from a thermal cracking furnace for ethene production, at Rheinische Olefin Werke (ROW) in Germany. However, the test gas did not contain SO_2 or dust. Furthermore, the CO_2 present in normal flue gas was substituted by nitrogen. Justification for this was concluded from Hofmann and Weidner (1989), who found that 0-20 vol. % of CO_2 does not influence the SCR reaction rate over denox catalysts. This was confirmed for the tested catalysts by a single experiment.

The range of test conditions is given in Table 6-2. The influence of catalyst activity and particle shape on E_{bed} was studied in module A, using the three catalysts described earlier—A, B and C. Module B was tested with catalyst C. All other modules were tested with catalyst A.

The experimental setup consisted of a gas-dosing section, a reactor section and an analysis section. Nitrogen and air were dosed using rotameters, NO and NH_3 were dosed using mass flow controllers. Water was pumped from a vessel placed on a

balance. The NO concentrations in reactor feed and effluent were continuously monitored using a Thermo Electron Model 10 chemiluminescence NO- NO_2 - NO_x analyzer. The sample gas was stripped of water and ammonia by leading it through concentrated phosphoric acid, because these components would lead to significant

Table 6-2 Test conditions for NO/ NH_3 conversion experiments in various PPR configurations.

v	[m/s]	0.65 — 10.7
Re_{ch}	[-]	200 — 5000
p	[MPa]	0.102 — 0.114
T	[°C]	158 — 163
Inlet gas composition:		
H_2O	[vol. %]	13.4 — 16.3
O_2	[vol. %]	4.9 — 5.9
NO	[ppmv]	27 — 139
NH_3	[ppmv]	11 — 60
N_2		balance

falsification of the NO_x signal. The ammonia concentrations in reactor feed and effluent were continuously monitored using a Bran & Luebbe "Ecometer". Furthermore, the ammonia concentrations were determined by titration of worked-up samples prepared from diluted sulfuric acid through which a known amount of test gas had been led. The results of the two types of ammonia analysis were generally in good agreement; in the case of disagreement the results of titration were used, as this method proved to be better reproducible.

In all experiments the pressure drop across the PPR modules was measured using an inclined manometer; the measured values were corrected for estimated inlet and outlet pressure losses.

Since the denox experiments in the "ideal" plug flow reactor were not influenced by interparticle mass transfer, it was possible to establish kinetic models of the denox reaction for the various catalysts. The catalyst particles were not so small as to exclude pore diffusion limitation. Because no corrections were made for this in the derivation of the kinetic models, the models could only describe the *apparent* kinetics of the tested catalysts. However, because the very same catalysts were used in the PPR experiments, it was possible to use these kinetic models for calculations in the PPR experiments.

5 Results and discussion

5.1 Pressure drop

In Fig. 6-5 the experimental friction factors of all PPR modules are plotted as a function of the Reynolds number (Re) in the gas channels. The friction factors become constant at Reynolds numbers of approximately 1,000, which implies that fully rough turbulent flow is already reached at this relatively low Re number. This is probably the result of the very rough "wall" of the gas channels, namely the wire gauze.

5.2 Catalyst bed efficiency

In Fig. 6-6 the values of E_{bed} of all three catalysts in PPR module A are plotted as a function of the Reynolds number in the gas channels. The lines represent trends at constant inlet concentrations of the reactants, which is important because E_{bed} depends on the concentrations. This can be understood from the fact that E_{bed} depends on the balance between diffusion rate and reaction rate; the diffusion rate is first order in the

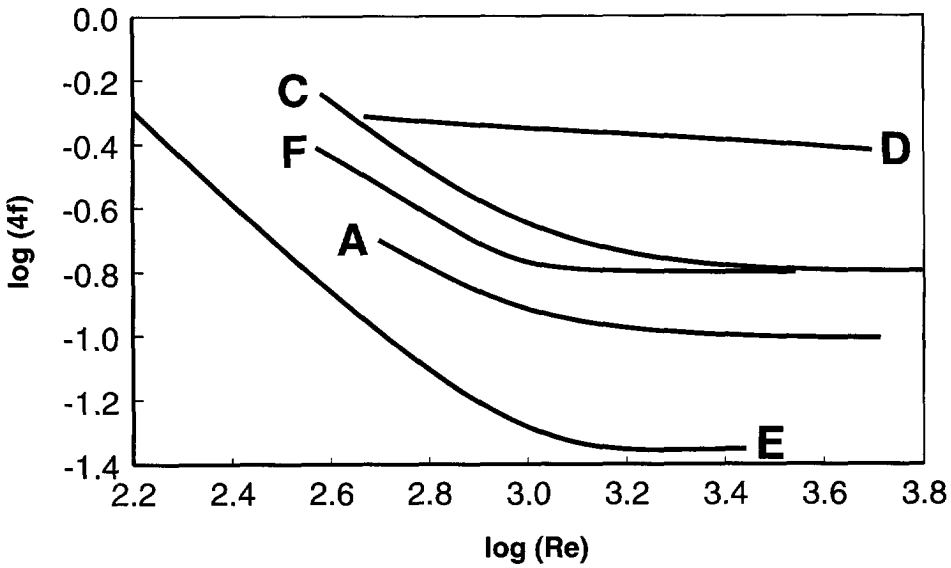


Figure 6-5 Experimental friction factors of the PPR modules (A, C-F) as a function of the Reynolds number in the gas channels.

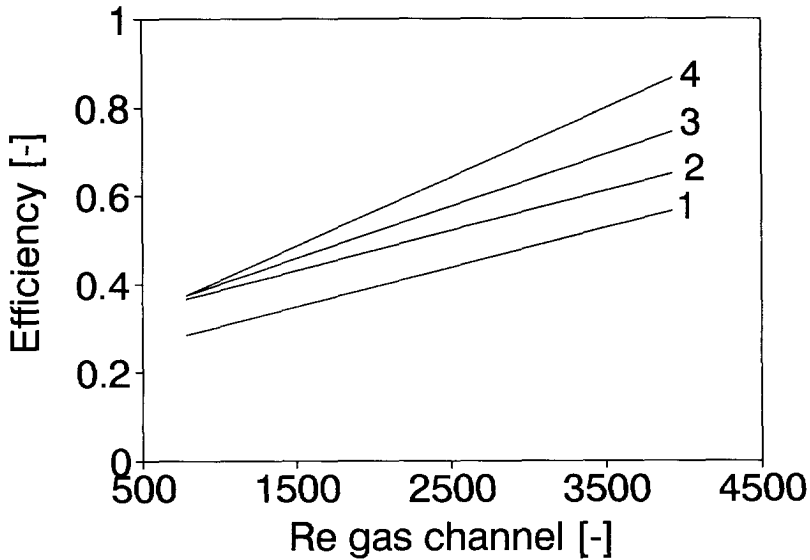


Figure 6-6 Efficiency of catalysts A, B and C in laboratory PPR modules A and B, versus the Reynolds number of the flow in the gas channels. Temperature, 160°C; inlet NO and NH₃ concentrations, 60 ppmv. 1, catalyst A in module A; 2, catalyst B in module A; 3, catalyst C in module A; 4, catalyst C in module B.

concentration whereas, in case of Selective Catalytic Reduction of NO with NH₃, the reaction rate is lower than first order in the concentrations (e.g. Bosch and Janssen, 1988). Consequently, E_{bed} increases with increasing reactant concentrations. For this reason it would have been better to perform all experiments at exactly the same concentrations, i.e. in a differential Parallel Passage Reactor, but then the results would have been dominated by inlet effects.

E_{bed} increases for all three catalysts with increasing velocity in the gas channels, as was expected from the predicted effect of flow rate on mass transfer in the catalyst beds. However, this graph might be misleading: since all experiments were performed with the same inlet concentrations, a higher Reynolds number (corresponding to a lower residence time and conversion) implies higher average reactant concentrations, thus a higher E_{bed} . It is estimated that this effect accounts for only 1/3 of the increase in E_{bed} . The rest of the increase in E_{bed} is attributed to improved interparticle mass transfer in the catalyst beds. This effect will be quantified later in this section.

Catalyst A shows a slightly lower E_{bed} than catalyst B. This can be understood from the higher activity of the first one: the more active a catalyst is, the bigger are the effects of (intra- and) interparticle diffusion limitation. Based on knowledge of the kinetics of the catalyst, it is estimated that the difference in activity between the two catalysts accounts for a difference of 5% in E_{bed} . This value corresponds to the observations.

Catalyst C shows a slightly higher E_{bed} than catalyst B, especially at high gas velocities. As these two catalysts have the same activity (expressed per unit catalyst bed volume), the higher E_{bed} of catalyst C indicates improved mass transfer, resulting from differences in voidage of the catalyst beds and shape of the particles.

Also in Fig. 6-6, the value of E_{bed} of catalyst C in PPR module B is plotted as a function of the Reynolds number in the gas channels. At high gas velocities the extra flow through the catalyst beds of module B, due to the holes in the otherwise blinded fronts of the beds, results in a significantly higher E_{bed} . However, the applicability of this method to improve the efficiency of a PPR is limited to low-dust flue gases: in a high-dust application the top part of the catalyst beds would rapidly be plugged with dust.

In Fig. 6-7 the value of E_{bed} of the catalyst A in modules A, C, D, E and F is plotted as functions of both the experimentally determined pressure gradient across the gas channels, and the gas velocity in the gas channels. Neither the wire thickness of the gauze nor the shape of the catalyst beds or gas channels seem to have a significant effect on E_{bed} . This follows from comparison of the values of modules A and C (effect of wire gauze thickness), and of the values of modules A and D (effect of catalyst bed shape); the experimental points can be represented by a single line.

The fact that interparticle mass transfer is rate limiting in most of the tested PPR modules is proved by the difference in E_{bed} between modules D and E, as the efficiency is almost inversely proportional with the catalyst bed thickness.

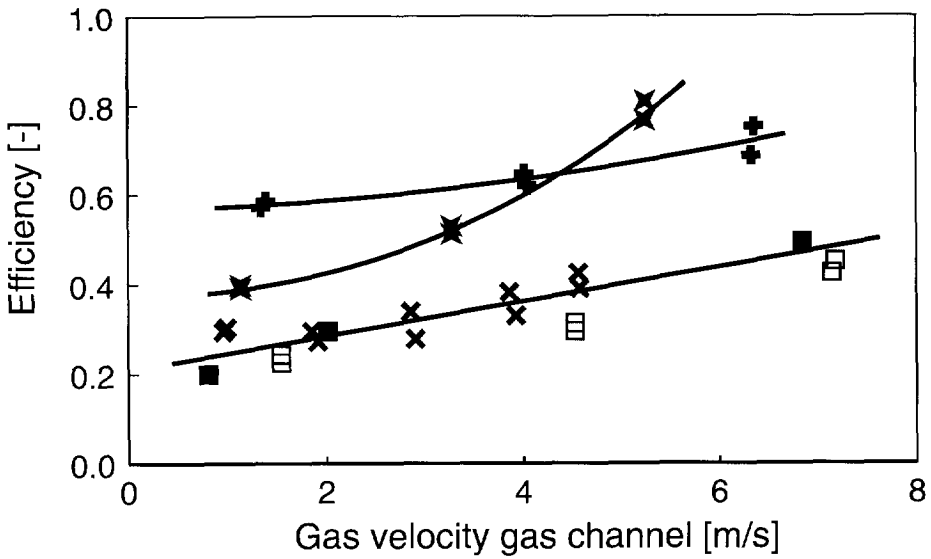
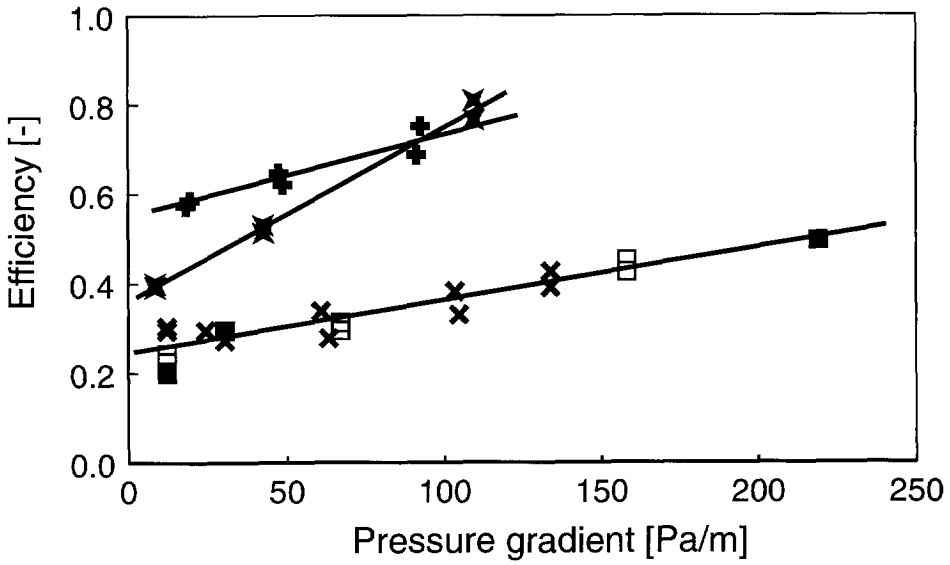


Figure 6-7 Efficiency of catalyst A in all PPR modules versus (top) the experimentally determined pressure gradient in the gas channels and (bottom) the linear gas velocity in the gas channels.

■, Module A; □, module C; ×, module D; + module E; ★, module F.

The expected "swing flow" in module F, i.e. small lateral gas flows through the catalyst beds driven by lateral pressure gradients, appears to have a significant effect on E_{bed} . At low gas velocities in the gas channels, the efficiency of module F lies between that of modules D and E. This corresponds to the thickness of the catalyst beds of these modules. However, the graph indicates that the efficiency of module F increases more rapidly with the gas velocity in the gas channels than that of the other modules. The geometry of module F is therefore considered to be the most interesting one at high gas velocities.

5.3 Estimation of the apparent bed dispersion coefficient

The results of the denox experiments in module A were used to verify a model describing mass transfer and chemical reaction in a PPR. This model was based on the following assumptions:

- The Sherwood number, Sh , that describes mass transfer from the gas channels to the catalyst beds (step 1), can be calculated from the experimentally determined friction factor, using the well-known Chilton-Colburn analogy (Chilton and Colburn, 1934):

$$j_D \left(\equiv \frac{Sh}{ReSc^{1/3}} \right) = j_H = \frac{4f}{8} \quad (6-11)$$

- Mass transfer steps 2 and 3 are fast enough not to influence the overall rate. This assumption was based on the work by Hoebink et al. (1993), discussed previously.
- Interparticle mass transfer in the catalyst beds can be described by eqs (6-2)-(6-10). The shape factors of catalysts A and B, and C, were assumed to equal those of spheres and cylinders, respectively. The superficial gas velocity in the catalyst beds was assumed to be uniform, and calculated from the experimentally determined pressure gradient using Eq. (6-1). This yields a conservative estimate of the gas velocity and, *ergo*, of the mass transfer rate (see theoretical discussion of mass transfer in a PPR).
- The apparent kinetics can be described by the kinetic models derived from the experiments performed with the "ideal" plug flow reactor.

This model was implemented in a computer program that numerically solves the partial differential equations arising from the material balance equations describing a PPR. Based on the conditions and measured pressure drop of each PPR experiment, the NO/NH₃ conversion of each experiment was predicted and compared with the measured value.

The conversions predicted by the model were all significantly lower than the measured values. This was attributed to the fact that the superficial gas velocity in the catalyst beds near the gauze is underestimated by Ergun's relation, resulting in an under-

estimation of the effective bed dispersion coefficient. To quantify this underestimation, the program was used iteratively to find for each experiment the value of the apparent effective bed dispersion coefficient D_{bed} with which the model would adequately predict the measured NO and NH₃ conversion.

In Fig. 6-8 the resulting apparent bed dispersion coefficients for catalysts A, B and C are plotted versus the velocity in the gas channels.

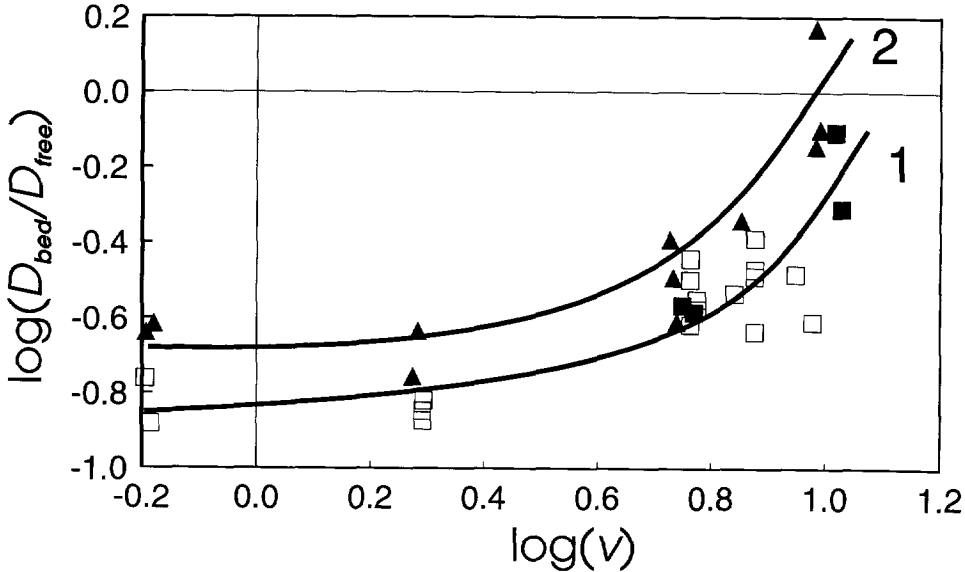


Figure 6-8 Apparent effective bed dispersion coefficient (relative to the free gas diffusivity) of catalysts A, B and C in laboratory PPR module A, versus the linear gas velocity in the gas channels.

□, Catalyst A; ■, catalyst B; ▲, catalyst C.

1, Fitted curve for catalysts A and B; 2, fitted curve for catalyst C.

Combining the apparent bed dispersion coefficients with the bed dispersion models of eqs (6-2)-(6-10), the bed tortuosity and the average superficial gas velocity in the catalyst bed can be fitted for each experiment. The results are listed in Table 6-3. The fitted bed tortuosities correspond to common values, indicating that the static contribution to D_{bed} can be modeled with Eq. (6-3). However, the fitted average gas velocities in the beds are a factor of 2.5 (catalyst C) to 9 (catalysts A and B) higher than predicted by Eq. (6-1) (based on the measured pressure gradient). This indicates that the superficial gas velocity in the catalyst beds is severely underestimated by Ergun's equation.

The higher gas velocity in the catalyst beds may result from the higher voidage near the wire gauze screen and from convective transfer of momentum through the gauze screen. As was previously mentioned, the voidage distribution accounts for only a factor of two in velocity distribution in the case of solid walls and beds of uniform

Table 6-3. Values of τ , the fitted catalyst bed tortuosity, and u_{fit}/u_{Ergun} , the ratio of the fitted superficial gas velocity in the catalyst bed to the velocity estimated by Eq. (1). Based on denox experiments in PPR module A.

Catalyst	τ [mm]	u_{fit}/u_{Ergun} [-]
A and B	1.75	9.2
C	1.49	2.5

spheres. Goodling *et al.* (1983) reported that in beds of non-uniformly sized particles (as used in the tested PPR modules), a less pronounced voidage distribution is encountered. Furthermore Koleskin (1982) reported that beds with porous walls (with wall pores in the order of magnitude of the particle diameter) also show a less pronounced voidage distribution. Based on these findings it is concluded that in the PPR beds, the relatively high gas velocity near the wire gauze screens, as well as the relatively high effective bed dispersion coefficient, result predominantly from convective transport of momentum through the screens. It results only to a small extent from the voidage distribution in the catalyst beds.

6 Conclusions

Interparticle mass transfer in the catalyst beds of a PPR is adequately described by common lateral bed dispersion models. However, models for describing flow profiles in packed beds with solid walls are inapplicable to the PPR, due to convective transfer of momentum through the wire gauze screens. The result of this momentum transfer is that under realistic conditions, up to a few particle diameters from the gauze interparticle mass transfer is up to ten times as fast as expected from the aforementioned models. Consequently, by designing the beds not wider than six to ten particle diameters, the decrease in catalyst bed efficiency due to interparticle mass transfer limitation can be kept small compared with the decrease due to intraparticle mass transfer. Furthermore, a higher efficiency can be obtained at the same pressure drop by increasing both the linear gas velocity in the gas channels and the spacing of the catalyst beds. Under this condition the PPR proves to be a very attractive alternative to the Honeycomb Reactor for full Selective Catalytic Reduction of nitric oxide, especially at low temperatures.

Acknowledgements

Shell Research B.V. is gratefully acknowledged for permission to publish this work. John van der Schaaf is gratefully acknowledged for his substantial contribution to the work reported in this chapter.

Notation

d_b	bed diameter	[m]
d_c	cylinder diameter	[m]
d_{char}	characteristic particle size	[m]
d_p	particle diameter	[m]
D_{bed}	lateral bed dispersion coefficient	[m ² /s]
D_{conv}	convective contribution to D_{bed}	[m ² /s]
D_{free}	free gas diffusion coefficient	[m ² /s]
D_{stat}	static contribution to D_{bed}	[m ² /s]
E_{bed}	catalyst bed efficiency factor	[-]
F_v	shape factor	[-]
j_D	mass transfer number	[-]
j_H	heat transfer number	[-]
K	parameter in Eq. (6-7)	[-]
l_c	cylinder length	[m]
l_g	mixing length	[m]
u	superficial gas velocity in catalyst bed	[m/s]
v	linear gas velocity in gas channel	[m/s]
x_m	mixing length	[m]
$4f$	friction factor	[-]
∇p	pressure gradient	[Pa/m]

Greek letters

ε	voidage of the catalyst bed	[m ³ _{void} /m ³ _{bed}]
μ	dynamic gas viscosity	[Pa·s]
ρ	gas density	[kg _{gas} /m ³ _{gas}]
τ	tortuosity of the catalyst bed	[m/m]

References

- Bauer, R., 1988, *VDI-Wärmeatlas*, 5. Auflage, pp. Mh1-Mh11. VDI-Verlag, Düsseldorf.
- Bauer, R. and Schlünder, E.U., 1978, Effective radial thermal conductivity of packings in gas flow. *In. Chem. Engng* **18**, 181-188.
- Bosch, H. and Janssen, F.J.J.G., 1988, Catalytic reduction of nitrogen oxides. A review on the fundamentals and technology. *Catal. Today* **2**, 369-521.
- Centi, G., Perathoner, S., Kartheuser, B., Rohan, D. and Hodnett, B.K., 1992, Assessment of copper-vanadium oxide on mixed alumina-titania supports as sulphur dioxide sorbents and as catalysts for the selective catalytic reduction of NO_x by ammonia. *Appl. Catal. B* **1**, 129-137.
- Chilton, T.H. and Colburn, A.P., 1934, Mass transfer (absorption) coefficients. *Ind. Engng Chem.* **26**, 1183-1187.
- Conser, R.E., 1973, The Shell flue gas desulfurization process — How does it stack up? *Petr. & Petrochem. Int.* **13**(7), 62-79; and **13**(8), 46-49.
- Dautzenberg, F.M., Naber, J.E. and Van Ginneken, A.J.J., 1971, Shell's flue gas desulfurization process. *Chem. Engng Prog.* **67**(8), 86-91.
- Van Dongen, F.G., 1989, unpublished work, Shell Research B.V.
- Ergun, S., 1952, Fluid flow through packed columns. *Chem. Engng Prog.* **48**, 89-94.
- Goodling, J.S., Vachon, R.I., Stelpflug, W.S. and Ying, S.J., 1983, Radial porosity distribution in cylindrical beds packed with spheres. *Powder Technol.* **35**, 23-29.
- Goudriaan, F., Calis, H.P., Van Dongen, F.G. and Groeneveld, M.J., 1991, Parallel Passage Reactor for catalytic denoxing, in *Proc. 4th World Congress of Chem. Engng*, 16-21 June, 1991, Karlsruhe, Paper 6.1-5.
- Van Helden, H.J.A. and Naber, J.E., 1969, Removal of sulfur dioxide from an oxygen-containing gas. British Patent 1,160,662, August 6.
- Hoebink, J.H.B.J., Mallens, E.P.J., Vonkeman, K.A. and Marin, G.B., 1993, Transport phenomena in a Parallel Passage Reactor, *A.I.Ch.E. 1993 Spring National Meeting*, 28 March - 1 April, 1993 Houston, Paper 67c.
- Hofmann, H. and Weidner, B., 1989, Kinetik der selektiven katalytische Reduktion von Stickoxiden mit Katalysatoren auf V-W-TiO₂-Basis. *DECHEMA-Monographien; Katalyse* **118**, 17-30.
- Kalthoff, O., and Vortmeyer, D., 1980, Ignition/extinction phenomena in a wall cooled fixed bed reactor. *Chem. Engng Sci.* **35**, 1637-1643.
- Kiel, J.H.A., Prins, W. and Van Swaaij, W.P.M., 1992, Performance of silica-supported copper oxide sorbents for SO_x/NO_x-removal from flue gas. *Appl. Catal. B* **1**, 13-39; and **1**, 41-60.

- Koleskin, V.N., Shtern, P.G., Turuntaev, S.V., Abaev G.N. and Popov, E.K., 1982, Effect of bouncing surfaces of porosity distribution in a granular medium. *Inzh. Fiz. Zh.* **42**(4), 578-582.
- Lerou, J.J. and Froment, G.F., 1977, Velocity, temperature and conversion profiles in fixed bed catalytic reactors. *Chem. Engng Sci.* **32**, 853-861.
- Linde, B.J. van der, 1982, an experimental study on the use of manganese oxide on γ -alumina acceptors for flue gas desulfurization, p. 161. Thesis, Delft University Press, Delft, The Netherlands.
- Ploeg, J.E.G., Akagi, E. and Kishi, K., 1974, How Shell's flue gas desulfurization unit has worked in Japan. *Petr. & Petrochem. Int.* **14**(7), 50-54.
- Schertz, W.W. and Bischof, K.B., 1969, Thermal and material transport in nonisothermal packed beds. *A.I.Ch.E. J.* **15**, 597-604.
- Schlünder, E.U. and Tsotsas, E., 1988, *Wärmeübertragung in Festbetten, durchmischten Schüttgütern und Wirbelschichten*, pp. 120-149. Georg Thieme Verlag, Stuttgart.
- Schrauwen, F.J.M., 1989, unpublished work, Shell Research B.V.
- Schwartz, C.E. and Smith, J.M., 1953, Flow distribution in packed beds. *Ind. Engng Chem.* **45**(6), 1209-1218.
- Siddiqi, A.A. and Tenini, J.W., 1981, NOx controls in review. *Hydrocarbon Processing* **60**(10), 115-124.
- Zehner, P. and Schlünder, E.U., 1970, Wärmeleitfähigkeit von Schüttungen bei mässigen Temperaturen. *Chem.-Ing.-Techn.* **43**, 933-941.
- Zehner, P. and Schlünder, E.U., 1972, Einfluss der Wärmestrahlung und des Druckes auf den Wärmetransport in nicht durchströmten Schüttungen. *Chem.-Ing.-Techn.* **44**, 1303-1308.

Chapter 7

Fouling of Bead String Reactors and Parallel Passage Reactors with dust

Contents

Summary	199
1 Introduction	200
2 Simple dust accumulation model	202
2.1 Transport of particles to the wall	202
2.2 Re-entrainment of deposited particles	206
3 Experimental	208
3.1 Equipment and materials used	208
3.2 Experimental procedures	211
3.3 Experiments performed	212
4 Results and discussion	213
4.1 Mass balance checks	213
4.2 Mass flow variation checks	214
4.3 Pressure drop characteristics of the clean packings	214
4.4 Reproducibility of the dust accumulation experiments	215
4.5 Effect of the type of dust	215
4.6 Time dependence of the dust accumulation	216
4.7 Effect of dust concentration	218
4.8 Effect of gas velocity	219
4.9 Effect of accumulated dust on the pressure drop	221
5 Assessment of the effect of accumulated dust on the catalyst efficiency	222
5.1 Bead String Reactor	222
5.2 Parallel Passage Reactor	224
6 Conclusions	227
Acknowledgements	228
Notation	228
References	229

Summary

To study the extent of dust accumulation in a Bead String Reactor (BSR) and a Parallel Passage Reactor (PPR), and its effect on the pressure drop across the reactors and the efficiency of the catalyst, dust-trapping experiments have been performed with two cold-flow lab-scale modules of these reactors. Dust-containing flue gas was simulated using dry air, to which either fly ash (obtained from an industrial, coal-fired power plant) or ceramic dust was added. The pressure drop and amount of dust accumulated in the reactors were measured as a function of time (0.5-7 hr), dust concentration ($4-13 \text{ g}_{\text{dust}}/\text{m}^3_{\text{gas}}$) and gas velocity (0.6-4.5 m/s). Reynolds numbers were in the range of 270-1900; pressure drop measurements indicated that in most experiments, the flow was laminar.

In the PPR, fly ash accumulated predominantly in the catalyst beds, which were gradually filled with dust from bottom to top. During the first seven hours on-stream apparently no re-entrainment of fly ash accumulated in the beds occurred, as the amount of accumulated fly ash increased linearly with time. At a linear gas velocity of *ca.* 1 m/s (laminar flow), the pressure drop was independent of the dust concentration in the gas and the amount of dust accumulated in the reactor.

In the BSR, re-entrainment of dust accumulated on the "strings" occurred, and the rate of dust accumulation decreased by a factor 2.5 within the first four hours on-stream. At low Reynolds numbers (laminar flow), the amount of accumulated dust did not affect the pressure drop across the reactor. At higher Reynolds numbers (transitional flow), 'smoothing' of the rods resulted in a small gradual decrease of the pressure drop (by up to 6 %) in the first hour on-stream, after which it remained constant.

For a linear gas velocity of 0.8 m/s and a run time of 3 h, the amount of fly ash accumulated in the BSR was found to depend linearly on the dust concentration in the gas. With increasing gas velocities, the amount of fly ash accumulated within three hours on-stream seemed to show a maximum at 3.6 m/s. It is expected that the amount of dust accumulated in the steady state situation, decreases with increasing gas velocity.

Although in most experiments the flow seemed laminar, the observations could be described qualitatively by a simple model pertaining to turbulent flow. However, quantitative prediction of the rate of dust accumulation in the tested reactors, starting from literature data only, is quite impossible. Only after fitting of the model parameters to experimental data, limited extrapolation seems justified.

Based on the results of the present study, it was estimated that for the investigated conditions the accumulation of dust in the BSR has no effect on the apparent activity of the catalyst material (under the assumption that dust accumulated on the catalyst

material has no chemical effect and only leads to an extra mass transfer resistance). For the PPR the effect of the extra mass transfer resistance due to accumulated dust depends on the rate determining step, and in the worst case could reduce the apparent catalyst activity by an estimated 94%. Although these figures support the claim that the BSR is more suitable in a high dust environment than a PPR, it should be noted that these figures will be strongly dependent on the type of dust and the process conditions.

1 Introduction

Since the main advantage of parallel flow type reactors such as the monolithic reactor and the PPR, namely the low pressure drop, is best exploited in processes with large flows at low pressures, a natural field of application of these reactors is end-of-pipe treatment of flue gases. In many cases the flue gas is not only contaminated with gaseous components like NO_x, but also with solid substances such as fly ash or, more general, dust. The amount of dust in flue gas can be quite significant; *e.g.*, Van den Kerkhof (1986) reported concentrations of 10-15 g_{dust}/m³_{gas} for coal-fired power plants in The Netherlands. At these high, but also at lower concentrations, dust causes four major problems with respect to the end-of-pipe catalytic reactors:

- blocking of the gas channels of the reactor;
- blocking of the catalyst surface;
- attrition of the catalyst surface; and
- contamination of the catalyst by components released by the dust.

All four problems are encountered in monolithic reactors; in Parallel Passage Reactors, the first and third problem will usually be unimportant.

The extent of the problems that dust may cause, can be appreciated from pictures of the inside of deNO_x installations that have been on-stream for several months, as presented by Schallert and Kaulitz (1986), Wahl (1987), Groeneveld (1991, 1992) and Hauenstein and Herr (1993). Usually dust accumulates in the ducts to the deNO_x installation, forming dunes with heights of up to half a meter. These dunes may collapse upon a change in process conditions, which may result in as much as crushing of ceramic honeycomb elements (Wahl, 1987).

The trivial solution to these problems is to place the deNO_x unit downstream of the electrostatic precipitator, which is present in almost any process that produces dust-containing flue gases. This configuration is known as the "low-dust system", as opposed to the "high-dust system", where the deNO_x unit is placed upstream of the dust removal unit. However, as Bosch and Janssen (1988) point out, high-dust systems are generally preferred to low-dust systems for coal-fired boilers, because:

- a cold electrostatic precipitator is less costly and more efficient than a hot one;
- the deposition of NH_4HSO_4 in the air preheater and on the catalyst is prevented because of the cleaning effect of the fly ash; and
- the finest particles of fly ash, which tend to slip through the hot electrostatic precipitator in the low-dust system, have a tendency to stick to the SCR catalyst, and can only be removed by soot-blowing.

In spite of the importance of dust with respect to the choices made during the design phase of a catalytic deNO_x unit, there is a wide gap between the theory derived from systematic studies of particle deposition on walls, and the application of that theory to dust trapping in structured catalyst packings. This might be justified by the fact that the behavior of dust strongly depends on its composition and on the process conditions—as a result of which predictive models have to contain experimentally determined parameters, that are only valid for the tested situation.

In this chapter, a modest attempt is made to study the most important trends of dust accumulation in the BSR and PPR in a systematic way and to explain the experimentally observed phenomena with the help of a simple model. This model, taken from the literature, is discussed in Section 2. This model, which strictly spoken is only applicable to turbulent flow, is presented here for application to the BSR and PPR, since in these reactors the flow turns turbulent at relatively low Reynolds numbers. The fact that in a BSR the dust is deposited on a convex surface (namely the outside of cylindrical rods or particles), whereas the described model, like most models reported in the literature, pertains to circular ducts and flat plates, is not taken into account. It is assumed that the strings of a BSR are flat on the scale of dust particles, and even on the scale of the dust layer thickness.

The experimental work, involving measurement of dust-trapping and pressure drop in lab-scale BSR and PPR modules, as a function of time, gas velocity and dust concentration, is described and discussed in Sections 3 and 4. Based on the results, the effect of dust accumulation on the efficiency of the catalyst in the reactors is estimated in Section 5, starting from the assumption that the accumulated dust only results in an extra mass transfer resistance. The possible chemical effect of the dust is not taken into consideration.

2 Simple dust accumulation model

The deposition of particles (*e.g.* dust) on walls, and the detachment or re-entrainment of dust deposited on a wall, have been systematically studied for over six decades now. Overviews and reviews of existing literature are given by Yiantsios and Karabelas (1994), Mollinger (1994), Epstein (1988) and Papavergos and Hedley (1984).

Three steps are identified in the accumulation of dust on the wall of a channel through which the fluid flows: 1) the transport of particles from the bulk flow to the wall surface; 2) the adhesion of the particles to the wall surface; 3) the re-entrainment of particles adhered to the wall, back into the bulk flow. In Section 2.1 the first step is discussed; in this discussion, gravitational and electrostatic forces are not considered, as they are estimated to be negligible in the present case. With respect to the second step, it is usually assumed that all particles that reach the wall, adhere to it. The third step is discussed in Section 2.2.

2.1 Transport of particles to the wall

An important distinction to be made in the discussion of particle transport to a wall, is between laminar and turbulent flow. In the following two paragraphs it is deduced that, if gravitational and electrostatic forces are not considered, only turbulent flow is expected to result in dust accumulation.

In laminar flow, the velocity gradient in the flow channel results in a force that pushes a spherical dust particle to the middle of the channel, *i.e.* away from the wall. The particle can only reach a wall as a result of its own inertia when the streamlines are bent by an obstacle, or as a result of Brownian diffusion. In the present case, we are dealing with parallel flow reactors and industrial dust. In parallel flow reactors the channels are straight, as a result of which there are no obstacles inside¹ the reactor on which the dust particles can impinge. This leaves only Brownian diffusion of the dust particles as a mechanism to reach the wall and accumulate there. However, the size of industrial dust particles, such as fly ash from coal fired power plants, is too big for diffusion to be an important transport mechanism. For example, using the median dust particle dimensions of $0.07 \mu\text{m}$ and $3 \mu\text{m}$ presented by Klingenberg (1984), and a residence time of one second in the reactor, the average displacement of the particles in the reactor as a result of diffusion (calculated using Einsteins's law of diffusion) is estimated to be in the order of magnitude of $1 \mu\text{m}$; from this it is

¹ Note, however, that in the ducts upstream of the reactor all obstacles usually get covered by dust dunes!

concluded that diffusion cannot result in a significant flux of fly ash to the wall of the flow channels in the reactor. Consequently, in case of spherical dust particles in a purely laminar flow, with no gravitational or electrostatic forces acting, no accumulation of dust is expected. The observed fly ash accumulation in industrial end-of-pipe reactors in which the flow is expected to be laminar (such as in monolithic catalyst packings), is explained by:

1. the collapse of dust dunes upstream of the reactor;
2. disturbance of the laminar flow at the entrance of the reactor;
3. deviation from spherical geometry of the dust particles (especially if agglomerates are present), which results in drag forces that can push the particle away from the center of the flow channel, projecting it toward the wall.

The general picture for transport of particles from a turbulent flow to a wall, is as follows. Dust particles, travelling in the bulk flow and having a certain momentum, are projected to the wall—in other words, "launched" into the viscous layer near the wall. The projected particles then move toward the wall, influenced by viscous drag forces and (in the case of very small particles) diffusion forces. Whether a particle makes it to the wall, depends on its initial momentum, the drag and diffusion forces acting on it, and the thickness of the viscous layer near the wall. Those particles lacking sufficient momentum to reach the wall, are assumed to pass out with the rest of the fluid, or to be transported back into the bulk flow as a result of lift forces acting upon them in the boundary layer.

As will be shown, the experiments discussed in this chapter were mainly in the laminar flow regime. Considering the fact that significant dust accumulation was observed, and assuming that this can be explained by the disturbance of the laminar flow at the reactor inlet and by the projection of non-spherical particles toward the wall, it was decided to attempt to describe the experimental observations with a model derived for turbulent flow. Therefore this model is further discussed in the remainder of this section and in the subsequent section.

The theories for transport of particles from a turbulent flow to the wall surface dating from before 1984, have been reviewed by Papavergos and Hedley (1984). They classified the theories into those based on the classical concepts of turbulence and those based on stochastic approaches. The most important differences between the two classes of theoretical models are the assumptions regarding the particle diffusivity and the velocity of the particles at the moment they are projected into the viscous layer near the wall. In the theories based on the classical concepts of turbulence, it is assumed that the particle diffusivity is equal (or proportional) to the eddy diffusivity of momentum. Furthermore it is assumed that the initial particle velocity is proportional to the mean axial fluid velocity. Although these assumptions are generally regarded as questionable, the resulting models are relatively simple and sufficiently accurate for certain applications.

In the theories based on stochastic approaches, it is assumed that each particle executes a random walk and interacts with the fluid eddies. The momentum of the particles

moving from the bulk flow toward the wall, which decides whether the wall is reached, then is a stochastic quantity. These theories are free of the questionable assumptions implied in the other class of theories, and provide a physical insight into the phenomena that occur. However, these phenomena are complex, as a result of which the stochastic models are more complex and need more input data.

The result of the theoretical models that is of practical importance for design purposes, are correlations to predict a mass transfer coefficient for transfer of particles to the wall. Obviously, this coefficient is an important quantity in the calculation of the fouling rate of the channel. The mass transfer coefficient is defined by:

$$\Phi_m'' \equiv k_d c_d \quad (7-1)$$

In this definition, it is assumed that the wall acts as a "dust sink", *i.e.* the dust concentration in the gas phase very close to the wall is zero.

On which quantities k_d depends, is most easily explained from the dust deposition models based on the classical concepts of turbulence. In these models, the particles are assumed to reach the region near the wall by turbulent fluctuations, and are "launched" into the laminar sub-layer. Whether a particle makes it to the wall, depends on its so-called *stopping distance*, relative to the thickness of the laminar sub-layer.

The stopping distance is the finite length that a particle with a given initial velocity travels through a viscous medium, before it is stopped by drag force; it depends on the ratio of the initial momentum to the (decreasing) drag force. When the particle relaxation time, τ_p , is defined as the time required for an initial particle velocity to be reduced by drag force to a fraction e^{-1} of its initial value, it easily follows that (at low particle Reynolds numbers, where Stokes' law is valid) the particle relaxation time is given by:

$$\tau_p = \frac{d_p^2 \rho_p}{18 \nu \rho} \quad (7-2)$$

and the stopping distance by:

$$S_p = \tau_p u_{p,0} \quad (7-3)$$

where $u_{p,0}$ is the initial particle velocity, at the moment when it is "launched" into the laminar sub-layer.

The concept of the laminar sub-layer was discussed briefly in Chapter 2, where it was stated that its thickness is estimated by:

$$y^+_{lam} \equiv \frac{u^+ y_{lam}}{\nu} = 5 \quad \text{with} \quad u^+ \equiv \sqrt{\frac{\tau_{f,w}}{\rho}} = \langle u \rangle \sqrt{\frac{f}{2}} \quad (7-4)$$

or:

$$y_{lam} = \frac{5 \nu}{u^+} \quad (7-5)$$

in which u^+ is the so-called *friction velocity*.

When the stopping distance is compared to the laminar sub-layer thickness, it should be realized that $u_{p,0}$ was assumed to be directly proportional to the axial fluid velocity of the bulk flow, which according to Eq. (7-4) is also proportional to the friction velocity. It then follows that whether a particle reaches the wall, depends on the dimensionless particle relaxation time, τ_p^+ , defined as:

$$\tau_p^+ \equiv \tau_p \frac{(u^+)^2}{\nu} \quad (7-6)$$

From this simple model it can be expected that the mass transfer coefficient k_d depends on τ_p^+ . It appears that simple correlations are obtained from experiments when the *dimensionless* mass transfer coefficient k_d^+ , defined as k_d/u^+ , is plotted as a function of τ_p^+ . Various models using the classical concepts of turbulence have been proposed (Friedlander and Johnstone, 1957; Levich, 1962; Davies, 1966; Beal, 1970; Liu and Ilori, 1973), with subtle distinctions between the assumptions made. The variation between the models in the prediction of k_d^+ as a function of τ_p^+ , is up to an order of magnitude. The experimental values of k_d^+ are scattered around the various models (Papavergos and Hedley, 1984), which implies that in this respect, all models are adequate. A parameter fit of the experimental data obtained for smooth, vertical channels, yielded the following results (Papavergos and Hedley, 1984):

$$\begin{aligned} k_d^+ &= 0.07 (Sc)^{-2/3} & \text{at} & \tau_p^+ < 0.2 \\ k_d^+ &= 3.5 \cdot 10^{-4} (\tau_p^+)^2 & \text{at} & 0.2 < \tau_p^+ < 20 \\ k_d^+ &= 0.18 & \text{at} & \tau_p^+ > 20 \end{aligned} \quad (7-7)$$

The various correlations for k_d^+ based on stochastic approaches (Reeks and Skyrme, 1976; Cleaver and Yates, 1975, Papavergos and Hedley, 1979), also vary up to an order of magnitude, and furthermore predict roughly the same values for k_d^+ as the models based on the classical concepts of turbulence.

Davies (1983) reported an analogous correlation for k_d^+ for channels with rough surfaces, in which the empirical roughness parameter C is introduced:

$$\begin{aligned} k_d^+ &= 0.070 (Sc)^{-1/2} & \text{at } \tau_p^+ < 0.22 \\ k_d^+ &= C(1 + \tau_p^+)(\rho/\rho_p) & \text{at } 0.22 < \tau_p^+ < 10 \\ k_d^+ &= 0.3 & \text{at } \tau_p^+ > 33 \end{aligned} \quad (7-8)$$

with C ranging from 0.05 for very smooth surfaces (*e.g.* polished brass) to 100 for very rough surfaces (*e.g.* filter paper).

The correlations presented here only consider the transfer of particles from the bulk flow to the wall, and not *vice versa*. This implies that these correlations in fact predict the initial accumulation rate of dust, when the wall surface is still free from particles. These correlations can be applied when the wall surface and/or the particles are very sticky, such that none of the deposited particles can detach. Note, however, that in the latter case the value of the roughness parameter C will change as a function of the amount of dust deposited (per unit area).

It also might be possible to predict the dust accumulation rate of PPR's using the correlations presented here, assuming that all particles that are deposited on the wall, fall into the catalyst bed, from which they cannot be re-entrained.

In other cases, however, after an amount of dust has accumulated, particles will start to be re-entrained back into the bulk flow. As the re-entrainment flux will increase with the amount of dust deposited on the wall (per unit area), it can be expected that after some time a steady state will be reached, at which the rate of deposition is balanced by the rate of re-entrainment. This topic is further discussed in Section 2.2.

2.2 Re-entrainment of deposited particles

Particles transported to the wall surface are usually assumed to be deposited on it by an instantaneous attachment step. How long a particle will remain attached to the wall, depends on the balance between adhesive forces and re-entrainment forces.

The main adhesive forces acting on deposited particles are Van der Waals forces, electrostatic forces, and the surface tension of adsorbed liquid films. These forces are difficult to quantify, as they are affected by 1) the material, shape and size of the particle, 2) the material, roughness and contamination of the wall surface, 3) the relative humidity, 4) the temperature, and 5) the duration of contact and the impact velocity.

The most important re-entrainment forces are forces due to fluid shear stresses, forces due to heavy particle impact, and gravitational force. A generally accepted picture of the re-entrainment mechanism is the occurrence of random motions of fluid close to the wall; see *e.g.* Braaten *et al.* (1993). The basic theory behind this picture was developed by Cleaver and Yates (1973), and was based on flow visualizations first

reported in the 1960s. According to this theory, the viscous sub-layer is continuously disrupted by locally highly unstable, instantaneous velocity distributions, called 'turbulent bursts', which act like tornados. More specifically, local and temporary ejections of low momentum fluid outward from the wall surface occur, as well as inrush movements toward the wall, accompanied by sweep movements almost parallel to the wall. The velocity distributions create lift and drag forces, which can detach deposited particles.

Based on flow visualizations, Cleaver and Yates (1973) estimated the spatial and temporal distribution of the bursts, and the effective area of each burst. They claimed that θ_{burst} , the fraction of the surface covered with burst sites at any instance, was constant (ca. 1/270), and that the burst impact frequency was proportional to $\nu/(u^*)^2$. Under two critical assumptions, Cleaver and Yates (1976) showed that the amount of dust deposited per unit area of wall surface increases asymptotically to an equilibrium value. The first assumption is that with each burst, a fixed fraction, α , of the particles deposited in the area of the burst, is detached and re-entrained. The second assumption is, that in the time between two bursts at the same spot, there is a constant deposition flux Φ_m'' to that spot. This deposition flux may be calculated with eq. (7-1). The time-dependent amount of particles deposited per A_{wall} m² of wall surface, starting with a clean wall at $t=0$, was shown to be:

$$M = \Phi_m'' A_{wall} \frac{100 \nu m}{u^{*2}} \left[1 - \exp\left(-\frac{u^{*2} t}{100 \nu m}\right) \right] \quad (7-9)$$

In this equation, m is defined by the aforementioned quantities α and θ_{burst} :

$$m = \frac{1}{\alpha \theta_{burst}} \quad (7-10)$$

Obviously, α depends on the adhesive forces acting on deposited particles, and therefore is a parameter that should be fitted from experiments. Nevertheless, Cleaver and Yates (1973) recommend a value of 0.01 for fully developed turbulent flow.

Although it is disputed whether the described turbulent bursts really account for the re-entrainment of particles 'deep' in the viscous sub-layer, rather than more continuous drag and lift forces (Yiantsios and Karabelas, 1994), this so-called 'surface renewal' model is still frequently used. For a more detailed discussion of the various models for re-entrainment of particles, reference is made to Mollinger (1994).

From the above it will have become clear that the modeling of dust deposition and re-entrainment involves a lot of assumptions. Though the model presented here is not the most sophisticated or most recent one proposed in the literature, it was deemed appropriate, considering the scope of this project, to use this simple model to attempt to explain the most important trends of dust accumulation in the BSR and PPR.

3 Experimental

Subjects of interest in the experimental study were 1) the rate of fouling of the lab-scale BSR and PPR modules as a function of time, flow rate, and dust concentration, 2) the effect of fouling on the pressure drop characteristics, and 3) the dependence of the first two quantities on the properties of the dust that was used. To this end an experimental set-up was constructed, which operated at room temperature and atmospheric pressure.

Due to the limited time that was available for these experiments, only short runs were done (0.5-7 hours on-stream). However, it will be shown that this was long enough to enable characterization of the dust trapping process under the present conditions. The equipment and materials used are described in Section 3.1, the experimental procedure in Section 3.2, and the experiments performed are described in Section 3.3.

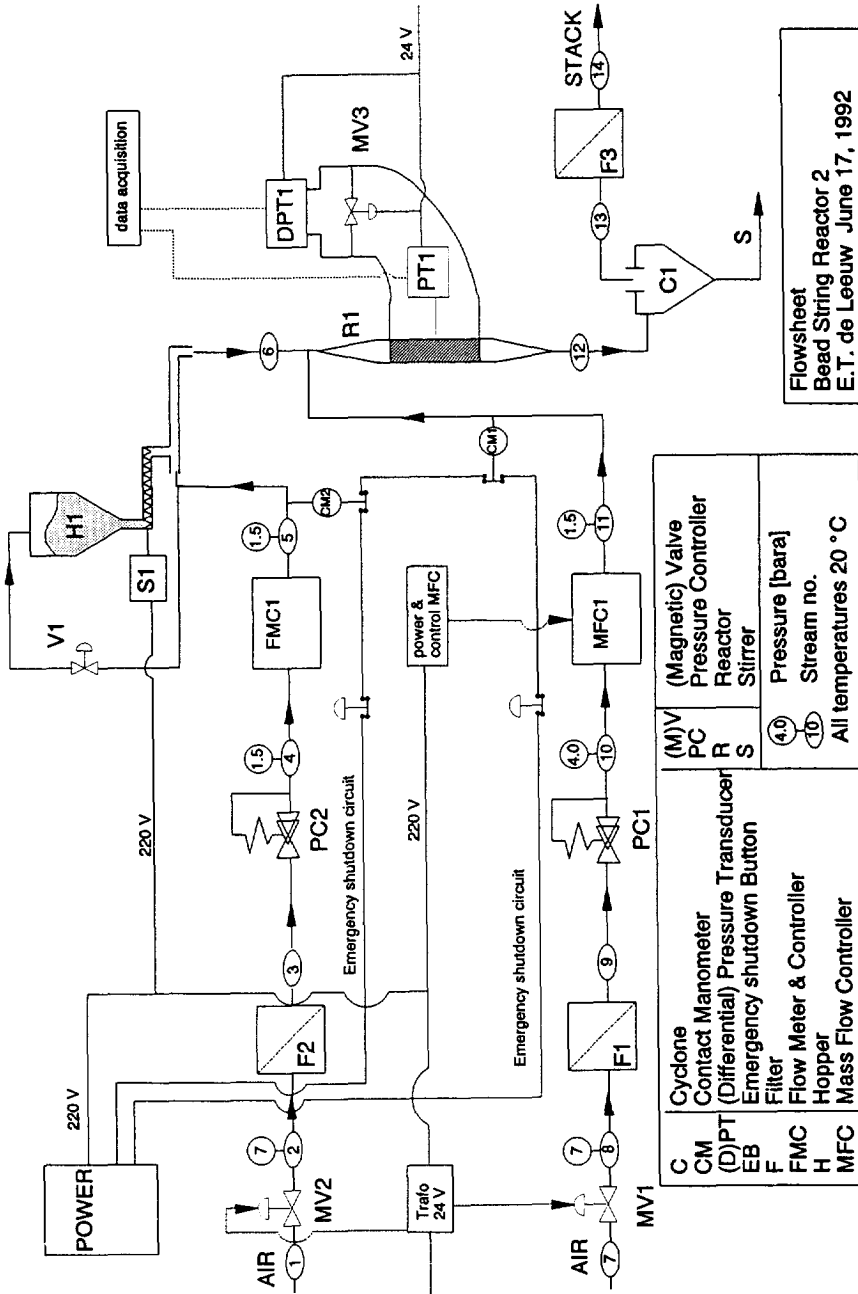
3.1 Equipment and materials used

A flow scheme of the experimental set-up is presented in Fig. 7-1. Dust was transported from hopper *HI* by a transport screw, the flow rate being controlled through the rotation speed. Downstream of the transport screw, the dust was conveyed by a small air flow controlled by rotameter *FMCI*. The hopper was pressurized to the same pressure as the end of the transport screw, to prevent back-flow of air through the screw into the hopper. The dust-containing air flow was mixed with the main air flow, which was controlled by mass flow controller *MFCI*. The mixture then flowed through the reactor module, after which it entered a cyclone and subsequently passed through a filter. The pressure drop across the reactor packing was measured, as well as the gauge pressure in the system.

Two types of dust were used (see Table 7-1), with very distinct flow properties:

- **ceramic dust**, a non-sticky, non-agglomerative, free-flowing dust obtained from Royal Sphinx BV, a manufacturer of ceramic products;
- **fly ash**, a slightly sticky and agglomerative dust with a tendency to bridge, obtained from a coal-fired power plant administered by EPON NV.

Three reactor packings were used, fitted into a reactor body with a length of 500 mm and a square cross-section of 70 mm. The details of the reactor packings are listed in Table 7-2.



Flowsheet
Bead String Reactor 2
E.T. de Leeuw June 17, 1992

Figure 7-1 Flow sheet of the experimental set-up.

Table 7-1 Properties of the two types of dust used.

Property		Ceramic dust	Fly ash
composition		SiO ₂	50 % SiO ₂ ⁽¹⁾
particle density	[kg _{part} /m ³ _{part}]	2631	2290
bulk voidage	[m ³ _{void} /m ³ _{bed}]	0.45 ⁽²⁾	0.66
particle size range	[μm]	1-120	2-400
median particle diameter	[μm]	22	30

⁽¹⁾ see Kok (1993)

⁽²⁾ estimated value

Table 7-2 Specifications of the reactor packings used.

	BSR	PPR	Fixed Bed
packing	M2 brass screw thread rods, Ø 1.9 mm	glass spheres, Ø 2.2 mm	glass spheres, Ø 2.2 mm
"catalyst" volume [ℓ _{part}]	0.51	0.51	0.51
packing voidage [m ³ _{void} /m ³ _{bed}]	0.79	0.79	0.40
pitch [mm]	3.5	11	-
configuration	19×19 rods, 450 mm long; square array.	6 slabs, 4×68×500 mm (T×W×H); 0.4 mm gauze thickness, 0.5 mm gauze mesh.	173 mm bed height

- A BSR, though not packed with strings of catalyst particles, but with brass screw thread rods. The thread was meant to simulate the space between the catalyst beads in a real BSR. This was done because only a limited number of real catalyst bead strings were available, which were saved for chemical experiments. The rods were connected to a wire mesh at the top of the reactor.
- A PPR, of which the envelopes were filled with beds of spherical glass beads. The envelopes were supported by a screen at the bottom of the reactor body. It must be noted that after filling the envelopes, they bulged out; the average thickness was 2 mm bigger than the nominal value listed in Table 7-2.
- A randomly packed Fixed Bed Reactor, acronymized FBR, consisting of spherical glass beads. The bed was supported by a piece of glass wool supported by a screen, at the bottom of the reactor.

To enable comparison of the dust trapping characteristics of the three packings, the same volume of "catalyst" was used: 0.51 ℓ brass in the BSR, 0.51 ℓ glass in the PPR and the FBR.

3.2 Experimental procedures

Each run consisted of seven steps:

1. measuring the tare weight of the clean reactor body and packing;
2. introducing a measured amount of dust into the hopper;
3. letting dust containing air flow through the reactor for 0.5-7 hours;
4. measuring the gross weight of the dust containing reactor body and packing;
5. estimating or measuring the weight of the dust accumulated on the supports of the FBR and the PPR, or the mesh to which the BSR rods were attached;
6. measuring the amount of dust remaining in the hopper;
7. cleaning the reactor body and packing, and the hopper, using pressurized air.

Although the dust flow rate was controlled through the rotation speed of the transport screw, it was found that constant attention of the operator was necessary, due to the tendency of the fly ash to bridge in the hopper outlet. To prevent bridging, only a few hundred grams of dust were put in the hopper at the beginning of each run, to limit the compaction pressure. This implied that extra dust had to be added during long run runs. Bridging could normally be overcome by tapping the hopper outlet.

No checks were done on the mixing of the dust in the radial direction of the pipes and the reactor. However, visual inspection of the reactor packings after the runs showed that the dust had accumulated uniformly over the reactor cross section, supporting the assumption that the dust was uniformly distributed over the gas flow. From this it was concluded that experimentally difficult measurements of the dust distribution in the gas flow were not necessary.

Furthermore no checks were done on the nature of dust agglomerates in the gas flow. Due to the nature of the dust feeding system (a transport screw) it cannot be ruled out that the dust in the gas is not present in the size distribution that was found from analysis of 'fresh' dust, but rather in the form of agglomerates of particles. Furthermore the size of the particles themselves might be reduced as a result of milling in the transport screw. However, considering the broad size distribution of the 'fresh' dust (see Table 7-1), no effort was taken to investigate these possible pitfalls.

The net amount of dust introduced into the system was calculated as the difference between the amount introduced into the hopper at step 2 and the amount left over at step 6. This introduces an error of about 10 percent, since from the mass balance check described in Section 3.3 it is known that on the time scale of the present experiments, this fraction of the introduced dust accumulates up-stream of the reactor.

However, this error was accepted, and no corrections were made to the experimental data.

The net amount of dust accumulated in the reactor body and packing was calculated as the difference between the weights of the dust containing reactor (step 4) and the clean reactor (step 1). A correction was made for the dust accumulated on the supporting glass wool in the FBR, the support screen of the PPR and the wire mesh of the BSR. The dust accumulated on these places was not taken into account, since the subject of interest in this study was the dust trapping characteristics of the reactor packings themselves, not of their supports. These corrections were less than 3% for the PPR and BSR, and less than 6% for the FBR. It could be argued that also the amount of dust accumulated on the wall of the reactor body should not be taken into account, because the relative amount of 'wall' in a commercial scale installation will be negligible compared to the amount of surface of the catalyst or the catalyst envelopes. It appeared that even in the lab-scale modules, the amount of dust accumulated on the wall of the reactor body was less than about 5 percent of the total amount accumulated in the reactor. Out of convenience, no corrections were made in this respect.

During the run time of a run (step 3), the gauge pressure in the reactor was measured through a pressure tap at the middle of the reactor height, with a frequency of 0.1 or 0.017 Hz (depending on the total run time). The pressure drop across the reactor packing was measured with the same frequency, through pressure taps 25 mm under the top of the packing and 25 mm above the bottom of the packing. In this way the pressure drop across the support screens was not taken into account. Separate experiments had already shown that the pressure drop across the support grid or screen of the BSR and PPR is usually less than 5 percent of the pressure drop across the complete reactor.

3.3 Experiments performed

Four categories of experiments were performed:

1. *Mass balance checks.* In these experiments it was checked whether all dust introduced into the system could be retrieved somewhere in the set-up. The mass balance check experiments were done both with the ceramic dust and the fly ash. The reactor packing consisted of the randomly packed bed of glass spheres.
2. *Dust flow variation checks.* In these experiments the variation of the fly ash mass flow rate from the hopper was measured by collecting the dust directly after the transport screw, in a container placed on a balance.
3. *Pressure drop experiments.* To find out whether the flow in the reactors was laminar or turbulent under the experimental conditions, the pressure drop across the (clean) packings was measured as a function of the gas flow rate. Furthermore,

during the dust accumulation experiments described below, the pressure drop was monitored as a function of time.

4. *Dust accumulation experiments in the FBR, PPR and BSR.* In these experiments four process variables were varied, namely the type of dust (ceramic dust or fly ash), the run time (0.5-7 h), the linear gas velocity (0.6-4.5 m/s), and the dust concentration (4-13 $\text{g}_{\text{dust}}/\text{m}^3_{\text{gas}}$). To obtain an estimate of the reproducibility of these experiments, five runs were replicated.

Since the influence of the type of dust was not the main objective of this study, no direct comparison was made; *i.e.*, no experiments were done in which only the type of dust was changed. This implies that the effect of the type of dust can only be estimated from comparison of runs differing not only in type of dust, but also in gas flow rate and dust concentration. As a result, only a rough estimate of the effect of the dust type is obtained, after a first order correction for differences in gas flow rate and dust concentration. The first order dependence of the dust accumulation rate on these two variables is shown in Sections 4.8 and 4.7, respectively.

The time dependence of the dust accumulation was studied by performing a series of six runs in both the PPR and BSR, with run times ranging from 0.5 to 7 hours, all other variables being kept constant, and measuring the amount of dust accumulated in the reactor within the run time. The effect of the dust concentration was studied by performing a series of six runs in a BSR, with a constant run time of three hours. The effect of gas velocity was studied by performing runs at 5 gas velocities in a BSR, at two concentrations per gas velocity setting.

The results of these experiments are discussed in the next section.

4 Results and discussion

4.1 Mass balance checks

In all four mass balance check runs, more than 98% of the fed dust was retrieved in the various parts of the set-up (including the final dust collection container and filter at the end of the set-up). About 10% had accumulated upstream of the reactor, 10 to 25% in the reactor, and the remaining part downstream of the reactor. The missing 2% either slipped through the dust filter system at the end of the set-up, or were lost during the disassembling of the set-up. This result was considered satisfactory.

4.2 Mass flow variation checks

Averaged over one minute, the variation of the dust mass flow was generally less than 10%. However, when the dust bridged in the hopper outlet, the flow stopped completely. Therefore the dust feeding system was constantly monitored during the runs.

4.3 Pressure drop characteristics of the clean packings

The pressure drop characteristics of the BSR module were studied following the procedure described in Chapter 2. In Fig. 7-2, the friction factor of the clean BSR (*i.e.* without any dust present) is plotted as a function of Re . It is seen that in the biggest part of the flow range, the flow is laminar. The deviation of the experimental points, at the lower Reynolds numbers, from the line representing the theory, may result from the fact that the rods were not fixed at the bottom end. As a result some of the subchannels were wider than the average, while others were smaller; such asymmetry leads to a **lower** pressure drop.

In Fig. 7-3 the friction factor of the clean PPR is plotted as a function of Re ; in the calculations a correction was made for the bulging of the envelopes. However, because of the bulging of the envelopes, no theoretical value of the geometry parameter could be calculated. Therefore the line representing the theory for laminar flow in Fig. 7-3 was simply fitted through the data point at the lowest Reynolds number; the slope is -1 , as predicted by the theory. The limited amount of data indicates that the laminar flow regime extends to a Reynolds number of about 1000.

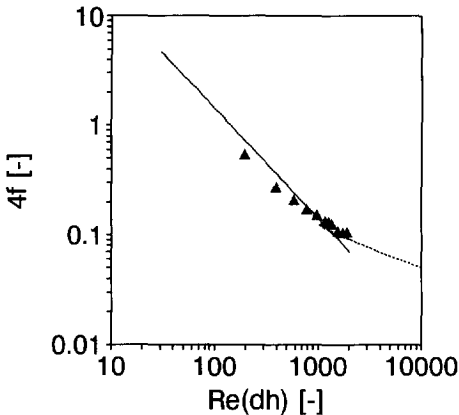


Figure 7-2 Friction factor vs. Re of the 'clean' BSR.

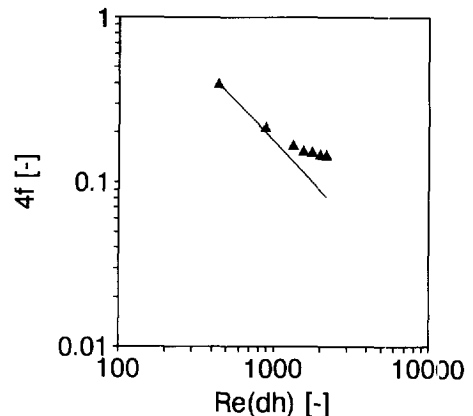


Figure 7-3 Friction factor vs. Re of the 'clean' PPR.

4.4 Reproducibility of the dust accumulation experiments

Five dust accumulation runs were replicated, one time each, yielding five pairs of runs. These pairs are identified in Table 7-3. For each replicated setting, the standard deviation (s) of the response variable can be expressed as a percentage of the average response value at this setting; the response variable is, *e.g.*, the amount of dust trapped per unit time. If it is assumed that the dust accumulation rate [g_{dust}/h] depends linearly on the dust concentration in the gas, as will be shown in Section 4.7, the response of each replicate can be corrected for the (inevitable) small difference of the dust concentration between the 'original' run and its replicate.

The uncorrected and corrected sample standard deviations are listed in Table 7-3. For the FBR no value is given, since in the first run the reactor got completely plugged after 76 minutes, whereas in the second run there was smooth operation for two hours. This illustrates the 'danger' of using randomly packed bed reactors in combination with dust containing gases. From the values for the PPR and BSR, it was concluded that the reproducibility of the dust trapping experiments, with these types of reactor, was sufficient. This assumption was supported by the small residuals of experimental data compared to low-order splines through all experimental points, as will be shown in Sections 4.6 and 4.7.

Table 7-3 Reproducibility of the dust trapping experiments.

Reactor	Type of dust	s [%]	$s_{\text{corr.}}$ [%]
FBR	Fly ash	-	-
PPR	Ceramic	10.5	1.5
PPR	Fly ash	8.8	7.1
PPR	Fly ash	10.7	7.3
BSR	Fly ash	3.6	0.6

4.5 Effect of the type of dust

The effect of the type of dust on the dust accumulation rate was estimated from the runs listed in Table 7-4. Since the runs with a specific type of reactor packing differed not only in type of dust, but also in gas flow rate and dust concentration, a first order

correction was made for the influence of the gas flow rate and the dust concentration on the (average) dust accumulation rate. In other words, the average dust accumulation rate [$\text{g}_{\text{dust}}/\text{h}$] was divided by the gas flow rate [$\text{m}^3_{\text{gas}}/\text{h}$] and the dust concentration [$\text{g}_{\text{dust}}/\text{m}^3_{\text{gas}}$]; this yields the fraction x of the dust introduced in the set-up, that is trapped in the reactor.

The values presented in Table 7-4, in relation to the values of the reproducibility discussed in the previous section, indicate that there is a significant effect of the type of dust on the dust accumulation rate. Obviously these few data do not enable explanation, let alone *prediction*, of the effect, quantitatively or even qualitatively.

Table 7-4 Effect of the type of dust on the dust accumulation rate.

Reactor	Dust type	u [m/s]	Δt [h]	c_{dust} [$\text{g}_{\text{dust}}/\text{m}^3_{\text{gas}}$]	dM/dt [g/h]	x [%]
BSR	Ceramic	0.77	5.0	10.5	11.2	9.9
	Fly ash	0.65	5.0	8.2	4.9	6.6
PPR	Ceramic	0.93	6.9	5.3	5.1	9.0
	Fly ash	0.98	7.0	9.3	11.6	11.0

4.6 Time dependence of the dust accumulation

Visual inspection of the PPR after each run, showed that the biggest part of the dust trapped in the reactor, had accumulated at the bottom of the catalyst envelopes. The bottom part of the envelopes had been completely filled with (fluffy) dust, and the level of the filled part became higher with increasing run time. Furthermore dust appeared to accumulate on the wire gauze and on top of the envelopes; the latter amount was not taken into account.

The amount of dust accumulated in the PPR as a function of time is shown graphically in Fig. 7-4. In these experiments the linear gas velocity was 1.4 m/s, corresponding to a Reynolds number of 840; from Fig. 7-3 it is seen that under these conditions, the flow is still laminar. The fly ash concentration was $(9.33 \pm 0.41) \text{ g}_{\text{dust}}/\text{m}^3_{\text{gas}}$. The fact that the amount of accumulated dust appears to increase linearly with time, indicates that under these conditions no re-entrainment occurs; indeed, re-entrainment would be expected to level off the accumulation rate until a steady state has been reached, where the accumulation rate has become zero. Apparently dust that had been trapped in the PPR envelopes, could not be re-entrained under the present conditions. If the constant accumulation rate would hold on, it would take about 20 hours to completely fill the envelopes under these conditions. Though it is possible that some

re-entrainment would occur when a large part of the envelopes is filled with dust, it is safe to assume that at steady state the envelopes will be completely filled with dust, corresponding to *ca.* $230 \text{ g}_{\text{dust}}$. The effect this will have on the efficiency of the catalyst in the envelopes, will be assessed in Section 5.

Visual inspection of the BSR after each run, showed that the biggest part of the dust trapped in the reactor, had accumulated on the grooves of the rods. Furthermore dust had accumulated in the springs that were used to fix the rods in the reactor, and on the grid to which the springs were attached. The latter two amounts were not taken into account.

In the six runs with run times varying from 1 to 5 hours, the gas velocity was kept constant at 0.7 m/s. This corresponds to a Reynolds number of 290. From Fig. 7-2 it is seen that at these conditions, the flow is still laminar.

Due to experimental difficulties with the dust transport screw, the dust concentration could not be kept constant between the six runs; instead it varied from 5 to $11 \text{ g}_{\text{dust}}/\text{m}^3_{\text{gas}}$. Therefore a first order correction was made: instead of plotting the amount of dust accumulated as a function of the run time, it was plotted as a function of the amount of dust introduced into the gas flow. This implies the assumption that the amount of dust accumulated in the reactor, depends linearly on the dust concentration; it will be shown in Section 4.7, that this assumption is fair.

The result is shown in Fig. 7-5. The rate of dust accumulation, *i.e.* the slope of the spline through the data points, is seen to decrease by a factor 2.5 within the first four hours on stream. This indicates the occurrence of re-entrainment. Extrapolating the spline, realizing that this implies a large inaccuracy, it is expected that under these conditions a steady state will be reached after 10 to 15 hours, at which the reactor will contain 30 to $40 \text{ g}_{\text{dust}}$. Note that this is about seven times less than the amount of dust trapped in the PPR at steady state, even though the two reactors contain the same volume of 'catalyst'. The effect of the accumulated dust on the efficiency of the catalyst in the BSR, will be assessed in Section 5.

Just to see where the dust accumulation model presented in Section 2 leads us, it will be applied to the presented experiments in the BSR, in spite of the fact that in those experiments the flow seemed to be laminar. From the data presented in Fig. 7-5, it is possible to fit the two parameters α (fraction of dust removed under a burst) and C (wall roughness parameter) from equations (7-10) and (7-8), respectively. This

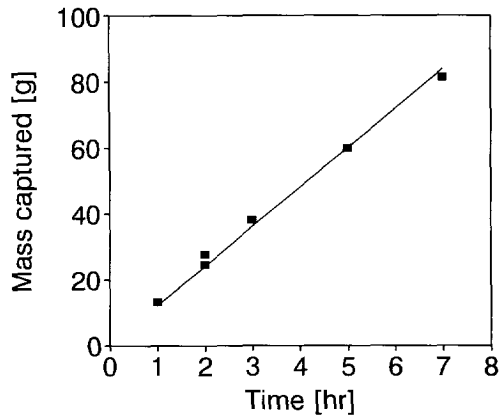


Figure 7-4 Amount of accumulated dust in the PPR vs. time.

yields values of $(15 \pm 3) \cdot 10^{-3}$ for α and 0.04 ± 0.005 for C . The fitted value for α agrees remarkably well with the value of 0.01 recommended by Cleaver and Yates (1973); obviously, due to the small amount of data in this experimental study and the fact that a turbulent flow model was applied to a laminar flow situation, it cannot be ruled out that this agreement is coincidental.

The fitted value for C corresponds to the value of 0.05 for *polished* brass (*i.e.*, smooth walls), published by Davies (1983). It is tempting to conclude that apparently the thread of the brass rods that were used in the BSR, had no influence on the 'wall roughness' of the rods, and that the rods were 'hydrodynamically smooth' under these conditions. This agrees with the earlier observation that in the experiments the flow was laminar, in which case the wall roughness plays no role. Based on the pressure drop data and estimates of the laminar sub-layer thickness (calculated using Eq. (7-4)), it is expected that the wall roughness starts to become important when the gas velocity is increased by a factor 5, and the flow enters the transitional flow regime. From the absolute roughness height of the rods (*ca.* 0.5 mm) and data provided by Davies (1983), values of C as high as 260 are expected in that situation, corresponding to much higher 'mass transfer coefficients' for dust than found in the present experiments.

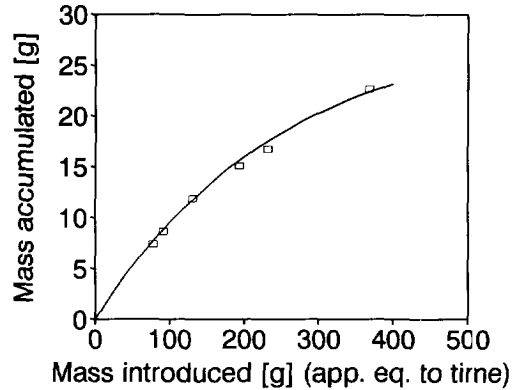


Figure 7-5 Amount of accumulated dust in the BSR vs. amount of dust introduced.

4.7 Effect of dust concentration

For a constant linear gas velocity of 0.9 m/s and a constant run time of 3 hours, the amount of fly ash accumulated in the BSR appeared to increase linearly with the dust concentration in the gas; see Fig. 7-6. The solid line in this figure is a fitted straight line, the dashed line represents the model of Section 2 with the fitted parameters of Section 4.6. Although the two lines do not coincide, it seems possible to obtain a rough prediction of the effect of the dust concentration by using the presented model in combination with fit parameters obtained from experiments at a constant concentration.

Although the origin of this figure seems a trivial experimental point, it is possible to explain why the straight line fitted through the experimental points in Fig. 7-6 does not cross the origin. In the model, which predicts a direct proportionality between the dust concentration and the dust accumulation rate, it is assumed that all dust is

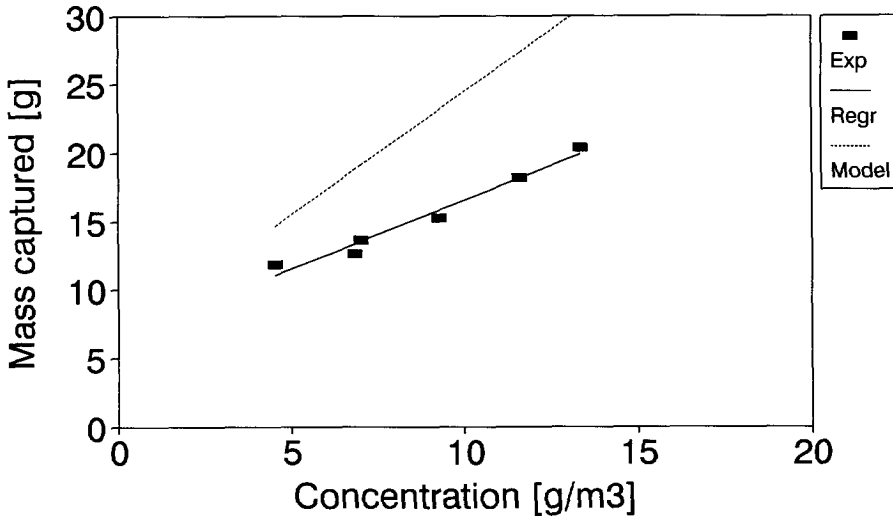


Figure 7-6 Amount of accumulated dust in the BSR in the first three hours on-stream vs. the dust concentration in the gas.

susceptible to re-entrainment. However, due to the nature of the screw-threaded rods used in the BSR, part of the dust might be considered as 'locked-up' in the grooves, covered (after some time) by a 'thick' layer of dust. When it is assumed that a certain amount of dust with mass M_0 is not susceptible to re-entrainment, Eq. (7-9) combined with Eq. (7-1) may be rewritten as:

$$M = M_0 + k_d c_d A_{wall} \frac{100 v m}{u^{*2}} \left[1 - \exp\left(-\frac{u^{*2} t}{100 v m}\right) \right] \quad (7-11)$$

Eq. (7-11) explains the observed regression line; unfortunately, a new parameter (M_0) is introduced, which must be found experimentally or estimated from the geometry or structure of the surface that is fouled.

4.8 Effect of gas velocity

Combination of Eqs. (7-4) to (7-8) shows that k_d , the mass transfer coefficient for dust transfer to the wall, is proportional to $\langle u \rangle^\beta$, where $\langle u \rangle$ is the average linear gas velocity and β is 0.5 for very low gas velocities (*i.e.* values of τ_p^+ smaller than 0.2), 1 at very high gas velocities (*i.e.* values of τ_p^+ bigger than 20), and passes through a maximum value of 3 in between. Based on the median dust characteristics and experimental pressure drop data, it can be calculated that in the present experiments, τ_p^+ ranges from 10 to 20. Consequently, k_d is expected to increase with the average

gas velocity, and for a clean wall (or short runs) the rate of dust accumulation is expected to increase with the gas velocity.

On the other hand, also the re-entrainment forces will become bigger with increasing gas velocities; this is shown by Eq. (7-9), which indicates that the re-entrainment rate increases with $(u^*)^2$ (note that u^* is proportional to $\langle u \rangle$). As a net result of these two effects, it is expected that the amount of dust accumulated on a wall in steady state is proportional to $\langle u \rangle^\psi$, where ψ is -1.5 at very low gas velocities, -1 at very high gas velocities, and passes through a maximum of +2 in between. In the experiments of the present study, however, the run time was 3 hours; from the data presented in the previous sections it has become clear that in that short time, a steady state was not yet reached.

All in all no prediction can be made with respect to the dependence of the amount of dust accumulated in three hours as a function of the gas velocity: both positive and negative trends are possible.

Because of the limited amount of available time and the physical limitations of the experimental set-up, runs at only two concentrations were done at each of the five tested velocities. Assuming a linear dependence of the amount of accumulated dust on the dust concentration, as discussed in the previous section, data points were generated for six different concentrations. The results are shown in Fig. 7-7.

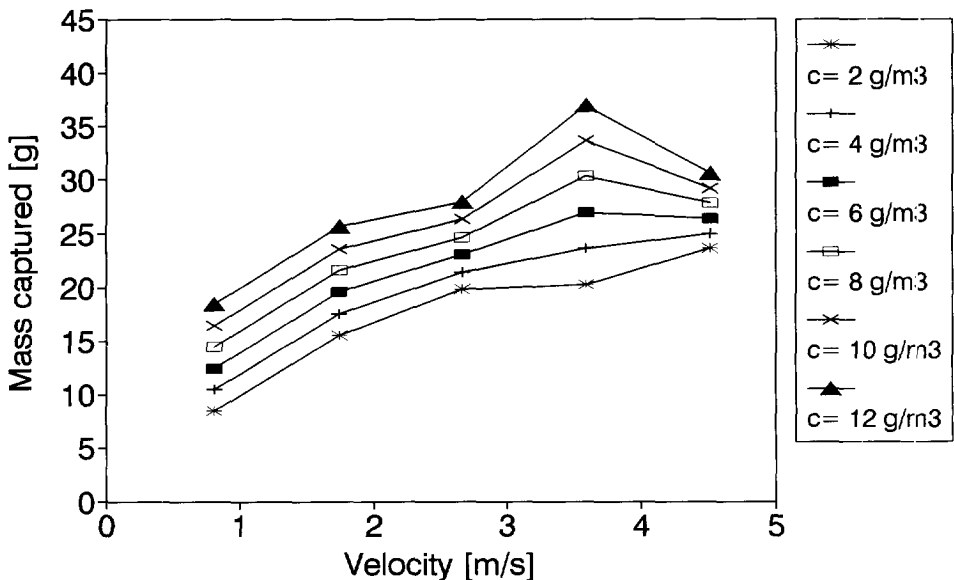


Figure 7-7 Amount of accumulated dust in the BSR in the first three hours on-stream vs. the gas velocity.

It appears that at the lower velocities the average accumulation rate increases with increasing gas velocity, and that this increase levels off or is even reversed at the highest velocities. It cannot be concluded whether the apparent maximum at 3.6 m/s

is true, since the six points at this velocity are fixed by only two experimental data, the highest of which might of course be an outlier. Nevertheless, the fact that the slopes of the lines level off or even become negative at increasing gas velocities, corresponds to the theory presented above, which predicts an inverse proportionality at very high gas velocities.

4.9 Effect of accumulated dust on the pressure drop

Two typical graphs of the pressure drop across the BSR packing versus time are presented in Fig. 7-8; the data points are smoothed over one minute. In the first graph, Re was *ca.* 370, indicating laminar flow. No significant change of the pressure drop is seen during the seven hours on-stream, in which *ca.* 26 g_{dust} accumulated on the rods (which is close to the expected equilibrium value under these conditions). The same was observed for the experiments with the PPR, which were also in the laminar flow regime.

In the second graph, Re was *ca.* 2040, indicating transitional flow. A small yet apparently significant decrease of the pressure drop, by about 6%, can be observed during the first hour on-stream.

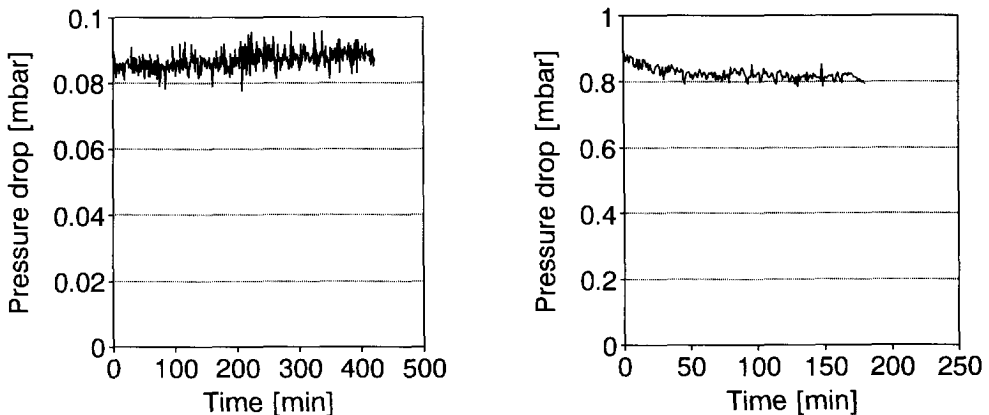


Figure 7-8 Friction factor of the BSR vs. time, during a dust accumulation run; a) laminar flow; b) transitional flow.

The small decrease of the pressure drop at the higher Reynolds numbers is attributed to 'smoothing' of the rods, in the sense that dust fills the grooves of the screw thread. The lower wall roughness then leads to a lower pressure drop. Obviously, this effect is not expected at the lower Reynolds number, since then the flow is laminar and the pressure drop is not affected by the wall roughness.

5 Assessment of the effect of accumulated dust on the catalyst efficiency

The results obtained in the previous section can be used to assess the effect that the accumulated dust in the BSR and PPR will have on the efficiency (or apparent activity) of the catalyst in these reactors. In this study it is assumed that the only effect of the dust is the introduction of an extra mass transfer resistance *outside* of the catalyst particles. The apparent catalyst activity will be decreased by the dust, because the reactants have to diffuse through the layer of dust. The possibility of pore blocking or poisoning is not considered, as it is beyond the scope of this project.

Only the steady state situation is considered for both reactors. For the PPR this implies that the *original* voids of the clean catalyst beds are completely filled with fluffy dust. Though this will be the true steady state in the case of the high dust concentrations used in this study ($4\text{--}13 \text{ g}_{\text{dust}}/\text{m}^3_{\text{gas}}$), in the case of much lower concentrations a steady state may be reached in which only the bottom part of all catalyst envelopes is filled with dust. In the latter case the effect of the dust will of course be less than calculated in this study.

5.1 Bead String Reactor

It is assumed that the dust accumulated in the BSR is located in a thin layer around the strings or rods of catalyst material; see Fig. 7-9. The chemical reaction then involves three subsequent steps:

1. mass transfer from the bulk flow to the surface of the dust layer;
2. diffusion through the dust layer;
3. diffusion, in parallel with reaction, in the catalyst particle.

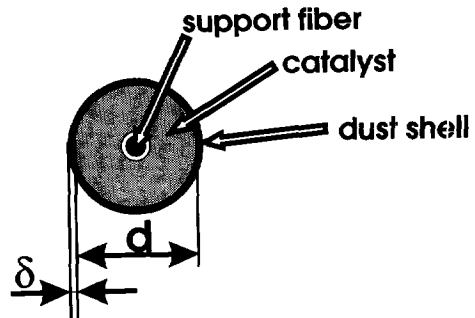


Figure 7-9 Idealized picture of a fouled BSR string or rod.

Each of these steps has a characteristic resistance, and the steps take place in series. To assess the importance of the dust layer, the extra resistance resulting from the dust layer should be compared to the resistance of the other two steps. This can be done by combining the three expressions that describe the molar flow of reactants for each three steps, which results in an expression for the overall rate constant of the process.

For a first order chemical reaction, it can be easily derived that the overall rate constant is given by:

$$k_{ov} = \frac{1}{\frac{d^2}{4k_g(d+2\delta)} + \frac{d\delta}{4D_d} + \frac{1}{k_r\eta_p}} \quad (7-12)$$

The magnitude of the two extra-particle resistances (steps 1 and 2) can be compared to the intraparticle resistance (step 3) by means of Biot numbers:

$$Bi_1 = \frac{k_r\eta_p d^2}{4k_g(d+2\delta)}; \quad Bi_2 = \frac{k_r\eta_p d\delta}{4D_d} \quad (7-13)$$

Obviously, Biot numbers bigger than one indicate a large extra-particle resistance compared to the intraparticle resistance. The relative influence of the diffusion through the dust layer compared to the film diffusion is reflected by the ratio of Bi_2 to Bi_1 ; from Eq. (7-13) it follows that this ratio is given by:

$$\frac{Bi_2}{Bi_1} = \frac{\delta}{D_d} k_g \quad (7-14)$$

In the derivation of Eqs. (7-12) and (7-14), it has been assumed that the dust layer thickness is small compared to the catalyst particle diameter. To check this, consider the case described in Fig. 7-5. It was estimated that under those conditions, the steady state amount of dust accumulated in the reactor is *ca.* 40 g. Assuming that this complete amount is present as a uniform layer around the rods, and assuming a dust density that is half the compacted bed density, the dust layer thickness is estimated to be 36 μm . This is indeed small compared to the diameter of the strings (1.9 mm). Note that this case the linear gas velocity was only 0.65 m/s, whereas in industrial practice probably a higher velocity would be chosen; in that case the steady state dust layer thickness would even be smaller than 36 μm .

To evaluate the Biot numbers, values should be found for the various parameters in Eq. (7-13). Consider the case defined in Table 7-5; the conditions are chosen identical to those of Fig. 7-5. The diffusivity of the reactants in the dust layer is related to the free gas diffusivity by:

$$D_d = \frac{\epsilon_d}{\tau_d} D_{free} \quad (7-15)$$

The value of the mass transfer coefficient is calculated with the relations presented in Chapter 3.

With these data, $Bi_1 = 0.055$ and $Bi_2 = 0.0044$. In other words, here the reaction rate is dominated by the kinetics of the reaction, and neither the film diffusion nor the diffusion through the dust layer is rate limiting. Comparing the two Biot numbers, it follows that the diffusion through the dust layer is much faster than through the film layer.

This leads to the conclusion that in the considered case, the dust has no effect on the efficiency of the catalyst material. This conclusion holds true for higher gas velocities. Depending on the flow regime, an increase of the gas velocity does or does not lead to an increase of k_g , which is constant for laminar flow or

proportional to $Re^{0.8}$ for turbulent flow (see Chapter 3). Furthermore the increased gas velocity will lead to a thinner dust layer around the catalyst material, as the dust re-entrainment rate is generally proportional to $Re^{1 \text{ to } 2}$. As a result, Bi_2/Bi_1 will decrease even further; in other words, the influence of the dust layer will become even smaller. The conclusion of this assessment is, that the amount of fly ash accumulated in a BSR is so small that it has no effect on the apparent activity of the catalyst. Note, however, that this conclusion might be reversed if other types of dust would be used, or if the dust blocks catalyst pores and/or chemically deactivates the catalyst.

Table 7-5 Specifications of the dust case-study.

k_r	5	$[m^3_{\text{gas}}/(m^3_{\text{cat}} \cdot s)]$
d	2	[mm]
D_p	10^{-6}	$[m^2/s]$
$\Rightarrow \eta_p$	0.72	[-]
δ	36	$[\mu m]$
ε_d	0.7	$[m^3_{\text{void}}/m^3_{\text{dust}}]$
τ_d	2	[-]
D_{free}	$4 \cdot 10^{-5}$	$[m^2/s]$
k_g	0.03	$[m/s]$

5.2 Parallel Passage Reactor

As was mentioned, it is assumed that the original voids of the catalyst beds are completely filled with fluffy dust; see Fig. 7-10. Out of convenience it is assumed in the following discussion that the catalyst particles are spherical and that the catalyst beds are flat.

To assess the effect of the dust on the apparent catalyst activity, the mass transfer relations presented in Chapter 6 will be used. As stated in Chapter 6, it is assumed that the mass transfer from the bulk flow in the gas channels to the catalyst beds is fast compared to the mass transfer in the catalyst beds themselves.

When the catalyst beds in a PPR are considered as catalyst 'slabs', of which the apparent activity is limited by diffusion/dispersion through the voids of the bed and diffusion/reaction in the catalyst particles, it follows that for a first order chemical

reaction the overall rate constant can be written as:

$$k_{ov} = k_r \eta_p \eta_s \quad (7-16)$$

In this equation, η_p represents the rate retardation resulting from the concentration gradient inside the particles, whereas η_s represents the extra rate retardation resulting from the concentration gradient in the interstitial space of the catalyst slab (between the particles). The two effectiveness factors η_p and η_s are related to two Thiele moduli, one for the particles and one for the 'slab':

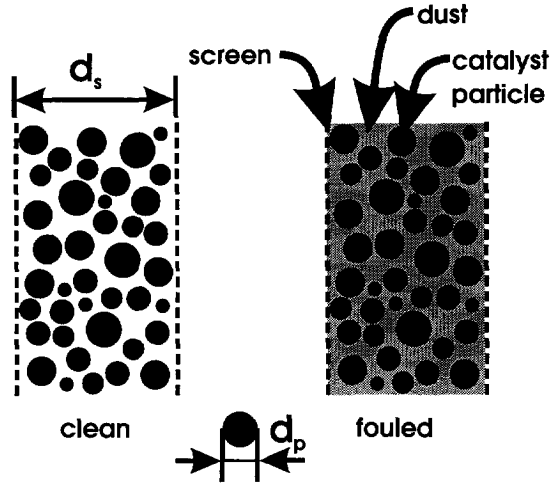


Figure 7-10 Idealized picture of a fouled PPR bed.

$$\phi_p = \frac{d_p}{6} \sqrt{\frac{k_r}{D_p}} ; \quad \phi_s = \frac{d_s}{2} \sqrt{\frac{k_r \eta_p (1 - \epsilon_b)}{D_{bed}}} \quad (7-17)$$

Note that the term $(1 - \epsilon_b)$ is used to calculate the amount of catalyst in the slab; this implies that ϵ_b is the voidage of the 'clean' catalyst beds, irrespective of the real voidage of the beds when they are filled with dust.

The only parameter in Eq. (7-17) that will change as a result of dust accumulation, is the effective lateral bed dispersion coefficient D_{bed} . In Chapter 6 it was shown that D_{bed} is often modeled as the summation of a static and a convective distribution:

$$D_{bed} = \frac{\epsilon_b'}{\tau_b'} D_{free} + l_g u \quad (7-18)$$

In this equation, the primes of ϵ_b' and τ_b' indicate that in the case of a PPR filled with dust, the actual voidage and tortuosity of the fouled catalyst bed should be used. Obviously, ϵ_b' is smaller than ϵ_b . The tortuosity of a fouled bed will be bigger than that of a clean bed, though probably not much, as the dust is rather fluffy. All in all this shows that the static contribution to D_{bed} will be decreased by the accumulation of dust in the beds.

However, not only the static contribution will be decreased, but also the convective contribution. This results from the decreased gas velocity u in the catalyst bed caused by the increased resistance to flow due to the dust. As was stated in Chapter 6, the gas velocity in the catalyst beds may be estimated using a relation for flow through a

porous medium, such as the Ergun equation or, since the flow in the beds will be laminar, the Blake-Kozeny equation. Unfortunately those relations were derived for beds of unimodal spherical particles, which is surely not valid for a bed fouled with dust particles. Therefore it is interesting to study the effect of dust in a packed bed on the (superficial) gas velocity, for a given pressure gradient.

When the bed of catalyst particles is fouled by dust, a fraction x_d of the bed volume is occupied by dust particles with an (average) particle diameter d_d ; a fraction x_c of the bed volume is occupied by catalyst particles with an (average) particle diameter d_c ; the rest of the bed volume is void. It is not difficult to show that for laminar flow and a given pressure gradient, the ratio of the superficial gas velocity in the fouled bed to the superficial gas velocity in the clean bed is given by:

$$\frac{u_0|_{x_d=x_d}}{u_0|_{x_d=0}} = \frac{\left(1 - \frac{x_d}{1-x_c}\right)^3}{\left(1 + \frac{x_d}{x_c} \frac{d_c}{d_d}\right)^2} \quad (7-19)$$

Eq. (7-19) was derived similarly to the original Blake-Kozeny relation.

To estimate the effect of the dust quantitatively, consider the experiments described in Section 4. Based on experimental data it is estimated that the bed voidage of the PPR beds is reduced from 0.40 to 0.26 when the voids of the catalyst beds are completely filled with fluffy dust—*i.e.* $x_c = 0.6$, $x_d = 0.14$. This will result in a decrease of the static contribution to D_{bed} by 35%, and a decrease of the convective contribution (according to Eq. (7-19), with $d_c = 1$ mm, $d_d = 30$ μ m) by no less than 99.6%. The consequences this has for the apparent overall catalyst activity, depend on the rate determining step in the 'clean' PPR. If the reaction kinetics alone would be the rate determining step, the dust would obviously have no effect at all. However, if the interparticle mass transfer alone would be the rate determining step, and it would be mainly caused by the convective contribution, the overall rate constant would drop by 94% (since in that case the 'slab' effectiveness factor would be proportional to the square root of the bed dispersion coefficient). Note that this conclusion is not affected by the statement in Chapter 6, that the mass transfer in a PPR is strongly enhanced by convective transfer of momentum from the gas channels, through the wire gauze screens, into the bed. Indeed, also this mechanism is driven by pressure gradients (in this case local), and it will be affected in the same way by the increased resistance to flow in the beds.

The conclusion of this assessment is, that depending on which of the steps in the reaction process is rate determining, dust accumulation in the PPR may result in a decrease of the apparent catalyst activity by 0 to 94%. Note that the worst value (94% decrease) can only be obtained in a steady state situation, after the voids of the catalyst beds have been completely filled with dust. Although it was shown in this chapter that at high dust concentrations in the gas this situation may be reached after as few as 20 hours, in practice it might take years when the dust concentrations are significantly

lower. Furthermore, in a properly designed PPR the rate determining step should never be the interparticle mass transfer alone!

6 Conclusions

In the PPR, the fly ash appeared to accumulate predominantly in the catalyst beds, which were gradually filled with dust from bottom to top. No re-entrainment of fly ash accumulated in the beds seemed to occur, as the amount of accumulated fly ash increased linearly with time, at least during the first seven hours on-stream. At a linear gas velocity of *ca.* 1 m/s, the pressure drop was independent of the dust concentration in the gas. Furthermore the pressure drop did not increase or decrease with the amount of accumulated dust.

In the BSR, re-entrainment of dust accumulated on the "strings" seemed to occur, as the rate of dust accumulation decreased by a factor 2.5 within the first four hours on-stream. At low Reynolds numbers (laminar flow), the amount of accumulated dust did not affect the pressure drop across the reactor. At higher Reynolds numbers (transitional flow), a small gradual decrease of the pressure drop (by up to 6 %) occurred in the first hour on-stream, after which it remained constant. This phenomenon was ascribed to smoothing of the "strings" resulting from accumulation of dust in the cavities of the "strings".

For a linear gas velocity of 0.8 m/s and a run time of 3 h, the amount of fly ash accumulated in the BSR was found to depend linearly on the dust concentration in the gas. With increasing gas velocities, the amount of fly ash accumulated within three hours on-stream seemed to show a maximum at 3.6 m/s. It is expected that the amount of dust accumulated in the steady state situation, decreases with increasing gas velocity.

Although in most experiments the flow seemed laminar, the observations could be described qualitatively by a simple model pertaining to turbulent flow. However, quantitative prediction of the rate of dust accumulation in the tested reactors, starting from literature data only, is quite impossible. Only after fitting of the model parameters to experimental data, limited extrapolation seems justified.

Based on the experimental data, it was estimated that for the investigated conditions the accumulation of dust in the BSR has no effect on the apparent activity of the catalyst material. For the PPR the effect of the accumulated dust depends on the rate determining step, and in the worst case could reduce the apparent catalyst activity by an estimated 94%. Although these figures support the claim that the BSR is more suitable in a high dust environment than a PPR, it should be noted that these figures will be strongly dependent on the type of dust and the process conditions.

Acknowledgements

EPON N.V. is gratefully acknowledged for providing the fly-ash used in the present study. Ernst de Leeuw and Lilian Kok are gratefully acknowledged for their substantial contribution to the work reported in this chapter.

Notation

A_{wall}	amount of wall area	$[m^2]$
C	roughness parameter	$[-]$
c_d	dust concentration in the gas	$[kg_{dust}/m^3_{gas}]$
d	diameter of the catalyst particles or BSR rods	$[m]$
d_c, d_d	diameter of catalyst or dust particles	$[m]$
d_p	dust or catalyst particle diameter	$[m]$
D_{bed}	effective lateral bed dispersion coefficient in PPR	$[m^2/s]$
D_d	effective molecular diffusion coefficient in dust layer	$[m^2/s]$
D_{free}	free molecular diffusion coefficient	$[m^2/s]$
D_p	effective molecular diffusion coefficient in catalyst particle	$[m^2/s]$
f	(Fanning) friction factor ($\equiv 4f/4$)	$[-]$
k_d	mass transfer coefficient of dust	$[m/s]$
k_d^+	dimensionless mass transfer coefficient of dust	$[-]$
k_g	molecular mass transfer coefficient	$[m/s]$
k_{ov}	overall rate constant of a chemical reaction influenced by mass transfer	$[1/s]$
k_r	first order reaction rate constant	$[m^3_{gas}/(m^3_{cat} \cdot s)]$
l_g	mixing length	$[m]$
m	'number of bursts'	$[-]$
M	amount of dust deposited on a wall	$[kg_{just}]$
M_0	amount of dust deposited on a wall that is not susceptible to re-entrainment	$[kg_{just}]$
S_p	stopping distance of a dust particle	$[m]$
t	time	$[s]$
u_0	superficial gas velocity in a bed	$[m/s]$

$\langle u \rangle$	average gas velocity in a channel	[m/s]
$u_{p,0}$	initial velocity of a dust particle	[m/s]
u^*	friction velocity	[m/s]
x	fraction of dust trapped in reactor	[kg _{trapped} /kg _{entered}]
x_c, x_d	volume fraction of catalyst or dust particles in a bed	[m ³ _{part} /m ³ _{bed}]
y_{lam}	thickness of the laminar sub-layer	[m]
y^+_{lam}	dimensionless thickness of the laminar sub-layer	[-]

Greek letters

α	fraction of particles removed under a burst	[-]
δ	dust layer thickness	[m]
ϵ_b	voidage of 'clean' bed of catalyst particles	[m ³ _{void} /m ³ _{dust 'bed'}]
ϵ'_b	voidage of fouled bed of catalyst particles	[m ³ _{void} /m ³ _{dust 'bed'}]
ϵ_d	voidage of dust 'bed'	[m ³ _{void} /m ³ _{dust 'bed'}]
η_p	effectiveness factor of a catalyst particle	[-]
η_s	effectiveness factor of a catalyst 'slab'	[-]
θ_{burst}	fraction of a surface covered with burst sites at any instant	[-]
ν	kinematic gas viscosity	[m ² /s]
ρ	density of the gas	[kg _{gas} /m ³ _{gas}]
ρ_p	density of a dust particle	[kg _{part} /m ³ _{part}]
τ_b	tortuosity of fouled bed of catalyst particles	[-]
τ_d	tortuosity of dust layer	[-]
$\tau_{f,w}$	friction stress exerted by the fluid on the wall	[N/m ²]
τ_p	particle relaxation time	[s]
τ_p^+	dimensionless particle relaxation time	[-]
ϕ_p	Thiele modulus of a spherical catalyst particle	[-]
ϕ_s	Thiele modulus of a PPR catalyst 'slab'	[-]
Φ_m''	mass flux of dust to the wall	[kg _{dust} /(m ² _{wall} ·s)]

References

Beal, S.K., 1970. *Nucl. Sci. Eng.* **40**, 1.
 Bosch, H. and Janssen, F.J.J.G., 1988, Catalytic Reduction of Nitrogen Oxides - A Review on the Fundamentals and Technology. *Catal. Today* **2**, 369-532.
 Braaten, D.A., Shaw, R.H. and Paw U, K.T., 1993, Boundary Layer Structures Associated with Particle Re-entrainment. *Boundary Layer Meteo.* **65**, 255-272.
 Cleaver, J.W. and Yates, B., 1973, Mechanism of Detachment of Colloidal Particles from a Flat Substrate in a Turbulent Flow. *J. Colloid Interface Sci.* **4**, 467-474.

- Cleaver, J.W. and Yates, B., 1975. *Chem. Engng. Sci* **30**, 983.
- Cleaver, J.W. and Yates, B., 1976, The Effect of Re-entrainment on Particle Deposition. *Chem. Engng. Sci* **31**, 147-151.
- Davies, 1983, A New Theory of Aerosol Deposition from Turbulent Fluids. *Chem. Engng. Sci* **38**(1), 135-139.
- Davies, C.N., 1966, *Aerosol Science*. Academic Press, London.
- Epstein, N., 1988, Particulate Fouling of Heat Transfer Surfaces: Mechanisms and Models, in *Fouling Science and Technology* (Edited by L.F. Melo, T.R. Bott and C.A. Bernardo), vol. Series E: Applied Sciences - Vol. 145, pp. 143-164. Kluwer Academic Publishers, London.
- Friedlander, S.K. and Johnstone, H.F., 1957. *Ind.Eng.Chem.* **49**, 1151.
- Groeneveld, L., 1991, *Internal report no. 63188-WPB on SCR demonstration project unit CG-12*. Elektriciteits-Produktie maatschappij Oost- en Noord-Nederland, Zwolle, The Netherlands.
- Groeneveld, L., 1992, Pilotproject levert hoopvolle resultaten. *Proces Technologie*, 30-34.
- Hauenstein, K. and Herr, W., 1993, Strömungsführung des Rauchgases in neuen und zu optimierenden DENOX-Reaktoren, in *VGB Conference*.
- Van den Kerkhof, F.M.G., 1986, Selectieve katalytische reductie van NOx uit rookgassen. *I2-Procestechnologie*, 35-39.
- Klingenberg, A., 1984, *Vliegias van kolengestookte elektriciteitscentrales - karakteristieken, vangstrendementen, effecten*. University of Groningen, Groningen, The Netherlands.
- Levich, V.G., 1962, *Physiochemical Hydrodynamics*. Prentice-Hall, Englewood Cliffs, NJ.
- Liu, B.Y.H. and Ilori, T.A., 1973, *ASME Symp Flow Studies in Air and Water Pollution*. Atlanta, GA.
- Mollinger, A.M., 1994, Particle Entrainment - Measurement of the Fluctuating Lift Force. *Ph.D. Dissertation*. Delft University of Technology, Delft, The Netherlands.
- Papavergos, P.G. and Hedley, A.B., 1979, in *2nd Multi-Phase Flow and Heat Transfer Symp. Workshop*. Miami.
- Papavergos, P.G. and Hedley, A.B., 1984, Particle Deposition Behaviour from Turbulent Flows. *Chemical Engineering Research & Design* **62**, 275-295.
- Reeks, M.W. and Skyrme, G., 1976. *J. Aerosol Sci.* **7**, 485.
- Schallert, B. and Kaulitz, J., 1986, Betriebserfahrungen mit SCR-DENOX-Versuchsanlagen unter verschiedenen Einsatzbedingungen. *VGB Kraftwerkstechnik* **66**(9), 852-858.
- Wahl, 1987, Neueste Erfahrungen mit den Entstickungsanlagen der VKR. *VGB Kraftwerkstechnik* **67**(12), 1198-1203.
- Yiantsios, S.G. and Karabelas, A.J., 1994, Fouling of Tube Surfaces: Modeling of Removal Kinetics. *AIChE J.* **40**(11), 1804-1813.

Chapter 8

Demonstration of the Zeolite-covered Screen Reactor concept

published as:

H.P. Calis, A.W. Gerritsen, C.M. van den Bleek, C.H. Legein, J.C. Jansen and
H. van Bekkum, 1995, Zeolites Grown on Wire Gauze: A New Structured Catalyst
Packing for Dustproof, Low Pressure Drop DeNO_x Processes.
Can. J. Chem. Eng. **73**(1), 120-129.

Contents

Summary	233
1 Introduction	233
2 Experimental	235
2.1 Description of the tested catalyst packing	235
2.2 Testing of the catalyst packing on denox-activity	237
2.2.1 Test conditions	237
2.2.2 Experimental set-up	237
2.2.3 Checks on falsification of observations	239
2.2.4 Kinetic experiments with Cu-ZSM-5 catalyst packing	240
3 Results and discussion	241
3.1 Checks on falsification of observations	241
3.2 Kinetic experiments with Cu-ZSM-5 catalyst packing	243
3.3 Comparison with amorphous vanadia-titania/silica catalysts	247
3.4 Applicability of supported Cu-ZSM-5 for dust, steam and SO ₂ containing flue gases	248
4 Conclusions	249
Acknowledgements	250
Notation	250
References	251

Summary

To prove the applicability of zeolite based catalysts in dustproof low pressure drop reactors, a novel structured catalyst packing has been developed consisting of ZSM-5 crystals *in situ* grown on metal wire gauze. Using this technique, mechanically strong catalyst packings of any required shape can be produced that give an extremely low pressure drop across the packing, and it can be expected that such packings allow dustproof operation. Such features make the packing especially suitable for end-of-pipe processes, like the catalytic removal of NO_x from large flows of dust containing flue gas. To demonstrate the feasibility of the packing as a catalyst, it was tested—after incorporating copper into the zeolites by ion exchange—on its activity for selective catalytic reduction of nitric oxide with ammonia at 350°C. Both the activity and selectivity of the catalyst packing proved—after correction for temperature differences—to be superior to conventional vanadia/titania catalysts.

1 Introduction

End-of-pipe processes applying heterogeneous catalysis to remove pollutants, such as Selective Catalytic Reduction (SCR) of nitric oxide, require dustproof, low pressure drop reactors. The demand of dustproof operation and low pressure drop conflicts with the need for intensive contact between the gas flow and the catalyst. To deal with this conflict, special end-of-pipe reactors with a more or less *structured* catalyst packing have been developed, such as the Honeycomb or Monolithic Reactor, Parallel Passage Reactor and Lateral Flow Reactor.

The currently most widely used catalyst for SCR of NO_x with ammonia consists of vanadia, often in combination with titania, on an amorphous silica or alumina carrier. In a Honeycomb Reactor the catalyst is present as a washcoat on the surface of the channels of the ceramic body. In the Parallel Passage Reactor and Lateral Flow Reactor the catalyst is shaped as particles with a size in the order of magnitude of a millimeter, which are contained in shallow "envelopes" of permeable wire gauze (*cf.* Chapter 1).

An interesting alternative to amorphous deNO_x-catalysts are zeolites of which the counter cations are (partially) exchanged with transition metals. Thanks to the high total surface area and well-defined pore system of zeolites, and the optimal dispersion of the exchanged metals, these systems show a high deNO_x-activity. Particularly the

MFI-type Cu-exchanged zeolites show special NO_x converting properties, not only for SCR with ammonia (e.g., Held et al., 1990, 1991) or hydrocarbons (e.g., Sato et al., 1991; Iwamoto et al., 1989; Teraoka et al., 1992; d'Itri and Sachtler, 1992; Montreuil and Shelef, 1992), but also for catalytic decomposition without additional reactants (e.g., Iwamoto et al., 1989; Iwamoto and Hamada, 1991; Li and Hall, 1991; Li and Armor, 1991; Giamello et al., 1992; Shelef, 1992; Hall and Valyon, 1992). Consequently, zeolites are gaining popularity among researchers working in the field of catalytic NO_x abatement.

For many applications zeolite crystals are compounded with an amorphous matrix to obtain particles with a size in the order of magnitude of a millimeter, to prevent an intolerably high pressure drop across the reactor and fast plugging of the catalyst bed with dust. Unfortunately, however, this counteracts the advantage of the high zeolite activity because of mass transfer limitation in the particles.

To make optimal use of the intrinsic high activity of zeolitic catalysts in end-of-pipe processes, it would therefore be desirable to manufacture a catalyst packing consisting of zeolite crystals that are rigidly mounted to a structured support. The packing should be mechanically stable and its structure should result in dustproof operation and low pressure drop.

It has been attempted to obtain such a packing by wash-coating prefabricated honeycomb structures with crystals or by co-extruding zeolite crystals with ceramic paste to form honeycomb structures (Lachman and Nordlie, 1986). A major drawback of these techniques is the mechanical weakness of the product, either in the sense of poorly bonded crystals (first technique) or of a weak honeycomb structure necessarily sintered at a relatively low temperature (second technique). A much better technique is to grow the zeolite crystals *in situ* on the support. This has been done by subjecting a ceramic honeycomb structure to a dilute aqueous solution of active silica at a high pH and elevated temperature (Lachman and Patil, 1989).

In situ growth of zeolites on various substrate materials has also been reported by Jansen et al. (1992). Their technique is based on zeolite synthesis through heterogeneous nucleation: under hydrothermal conditions a solid material serves as the preferred nucleation center for condensation reactions. Stable nuclei are formed at the substrate surface and subsequent crystallization yields zeolite crystals that are chemically bonded to the substrate surface. The mechanical strength of the zeolite/substrate bonding is high: the crystals can only be removed from the substrate by scratching with a sharp tool, leading to breakage of the crystals themselves but not to breakage of the zeolite/substrate bond. Further it was found that the size and shape of the crystals, as well as the orientation of the crystals with respect to the substrate surface, can be widely manipulated through the synthesis conditions.

This paper aims to assess the feasibility of a novel structured zeolitic catalyst packing, prepared according to Jansen et al. (1992), as a replacement for packings of amorphous vanadia catalysts currently used in deNO_x reactors. The novel catalyst packing consists of ZSM-5 zeolites *in situ* grown on stainless steel wire gauze, that is shaped in such a way as to achieve dustproof, low pressure drop operation. The

packing is made catalytically active by introduction of copper through ion exchange. Attention will be focused on testing the deNO_x activity of the composite catalyst packing, with ammonia as the reductant of NO, under various flue gas conditions. This will lead to an empirical rate equation, allowing comparison with the traditional vanadia/silica catalyst.

The main reason to use ammonia as the reductant of NO, although short hydrocarbons currently receive much attention concerning automotive exhaust gas treatment, is the fact that ammonia, or, more general, ammonia-type reductants, are much more effective for NO reduction than hydrocarbons, due to the intrinsic high reactivity of ammonia toward NO_x species to produce an N≡N bond. The advantages of the novel catalyst packing are believed to be best exploited in processes characterized by high reactivities and high space velocities. Another reason is that the use of ammonia in this study simplifies comparison of the novel catalyst packing with the traditional catalysts, since most industrial deNO_x units use ammonia as well.

2 Experimental

2.1 Description of the tested catalyst packing

The catalyst packing was prepared according to the method described by Jansen et al. (1992) and involved pre-treatment of the support material, zeolite synthesis, calcination, and ion exchange.

As support material, strips of stainless steel (316) wire gauze were used with 35 μm wire thickness and 44 μm mesh size. The gauze was pre-shaped in rolls. Note that in an industrial application, the compound catalyst might be shaped as stretched, corrugated or folded sheets.

The zeolites were grown on the gauze from a synthesis mixture containing tetraethyl orthosilicate (TEOS), sodium aluminate, tetrapropylammonium hydroxide (TPA-OH) and sodium chloride in water, in a molar ratio of 2.6 : 1 : 0.059 : 1.6 : 1767. The synthesis was performed at 170°C and autogenic pressure, for 21.5 h. Calcination was done at 500°C for 10 h. After this, copper ions were introduced by contacting the samples with an aqueous 0.017 mol/L copper acetate solution at room temperature, three times consecutively for 24 h, each time with a fresh solution. Finally, the samples were dried in air at 100°C for 1 h.

SEM photos of the tested catalyst packing are shown in Fig. 8-1. Average crystal dimensions are 7.3 x 5.1 x 2.2 μm.

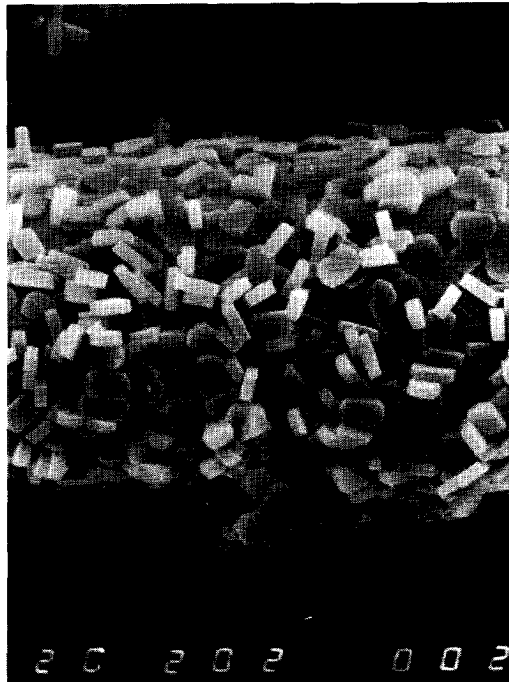
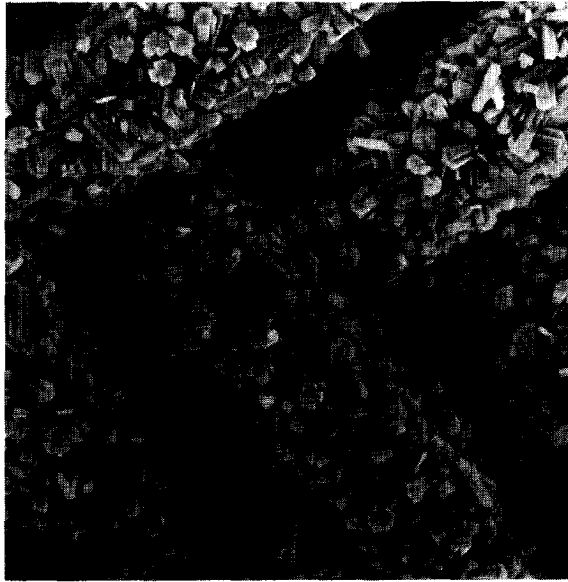


Figure 8-1 SEM pictures of the ZSM-5 zeolite *in situ* grown on stainless steel wire gauze. The wire diameter is 35 μm .

The Si/Al ratio of the crystals, as determined through ICP-AES analysis, was 44.1. The Al/Cu ratio was 0.88, corresponding to an exchange level of 227% as one Cu counterion is needed per two Al in the tetrahedral framework. Excess ion exchange capacity is not unusual for ZSM-5; cf. Kharas (1993) for a brief discussion and references, and Datka and Tuznik (1985) or Dessau (1990). The phenomenon has been attributed to the presence of SiOH and SiO⁻ groups in the ZSM-5 lattice, and to the intermediacy of species like [CuOH]⁺ or [Cu-O-Cu]⁺ during ion exchange.

The micropore surface area of the crystals, as determined through nitrogen adsorption analysis using a Micromeritics (Norcross (Georgia), USA) ASAP 2000 M apparatus was 352 m²/g_{ZSM-5}, and the micropore volume was 0.17 cm³/g_{ZSM-5}. The BET surface area was 435 m²/g_{ZSM-5}. The micropore size distribution was very small, with a median pore diameter of 0.5 nm, which agrees with the crystallographic zeolite pore dimensions.

The tested catalyst packing had a total mass of 8.4 g, consisting of 96.5% mass support material (gauze), 3.5% mass ZSM-5 type zeolite and 0.1% mass copper.

2.2 Testing of the catalyst packing on denox-activity

2.2.1 Test conditions

The prepared catalyst packing was tested on its activity for SCR of nitric oxide with ammonia under various flue gas conditions. The test gas contained neither dust nor sulfur dioxide. Furthermore, inert gases present in a typical flue gas besides nitrogen (notably carbon dioxide and argon), were substituted by nitrogen for the sake of simplicity. The fact that carbon dioxide is inert under flue gas conditions is concluded from Hofmann and Weidner (1989), who found that in the concentration range of 0 to 20 vol. %, carbon dioxide has no effect on the SCR reaction rate with ammonia over V/W/TiO₂ deNOx-catalysts.

The experimental conditions of the present study are listed in Table 8-1.

Table 8-1 Experimental conditions for tests on deNOx activity.

p	[kPa]	110
T	[°C]	350
c_{NO}	[ppmv]	20—200
c_{NH_3}	[ppmv]	30—1000
c_{O_2}	[vol. %]	0/5
$c_{\text{H}_2\text{O}}$	[vol. %]	0/15
c_{N_2}		balance

2.2.2 Experimental set-up

A simplified flow sheet of the experimental set-up is given in Fig. 8-2. Nitrogen, air, nitric oxide and ammonia were dosed using mass flow controllers; water was dosed using a peristaltic pump. The gases and water were heated, mixed, and either led through the reactor or by-passed.

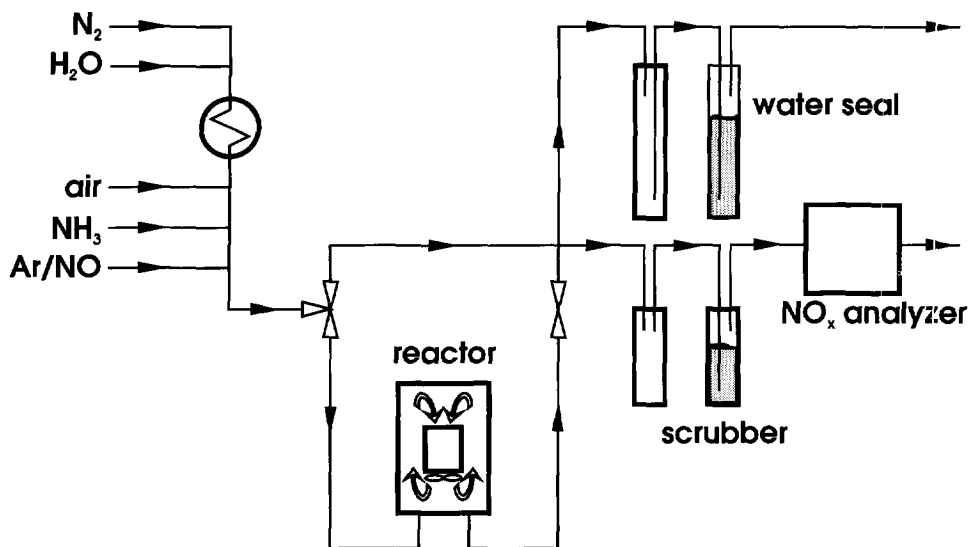


Figure 8-2 Simplified flow sheet of the experimental set-up used for the kinetic experiments.

The experiments were performed in a RotoBerty[®] (Berty Reactor Engineers, Ltd., Fogelsville (Pennsylvania), USA) internal recycle reactor, described in Chapter 4. Thanks to the design of the experimental catalyst packing, the pressure drop across the packing was so low that in all experiments the recycle ratio was higher than 50. Under the experimental conditions, this value fully justifies the use of reactor equations pertaining to an ideal Continuous Stirred Tank Reactor (CSTR) for evaluation of the experimental data.

Constant pressure in the system was obtained by using a water seal, generating a static back pressure of 10 kPa. The constant pressure in the system ensured a constant gas flow to the analyzing equipment.

Part of the by-pass flow or the product stream was stripped from water and ammonia using gas-washbottles filled with 85% mass phosphoric acid. The gas was analyzed on nitrogen oxides content using a chemiluminescence meter, equipped with a thermal convertor, which allowed measurement of either only the NO concentration, or the sum of the NO and NO_2 concentrations. In the kinetic experiments of the present study, always the sum of the NO and NO_2 concentrations was measured. Removal of water is necessary because it has a significant quenching effect on the NO-signal in the chemiluminescence equipment. Removal of ammonia is necessary because it is converted to NO and NO_2 in the thermal convertor, leading to erroneous NO readings. The experimental set-up operated fully automatically, controlled by a personal computer.

2.2.3 Checks on falsification of observations

Although the interpretation of kinetic data obtained from a recycle reactor is essentially straightforward, great care has to be taken to avoid experimental pitfalls that might easily falsify observations during the kinetic experiments. Four possible pitfalls were identified that might result in an erroneous characterization of the deNO_x-activity of the supported Cu-ZSM-5 catalyst:

- 1) Stripping of nitrogen oxides by phosphoric acid in the gas-washbottles during NO_x-analysis.
- 2) Oxidation of nitric oxide by oxygen in the reactor, thermal or catalyzed by the steel surface of the reactor or by the Cu-ZSM-5 packing.
- 3) Non-selective oxidation of ammonia by oxygen, to form nitric oxide, thermal or catalyzed by the steel surface of the reactor, the wire gauze or the ZSM-5 crystal lattice (i.e., over zeolite sites other than the Cu-sites).
- 4) Heterogeneously catalyzed reduction of nitric oxide by ammonia, over the steel surface of the reactor or the wire gauze, over the graphite bearings of the shaft or over the ZSM-5 crystal lattice.

Stripping of NO and NO₂ by phosphoric acid in the gas washbottles was checked using calibration gases with known concentrations of either NO or NO₂. These gases were either by-passed or led through the washbottles filled with phosphoric acid, at the same flow rate as during the kinetic experiments.

Oxidation of NO by oxygen, thermal or catalyzed by the reactor wall, was checked by measuring the conversion of NO and the production of NO₂ when a mixture of 5 vol. % oxygen, 0 or 15 vol. % water, 100 ppmv NO, balance nitrogen, was passed through the empty reactor. Oxidation catalyzed by the Cu-ZSM-5 packing was checked occasionally during the kinetic experiments by comparing the NO signal with the NO + NO₂ signal.

Reduction of nitric oxide by ammonia and non-selective oxidation of ammonia by oxygen to nitric oxide, thermally or heterogeneously catalyzed otherwise than over the Cu-sites of the zeolites, was checked by measuring the net consumption rate of nitric oxide when a mixture of 5 vol. % oxygen, 0 or 15 vol. % water, 100 ppmv nitric oxide, 1000 ppmv ammonia, balance nitrogen, was passed through the reactor. In these experiments, the reactor contained either no catalyst packing at all, bare wire gauze, or wire gauze with *in situ* grown ZSM-5 that was not Cu-exchanged yet. In the latter case, 0.29 g of non-exchanged, supported ZSM-5 was used. The net consumption rate of nitric oxide is defined as the difference between the molar flows of nitric oxide in the feed and product streams; actually it is the difference between the reduction rate of nitric oxide and the rate of ammonia oxidation by oxygen to nitric oxide. Note that since the sum of NO and NO₂ concentrations was always measured, oxidation of NO to NO₂ was not measured as "consumption" of NO.

2.2.4 Kinetic experiments with Cu-ZSM-5 catalyst packing

Each kinetic experiment consisted of three stages. First, the system was flushed with nitrogen for 20 min. Secondly, the test gas was passed through the reactor for 80 min and the product stream was analyzed on NO + NO₂ content. Thirdly, the reactor was bypassed for 80 min and the test gas (i.e., the feed stream) was analyzed on NO + NO₂ content. The chemiluminescence meter was calibrated (baseline and span) before each experiment. In all experiments, the catalyst packing consisted of two rolls of wire gauze, both covered with Cu-ZSM-5 prepared under identical conditions.

Four series of experiments were performed, in which the effect on the reaction rate and selectivity was studied of the nitric oxide, water, ammonia and oxygen concentrations. The standard feed composition was: 15 vol. % water, 5 vol. % oxygen, 1000 ppmv ammonia, 20 to 200 ppmv nitric oxide, balance nitrogen. The effect of the water, ammonia and oxygen concentration was studied by replacing one or more of the components partly or completely by nitrogen.

Most kinetic experiments were performed with a large excess of ammonia: the feed contained 1000 ppmv ammonia, compared to only 20 to 200 ppmv nitric oxide. Due to this large excess, the ammonia concentration does not change significantly during reaction, and can therefore be considered (pseudo) constant. As a result, the nitric oxide reduction rate becomes independent of the ammonia concentration, which simplifies the interpretation of the experimental data. However, in an industrial deNO_x process no excess ammonia is allowed at present, because all excess ammonia would leave the process unreacted and would be emitted with the flue gas. This is intolerable, since emission limits on ammonia are even stricter than on NO_x. Therefore it is common practice in industry to dose stoichiometric or slightly substoichiometric amounts of ammonia. To study the dependency of the nitric oxide reduction rate on the ammonia concentration, experiments were also performed at a stoichiometric nitric oxide : ammonia ratio. It is interesting in this respect, that recently cerium-exchanged zeolite catalysts were found to be a possible solution to the problem of ammonia slip. Ito et al. (1994) report that cerium-exchanged Mordenite zeolite allows the use of an NH₃/NO ratio of up to 1.3 without ammonia slip: all excess ammonia is oxidized selectively to N₂.

All experiments were performed at 350°C, because at this temperature the optimum trade-off was expected between deNO_x-activity and non-selective ammonia oxidation.

All experiments were performed at a weight hourly space velocity (WHSV) of 1340 h⁻¹ (based on the mass of the Cu-ZSM-5 crystals, excluding the mass of the support). This corresponds to a space time of 3.9 s. Only the experiments without oxygen were performed at a lower WHSV, 300 h⁻¹.

3 Results and discussion

3.1 Checks on falsification of observations

During stripping of water and ammonia from the sample gas to the chemiluminescence meter by leading it through phosphoric acid, about 3% of the NO and 8% of the NO₂ was absorbed as well. These values were obtained for gas phase concentrations of 50 to 100 ppmv NO and 35 to 70 ppmv NO₂. In this range of gas phase concentrations, the absorption of NO and NO₂ did not depend on their concentrations, neither did it decrease in time. This suggests that the absorption is a first order process, limited by the mass transfer rate from the gas phase to the liquid phase. To correct for the loss of NO, all measured NO concentrations were multiplied by 1/0.97. Because the amount of NO₂ in the test gas, formed through oxidation of NO, was negligible (see next paragraph), no corrections were needed for NO₂ loss in the washbottles.

Experiments on NO oxidation were done at a space time of 33 s, which is about ten times as large as during the kinetic experiments described below; this was done because the longer space time resulted in a higher NO to NO₂ conversion, resulting in a more accurate analysis. In a test gas consisting of 5 vol. % oxygen, 100 ppmv NO and balance nitrogen, 5.7% of the NO fed to the empty recycle reactor was oxidized to NO₂ at 350°C. When 15 vol. % water was added to the gas mixture, the NO to NO₂ conversion dropped to 2.4%. Based on these results, it was estimated that at a space time of 3.9 s, the NO to NO₂ conversion would be smaller than 1% in both cases. Furthermore it can be expected that any NO₂ formed during the kinetic experiments, will be rapidly reduced back to NO by ammonia (Van den Bleek and Van den Berg, 1980). This was confirmed experimentally during some of the kinetic experiments by measuring the NO signal only (by-passing the convertor of the chemiluminescence meter) and comparing it with the NO + NO₂ signal. For these reasons, oxidation of NO to NO₂ during the kinetic experiments was neglected.

In Fig. 8-3 the net consumption rate of nitric oxide is plotted versus the nitric oxide concentration in the reactor, i) for a reactor with no packing at all, ii) with a packing of bare stainless steel wire gauze, and iii) with a packing of gauze covered with non-exchanged ZSM-5. The net consumption of nitric oxide is the overall result of two parallel reactions: (1) the reduction of nitric oxide by ammonia to nitrogen, and (2) the non-selective oxidation of ammonia by oxygen to nitric oxide:

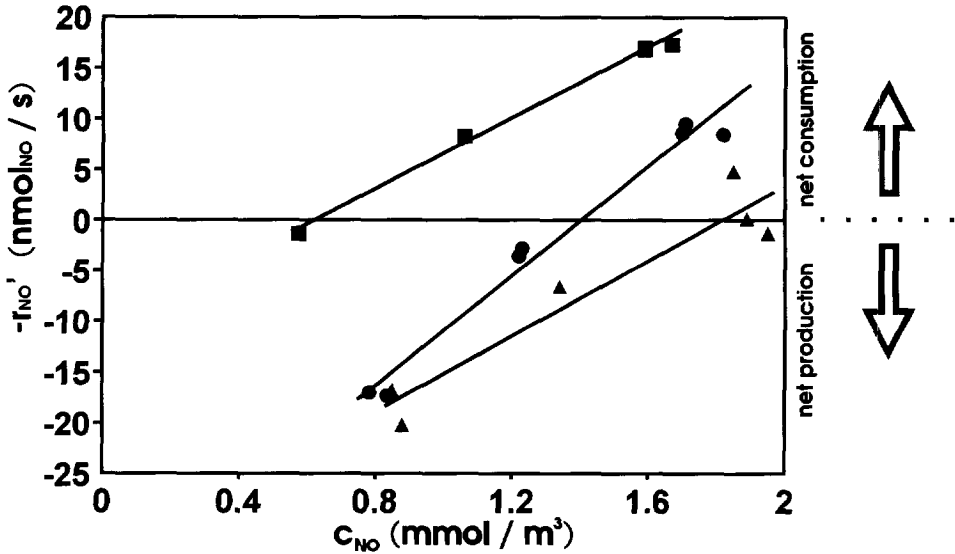
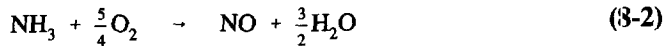
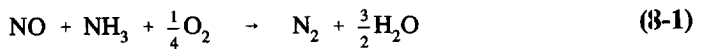


Figure 8-3 Net consumption rate of nitric oxide ($-r_{NO}'$) versus nitric oxide concentration in the reactor (c_{NO}) at 350°C; gas composition besides nitric oxide: 5 vol. % oxygen, 1000 ppmv ammonia, balance nitrogen. (●) empty reactor; (▲) bare wire gauze; (■) wire gauze with *in situ* grown ZSM-5 (not Cu-exchanged).



For both reactions (1) and (2) one could write down a reaction rate expression in a power law form:

$$r_1' \text{ [mol/s]} = \sum_i k_{1,i} S_{1,i} c_{NO}^A c_{NH_3}^B \quad (8-3)$$

$$r_2' \text{ [mol/s]} = \sum_i k_{2,i} S_{2,i} c_{NH_3}^D \quad (8-4)$$

In these expressions, $k_{1,i}$ and $k_{2,i}$ represent rate constants with respect to reactions (1) and (2) over a specific type (i) of surface: reactor wall, wire gauze, ZSM-5, or (in the next section) Cu-ZSM-5. It is to be expected that these rate constants depend on the oxygen and water concentrations. $S_{1,i}$ and $S_{2,i}$ are the total surface areas of type i

active in reactions 1 and 2, respectively. The net consumption rate of nitric oxide is the difference in rate between the two reactions:

$$-r'_{\text{NO}} [\text{mol}_{\text{NO}}/\text{s}] = r'_1 - r'_2 = \sum_i k_{1,i} S_{1,i} c_{\text{NO}}^A c_{\text{NH}_3}^B - \sum_i k_{2,i} S_{2,i} c_{\text{NH}_3}^D \quad (8-5)$$

The negative net nitric oxide consumption rates at low nitric oxide concentrations in Fig. 8-3 indicate that non-selective ammonia oxidation by oxygen, i.e., reaction (2), does indeed take place. The linear increase of the net nitric oxide consumption rate with the nitric oxide concentration suggests that the reduction of nitric oxide is first order in the nitric oxide concentration, i.e., that constant A equals 1.

It will be made plausible in the following section that the reduction of nitric oxide is zero order in ammonia ($B = 0$), and that the oxidation of ammonia to nitric oxide is first order in ammonia ($D = 1$). From the reactor equations of an ideal CSTR, the dependence can then be derived of the net nitric oxide consumption rate on the volumetric flowrate ϕ_V , the inlet ammonia concentration and the outlet nitric oxide concentration:

$$-r'_{\text{NO}} [\text{mol}_{\text{NO}}/\text{s}] = \left[1 + \left(\frac{1}{\frac{\phi_V}{\sum_i k_{2,i} S_{2,i}} + 1} \right) \right] \left(\sum_i k_{1,i} S_{1,i} \right) c_{\text{NO}} - \left[\frac{1}{\frac{\phi_V}{\sum_i k_{2,i} S_{2,i}} + 1} \right] c_{\text{NH}_3, \text{feed}} \quad (8-6)$$

Eq. (8-6) shows that the values of $\sum k_{1,i} S_{1,i}$ and $\sum k_{2,i} S_{2,i}$ can be estimated from the slope and vertical axis intercept of Fig. 8-3. The results of this procedure are given in the upper part of Table 8-2. A striking result is that $\sum k_{1,i} S_{1,i}$ and $\sum k_{2,i} S_{2,i}$ are highest for the empty reactor. In other words, the reduction of nitric oxide or the oxidation of ammonia to nitric oxide by the wire gauze or the non-exchanged supported ZSM-5 crystals, is insignificant.

As will be shown in the following section, the values of $\sum k_{1,i} S_{1,i}$ and $\sum k_{2,i} S_{2,i}$ found with an empty reactor or with bare wire gauze or non-exchanged supported ZSM-5, are small compared to those obtained in the presence of Cu-ZSM-5. This implies that the kinetic data are not significantly falsified by the catalytic effect of surfaces other than that of Cu-ZSM-5.

3.2 Kinetic experiments with Cu-ZSM-5 catalyst packing

The results of the tests on deNO_x-activity of the prepared Cu-ZSM-5 catalyst packing, and the effect of water, oxygen and ammonia on this activity, are presented in Fig. 8-4. These results were not corrected for catalytic effects of the reactor wall etc., discussed in the previous section. The straight lines suggest that the reduction of nitric

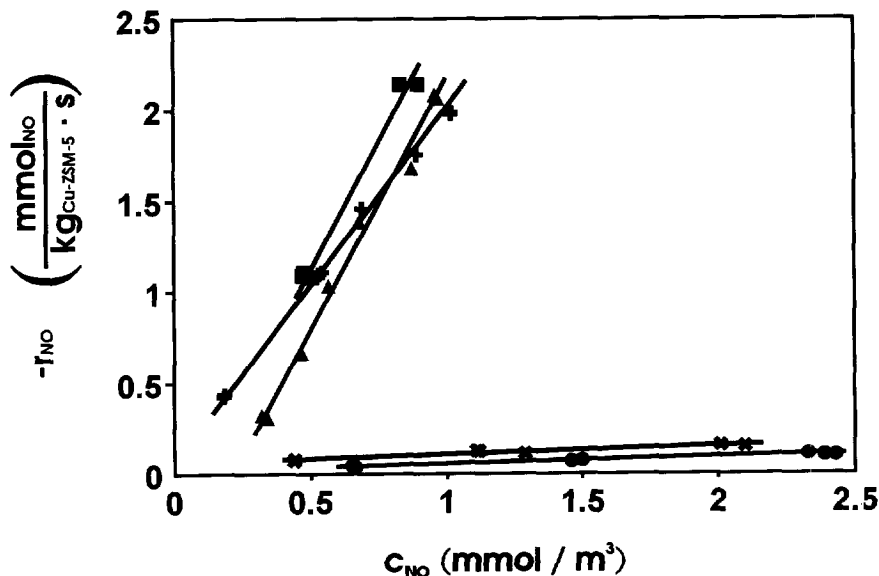


Figure 8-4 Net consumption rate of nitric oxide ($-r_{\text{NO}}$) versus nitric oxide concentration in the reactor (c_{NO}), over Cu-ZSM-5 *in situ* grown on wire gauze, at 350°C; gas composition besides nitric oxide (balance nitrogen): (+) 15 vol. % water, 5 vol. % oxygen, 1000 ppmv ammonia; (▲) 5 vol. % oxygen, 1000 ppmv ammonia; (X) 15 vol. % water, 1000 ppmv ammonia; (●) 1000 ppmv ammonia; (■) 5 vol. % oxygen, ammonia:NO 1:1.

oxide over Cu-ZSM-5 is first order in the nitric oxide concentration; this corresponds with literature on Cu-exchanged H-mordenite (Nam et al., 1987). The values of $\Sigma k_{1,i}S_{1,i}$ and $\Sigma k_{2,i}S_{2,i}$ were deduced using Eq. (8-6); the results are given in the lower part of Table 8-2. It is important to realize, that the value in each cell of the table is the sum of the catalytic effects of all types of surface present in the reactor during that test.

Table 8-2 shows that for a fixed test gas composition $\Sigma k_{2,i}S_{2,i}$ is about five times higher in the presence of supported Cu-ZSM-5, than in the empty reactor. The value of $\Sigma k_{1,i}S_{1,i}$ is about 30 times higher in the presence of supported Cu-ZSM-5 than in the empty reactor. Consequently, the catalytic effect of surfaces other than that of Cu-ZSM-5 is negligible. Consequently the net NO consumption rate plotted in Fig. 8-4 is expressed per unit mass of Cu-ZSM-5.

The ratio of the rate constants for reactions (1) and (2), is a measure for the selectivity of the Cu-ZSM-5 catalyst. From Table 8-2 it follows that this selectivity is about 93:1 in the absence of water.

Water appears to have a strong effect on the oxidation of ammonia to nitric oxide over Cu-ZSM-5: the presence of 15 vol. % water in the test gas virtually eliminates oxidation of ammonia to nitric oxide. The effect of water on the reduction of nitric oxide is less profound: as Table 8-2 shows, the presence of 15 vol. % water reduces

Table 8-2 Catalytic effects of the empty reactor, bare wire gauze, non-exchanged ZSM-5, and Cu-ZSM-5, for oxidation of NH₃ to NO ($\Sigma k_{2,i} S_{2,i}$) and reduction of NO ($\Sigma k_{1,i} S_{1,i}$), under various conditions, all at 350°C.

surface	gas composition (balance N ₂)	$\Sigma k_{2,i} S_{2,i}$ [m ³ /s]	$\Sigma k_{1,i} S_{1,i}$ [m ³ /s]
empty reactor	0% H ₂ O 5 vol. % O ₂ 1000 ppmv NH ₃	1.86 x 10 ⁻⁶	2.63 x 10 ⁻⁵
gauze	0% H ₂ O 5 vol. % O ₂ 1000 ppmv NH ₃	1.64 x 10 ⁻⁶	1.85 x 10 ⁻⁵
ZSM-5	0% H ₂ O 5 vol. % O ₂ 1000 ppmv NH ₃	5.21 x 10 ⁻⁷	1.72 x 10 ⁻⁵
Cu-ZSM-5	0% H ₂ O 5 vol. % O ₂ 1000 ppmv NH ₃	8.19 x 10 ⁻⁶	7.66 x 10 ⁻⁴
Cu-ZSM-5	15 vol. % H ₂ O 5 vol. % O ₂ 1000 ppmv NH ₃	≪ 8 x 10 ⁻⁶	5.44 x 10 ⁻⁴
Cu-ZSM-5	0% H ₂ O 5 vol. % O ₂ 1:1 ppmv NH ₃	8.10 x 10 ⁻⁶	7.14 x 10 ⁻⁴
Cu-ZSM-5	0% H ₂ O 0% O ₂ 1000 ppmv NH ₃		≈ 1.04 x 10 ⁻⁵
Cu-ZSM-5	15 vol. % H ₂ O 0% O ₂ 1000 ppmv NH ₃		≈ 1.46 x 10 ⁻⁵

the nitric oxide reduction rate by only 30%. Consequently, the selectivity of the catalyst is increased to at least 10³:1. A striking result of the increased selectivity due to water, is the fact that at low nitric oxide concentrations (< 20 ppmv) the net NO consumption rate is larger in the presence of 15 vol. % water than in its absence. The effect of water is believed to be caused by competition between ammonia and water for coordination of the ionic copper sites in the zeolite. As is shown in this paper, these sites dominate both the NO reduction rate and the non-selective ammonia oxidation rate.

It should be noted that due to the type of reactor used for this investigation, it is almost impossible to fully exclude water from the reaction mixture. Even when the feed gas contains no water, the gas mixture in the reactor will contain water produced

by both reactions (1) and (2). Furthermore, the compressed air used as the oxygen source of the gas mixture, contained about 1000 ppmv water. Under the given conditions, when no water is added to the gas mixture, the water concentration in the reactor was estimated to be 400 ppmv, most of which came with the compressed air. It has been assumed that this concentration is negligible in the kinetic investigation, especially when compared to the 15 vol. % water used in the rest of the experiments. The reason for this assumption is the fact that the interaction between water and the Lewis acidic ionic copper sites of the zeolitic catalyst is much weaker than between ammonia and the sites, since the basicity of ammonia is much higher than that of water. Consequently, the influence of 400 ppmv water is expected to be negligible in the presence of 1000 ppmv ammonia.

Oxygen, like water, also has a strong effect on the nitric oxide reduction rate. Exclusion of oxygen from the test gas reduces the nitric oxide reduction rate with more than 97%, both in the presence and absence of 15 vol. % water in the test gas. This can be understood from the fact that oxygen is needed for the reaction.

Reduction of the large excess of ammonia to a stoichiometric ratio nitric oxide : ammonia of 1 : 1, has only a small effect on the nitric oxide reduction rate: the rate constant of nitric oxide reduction decreases with merely 7%, upon a 95% decrease of the ammonia concentration in the reactor. This indicates that down to stoichiometric nitric oxide : ammonia ratios, the nitric oxide reduction rate is almost independent of the ammonia concentration; it confirms the assumption made in the previous section, that the constant B in Eq. (8-3), is close to 0. It also shows that the conclusions of this kinetic study can be extended to a stoichiometric NO/NH₃ ratio, which is relevant for industrial applications.

The intercept with the vertical axis of the line representing the experiments at stoichiometric NO/NH₃ ratios in Fig. 8-4, is very small compared to the one of the experiments at a large ammonia excess. In fact the 95% confidence interval of the line includes the origin. According to Eq. (8-6), the (absolute) value of the intercept is a measure of the rate of reaction (2). Consequently, these results show that the rate of reaction (2) depends on the ammonia concentration, i.e., that constant D does not equal 0. The fact that the value of the intercept is statistically insignificant, corresponds to a value of 1 for constant D when the rate of reaction (2) is very small compared to that of reaction (1). In that case (i.e., [NH₃/NO]_{feed} = 1, A = 1, B = 0, D = 1, r₂ ≪ r₁) the ammonia concentration in the reactor will be approximately equal to the NO concentration, and Eq. (8-5) can be rewritten into:

$$-r_{\text{NO}} \left[\frac{\text{mol}_{\text{NO}}}{\text{kg}_{\text{Cu-ZSM-5}} \text{ s}} \right] = (k_1 - k_2) c_{\text{NO}} \quad (8-7)$$

where k_1 and k_2 are the rate constants of reactions (1) and (2) over Cu-ZSM-5. Consequently, the (straight) line would go through the origin, and the only effect of reaction (2) would be a very small decrease of the slope compared to the experiments with a large ammonia excess. This corresponds to what is observed.

From this reasoning it is concluded that the constant D is closer to 1 than to 0. At lower ammonia concentrations the order will be even closer to 1, because the reaction proceeds through adsorption of ammonia on the catalytic sites.

3.3 Comparison with amorphous vanadia-titania/silica catalysts

The activity of the Cu-ZSM-5 catalyst packing was compared with that of a catalyst consisting of 5 % mass vanadia and titania on amorphous silica.

The activity can be compared on various bases. For a catalyst researcher, comparison based on turn-over frequency (TOF) is relevant. However, for a chemical engineer, comparison based on activity per kg catalyst (i.e., carrier plus active metals), per kg catalyst packing (i.e., including a support or structure), or per m³ packing (so defining the reactor size), is more relevant. Table 8-3 lists three ways of comparison.

Table 8-3 Comparison of the activity of the prepared Cu-ZSM-5 catalyst packing with the activity of a vanadia-titania/silica deNO_x catalyst, at 350°C.

basis of comparison	activity of supported Cu-ZSM-5 relative to V-Ti/silica
mole of active metal	30
kg of carrier plus active metal	3.5
kg of catalyst packing	0.13

The much higher activity per atom of active metal of the Cu-ZSM-5 underlines the great potential of exchanged zeolites as heterogeneous catalysts. The activity per kg of zeolite could be further increased by reducing the Si/Al ratio from 44.1 to the theoretical minimum of 12, thus enhancing the ion exchange capacity. Finally, the activity per kg of catalyst packing could be increased by growing more or larger crystals on the support: the tested catalyst packing contained only 3.5 % mass zeolite crystals, whereas recently packings containing 44 % mass zeolite crystals have been prepared (Wolterbeek, 1993).

Therefore, the activity per kg of catalyst packing could be increased significantly (presumably by a factor 20), resulting in a packing that is about twice as active (based on total mass, including support material) as the commercially used amorphous vanadia-titania/silica catalysts.

3.4 Applicability of supported Cu-ZSM-5 for dust, steam and SO₂ containing flue gases

Features of the prepared catalyst packing that are important with respect to application for real flue gases, are its stability toward dust, steam and SO₂. Stability toward abrasive forces of dust particles in the flue gas is expected to be sufficient, because the crystals are chemically bonded to the surface. As was mentioned before, the zeolites can only be removed from the support by breaking the crystals themselves (and not the crystal-support bond), using a sharp tool. Yet the mechanical stability will be subject of further investigation.

Stability toward steam is an issue, because the combination of steam and high temperature is known to cause dealumination of zeolites, leading to loss of catalytic activity. Even ZSM-5, which is regarded an unusually stable zeolite, was shown to suffer from dramatic dealumination under severe conditions, i.e., 100% steam at 600°C (Sano et al., 1987). However, in the present study no signs of deactivation were found during the experiments (five days on stream). The first explanation is the significant activation energy of ZSM-5 dealumination (88 kJ/mol at 500-600°C, according to Sano et al. (1987)), which predicts a 130 times lower dealumination rate at 350°C (present study) than at 600°C (Sano et al.). The second explanation is the fact that hydrothermal dealumination has been found to be inhibited by cation exchange into the zeolite, such as alkaline earth metal ions (Fujisawa et al., 1987), alkali metal ions (Suzuki et al., 1987) and also copper ions (Shelef, 1993; Kharas et al., 1993). However, literature is not univocal on this subject: whereas Shelef (1993) reported that still "a certain fraction" of the Al-ions is rapidly lost from the framework of Cu-ZSM-5 in a stream containing 10% steam at 410°C, Kharas et al. (1993) concluded that Cu-ZSM-5 is "stable" with respect to dealumination under catalytic conditions, even at temperatures higher than 600°C.

The stability of Cu-ZSM-5 toward SO₂ is interesting because of the known inhibitive effect of SO₂ on CuO- γ -Al₂O₃ three-way catalysts for automotive exhaust cleaning. However, Iwamoto et al. (1991) concluded that SCR of NO by propene over Cu-ZSM-5, in the presence of oxygen, has a high resistance to the inhibition by SO₂. Furthermore Ham et al. (1992) reported that Cu-exchanged hydrogen-mordenite zeolite did not lose its initial activity during up to 50 h of operation at temperatures over 300°C, despite SO₂ concentrations ranging from 500 to 20,000 ppmv. Finally, Kharas (1993) concludes that Cu-ZSM-5 is relatively insensitive to inhibition by SO₂ in automotive exhaust gas. Based on this literature it is concluded that the possible interaction between the copper ions in Cu-ZSM-5 and SO₂ does not lead to direct deactivation of the catalyst. Indirect deactivation may occur, however, due to oxidation of SO₂ to SO₃ (favored by a high temperature) and subsequent reaction with ammonia

to form ammoniumsulfates (favored by a low temperature) that block the catalyst pores (cf., e.g., Ham et al. (1992)).

Although the information presented here suggests that the prepared catalyst packing is stable in a flue gas, it should be noted that a recent study (Kharas et al., 1993) has shown that at temperatures higher than 600°C, sintering of Cu in Cu-ZSM-5 may occur. It is suspected by these authors that at such high temperatures, catalysis causes copper ions to become highly mobile, resulting in sintering to form CuO and Cu₂O. This reduces the number of catalytic sites; furthermore the growth of copper oxide crystallites may destroy the zeolite framework. This phenomenon would imply that the prepared catalyst packing is less suitable for automotive exhaust cleaning processes, where gas temperatures higher than 600°C are common. However, application for industrial flue gas treatment remains feasible, since typical flue gas temperatures are between 130 and 400°C.

4 Conclusions

In situ growth of zeolite crystals on a structured support is a promising new technique to apply zeolitic catalysts in dustproof, low pressure drop reactors. The catalyst packing consisting of Cu-exchanged ZSM-5 zeolite, *in situ* grown on metal wire gauze, promises to be very suitable for industrial deNO_x processes, for the following reasons:

1. the activity per atom of active metal is 30 times higher than for commercially used amorphous vanadia-titania/silica catalysts; the activity per kg of catalyst packing can be increased to become significantly higher than for amorphous vanadia-titania/silica catalysts;
2. at realistic deNO_x conditions the activity of the prepared catalyst packing toward reduction of nitric oxide is more than 1000 times higher than toward oxidation of ammonia to nitric oxide, so the catalyst has a very high selectivity;
3. the metal wire gauze can be shaped prior to zeolite synthesis, so a structured catalyst packing can be produced that gives an extremely low pressure drop across the packing; such packings are also expected to allow dustproof operation.

The nitric oxide reduction rate can be described with the following empirical rate equation:

$$-r_{\text{NO}} = k \cdot c_{\text{NO}}^{1.0} c_{\text{NH}_3}^{0.0} c_{\text{O}_2}^n c_{\text{H}_2\text{O}}^m \quad (8-8)$$

in which n is bigger than zero and m is smaller than zero. This rate equation pertains to ammonia to nitric oxide ratios of one and higher.

Although the feasibility of the *in situ* grown supported zeolites was illustrated with SCR of NO over Cu-ZSM-5, it is obvious that this technique to employ zeolite catalysts in dustproof, low pressure drop reactors can be applied for many other combinations of zeolite and active metal.

Acknowledgements

Colette Legein, Willem Wolterbeek and Ben Leung are gratefully acknowledged for their substantial contribution to the work reported in this chapter.

Notation

c_A	gas phase concentration of component A in reactor and product stream	$[\text{mol}_A / \text{m}^3_{\text{gas}}]$
$c_{A,\text{feed}}$	gas phase concentration of component A in feed mixture	$[\text{mol}_A / \text{m}^3_{\text{gas}}]$
k	reaction rate constant for NO reduction	$[\text{m}^3_{\text{gas}} \cdot (\text{m}^3_{\text{gas}} / \text{mol})^{n+m} / \text{kg}_{\text{Cu-ZSM-5}} \cdot \text{s}]$
k_1, k_2	rate constant of reactions (1) and (2) over Cu-ZSM-5	$[\text{m}^3_{\text{gas}} / \text{kg}_{\text{Cu-ZSM-5}} \cdot \text{s}]$
$k_{1,i}$	rate constant pertaining to reaction (1), over surface type i	$[\text{m}^3_{\text{gas}} / \text{m}^2_i \cdot \text{s}]$
n, m	reaction rate orders of NO reduction in oxygen and water, respectively	$[-]$
r_1'	rate of reaction (1)	$[\text{mol}/\text{s}]$
$-r_{\text{NO}}$	nitric oxide consumption rate	$[\text{mol}_{\text{NO}} / \text{kg}_{\text{cat}} \cdot \text{s}]$
$-r'_{\text{NO}}$	nitric oxide consumption rate	$[\text{mol}_{\text{NO}} / \text{s}]$
$S_{1,i}$	surface of type i , active in reaction (1)	$[\text{m}^2_i]$

Greek letter

ϕ_V	volumetric flowrate to (and from) the reactor	$[\text{m}^3_{\text{gas}} / \text{s}]$
----------	-----------------------------------------------	----------------------------------------

References

- Van den Bleek, C.M. and Van den Berg, P.J., 1980, The Difficulty of Reducing Nitrogen Oxides in the Presence of Oxygen. *J. Chem. Tech. Biotechnol.* **30**, 467-475.
- Datka, J. and Tuznik, E., 1985, Hydroxyl groups and acid sites in Na-ZSM-5 zeolites studied by I.R. spectroscopy. *Zeolites* **5**, 230-232.
- Dessau, R.M., 1990, Base- and acid-catalysed cyclization of diketones over ZSM-5. *Zeolites* **10**, 205-206.
- Fujisawa, K., Sano, T., Suzuki, K., Okado, H., Kawamura, K., Kohtoku, Y., Shin, S., Hagiwara, H. and Takaya, H., 1987, The Steam Stability of H-ZSM-5-Type Zeolites Containing Alkaline Earth Metals. *Bull. Chem. Soc. Jpn.* **60**, 791-793.
- Giamello, E., Murphy, D., Magnacca, G., Morterra, C., Shioya, Y., Nomura, T. and Anpo, M., 1992, The Interaction of NO with Copper Ions in ZSM5: An EPR and IR Investigation. *J. Catal.* **136**, 510-520.
- Hall, W.K. and Valyon, J., 1992, Mechanism of NO decomposition over Cu-ZSM-5. *Catal. Lett.* **15**, 311-315.
- Ham, S., Choi, H., Nam, I. and Kim, Y.G., 1992, Deactivation of copper-ion-exchanged hydrogen-mordenite-type zeolite catalyst by SO₂ for NO reduction by NH₃. *Catal. Today* **11**, 611-621.
- Held, W., Koenig, A. and Puppe, L., 1990, Nitrogen oxide reduction process for diesel exhaust gases using zeolite-containing catalysts. German Patent 3,830,045, 15 March 1990.
- Held, W., Koenig, A. and Puppe, L., 1991, Reduction of nitrogen oxides in waste gases. German Patent 4,003,515, 8 August 1991.
- Hofmann, H. and Weidner, B., 1989, Kinetik der selektiven katalytische Reduktion von Stickoxiden mit Katalysatoren auf V-W-TiO₂-Basis. *DECHEMA Monographien* **118**, 17-30.
- Ito, E., Hultermans, R.J., Lugt, P.M., Burgers, M.H.W., Van Bekkum, H. and Van den Bleek, C.M., 1994a, Selective Reduction of NO_x with Ammonia over Cerium Exchanged Zeolite Catalysts: Towards a Solution for an Ammonia Slip Problem, in *Preprints of the Third Int. Congress On Catalysis and Automotive Pollution Control (CAPOC3)*, 20-22 April (Edited by A. Frennet and J.M. Bastin), pp. 419-428. Brussels.

- Ito, E., Hultermans, R.J., Lugt, P.M., Burgers, M.H.W., Rigutto, M.S., Van Bekkum, H. and Van den Bleek, C.M., 1994b, Selective Reduction of NO with Ammonia over Cerium-exchanged Mordenite. *Appl. Catal. B* **4**, 95-104.
- d'Itri, J.L. and Sachtler, W.M.H., 1992, Reduction of NO over impregnated Cu/ZSM-5 in the presence of O₂. *Catal. Lett.* **15**, 289-295.
- Iwamoto, M. and Hamada, H., 1991, Removal of Nitrogen Monoxide from Exhaust Gases through Novel Catalytic Processes. *Catal. Today* **10**, 57-71.
- Iwamoto, M., Yahiro, H., Mine, Y. and Kagawa, S., 1989, Excessively Copper Ion-exchanged ZSM-5 Zeolites as Highly Active Catalysts for Direct Decomposition of Nitrogen Monoxide. *Chem. Lett.*, 213-216.
- Iwamoto, M., Yahiro, H., Shundo, S., Yu-u, Y. and Mizuno, N., 1991, Influence of sulfur dioxide on catalytic removal of nitric oxide over copper ion-exchanged ZSM-5 zeolite. *Appl. Catal.* **69**, L15-L19.
- Jansen, J.C., Nugroho, W. and Van Bekkum, H., 1992, Controlled Growth of Thin Films of Molecular Sieves on Various Supports, in *Proc. 9th Int. Zeolite Conf.*, 5-10 July (Edited by R. Von Ballmoos, J.B. Higgins and M.M.J. Treacy), pp. 247-254. Montreal.
- Kharas, K.C.C., 1993, Performance, selectivity, and mechanism in Cu-ZSM-5 lean-burn catalysts. *Appl. Catal. B* **2**, 207-224.
- Kharas, K.C.C., Robota, H.J. and Liu, D.J., 1993, Deactivation in Cu-ZSM-5 lean-burn catalysts. *Appl. Catal. B* **2**, 225-237.
- Lachman, I.M. and Nordlie, L.A., 1986, High-strength High-surface-area Catalyst Supports. European Patent 197,645 A1, 23 December 1986.
- Lachman, I.M. and Patil, M.D., 1989, Method of Crystallizing a Zeolite on the Surface of a Monolithic Ceramic Substrate for Catalytic Use. European Patent 314,336 A2, 24 January 1989.
- Li, Y. and Armor, J.N., 1991, Temperature-programmed desorption of nitric oxide over Cu-ZSM-5. *Appl. Catal.* **76**, L1-L8.
- Li, Y. and Hall, W.K., 1991, Catalytic Decomposition of Nitric Oxide over Cu-Zeolites. *J. Catal.* **129**, 202-215.
- Montreuil, C.N. and Shelef, M., 1992, Selective reduction of nitric oxide over Cu-ZSM-5 zeolite by water-soluble oxygen-containing organic compounds. *Appl. Catal. B* **1**, L1-L8.
- Nam, I., Eldridge, J.W. and Kittrell, J.R., 1987, Nitric Oxide Reduction by Ammonia on Copper Exchanged Hydrogen Mordenite. *Stud. Surf. Sci. Catal.* **38**, 589-600.

- Sano, T., Suzuki, K., Shoji, H., Ikai, S., Okabe, K. and Murakami, T., 1987, Dealumination of ZSM-5 Zeolites with Water. *Chem. Lett.*, 1421-1424.
- Sato, S., Yu-u, Y., Yahiro, H., Mizuno, N. and Iwamoto, M., 1991, Cu-ZSM-5 zeolite as highly active catalyst for removal of nitrogen monoxide from emission of diesel engines. *Appl. Catal.* **70**, L1-L5.
- Shelef, M., 1992, On the mechanism of nitric oxide decomposition over Cu-ZSM-5. *Catal. Lett.* **15**, 305-310.
- Shelef, M., 1993, Nitric Oxide Reactions over Cu-ZSM-5: Mechanism and Applications. in *Book of Abstracts of the 1st European Congress on Catalysis*, 12-17 September, p. 878. Montpellier.
- Suzuki, K., Sano, T., Shoji, H., Murakami, T., Ikai, S., Shin, S., Hagiwara, H. and Takaya, H., 1987, Inhibition of Dealumination of ZSM-5 Zeolites by Alkali Metals. *Chem. Lett.*, 1507-1510.
- Teraoka, Y., Ogawa, H., Furukawa, H. and Kagawa, S., 1992, Influence of cocations on catalytic activity of copper ion-exchanged ZSM-5 zeolite for reduction of nitric oxide with ethene in the presence of oxygen. *Catal. Lett.* **12**, 361-366.
- Wolterbeek, W., 1993, Het prepareren, karakteriseren en testen van een systeem bestaande uit vanadium- en titaniumoxides op silicaliet, gegroeid op rvs gaas, ter verkrijging van een gestructureerde denox katalysator voor een lage-drukvalreactor. *MSc. Thesis*. Delft University of Technology, Delft.

Samenvatting



Ontwikkeling van stoffbestendige lage-drukvalreactoren met gestructureerde katalysatorpakkingen

— de Bead String Reactor en de Zeolite-covered Screen Reactor

Samenvatting

Diverse typen lage-drukvalreactoren met een min of meer gestructureerde katalysatorpakking worden op de markt aangeboden; commercieel succesvolle typen zijn de monolietreactor, de *radial flow* reactor, de *lateral flow* reactor en de *parallel passage* reactor. Als aanvulling op en als alternatief voor deze bestaande reactoren, worden in dit proefschrift twee nieuwe concepten voorgesteld: de *Bead String Reactor* (BSR) en de *Zeolite-covered Screen Reactor* (ZSR).

De BSR wordt gekarakteriseerd door het feit dat het katalysatormateriaal is bevestigd (door middel van zijn vorm) op draden, zodat 'kralenkettingen' ontstaan die parallel aan elkaar in de reactor zijn geordend, parallel aan (of dwars op) de stromingsrichting. Dit reactorconcept lijkt diverse aantrekkelijke mogelijkheden te bieden: een lage drukval over de reactor; de ontwerpvrijheid om de reactorporositeit te kiezen tussen de ongekend brede grenzen van 100% tot 10%; de mogelijkheid van lateraal transport van warmte en reactanten over de gehele reactordiameter; relatief goede stof- en warmte-overdracht tussen de fluïdumfase en de katalysatorfase; de mogelijkheid de reactor te vullen met (m.a.w. 'kralenkettingen' te maken van) standaard ringvormige of holle katalysatordeeltjes; de stoffbestendigheid van de reactor; het voorkomen van maldistributie van gas of vloeistof in driefasenprocessen; de mogelijkheid driefasenprocessen niet alleen in meestroom, maar ook in tegenstroom te bedrijven bij hoge gas- en vloeistofbelastingen; en tot slot de mogelijkheid om direkt warmte naar de katalysator massa te voeren door de draden waarop de katalysator is bevestigd, als elektrische verwarmingselementen te gebruiken.

In een eerste stap om de haalbaarheid van het BSR-concept voor gas/vast-processen vast te stellen, zijn drie reactorkundige aspecten van de BSR theoretisch en experimenteel onderzocht:

- (i) impulsoverdracht (d.w.z. drukval en gasverdeling);
- (ii) stofoverdracht (tussen fluïdum en katalysator);
- (iii) gevoeligheid voor vervuiling door stofdeeltjes.

-
- ad (i)* Voor het onderzoek aan impulsoverdracht in een BSR is een *cold flow* proefopstelling gebruikt met BSR modules op laboratoriumschaal, die waren gevuld met gladde staven, kettingen van keramische kralen en kettingen van geëxtrudeerde katalysatordeeltjes; het vaste materiaal was telkens in een regelmatige, vierkante ordening aangebracht. Met behulp van deze proefopstelling is de drukval over een representatief deel van de reactor gemeten, als functie van de staaf- of deeltjesdiameter, de relatieve steek van de staven of kettingen, de ruwheid van de staven of kettingen, en de gassnelheid. Met de theorie en experimentele gegevens die in dit proefschrift worden besproken, is het mogelijk de drukval over een typische BSR te voorspellen met een onnauwkeurigheid van enkele procenten (bij laminaire stroming of bij een kleine relatieve ruwheid) tot ca. 50% (bij overgangsstroming of bij volledig ruwe turbulente stroming).
- ad (ii)* Er zijn theoretische relaties afgeleid die de stofoverdrachtsnelheid beschrijven bij laminaire stroming, als functie van de reactor porositeit en de verhouding van de tijdconstanten voor reactie en stofoverdracht. Voor turbulente stroming zijn stofoverdrachtcoëfficiënten experimenteel bepaald via het meten van de gewichtsafname van sublimerende naftaleendeeltjes die in de 'kralenkettingen' waren geplaatst. Met deze experimenten is de invloed op de stofoverdrachtcoëfficiënt onderzocht van de axiale en laterale positie van de naftaleendeeltjes in de reactor, de diameter van de deeltjes, de steek van de 'kralenkettingen' en de gassnelheid. De belangrijkste conclusie van dit experimentele werk is dat op basis van eenvoudige drukvalmetingen, de stofoverdrachtcoëfficiënt in een typische BSR kan worden voorspeld met een onnauwkeurigheid van ca. 30%, door gebruik te maken van de Chilton-Colburn analogie tussen impuls- en stofoverdracht.
- ad (iii)* De gevoeligheid voor vervuiling van de BSR door stof, is onderzocht in een *cold flow* proefopstelling. Hierbij is industrieel vliegias van een kolengestookte elektriciteitscentrale gebruikt. Ter vergelijking zijn ook de stofvangsteigenschappen van de *parallel passage reactor* (PPR) onderzocht. Onder de condities die experimenteel zijn onderzocht, heeft de vervuiling door stof in geen van beide reactoren een significante invloed op de drukval. Er wordt verwacht dat de extra stofoverdrachtweerstand die wordt veroorzaakt door opgehoopt stof in de reactor, geen significante invloed zal hebben op de prestaties van de BSR. Echter, in de PPR kan opgehoopt stof leiden tot een decimering van de katalysatorbenutting.

Om de prestaties van een BSR te kunnen voorspellen, is een aantal mathematische modellen ontwikkeld. Deze modellen zijn experimenteel gevalideerd, waarbij de selectieve katalytische reductie (SCR) van stikstofmonoxide (NO) met een overmaat ammoniak, zuurstof en water als test-reactie diende. De NO-conversie in lab-schaal BSR-modules kon adequaat worden voorspeld (met een gemiddelde relatieve afwijking van 5%) m.b.v. een eenvoudig model dat slechts één gewone differentiaalvergelijking bevat en waarin de katalysatorbenuttingsgraad wordt geschat met gegeneraliseerde algebraïsche vergelijkingen. Complexere modellen geven een systematische over- of onderschatting van de conversie, wat verklaard kan worden uit de onderliggende aannames; deze modellen vertoonden

gemiddelde relatieve afwijkingen van ca. 10%. De nauwkeurigheid van de mathematische BSR-modellen is bevredigend, gezien het feit dat de modellen geen parameters bevatten die zijn gefit aan de validatie-experimenten: alle parameters in de modellen zijn op voorhand geschat op grond van theoretische relaties of onafhankelijke experimenten aan drukval, stofoverdracht, reactiekinetiek en katalysatorporiediffusie. De laatste twee typen experimenten zijn verricht in een interne *recycle reactor* van het Berty-type.

Op grond van deze studie kunnen de geclaimde voordelen van de BSR niet verworpen worden. Echter, of het BSR-concept al dan niet economisch haalbaar is, hangt volledig af van de prijzen die worden ingezet voor drukval, stofoverdracht, benutting van het reactorvolume, *etc.*, en van de vervaardigingskosten van modules met katalysator-kettingen. De kosten van het mechanisch rijgen van katalysatordeeltjes wordt geschat op een paar gulden per kilogram, wat een overkomelijk bedrag lijkt voor de wat duurdere katalysatoren. Derhalve is de conclusie gerechtvaardigd, dat een BSR voor gas/vast processen economisch aantrekkelijk zal zijn indien drukval duur is (*i.e.* indien sprake is van hoge gasdebieten en lage drukken), indien reactorvolume duur is (vanwege hoge drukken of ruimtebeperkingen) en/of indien intensieve of snelle verwarming van het katalysatormateriaal belangrijk is. De haalbaarheid van de BSR en gerelateerde reactoren voor gas/vloeistof/vast-systemen (*trickle flow*) zal worden onderzocht in een volgend promotie-onderzoek.

De tweede nieuwe reactor die in dit proefschrift wordt gepresenteerd, de *Zeolite-covered Screen Reactor* (ZSR), wordt gekarakteriseerd door katalysatorpakkingen die zijn vervaardigd door *in situ* kristallisatie van zeolietkristallen op een gestructureerde drager. De drager kan bestaan uit bijvoorbeeld metaalgaas of metaalfolie, waarvan vlakke of geribbelde platen worden opgestapeld of opgerold tot een pakkingselement. Het ZSR-concept opent de weg naar lage-drukvalreactoren met zeolietkatalysatoren die optimaal toegankelijk zijn voor de reactanten. De ZSR deelt de voordelen van de monolietreactor bestaande uit een *washcoat* op een metalen of keramieken drager, en zal derhalve vooral aantrekkelijk zijn ingeval van zeer snelle reacties. Mogelijke toepassingen zijn katalytische rookgasreiniging en koolwaterstofomzettingen, zoals de selectieve partiële oxidatie van kleine koolwaterstoffen. Vooral in de laatste toepassing is het voordeel van de goede katalysator-toegankelijkheid belangrijk, omdat een korte contacttijd een hoge selectiviteit bevordert.

Om het ZSR-concept te demonstreren, is een pakking vervaardigd door *in situ* kristallisatie van de zeoliet ZSM-5 op metaalgaas. Nadat koperionen waren ingebracht d.m.v. ionenwisseling, werd de pakking getest op activiteit voor de SCR van stikstofmonoxide met ammoniak bij 350°C. Zowel de activiteit als de selectiviteit van de katalysatorpakking bleken hoger te zijn dan die van 'conventionele' vanadium/titaniumkatalysatoren. Dit toont de haalbaarheid van het ZSR-concept aan, en derhalve zal dit type reactor verder worden ontwikkeld in een volgend promotie-onderzoek.

Dankwoord



Dankwoord

Het feit dat ik de afgelopen vier jaar met veel plezier¹ ongeveer duizend keer tussen Nootdorp en De Proeffabriek heen en weer fietste, heeft niet alleen te maken met de aard van het promotie-onderzoek, maar vooral met de mensen op de werkplek. Hoewel de meesten meewarig het hoofd schudden als ik weer eens met een prototype van een gestructureerde reactorpakking onder de arm langs kwam rennen in de gangen van ons fraaie gebouw, hebben allen zich op gezette tijden ingespannen om technische, psychische, bureaucratische, wetenschappelijke, filosofische of fysieke bijstand te geven. Het was vooral erg ontroerend om dertig vrijwilligers een middag lang katalysatorkralen met gaatjes van 0,4 mmØ te zien rijgen. Daarom wil ik alle technische, ondersteunende, beherende, wetenschappelijke en opgeleid wordende collega's bedanken voor de gezelligheid en het mede mogelijk maken van het onderzoek.

De meeste dank ben ik echter verschuldigd aan alle afstudeerders die hun afstudeeronderzoek hebben verricht binnen of grenzend aan de 'kralenclub' en die zich geheel belangeloos 6+ maanden te pletter hebben gewerkt om de wetenschap vooruit te duwen. In chronologische volgorde: Freddy, Jos, Marco, Arie, Dorus, Ben, Christien, Joeri, Joke, Colette, Else, Willem, Otto, Paul, Lilian, John, Sico, Frank, Adi, Martin, Niek en Henk. Zij hebben nagenoeg alle metingen verricht die in dit proefschrift beschreven staan, en bovendien de basis gelegd voor de modellering van de BSR en de PPR. Hoewel niet al het afstudeerwerk in dit proefschrift beschreven staat (b.v. omdat het buiten de 'scope' van het verhaal viel of omdat het boekje anders nóg dikker zou worden), heeft elk stuk onderzoek en ontwikkeling er in belangrijke mate aan bijgedragen.

Daarnaast wil ik Kálmán en Åsa bedanken voor hun inzet als 'research fellows', waarmee ook zij het onderzoek in belangrijke mate hebben voortgestuwd. In dit rijtje hoort ook Ernst thuis, enerzijds vanwege het op poten zetten van het stofvangstonderzoek in zijn TWAIO-tijd, anderzijds vanwege de samenwerking in de 'lustrumactiviteiten'.

Tot slot wil ik Albert, Angela, Anton, Cock en Jaap, de 'vaste staffers' die samen het cement vormen dat de bonte club van Chemical Reactor Engineers in Delft bijeenhoudt, bedanken voor alle aanmoedigingen, tegensputtingen, ideeën, belangstelling, hulp, vertrouwen, enthousiasme en wijze raad gedurende de afgelopen vier jaar.

¹ behalve die 500 keren dat het regende...



Curriculum Vitae



Curriculum Vitae

Naam: Hans Peter Alexander Calis (HP)

Geboortedatum en -plaats: 30 januari 1967, Woudenberg

Middelbare school: 1979-1985, VWO

Universitaire studie: 1985-1990, Scheikundige Technologie aan de Technische Universiteit Delft

Kwalificaties getuigschriften: Propaedeutisch en doctoraal examen behaald met lof
